PASSIVE WIRELESS WALL SHEAR STRESS SENSORS

By

JEREMY SELLS

A DISSERTATION PRESENTED TO THE GRADUATE SCHOOL
OF THE UNIVERSITY OF FLORIDA IN PARTIAL FULFILLMENT
OF THE REQUIREMENTS FOR THE DEGREE OF
DOCTOR OF PHILOSOPHY

UNIVERSITY OF FLORIDA

2011

المنارة للاستشارات

www.manaraa.com

UMI Number: 3492545

All rights reserved

INFORMATION TO ALL USERS
The quality of this reproduction is dependent on the quality of the copy submitted.

In the unlikely event that the author did not send a complete manuscript
and there are missing pages, these will be noted. Also, if material had to be removed,
a note will indicate the deletion.

UMI 3492545

Copyright 2012 by ProQuest LLC.

All rights reserved. This edition of the work is protected against
unauthorized copying under Title 17, United States Code.

ProQuest LLC.
789 East Eisenhower Parkway
P.O. Box 1346
Ann Arbor, MI 48106 - 1346

المنارة للاستشارات

www.manaraa.com

© 2011 Jeremy Sells

المنارة للاستشارات
www.manaraa.com

To my loving wife, Keri, who supported me
through all the late nights and long hours

المنارة للاستشارات
www.manaraa.com

ACKNOWLEDGMENTS

I would like to start by acknowledging my chairman, Dr. David P. Arnold. He has been a great teacher, mentor, and professional advisor. He has provided me with the many opportunities that have propelled me to this point in my career. This work would not have been possible without his guidance. I would also like to thank the rest of my committee: Dr. Mark Sheplak whose work in the field of shear stress sensors is the basis of much of this work, Dr. Henry Zmuda who is one of my professors and technical advisors in the area of electromagnetic field theory, and Dr. Louis Cattafesta whose tutelage resulted in much of my experimental and data analysis knowledge.

I would like to thank my technical mentors at the National Aeronautics and Space Administration (NASA) Langley Research Center: Catherine McGinley and George Beeler who helped to coordinate my two summer internships in 2008 and 2009. These experiences provided me with the expertise, skills, and confidence to excel in both an academic and professional work place.

Most of all, I have to thank all of my colleagues and peers in the Interdisciplinary Microsystems Group (IMG). More than any other source, the hours of discussion in front of a white board have produced the seeds of ideas presented in this work. Specifically, I have to thank Dr. Vijay Chandrasekharan who was my partner on the NASA project. His dissertation work on the wired version of the first generation sensors paved the way for the wireless sensor's success. My newest partner on the NASA project has been Jess Meloy, who has replaced Vijay on the wired sensors since his graduation. I also have to thank my undergraduate assistant, Zachary Kaufman, who collected a lot of the data presented in this dissertation and who built the circuitry for the electrostatic actuation test. Tai-An Chen gave me my first introduction and training on microfabrication in the cleanroom. I also received fabrication and characterization help from

www.manaraa.com

Niagong Wang, Sheetal Shetye, and Janhavi Agashe. I had many academic discussions with officemates, Alex Phipps, Drew Wetzel and Matt Williams where I learned things from other fields that I was able to use for my own work.

Two sensor generations were fabricated and packaged entirely in-house here in the Nanoscale Research Facility (NRF) at the University of Florida. I would like to thank all of the support staff at NRF and especially the cleanroom techs, Al Ogden, Bill Lewis, David Hays, and Ivan Kravchenko. Packaging and testing of the sensors would not have been possible without Ken Reed at TMR Engineering.

I have to thank NASA for the financial support of this work. This project was supported by NRA Grant NNX07AB27A under the Subsonic Fixed Wing Project, which is a part of the Aeronautics Research Mission Directorate. Personal funding was supplied by a NASA GSRP fellowship and ARMD scholarship under Grant NNXO7AT43H. Anthony Springer at NASA headquarters and Angela Medyk with the University of Florida Grants Office went above and beyond to help me with my fellowship.

There are many people that I have to thank for help in editing this dissertation. My advisor, Dr. David Arnold, went above and beyond in helping me edit this document, both for grammar and language as well as for technical accuracy. Dr. Zmuda, Dr. Catafesta, and Dr. Sheplak of my committee contributed technical edits toward the completion of this work. The copy editing of this dissertation was performed by Dr. Victoria of www.Edit911.com. I owe both Dr. Victoria and Dr. Baldwin, the Editor in Chief of Edit911, a huge debt of gratitude for coming through for me when my deadlines were looming. I also had help with individual chapter edits from some of my colleagues at IMG, specifically Dr. Vijay Chandrasekharan, Jess Meloy, Brandon Bertolucci, and Erin Patrick.

المنارة للاستشارات
www.manaraa.com

TABLE OF CONTENTS

page

ACKNOWLEDGMENTS 4

LIST OF TABLES 9

LIST OF FIGURES 11

ABSTRACT....18

CHAPTER

1 INTRODUCTION 19

1.1 Basic Sensor Operation 22
1.2 Specific Applications 24
1.3 Dissertation Organization....28

2 BACKGROUND 29

2.1 Wireless Sensor History....29
2.2 Passive Wireless Literature Review....31
2.2.1 Review of Work Done at the Institute for Visual Sciences....32
2.2.2 Review of Work Done at Uppsala University in Sweden 33
2.2.3 Review of Work Done at the Korean Institute of Science and Technology.....34
2.2.4 Review of Work Done at Pennsylvania State University....36
2.2.5 Review of Work Done at the University of Michigan....37
2.2.6 Review of Work Done at the University of Minnesota....38
2.2.7 Review of Work Done at the Georgia Institute of Technology....39
2.2.8 Review of Work Done at the California Institute of Technology 40
2.3 Summary 40

3 SENSOR MODELING....44

3.1 Coil and Antenna Models 44
3.1.1 Sensor Coil and Antenna Inductance....45
3.1.2 Mutual-Inductance....50
3.1.3 Parasitics....52
3.2 Capacitive Shear Stress Sensor 55
3.2.1 Mechanical Model 55
3.2.2 Capacitance Model 57
3.2.3 Parasitics....62
3.3 Full Sensor Model....69
3.3.1 Single Sensor Model....70
3.3.2 Coupled Resonators....72
3.3.3 Quality Factor at Resonance....76

المنارة للاستشارات
www.manaraa.com

3.3.4 Multiple Sensor Array Model 77

4 EXPERIMENTAL SETUPS 80

4.1 Die Level Testing 80
4.1.1 Electrical Impedance Testing 80
4.1.2 Electrostatic Actuation Testing 82
4.2 Wireless Sensor Testing 84
4.2.1 Network Analyzer Resonance Tracking 84
4.2.2 Noise Floor and Frequency Stability Testing 86
4.2.3 Humidity Sensitivity Testing 87
4.2.4 Static Calibration Testing 89
4.2.5 Wind Tunnel Testing 91

5 FIRST-GENERATION DEVICES 97

5.1 Device Overview 97
5.1.1 Coil and Antenna Modeling Results 98
5.1.2 Capacitive Sensor Modeling Results 103
5.1.3 Completed Model Results 107
5.2 Fabrication and Packaging 108
5.2.1 Process Flow 109
5.2.2 Hybrid Packaging 111
5.3 Experimental Results 113
5.3.1 Impedance Characterization 114
5.3.2 Electrostatic Actuation Test 117
5.3.3 Wireless Resonant Frequency, Stability, and Noise Floor 118
5.3.4 Static Shear Flow Calibrations 122
5.3.5 Wireless Range Test for Design 1 124
5.3.6 Wireless Humidity Test for Design 1 126
5.3.7 NASA 20 x 28 Wind Tunnel Test of Design 2 127

6 SECOND-GENERATION DEVICES 131

6.1 Design Improvements 132
6.1.1 Sensor Structure 132
6.1.2 Parasitics 134
6.1.3 Humidity Sensitivity 134
6.2 Device Overview 136
6.2.1 Coil and Antenna Modeling Results 136
6.2.2 Capacitive Sensor Modeling Results 137
6.2.3 Completed Model Results 140
6.3 Fabrication And Packaging 142
6.4 Experimental Results 144
6.4.1 Impedance Characterization 145
6.4.2 Wireless Resonance Stability 146
6.4.3 Wireless Humidity Tests 147

للاستشارات المنارة
www.manaraa.com

6.4.4 Static Shear Flow Calibrations 148

7 CONCLUSIONS AND FUTURE WORK 152

7.1 Summary 152
7.2 Research Contributions 154
7.3 Future Work 154
7.3.1 Future Generations 155
7.3.2 Additional Testing 157
7.3.3 System Optimization 159

APPENDIX

A LINEARITY DERIVATIONS 161

A.1 Mechanical Nonlinearity 161
A.2 Capacitive Nonlinearity 162
A.3 Resonant Nonlinearity 163
A.4 Cascaded Results 165

B IMPEDANCE DERIVATIONS 166

B.1 Single Sensor 166
B.2 Array of Sensors With No Inter-Sensor Coupling 167
B.3 Array of Sensor With Inter-Sensor Coupling 168

C COUPLED RESONATOR FREQUENCY DEPENDANCE 170

C.1 Same Resonant Frequencies 170
C.2 Different Resonant Frequencies 172

D QUALITY FACTOR DERIVATIONS 175

D.1 Inductors and Capacitors 175
D.2 Simple RLC Resonant Circuits 177
D.3 Wireless Shear Stress Sensor Quality Factor 178

E COMB FINGER ELECTROSTATIC PULL-IN DERIVATIONS 180

E.1 Parallel Plates 180
E.2 Comb Fingers 182

LIST OF REFERENCES 184

BIOGRAPHICAL SKETCH 192

المنارة للاستشارات
www.manaraa.com

LIST OF TABLES

Table page

2-1 Passive wireless sensor quantities from literature review 41

4-1 Agilent E4991A material property analyzer settings. 81

4-2 HP 4294A impedance analyzer settings. 82

4-3 Agilent 8719D network analyzer settings. 86

4-4 NASA tunnel test configuration settings and conditions 93

5-1 Geometric parameters used for the spiral coil inductors and loop antenna in the first generation wireless design. 99

5-2 Parameter values extracted numerically, analytically, and experimentally for the coupled inductor model. 103

5-3 Geometric parameters from the two capacitive MEMS sensors used for the first generation wireless tests. 104

5-4 Analytical modeling results for the MEMS capacitive sensors. 105

5-5 Geometries of parasitic capacitive structures in the capacitive MEMS sensors. 106

5-6 Parasitic results for the MEMS sensor derived using analytical, numerical and experimental models. 106

5-7 Full wireless system resonance and sensitivity results. 108

5-8 Electrostatic pull-in parameters for the first-generation designs. 118

5-9 Results predicted by the model. 121

5-10 Final experimental sensitivity, minimum detectable signal and dynamic range. 124

5-11 Flat plate turbulent boundary layer test results 129

6-1 Parameter values extracted numerically, analytically, and experimentally for the coupled inductor model. 136

6-2 Geometric parameters for the second-generation capacitive sensor. 139

6-3 Analytical modeling results for the second-generation capacitive sensor. 139

6-4 Geometries of parasitic capacitive structures in the second-generation capacitive sensors. 140

المنارة للاستشارات
www.manaraa.com

6-5 Parasitic results for the second-generation capacitive sensor derived using numerical and experimental models. 140

6-6 Full wireless system resonance and sensitivity results for the second-generation wireless sensor. 141

6-7 Results predicted by the model for the second-generation device..................................147

6-8 Final experimental sensitivity, minimum detectable signal, and dynamic range for the second-generation sensor. 149

7-1 Performance summary and comparison with previous work from the literature.............154

المنارة للاستشارات
www.manaraa.com

LIST OF FIGURES

Figure page

1-1 Simplified aerodynamic geometries in two-dimensional flow. 20

1-2 General concept for a passive wireless shear stress sensor....23

1-3 General concept for a wireless array....24

1-4 Sensor cabling requirement comparison. 25

1-5 Basic diagram of flow over an airfoil with laminar and turbulent regions. 25

1-6 Illustration of a separated boundary layer on an airfoil. 27

1-7 Illustration of the sensor being used for non-intrusive wireless measurement of the flow rate inside a pipe. 27

2-1 Wireless sensor categories, with the LC resonant passive wireless sensor technique used in this research highlighted. 30

2-2 Reprint of Figure 2 from Carter Collins, "Miniature passive pressure transensor for implanting in the eye," 1967, *IEEE Transactions on Biomedical Engineering*, reprinted with permission from IEEE. 33

2-3 Reprint of Figure 1a from Lars Rosengren, "A system for passive implantable pressure sensors," 1994, *Sensors and Actuators A: Physical*, reprinted with permission from Elsevier. 34

2-4 Reprint of Figure 1 from Park, E.C., "Hermetically sealed inductor-capacitor (LC) resonator for remote pressure monitoring," 1998, Japanese *Journal of Applied Physics*, reprinted with permission from the Japan Society of Applied Physics. 35

2-5 Reprint of Figure 1b from Keat Ong, "Design and application of a wireless, passive, resonant-circuit environmental monitoring sensor," 2001, *Sensors and Actuators A: Physical*, reprinted with permission from Elsevier. 36

2-6 Reprint of Figure 1 from Orhan Akar, "A wireless batch sealed absolute capacitive pressure sensor," 2001, *Sensors and Actuators A: Physical*, reprinted with permission from Elsevier. 38

2-7 Reprint of Figure 1a from Antonio Baldi, "A self-resonant frequency-modulated micromachined passive pressure transensor," 2003, *IEEE Sensors Journal*, reprinted with permission from IEEE. 39

www.manaraa.com

2-8 Reprints of figures from Michael A. Fonseca, "Flexible wireless passive pressure sensors for biomedical applications," 2006 Hilton Head Workshop on Sensors and Actuators, reprinted with the permission of the author and the Transducer Research Foundation. A) A reprint of Figure 3b. B) A reprint of Figure 4b. 39

2-9 Reprint of Figure 3 from Po-Jui Chen, "Wireless intraocular pressure sensing using microfabricated minimally invasive flexible-coiled LC sensor implant," 2010, *Journal of Microelectromechanical Systems*, reprinted with permission from IEEE. 41

3-1 Basic circuit model for the wireless shear stress sensor. 44

3-2 A 3D diagram of a single layer 2-turn spiral coil. 46

3-3 Cross-sections of spiral coil from Figure 3-2 with geometric parameters indicated. 46

3-4 Skin depth effect on current density inside a conductor. 48

3-5 Discretization of wire segments for high frequency compensation. 49

3-6 Qualitative current-density distributions in various wire bend configurations. 50

3-7 Equivalent transformer model circuits for coupled coils. 52

3-8 Non-ideal circuit model for the sensor coil. 52

3-9 Non-ideal circuit model for the antenna. 52

3-10 Cross section side view showing two wires of the coil. 55

3-11 Mechanical diagram of the floating element sensor structure. 56

3-12 Simplified clamped-clamped beam mechanical model of sensor with force vectors. 56

3-13 A 3D graphic of the sensor with variable capacitive structures indicated (not to scale). 58

3-14 Zoomed in 3D graphic showing capacitive comb fingers (not to scale). 60

3-15 Zoomed in 3D graphic showing element end capacitance (not to scale). 61

3-16 Zoomed in 3D graphic showing tether capacitance (not to scale). 61

3-17 Non-ideal circuit model for capacitive shear stress sensor. 62

3-18 Two 3D pad structures showing dimensions for parasitic calculations. 63

3-19 Finger fringe simulation results. 65

3-20 Element end fringe field simulation results. 65

المنارة للاستشارات
www.manaraa.com

3-21 Tether cross sections and fringing simulation results. 66

3-22 Pad gap cross section showing simulated fringing fields and the effect of the substrate beneath the pads. 66

3-23 A 3D graphic showing the side view of the pads with overlaid circuit model of the bulk parasitic capacitive structures (not to scale). 68

3-24 Equivalent circuit models for pad-to-bulk parasitics. 68

3-25 A generic waterfall plot showing a resonant frequency shifting in time. 69

3-26 Full circuit model for a single wireless shear stress sensor. 70

3-27 Sensor spectrum showing resonant peak and the shift due to a change in capacitance. 71

3-28 Normalized sensitivity of the sensor response to 10 % variations in fabricated geometries. 73

3-29 Basic T circuit for magnetically coupled resonators. 74

3-30 Coupled resonator plot showing overlapping and separated resonances. 74

3-31 Resonant frequency sensitivities to electrical parameters. 75

3-32 Resonant frequency sensitivities to electrical parameters. 76

3-33 Plot showing MDS dependence on Q. 77

3-34 Circuit model for a 2 x 2 sensor array. 79

3-35 Array spectrum sowing individual bandwidths for four sensors. 79

4-1 Probe station setup for impedance characterizations. 81

4-2 Electrostatic actuation test setup. 83

4-3 Network analyzer operation. 85

4-4 Diagram of a single sensor placed in a faraday cage to reduce external noise. 87

4-5 Humidity sensitivity test setup. 88

4-6 Static calibration flow cell. 89

4-7 NASA 20" x 28" wind tunnel setup showing the location of the sensor in the model. 91

4-8 Pressure tap readings from the ceiling of the Shear Flow Control Tunnel for all test points. 94

المنارة للاستشارات
www.manaraa.com

4-9 Turbulent boundary layer profile for 15 m/s flow over a flat plate. 95

4-10 Turbulent boundary layer plotted in + units to illustrate the Law of The Wall. 95

5-1 Optical image showing the Design 2 capacitive shear stress sensor next to a pencil for scale. 97

5-2 Coil designs showing simulated and realized inductors. 98

5-3 Design showing both the simulated and realized loop antenna. 98

5-4 Skin depth vs. frequency for copper. 100

5-5 Coil discretization plot looking at the cross-sectional area of a wire trace. 100

5-6 Inductive coupling was simulated with the coil and antenna coaxially aligned with a 1.5 mm separation. 100

5-7 FastHenry simulation results for Design 1 101

5-8 FastHenry simulation results for Design 2. 101

5-9 Parasitic capacitance due to RF connectors between the network analyzer and the loop antenna. 102

5-10 Optical images of the MEMS capacitive sensors highlighting the vital components......104

5-11 Simulated capacitance and conductance factoring in the bulk layer model. 107

5-12 Resonant dips in the reflection coefficient predicted by the model for both Design 1 and Design 2. 109

5-13 Generation 1 MEMS sensor fabrication process flow. 110

5-14 Photolithography dark field mask set used to define etches in the process flow.............110

5-15 Packaging concept for hybrid wireless shear stress sensors. 111

5-16 Process flow for hybrid wireless packaging. 112

5-17 Final packaged wireless sensor shown next to a U.S. penny for perspective. 112

5-18 Wireless sensor boards flush mounted in test plugs used for the flow cell calibration and wind tunnel tests. 113

5-19 Capacitance measurement and error for Design 1 and 2. 115

5-20 Die level high frequency impedance sweeps for six Design 1 sensors............................116

المنارة للاستشارات
www.manaraa.com

5-21 Die level high frequency impedance sweeps for six Design 2 sensors............................117

5-22 Video frame from electrostatic forcing test. 118

5-23 Displacement results processed by MATLAB. 119

5-24 Resonant dips showing the accuracy of the model.. 120

5-25 Sensor resonance drift..121

5-26 Noise plot. 122

5-27 Linear static calibration for sensor Design 1. 122

5-28 Static shear stress calibration for Design 2. 123

5-29 Repeatability shear stress calibrations for Design 2. 124

5-30 Frequency sweeps showing resonant frequency dip height reduction with increasing coil antenna separation...125

5-31 Range test results showing the maximum separation within which resonance can be determined...126

5-32 Wireless sensor response to humidity...127

5-33 Boundary layer profiles for all test cases...128

5-34 Wind tunnel calibration for Design 2...129

6-1 Optical image showing the second-generation capacitive shear stress sensor next to a pencil for scale. 131

6-2 Representations of the sensor structures shown out-of-scale. 133

6-3 Pressure driven flow diagrams...133

6-4 Illustration of second-generation sensor bond pad. 134

6-5 Backlit photograph of the second-generation wireless sensor showing a 6-turn coil with a 3.5 mm inner diameter and diamond-design capacitive sensor. 137

6-6 SEM image of the second-generation sensor die highlighting the vital components. 138

6-7 Second-generation frequency response showing the accuracy of the model and a comparison to the first generation...141

6-8 Fabrication process flow for second-generation device..143

المنارة للاستشارات
www.manaraa.com

6-9 Mask set used for photolithography in steps 3 and 9. 144

6-10 Capacitance and conductance impedance sweeps for second-generation sensor. 146

6-11 Measured second-generation device drift. 147

6-12 Second-generation sensor response to humidity. 148

6-13 Linear static calibration for the second-generation sensor. 149

6-14 Second-generation hysteresis test results showing two full cycles. 150

6-15 Rotation test illustration. 151

6-16 Rotation test results showing directional response of the sensor. 151

7-1 Back side of the third generation concept sensors. 155

7-2 Fabrication technologies required to realize third-generation integrated wireless shear stress sensors. 156

7-3 Wireless arrays realized by dicing devices in blocks. 157

7-4 Basic concept for RF circuitry that would enable dynamic shear stress testing. 158

7-5 Diagram of the plane wave tube used for dynamic shear stress characterization. 159

7-6 General system optimization loop. 160

A-1 Capacitive shear stress sensor mechanical nonlinearity plot. 164

A-2 Capacitive shear stress sensor capacitive nonlinearity plot. 164

A-3 Capacitive shear stress sensor resonant nonlinearity plot. 165

A-4 Capacitive shear stress sensor cascaded nonlinearity plot. 165

B-1 Full single wireless sensor model for impedance derivations. 167

B-2 Wireless sensor array model for impedance derivations with no inter-sensor coupling. 168

B-3 Wireless sensor array for impedance derivations with full coupling model. 169

B-4 Multiport impedance model. 169

C-1 Simple coupled resonator circuit. 172

C-2 Coupled resonator circuit. 174

المنارة للاستشارات

www.manaraa.com

D-1 Simple *RL* and *GC* circuits. 175

D-2 Simple *RLC* and *GLC* resonant circuits. 177

D-3 Wireless shear stress sensor circuit including parasitics....178

E-1 Basic parallel plate diagram for electrostatic pull-in derivation. 181

E-2 Comb finger diagram for electrostatic pull-in derivation. 183

المنارة للاستشارات
www.manaraa.com

Abstract of Dissertation Presented to the Graduate School
of the University of Florida in Partial Fulfillment of the
Requirements for the Degree of Doctor of Philosophy

PASSIVE WIRELESS WALL SHEAR STRESS SENSORS

By

Jeremy Sells

May 2011

Chair: David P. Arnold
Major: Electrical and Computer Engineering

The design and realization of the first ever passive wireless wall shear stress sensors are presented. The sensors are capable of directly measuring shear forces, 4 mPa to 4 Pa, created at the solid-fluid boundary of a flow. To capture the spatially small structures of a turbulent flow, a micromachined, variable-capacitor floating element sensor is designed. Passive wireless capability is achieved with the addition of an inductive coil and interrogating antenna. These sensors will enable characterization of complex flow phenomena.

The primary benefit of the system is that the sensors operate without the need of a direct electrical connection. This simplifies installation of the sensors and enables their placement in locations where the rest of the system either will not fit or cannot survive. By using a passive wireless technique, a power source is not required, extending the life of the sensor and simplifying fabrication. The system makes use of frequency separation, allowing one interrogating antenna to query multiple sensors configured as an array simultaneously.

Two generations of the wireless sensor are presented. The design, fabrication, packaging, and characterization of two first-generation sensors have dynamic ranges of 37 and 52 dB. Following this work, specific design improvements were identified and integrated into a second-generation sensor design, resulting in an improvement to 62 dB dynamic range and an order of magnitude reduction in parasitic capacitance and humidity sensitivity. Ideas for a third generation are presented, but realization of this design is left for future work.

المنارة للاستشارات
www.manaraa.com

CHAPTER 1
INTRODUCTION

Transportation of people and goods is essential to modern society. We use cars to travel back and forth from work or school every day, and aircraft allow us to cross continents and oceans. Trucks deliver goods to our local stores, and trains transport huge quantities of cargo across the county. Nearly every individual and business depends on some form of transportation. With rising fuel prices and enormous demand, technologies that can help to improve the performance (speed, safety, efficiency, etc.) of these vehicles are needed. The growing green economy is also creating a greater demand for more fuel-efficient vehicles.

All terrestrial vehicles must travel through a fluidic medium, air for cars and planes, to get from point A to point B. Like gravity, many of us forget about the air around us until we are hit by a large gust of wind. However, a moving vehicle must constantly overcome forces imposed on it by the air to accelerate or maintain a constant velocity. This resistance to motion is referred to as drag and includes any force on the outer surface of the vehicle body that is opposite to the direction of travel. For subsonic and transonic vehicles, the total drag includes two primary components, pressure drag and friction drag. The dominant source depends on the geometry of the body and the direction of the airflow [1], as illustrated in Figure 1-1. The lowest total drag is achieved with aerodynamic geometries, and the more aerodynamic the structure is the greater the influence of friction drag. Reduction of friction drag is therefore a vital objective in improving the efficiency of future aircraft and other vehicles.

Aerodynamic geometries used in modern vehicle designs are often dominated by friction drag. For a modern business jet, the friction drag accounts for up to 53% of the total drag [2]. For modern high speed trains the ratio of the friction drag to the pressure drag depends on the length of the train [3]. The pressure drag is related to the effective frontal area of the train while the

المنارة للاستشارات
www.manaraa.com

friction drag is related to the total surface area of the train, assuming the flow is attached all the way to the trailing edge. For a single standard car 60' long x 9' wide x 11' tall, the friction drag will only be about 5% of the total drag. For a passenger train with 9 cars, the friction drag approaches 52% of the total aerodynamic drag. As the train gets longer, the contribution from friction drag rises higher still.

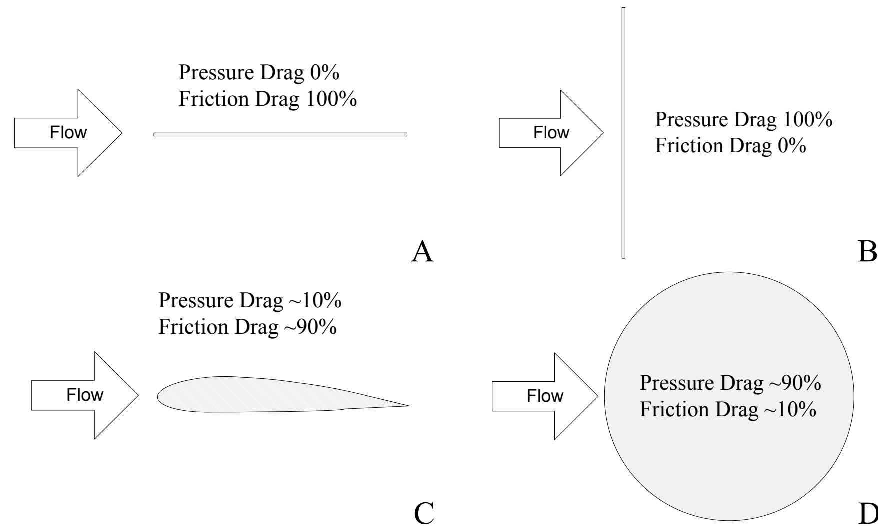

Figure 1-1. Simplified aerodynamic geometries in two-dimensional flow. A) Infinitely thin plate parallel to the flow. B) Infinitely thin plate perpendicular to the flow. C) Teardrop airfoil geometry. D) Cylinder.

Reducing friction drag in future aerodynamic vehicles requires ongoing effort by the scientific and engineering community. Numerical modeling using computational fluid dynamics (CFD) has been advancing rapidly, enabled by the huge growth of computational power over the last few decades [4]. CFD can be very beneficial in studying how structures interact with flows, and even for predicting skin friction. However, no matter how advanced computers get, the accuracy of these simulations is only as good as the underlying physical models, so experimental measurement and validation of fundamental physical phenomena—including shear stress—is needed.

المنارة للاستشارات
www.manaraa.com

Unfortunately, there are very few viable sensors for measuring friction drag. This is largely due to the technical challenges involved in making these measurements [5-7]. Shear stress τ is the fundamental physical quantity associated with friction drag. Shear stress is defined as force per unit area (areal force density) acting tangential to the body's surface and has units of $Pa = N/m^2$. To quantify the flow over a body, the sensors have to be exposed to the flow. This makes packaging very difficult and leaves the sensors vulnerable to other changes in the environment, such as temperature, humidity, vibrations, etc. The shear forces are very small compared to the pressure forces, which make it difficult to isolate them from each other. Also the shear stress levels can vary greatly across a surface, making it necessary to make measurements at multiple locations.

The lack of suitable measurement technologies is a primary motivation for the work presented in this dissertation. The development of a sensor capable of providing accurate, time-resolved, directional shear data with high spatial resolution will present a major advancement for aerodynamic testing.

In addition to meeting the requirements to accurately measure shear stress, the sensors will be capable of being tested wirelessly. This allows the sensor to be separated from the electronics and multiple sensors grouped into arrays to be monitored with a single antenna. A passive wireless detection scheme both powers the sensors and allows the response to be tracked by an external antenna. The design is an elegantly simple extension of a wired sensor design[8] that does not require any complex transceiver circuitry for the wireless link. The sensor and wireless capability are combined into a single device as described in the following section.

المنارة للاستشارات
www.manaraa.com

1.1 Basic Sensor Operation

Shear stress will be measured directly with a microelectromechanical (MEMS) sensor. A floating element structure on the surface of the sensor is suspended by flexible tethers and located at the solid/fluid interface. The tangential drag force on the surface area of the floating element causes it to move in the same direction as the flow. The physical displacement of the plate is then detected electrically by choosing a suitable transduction scheme. There are many transduction methods, such as optical [9-11], piezoresistive [12,13], and capacitive [8,14-16] that have been used in previous shear stress sensors.

Capacitive transduction offers advantages in sensitivity, noise and packaging simplicity over the other techniques [17]. More importantly, it is essential for the passive wireless readout technique being proposed here. A capacitor is a device consisting of two electrically isolated conductors. Capacitance is a function of the geometry of the conductors, the distance between them, and the dielectric material in between. The edge of the moving, floating element serves as one conductor, while an adjacent fixed surface serves as the second conductor. Displacement of the floating element changes the separation, resulting in a change in capacitance.

The proposed wireless detection scheme is shown in Figure 1-2. It relies on tracking the resonant frequency of an "LC tank" circuit. A LC tank circuit is an electrical second-order resonator consisting of a capacitor and an inductor. The natural frequency in Hz is given by

$$f_0 = \frac{1}{2\pi\sqrt{LC}}, \tag{1-1}$$

where L is inductance in Henrys and C is capacitance in Farads. The MEMS shear stress sensor provides the capacitance for the tank circuit. A spiral coil connected across the terminals of the sensor provides the inductance and completes the tank. An input shear force will change the sensor capacitance, changing the resonant frequency of the tank circuit.

المنارة للاستشارات
www.manaraa.com

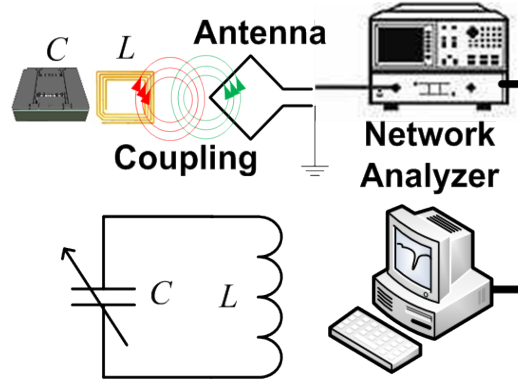

Figure 1-2. General concept for a passive wireless shear stress sensor. A single sensor along with the interrogation setup and a basic circuit representation are shown.

Wireless detection of the resonant frequency is achieved by placing a loop antenna in proximity to the sensor's inductor. The loop antenna and the sensor inductor become magnetically coupled, and a drop in the reflection coefficient of the antenna identifies the resonance of the tank circuit . Changes in the sensor's capacitance show up as frequency shifts in the resonant dip generated by the sensor.

One advantage of this passive wireless approach is that the resonant frequency tracking technique makes the measurement less susceptible to electromagnetic interference (EMI)-induced amplitude noise. EMI can be especially problematic for high impedance devices, such as capacitive sensors. High impedance devices pick up EMI from the environment. The LC circuit will naturally filter out EMI and any remaining signals will show up in the output as noise in the output spectrum. This may make determining the resonant frequency more difficult and raise the noise floor, but it will not mimic a frequency shift from an input shear stress.

Another key advantage of the passive wireless approach is that more than one sensor can be interrogated by the same antenna, lending this technique to an array of sensors, as shown in Figure 1-3. For this to work, each sensor in the array must operate in a different frequency bandwidth. The frequency range of the spectrum can be set to include all of the sensors in the array, and sensors can be designed to operate within separate bands. This can be accomplished in

المنارة للاستشارات
www.manaraa.com

two ways. First, identical shear stress sensors can be used, and different coils can be designed for each sensor, such that L is different for each. Alternatively, sensors with differing capacitances can be designed. Then identical inductors can be used for each sensor, again resulting in each sensor occupying a different band.

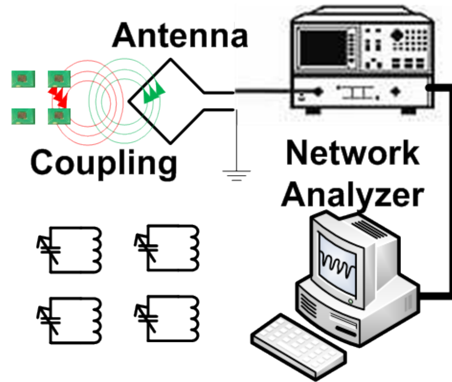

Figure 1-3. General concept for a wireless array. A 2 x 2 array is represented along with the spectrum indicating four resonances.

A significant problem for any experimentalist that uses sensor arrays is the mass of wires or other connections that have to be routed between each individual sensor and the detection circuitry. Working these webs of wires into a wind tunnel test model while preventing things, such as cross talk between adjacent channels, can be a big problem. By using different frequencies for all of the sensors in the array, a single antenna with only one set of wires can be used to interrogate the entire array of sensors. A comparison is illustrated in Figure 1-4. Using wireless arrays can greatly simplify model construction/wiring and increase flexibility for sensor configurations within the array.

1.2 Specific Applications

Aerospace engineers are interested in the development of shear stress sensors for fundamental flow studies of airfoils [6]. The knowledge gained from these studies can be applied to improving the designs of future airfoils. A basic diagram for external flow over an airfoil is shown in Figure 1-5. Streamlines are shown to represent the velocity field, and the boundary

المنارة للاستشارات
www.manaraa.com

layer is highlighted. Flow velocity *u(y)* at the surface of the airfoil is zero due to the no-slip boundary condition and increases to the free stream velocity U_∞. The boundary layer δ is the region bounded by the surface and extends to where the local velocity reaches 99% of the free stream value. Boundary layers originate at the stagnation point (the point at the leading edge where the flow velocity is zero) and grow until they are shed at the trailing edge or when a separation condition is reached.

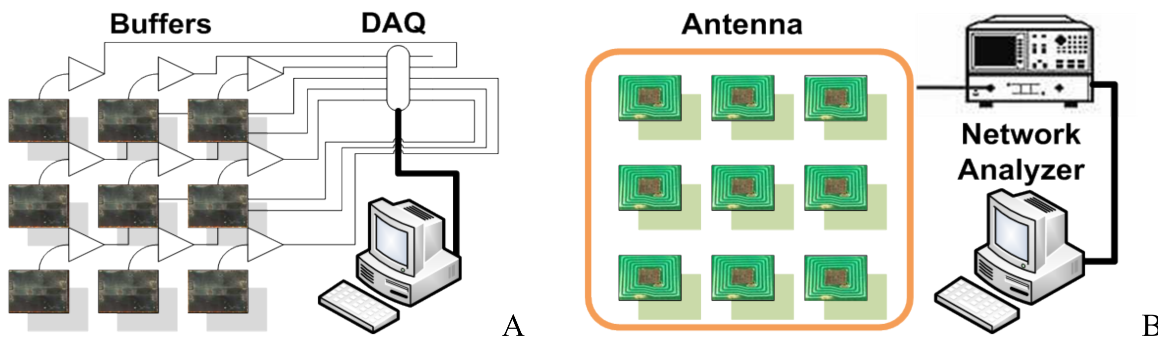

Figure 1-4. Sensor cabling requirement comparison. A) The mess associated with a wired sensor array. B) Simplified to a single wire with the wireless sensor array.

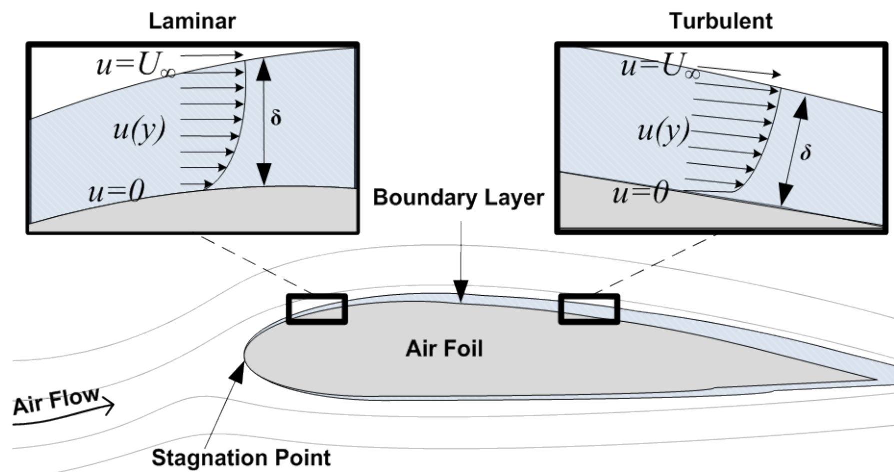

Figure 1-5. Basic diagram of flow over an airfoil with laminar and turbulent regions.

There are three flow regimes in a boundary layer [1]; laminar, transitional and turbulent. Laminar flow is steady and organized with no mixing in any direction and is characterized by a constant shear stress at the surface. When the flow is either tripped or the inertial forces in the flow overcome the viscous forces, eddies that break up the orderly flow form in the boundary

المنارة للاستشارات
www.manaraa.com

layer. At first there will be both laminar and turbulent regions in the boundary layer, which is referred to as a transitional flow. Once these eddies permeate the entire boundary layer, the flow is referred to as turbulent. Turbulence is stochastic and contributes both mean and dynamic shear stress at the surface. A shear stress sensor capable of mean measurements can be used to measure the characteristics of all three regimes, while a dynamic sensor is only useful for turbulence studies. The ultimate goal is a sensor capable of measuring both mean and fluctuating shear stress at the same time.

Under certain conditions, often at high angle of attack α, the boundary layer can separate before the trailing edge of the wing. This phenomenon is known as separation and can cause a vehicle to stall if it progresses too far up the wing. When the adverse pressure gradient in a two-dimensional flow becomes too large, it can retard the flow to the point where the reduced momentum is enough to cause a separation of the boundary layer as shown in Figure 1-6. The shear stress at the point of separation is zero, while further downstream from the separation point recirculation can cause a small shear in the opposite direction. A mean measurement of shear stress can detect the onset of separation, and the spatial location can be found by using a 1 x N array oriented along the stream-wise direction. The onset, detection and location of separation forms another important application area, which may be useful for active flow control strategies [18,19].

In addition to aerospace applications, the sensor could be used to measure the flow rate inside pipes. The wireless readout of the sensors would be particularly useful in this application, because it would enable measurement without any holes in the sidewalls. A wired sensor would require a port for the wires to exit, which could compromise the integrity of the pipe walls. Fifty-percent of all modern pipelines, including natural gas pipelines, are made of plastic [20].

المنارة للاستشارات
www.manaraa.com

The non-conductive plastic construction enables a sensor mounted on the inner sidewall to be interrogated by an antenna located just outside the pipe, as shown in Figure 1-7. A velocity profile can be determined by measuring the mean shear stress at the pipe wall under certain conditions [1]. The pipe must contain a Newtonian fluid, and the flow must be fully developed. Once the velocity profile is inferred, volumetric flow rate can be found by multiplying the average velocity by the cross-sectional area of the pipe. The result is a sensor capable of wirelessly measuring the flow rate without adding any head loss to the pipe.

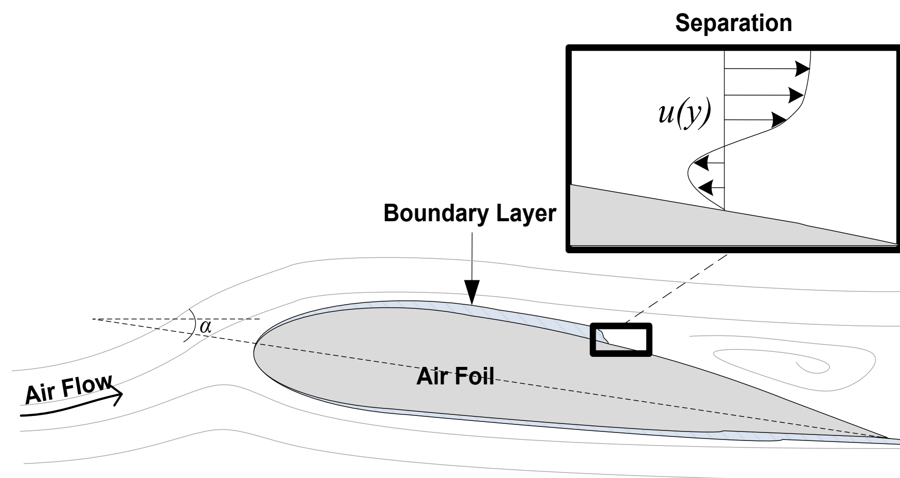

Figure 1-6. Illustration of a separated boundary layer on an airfoil.

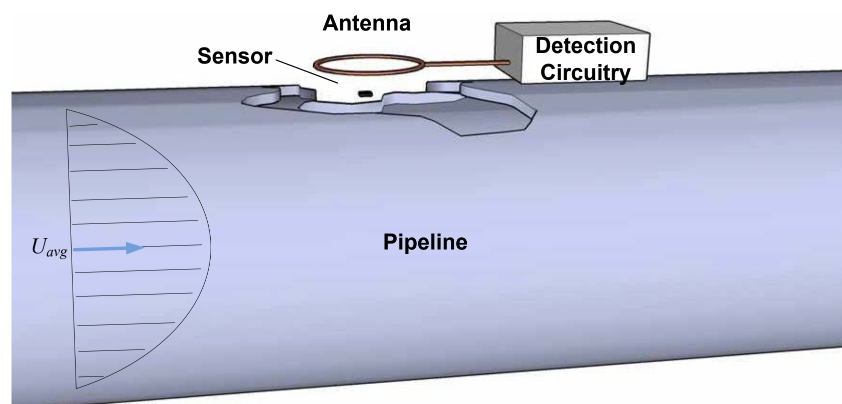

Figure 1-7. Illustration of the sensor being used for non-intrusive wireless measurement of the flow rate inside a pipe.

المنارة للاستشارات
www.manaraa.com

1.3 Dissertation Organization

This dissertation is organized as follows: Chapter 2 presents an in-depth literature review of passive wireless sensors, including the current state of the art. Chapter 3 provides a comprehensive model of the sensor and wireless detection strategy. The sensor system is first segmented into mechanical, electrostatic, and magnetostatic models, each of which is described in detail. At the end of Chapter 3, these sub-models are combined into a complete system model to predict the sensor's behavior. Chapter 4 gives details of the experimental setups used to characterize the wireless shear stress sensors. A first-generation of the sensor, including design, fabrication, and experimental results, is presented in Chapter 5. Chapter 6 addresses shortcomings of the first-generation devices, and presents an improved second-generation design, including the fabrication and test results. The final chapter gives concluding remarks, including future work for the existing sensors and suggestions for the next generation of the sensor.

المنارة للاستشارات
www.manaraa.com

CHAPTER 2
BACKGROUND

This chapter provides a review of the relevant literature for wireless sensors. A shear stress sensor that is the first of its kind is presented so there are no precedents to compare it to. To give adequate background for comparison with previous work, a brief history of wireless sensors is given, followed by an in-depth review of eight passive wireless pressure force sensors. A summary is provided at the end with a table of relevant metrics for comparison.

The emphasis here is more on the wireless sensing, particularly passive wireless sensing, and less on the design/optimization of the shear stress sensor itself. For a detailed review of the previous work on shear stress sensors see the review papers by Sheplak et al., Naughton et al. and Etabari [5-7] and the background chapters of dissertations by V. Chandrasekharan [21], and Y. Li [22].

2.1 Wireless Sensor History

Early miniaturization of wireless sensors was proposed to enable the monitoring of biological processes inside the body without the need for wires protruding through the skin. In 1957 three separate groups, Mackay [23] in Sweden, Farrar [24] in the U.S., and Sprung [25] in Germany, reported on wireless sensors, referred to as “endoradiosondes.” These devices took the form of a pill with the sensor, electronics, and battery all sealed in a biocompatible casing. The internal battery power source enabled the devices to transmit the digitized sensor data to base units worn on the patients or carried by the physicians. These devices were intended to interrogate intestinal processes. The pill was to be swallowed and then disposed of, so the limited lifetime of the battery was not a restrictive issue.

Many battery-powered wireless sensors [26-30] have been developed since these first works, but a need existed for longer-lasting wireless sensors that could be powered and

للاستشارات المنارة
www.manaraa.com

interrogated by an external antenna. The idea for passive wireless sensors was mentioned in Mackay's work [23], but it was not realized until 1967 by another researcher, Collins [31], who had collaborated with Mackay.

There are two categories of devices described in the literature as passive wireless sensors. Figure 2-1 shows the classification of wireless sensors used here. Both digital and analog wireless sensors are passive, meaning neither type requires an integrated power source. Digital wireless sensors are similar to radio frequency identification (RFID), in which the interrogating antenna is used both to power the device and receive the data [32-34]. Like their battery-powered counterparts, they have the added benefit of using digital coding to improve the signal-to-noise ratio. However, they require integrated RF to dc power conversion and encoding circuits, making them more complicated to design and fabricate.

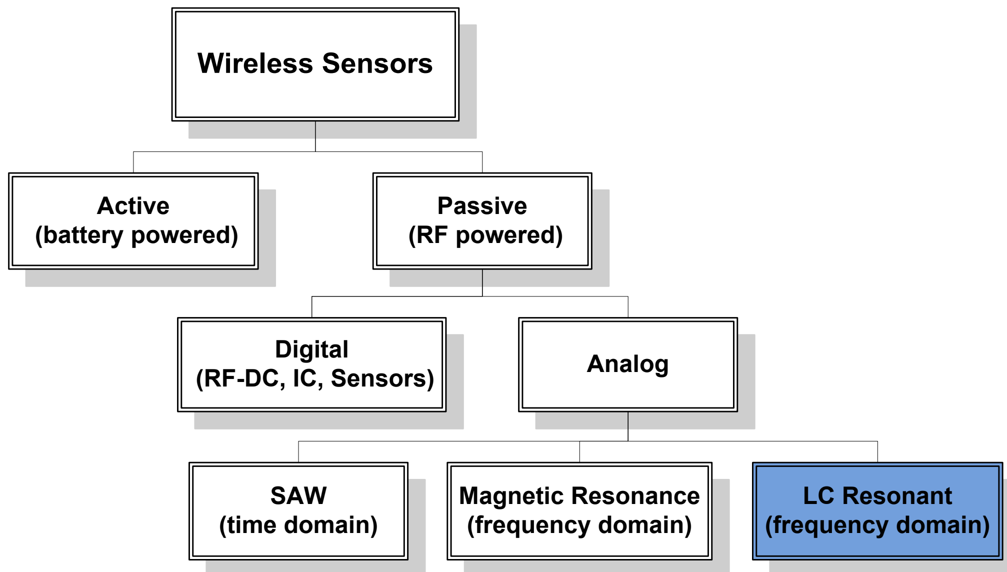

Figure 2-1. Wireless sensor categories, with the LC resonant passive wireless sensor technique used in this research highlighted.

Analog passive wireless sensors can be further separated into surface acoustic wave (SAW), magnetic resonance, or LC resonant devices. SAW devices rely on a change in the mechanical resonance of the sensor structure to detect changes in their environment [35-37]. An

المنارة للاستشارات
www.manaraa.com

RF pulse is sent to the sensor, where it generates a traveling acoustic wave. This wave propagates down the length of the sensor and is converted back to an RF electrical signal. Time domain analysis is used to track these echo pulses and identify any perturbations. Magnetic resonance devices [38-40] operate based on the principles of magnetostriction, where a magnetic field causes a mechanical strain in certain materials. Similar to the SAW devices, an RF pulse is sent that causes mechanical changes in the material. These perturbations are selective to the mechanical resonant frequency, which will change depending on the sensor's environment. Magnetostriction is reciprocal, so the mechanical strains produce an RF tone at the mechanical resonant frequency. Lastly, LC resonant sensors operate by tracking a change in electrical resonance in order to sense changes in their environment. Changes in either the inductance, L or the capacitance, C cause the resonant frequency to shift. The resonant frequency changes are detected via an external antenna, which is inductively coupled to the inductor in the LC tank. To maintain consistent terminology, "passive wireless" will be used in the rest of this document to refer to the LC resonant category highlighted in Figure 2-1.

2.2 Passive Wireless Literature Review

There are many passive wireless devices reported in the literature from as far back as 1967 with the first work by Collins [31]. Devices targeting pressure [31], humidity [41], temperature [42], pH [43], glucose [44], biological pathogens [45], and chemical agents [46] are all realizable using this technique. The pressure sensors are the most relevant for comparison to this work because they measure forces, so they are chosen for this review. The following reviews are placed in chronological order starting with Collins [31]. Many of these papers use mmHg, psi, kPa, or bar for pressure, so in order to simplify comparison all pressure values have been converted to Pa.

www.manaraa.com

2.2.1 Review of Work Done at the Institute for Visual Sciences

Carter C. Collins, of the Institute for Visual Sciences, San Francisco, California, presented the first passive wireless sensor in 1967 [31]. The primary purpose of the device was for testing intraocular pressure in the eye, but was presented as an absolute pressure sensor viable for any part of the body within a few cm of the skin. His design took the same plastic encapsulated pill form as the devices made by Mackay, Farrar, and Sprung [23-25]. The device was hand-fabricated, but it had dimensions (2 mm diameter, 1 mm thick, 80 µm diameter wire, and 62.5 µm thick diaphragms) comparable to modern microfabricated devices.

The cross section of the basic device is shown in Figure 2-2. The pill had a sealed chamber with a compliant polymer film stretched over the top and bottom. Coils were attached to the top and bottom films and were free to move with them. This created an absolute pressure sensor that could detect the compression or expansion of the pill from changes in the external pressure relative to the internal pressure. The sensor inductance was from the wire coils and the capacitance from between the coils. As the pill contracted, the coils got closer together, and both the mutual inductance and the capacitance increased, decreasing the self-resonant frequency of the device. The coils were configured so that they had a positive mutual coupling and were connected at the outer diameter of the winding. The device operated at a resonant frequency of 120 MHz and had a quality factor (Q) of 80. This is the highest Q reported to date. The response of the device was predicted up to 133 kPa, but the calibration test was only performed up to 13 kPa. The sensitivity reported was 0.75 kHz/Pa. The discrepancy came from the fact that several different devices were reported. Drift, frequency sensitivity to coil coupling, and acceleration sensitivities were all tested and combined to find the precision of the device. The minimum detectible pressure was 67 Pa, which corresponds to a 167.5 kHz shift in frequency.

المنارة للاستشارات
www.manaraa.com

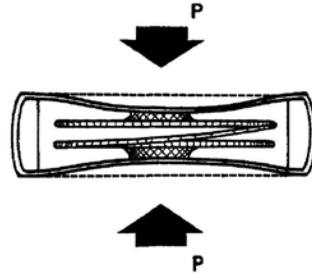

Figure 2-2. Reprint of Figure 2 from Carter Collins, "Miniature passive pressure transensor for implanting in the eye," 1967, *IEEE Transactions on Biomedical Engineering*, reprinted with permission from IEEE.

The electronics used for Collins' research were referred to as a grid-dip oscillator absorption detector. The electronics were based on a voltage-controlled oscillator (VCO) and a phase detector. The VCO was fed a triangle wave input to sweep through a range of frequencies. At resonance, a phase dip detector output the voltage of the triangle wave, which corresponded to a specific frequency in the VCO. Using this circuitry, the sensor was successfully tested both *in vitro* and *in vivo* in rabbit eyes.

2.2.2 Review of Work Done at Uppsala University in Sweden

There is a large gap in time before the next significant work was presented in this area. There are several articles in the medical literature on clinical trials [47,48] of devices similar to Collins', but no new sensors were presented until the early 90s. Backlund and Rosengren, from Sweden, presented a sensor for measuring the absolute pressure of the eye [49,50] in 1994. This was also the first work to use microfabrication technologies to build the capacitive sensor.

The sensor shown in Figure 2-3 was made by attaching a coil to a silicon capacitive pressure sensor. The coil was wound around a form that housed the sensor chip and was then coated in a silicon rubber. The size of the entire device was 5 mm in diameter by 2 mm thick. The wire was 50 μm diameter gold wire. The sensor was made by using a KOH etch on the front and back side of a silicon wafer. This wafer was then bonded to another silicon wafer with a

المنارة للاستشارات
www.manaraa.com

1 μm thermal oxide for electrical isolation. The cavity formed during this bond was 10 μm deep, and the membrane was 20 μm thick. The wafers formed the two conductors of the capacitor.

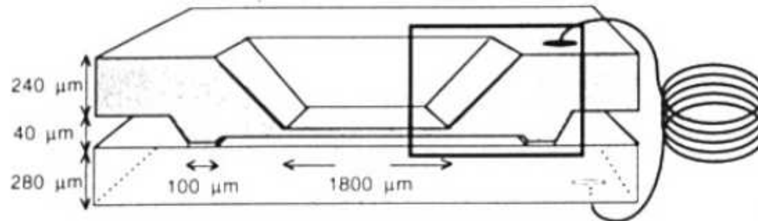

Figure 2-3. Reprint of Figure 1a from Lars Rosengren, "A system for passive implantable pressure sensors," 1994, *Sensors and Actuators A: Physical*, reprinted with permission from Elsevier.

The device operated at 43.6 MHz and used a grid-dip oscillator, similar to the circuit used by Collins [31], to detect the resonant frequency. In the first-generation [49], a low Q of 5.5 was obtained, which limited the performance of the device. The problem was attributed to parasitics within the silicon, but careful doping of the wafers brought the Q up to around 30 in the second-generation [50]. The sensitivity of this circuit was 4 mV/kHz, and the sensitivity of the sensor was 7.5 Hz/Pa. The sensor was tested from zero to 10.7 kPa in 1.3 kPa steps. The minimum shift detected in this work was 9.75 kHz. Rosengren alluded to significant drift and coupling sensitivity but did not quantify the problems or isolate their sources.

2.2.3 Review of Work Done at the Korean Institute of Science and Technology

The next logical step was to integrate the inductor into the MEMS design, thus simplifying the packaging. Figure 2-4 shows the sensor developed in Korea by Park et al. [51], which incorporates a copper coil into the sensor. An anodic wafer bonding technique was used to form the cavity. The bottom substrate was glass instead of silicon, which reduces the coils' substrate parasitic capacitance and conduction losses. The bottom plate was formed by a gold lift-off process, and the coil ran from this plate out to the doped silicon cap. Electroplating copper up through a 30 μm-photoresist mold formed the square spiral coil. Instead of using a timed KOH

المنارة للاستشارات
www.manaraa.com

etch for the membrane, an electrochemical etch stop was used in which the silicon left behind was defined by a doped region. This gave better control of the diaphragm thickness, which was set to 3 μm by 7 h boron diffusion. All of the metal was encapsulated in the cavity, so no further packaging was required. The device measured 3mm x 3mm x 0.6 mm.

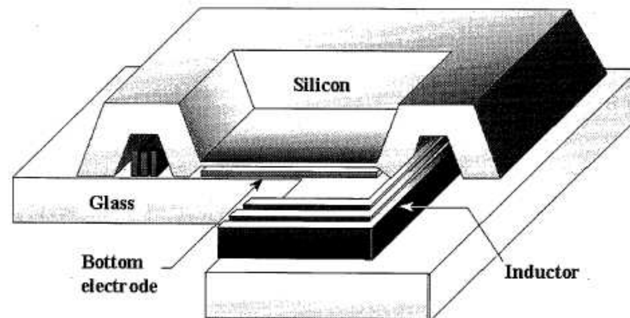

Figure 2-4. Reprint of Figure 1 from Park, E.C., "Hermetically sealed inductor-capacitor (LC) resonator for remote pressure monitoring," 1998, Japanese *Journal of Applied Physics*, reprinted with permission from the Japan Society of Applied Physics.

The inductor was well designed and characterized in the work as having an inductance of 220 nH, resistance of 3 Ω, and parasitic capacitance of only 380 fF. The sensor capacitance, nominally 3 pF, was also characterized and measured under pressure loading of up to 13 kPa. The data showed obvious nonlinearity with a 9x change in capacitance. The diaphragm was poorly designed for these pressures. The over-compliant diaphragm was collapsing onto the bottom electrode. The grid dip oscillator was used again in this work and displayed a self-resonant frequency of 120 MHz with no loading. This did not correspond with the inductor and capacitor values given and likely pointed to problems with the sensors. No pressure data was given as a result of these problems. Despite the outcome of this design, the inclusion of the coil into the fabrication was a significant contribution that was repeated in more recent work by other groups.

المنارة للاستشارات
www.manaraa.com

2.2.4 Review of Work Done at Pennsylvania State University

All of the devices presented thus far are absolute pressure sensors for biological applications. In 2000, Keat Ong et al., part of Craig Grimes' group at Pennsylvania State University, published their work on a passive wireless sensor platform [52] that could, with slight modifications, be used for sensing pressure, humidity, temperature [42], relative permittivity changes, bacterial growth [45], and chemical gasses [46]. The pressure sensor is shown in Figure 2-5 and was very similar to the previous designs, in which a cavity was formed separating two conductive plates that are attached to a coil. In contrast to most of the other sensors in this review, the devices here were very large, ranging from 3 cm x 3 cm to 6 cm x 6 cm. The increased size, along with different interrogation techniques enabled monitoring from up to 1.5 m away for the larger sensors. These sensors were similar in size and construction to the RF anti-theft tags, which also work up to a few meters away, used in retail stores.

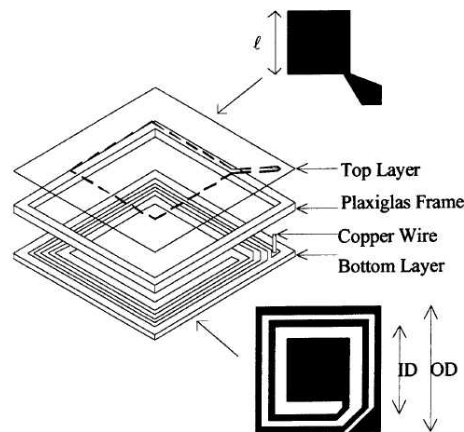

Figure 2-5. Reprint of Figure 1b from Keat Ong, "Design and application of a wireless, passive, resonant-circuit environmental monitoring sensor," 2001, *Sensors and Actuators A: Physical*, reprinted with permission from Elsevier.

Two monitoring techniques were characterized and used for these sensors. The first was an impedance analyzer used with a single antenna to measure impedance spectra. The second technique employed two antennas. A single frequency tone was applied to the input of the first

المنارة للاستشارات
www.manaraa.com

antenna and resulted in a voltage appearing at the terminals of the second. This voltage changed as the tone frequency was swept across a range of frequencies believed to contain the resonance. The resulting spectra traces out a curve very much like the impedance spectra from which the resonance is determined. This measurement scheme was used to increase the separation between the sensor and the detector coils, but the sensor had to be between the two coils for this approach to work. Antenna characterization was also presented, giving detection ranges as a function of number of turns and turn radius.

Ong showed the potential of the wireless LC sensor techniques for many different applications and presented an analysis of the coil and antenna interactions. Due to the wide breadth of his work, little detail was given for any one sensor. The resonant frequency of the pressure sensor was 57 MHz, and a frequency shift of 6.4 MHz was shown to be linear with an input pressure from 0 to 34 kPa. No inductance, capacitance, Q, resolution, or drift data was given.

2.2.5 Review of Work Done at the University of Michigan

Orhan Akar, part of Khalil Najafi and Kendsall Wise's group at the University of Michigan, took the design from Park's [51] sensor and improved upon it to create a working device [53]. The same fabrication procedure was used to make the device shown in Figure 2-6. The first and most important change was a thicker, less compliant diaphragm that limited the maximum deflection to 400 nm. This corresponded to a capacitance change of 14% full-scale with 13 kPa-maximum input pressure. The coil had a higher inductance at 1.2 μH, made possible by using more closely spaced turns. The overall dimensions of the device were smaller at 2.6 mm x 1.6 mm.

The measured Q of this device was 8 and required a network analyzer to be used as the detection electronics. The network analyzer was used to obtain impedance spectra from which

المنارة للاستشارات
www.manaraa.com

the resonant frequency was determined. It was slower and did not give a voltage output as did the grid dip detector, but it was much more sensitive and was capable of detecting sensors with poor *Q*. This sensor operated at 76 MHz and had a full-scale shift of 6 MHz for a 13 kPa input. This corresponded to a sensitivity of 900 Hz/Pa. The response was measured in 3.3 kPa steps, so the smallest detected shift was 3 MHz.

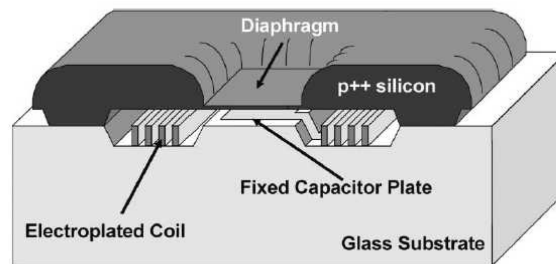

Figure 2-6. Reprint of Figure 1 from Orhan Akar, "A wireless batch sealed absolute capacitive pressure sensor," 2001, *Sensors and Actuators A: Physical*, reprinted with permission from Elsevier.

2.2.6 Review of Work Done at the University of Minnesota

A new idea for a passive wireless pressure sensor was explored at the University of Minnesota. Antonio Baldi published a paper in 2003 [54] in which, instead of having a variable capacitive sensor, he attached a ferrite core to the diaphragm making it a variable inductor sensor. The capacitance was supplied by the coils' intrinsic capacitance. The device was 3 mm x 3 mm overall and used a 0.95 mm diameter, 0.5 mm thick ferrite disk. The device was fabricated in two pieces and glued together, creating the sealed cavity shown in Figure 2-7. The coil was electroplated on oxide-coated Si, which causes the device to have a poor *Q* of only 5.4.

The device displayed a linear range of 60 kPa before the ferrite hit the bottom of the cavity. The cavity was 1 mm deep with a 2 mm diameter. This meant that the deflection of the diaphragm was 0.5 mm at the upper limit. This sensor was collapsing similar to the sensor in Park et al. [51] and would also have benefited from a stiffer diaphragm. The linear sensitivity measured with an impedance analyzer was 9.6 Hz/Pa with a nominal resonance of 31.8 MHz.

المنارة للاستشارات
www.manaraa.com

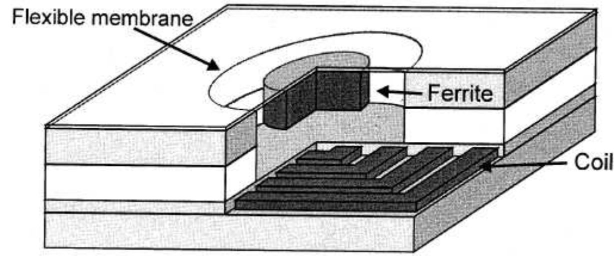

Figure 2-7. Reprint of Figure 1a from Antonio Baldi, "A self-resonant frequency-modulated micromachined passive pressure transensor," 2003, *IEEE Sensors Journal*, reprinted with permission from IEEE.

2.2.7 Review of Work Done at the Georgia Institute of Technology

A sensor for measuring aortic pressure was commercialized by CardioMEMS. This sensor was presented in papers by English [55,56] and Fonseca [57,58], who were part of Mark Allen's [59] group at the Georgia Institute of Technology. The device is shown in two configurations in Figure 2-8 consisted of two round spiral coils surrounding a sealed chamber with conductive plates on its top and bottom. The devices were made from Cu-clad polymers and, in the second design, a ceramic chamber. They were roughly 10 mm in diameter and could be folded during implantation into the subject.

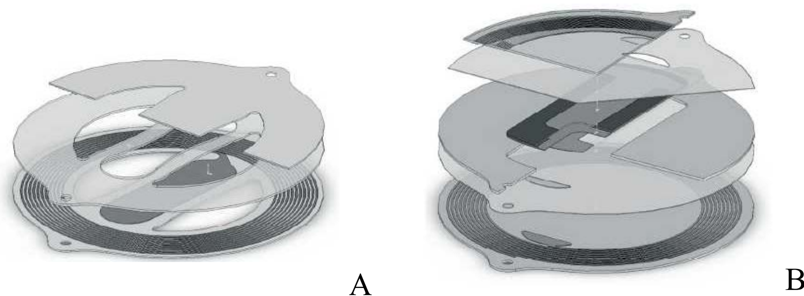

Figure 2-8. Reprints of figures from Michael A. Fonseca, "Flexible wireless passive pressure sensors for biomedical applications," 2006 Hilton Head Workshop on Sensors and Actuators, reprinted with the permission of the author and the Transducer Research Foundation. A) A reprint of Figure 3b. B) A reprint of Figure 4b.

The devices made use of the circular coil design used by Collins [31] and the lack of a conductive substrate to achieve Q values of up to 77, the highest reported since Collins [31]. The impedance phase dip was used to characterize the system, but for clinical trials a new system was

المنارة للاستشارات
www.manaraa.com

used. Little detail is given in the technical literature, but the basic idea is as follows: An RF burst is sent to the sensor to charge the tank circuit. At the end of the burst, a decaying sine wave in the sensor's resonant frequency is detected. The dynamic requirement of the system is set by the heart rate, which is at a maximum 200 beats per minute or 3.33 Hz. This system tracked the resonance at 35.7 MHz with a sensitivity of 43 Hz/Pa for the stiffer ceramic chamber device. Frequency shifts of 120 kHz were detected at a 2 Hz heart rate. The sensor was successful in animal testing with a range of up to 20 cm coil separation. This was a very successful device that proved that this technology could be commercially viable.

2.2.8 Review of Work Done at the California Institute of Technology

Po-Jui Chen et al. of the California Institute of Technology presented in 2010 the most recent passive wireless sensor found [60]. They reported a new generation of wireless intraocular pressure sensors that were previously published in 2008 [61]. The updated design is shown in Figure 2-9. They achieved much higher quality factors by removing the silicon substrate from beneath the coils. This also allowed the device to be folded for implantation, as are the CardioMEMS sensors. This group used impedance spectra from a network analyzer for resonance detection. The device had a radius of 4 mm and was 4 mm x 1.5 mm when folded for implantation. The device was characterized from 0 to 13.3 kPa with 1.33 kPa resolution. This corresponded to a detected frequency shift of 1.6 MHz. They also determined the range of the sensor to be 2 cm. The sensors were tested *in vivo* in rabbit eyes.

2.3 Summary

A summary of metrics is presented in Table 2-1. The nominal static capacitance of the device is listed as C_o, and static inductance is listed as L. The nominal resonant frequency, quality factor and full-scale shift are listed under f_o, Q and Δf_{fs}, respectively. The sensitivity of the sensors to changes in pressure is given as S with units of kHz/Pa. All of the sensors reviewed

المنارة للاستشارات
www.manaraa.com

operate at different frequencies, so it is useful to compare a normalized sensitivity given by dividing the sensitivity S by the resonant frequency f_o. The resulting normalized sensitivity, S_n is reported in ppm/Pa. To account for the variation in diaphragm size this is further normalized by the area to give the normalized force sensitivity S_F in 1/N. Values inferred from the data presented in the paper are *italicized*. All pressure units are converted to Pa for ease of comparison.

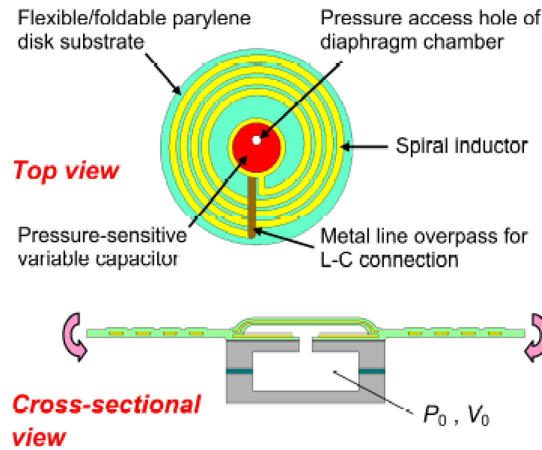

Figure 2-9. Reprint of Figure 3 from Po-Jui Chen, "Wireless intraocular pressure sensing using microfabricated minimally invasive flexible-coiled LC sensor implant," 2010, *Journal of Microelectromechanical Systems*, reprinted with permission from IEEE.

Table 2-1. Passive wireless sensor quantities from literature review

Citation	Interrogation Circuit	C_o [pF]	L [μH]	Q	f_o [MHz]	Δf_{fs} [MHz]	S [kHz/Pa]	S_n [ppm/Pa]	S_F [1/N]
Collins	Grid-Dip	0.16	2.5	80	120	*32.5*	*0.75*	*6.25*	*0.079*
Rosengren	Grid-Dip	-	-	30	*43.6*	*0.08*	0.007	*0.161*	*0.049*
Park	Grid-Dip	3	0.22	-	120	-	15.0*	*125**	*500.0**
Ong	Z Spectra	-	-	-	57	*6.4*	0.18	*3.15*	*0.004*
Akar	Z Spectra	3.65	1.2	8	76	6	0.9	11.9	*12.87*
Baldi	Z Spectra	-	1.7	5.4	31.8	*0.19*	0.009	*0.283*	*0.022*
Fonseca	Z Spectra	-	-	77	35.7	-	0.043	*1.21*	*0.091*
Chen	Z Spectra	3.6	0.057	30	350	*16*	1.20	3.41	*1.085*

*Predicted.

المنارة للاستشارات
www.manaraa.com

All of the reviewed papers have a few things in common. They all used frequency sweep methods to characterize the sensor. Regardless of whether a grid dip oscillator, network analyzer, or impedance analyzer was used, they captured data from a sweep of frequencies before the exact resonant frequency was determined. They all used a loop antenna to monitor the sensors, and close proximity was required between the sensor and antenna. All of the authors modeled this link as a pair of magnetically coupled coils with a mutual inductance M. This near-field magnetostatic analysis assumed that the sensor and the antenna were not moving with respect to each other. This is an important consideration for packaging and testing passive wireless sensors.

The biggest conclusion that can be taken away from these works is the critical importance of Q. The Q determines the sharpness of the detected peaks that are used to determine the resonant frequency of these devices. In the case of the grid dip oscillator, there is a minimum Q for the circuit to lock onto the resonance. For values below this, the circuit will not work. For the other measurement techniques, the sharper the peak the more precisely the shift can be quantified. This means that the resolution, or minimum detectable signal (*MDS*), is directly related to the Q. An important lesson can be learned by comparing the sensors above that achieved Q's of 30 or more with those that had Q's of less than 10. The common difference between them was the location of the coil and its surrounding medium. All of the high Q devices had coils encased in polymers rather than on the conductive silicon die. This important knowledge led to the development of a new packaging technique for the wireless shear stress sensor with the coils embedded in the dielectric package around the capacitive sensor.

There is another issue that deserves mentioning for adaptation of this passive wireless technique for use in shear stress measurements. The force sensitivities seen in all of these devices are too small for this application. In general forces that are normal to the surface (pressure) are

المنارة للاستشارات
www.manaraa.com

several orders of magnitude larger than the forces that are tangential to the surface (shear). The reviewed works focused on environments where the pressure forces were between 10 to 60 kPa, so these sensitivities were adequate for detection. The target shear stress levels for the sensors presented in this dissertation are around 5 Pa. In Chen's work [60], for example, with a sensitivity of 1.2 kHz/Pa, a 5 Pa shear stress (considering only the magnitude of the force and ignoring the direction) would give only a 6 kHz full-scale shift. To achieve even a meager 40 dB of dynamic range requires a resolution of 60 Hz and a Q of over 600. A similar comparison made with any of the reviewed device parameters would arrive at the same conclusion. The sensitivity of the wireless shear stress sensor must be improved by several orders of magnitude in order to reach a practical detection level.

المنارة للاستشارات
www.manaraa.com

CHAPTER 3
SENSOR MODELING

A comprehensive electromagnetic model for the wireless shear stress sensor is presented in this chapter. The sensor is separated into discrete circuit components. Models for the coils and antenna are first explained, after which the capacitive shear stress sensor is described in detail. At the end of the chapter, the sub-models are consolidated and used to predict the overall response of the system to an input shear stress. A complete model is presented for both a single sensor as well as an array.

The most simplistic circuit model for the wireless sensor is shown in Figure 3-1. The capacitive shear stress sensor is represented by the variable capacitance, C_s whose value is a function of the input shear. The inductor, L_c connected to the sensor capacitance is referred to as the "sensor coil" and is used to establish the primary resonance in the system. The second inductor, L_a represents the loop antenna. Inductive coupling of the two is represented by the mutual coupling, M. Note that throughout the remainder of the dissertation the term "coil" is often used to refer to the inductor coil and its associated inductance, whereas the term "antenna" is used to refer to the antenna (also technically a coil) and its inductance.

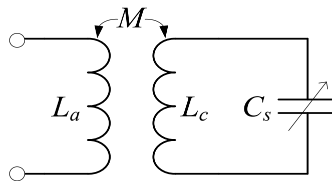

Figure 3-1. Basic circuit model for the wireless shear stress sensor.

3.1 Coil and Antenna Models

In this section the inductances of the sensor coil and antenna are presented. The wireless link is achieved through mutual coupling of these two coils. The simplistic model shown in Figure 3-1 represents the ideal behavior. In reality, however, there are both reactive and resistive

www.manaraa.com

parasitics present. The major sources of these parasitics and their incorporation into the model are presented at the end of the section.

3.1.1 Sensor Coil and Antenna Inductance

There is a wide range of inductive geometries and materials that can be used for the coil and the antenna. For this work, space and fabrication complexity are considered in order to choose appropriate coil and antenna designs.

First consider the LC tank. The sensor capacitance is expected to be in the low pF range, so an inductance on the order of a few hundred nH is required to achieve the desired MHz resonant frequency range. This relatively high inductance level rules out meander line inductors [62]. Fabrication complexities rule out solenoid or multilayer coils, at least for the initial design. Instead, planar spiral coils are used, which facilitate high inductance and simple, single-layer construction. The inductance of a planar spiral is proportional to the area bounded by the coil and the number of turns. The capacitive shear stress sensors are made using a wafer-level microfabrication process and are cut from silicon wafers into square die. With this consideration, the bounded area and number of turns can be maximized—thereby maximizing inductance—by using square coils. A 3D schematic of a square spiral coil is shown in Figure 3-2.

A coil's inductance is defined by both geometric and material parameters. As a general rule, inductance is proportional to the permeability μ of the surrounding medium, the area bounded by the turns, and the square of the number of turns, N. Closed-form approximations exist for simplified geometries, such as long solenoids and filamentary loops, but not for planar spiral coils. There are also empirical approximations [63-66], but these models are inaccurate for spirals of fewer than 10 turns and for frequencies above the kHz range.

المنارة للاستشارات
www.manaraa.com

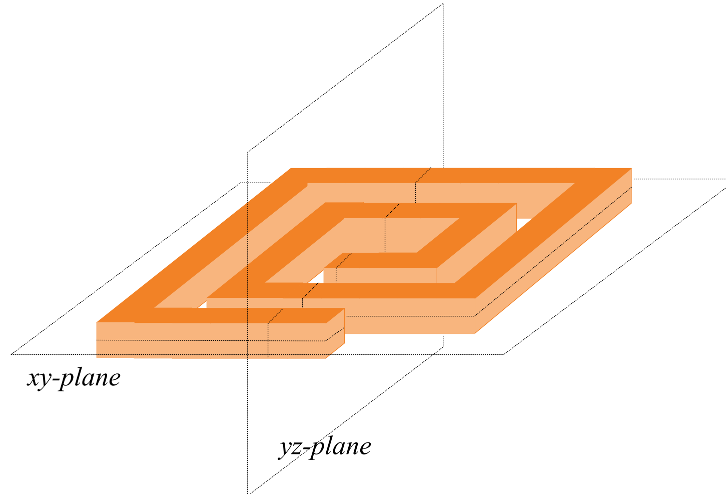

Figure 3-2. A 3D diagram of a single layer 2-turn spiral coil. The xy and yz planes are indicated for reference to Figure 3-3.

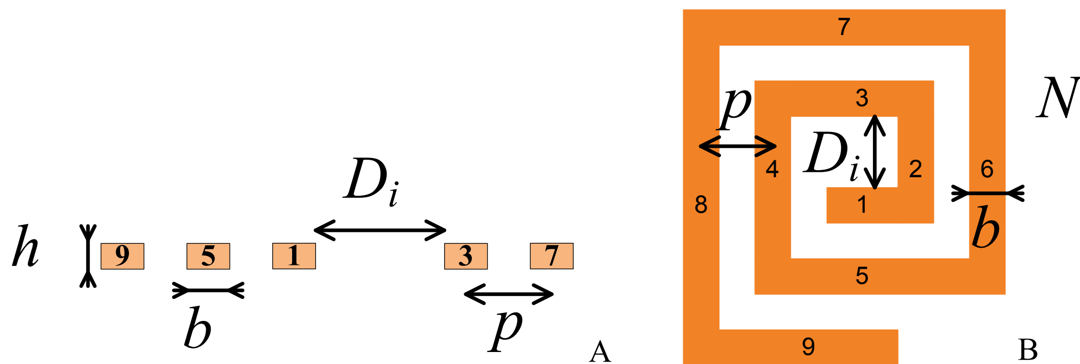

Figure 3-3. Cross-sections of spiral coil from Figure 3-2 with geometric parameters indicated. A) A yz-plane side view showing crosscut coil lines. B) A xy-plane top view showing the spiral pattern.

A common technique [67] to calculate the inductance for square spiral coils is to break them up into sections, as shown in Figure 3-3B. Considering each section separately, the system will have an inductance matrix of

$$\begin{pmatrix} L_1 & M_{12} \cdots M_{1n} \\ M_{21} & L_2 \quad \cdots \quad \vdots \\ \vdots & \vdots \quad \ddots \quad \vdots \\ M_{m1} & \cdots \quad \cdots \quad L_n \end{pmatrix}. \tag{3-1}$$

The self-inductance, L_n for a straight wire segment is

المنارة للاستشارات
www.manaraa.com

$$L_n = \frac{\mu_o l}{2\pi}\left[\ln\left(\frac{2l}{b+h}\right)+\frac{1}{2}\right], \quad (3\text{-}2)$$

where l is the length, b is the width, and h is the height of the segment. Assuming parallel, straight wire filaments the mutual-inductance, M_{nm} is given by

$$M_{nm} = \pm\frac{\mu_o l}{2\pi}\left[\ln\left(\frac{l}{p}+\sqrt{1+\frac{l^2}{p^2}}\right)-\sqrt{1+\frac{l^2}{p^2}}+\frac{p}{l}\right], \quad (3\text{-}3)$$

in which l is the length of the filaments and p is the distance between them.

Consider a two-turn square spiral as shown in Figure 3-3. This structure will contain 9 segments giving self-inductances (L_1, L_2, …, L_9) and 72 mutual-inductances (M_{12}, M_{13}, … M_{89}, M_{98}, ... M_{31}, M_{21}). The inductance matrix is reciprocal so $M_{nm} = M_{mn}$, and the total number of unique mutual-inductances is reduced to 36 (M_{12}, M_{13}, … M_{89}). The sign of the mutual-inductance depends on the current direction in the wires—positive for wires with current in the same direction and negative for wires with current in opposite directions. Wires at 90° angles do not contribute any mutual-inductance so

$$M_{12} = M_{14} = M_{16} = M_{18} = M_{23} = M_{25} = M_{27} = M_{29} = M_{34} = M_{36} = 0 \quad (3\text{-}4)$$

and $$M_{38} = M_{45} = M_{47} = M_{49} = M_{56} = M_{58} = M_{67} = M_{69} = M_{78} = M_{89} = 0. \quad (3\text{-}5)$$

The total inductance

$$L_{tot} = L_{self} + 2\left(M_+\right) - 2\left(M_-\right) \quad (3\text{-}6)$$

is the sum of the self-inductances of each segment

$$L_{self} = L_1 + L_2 + L_3 + L_4 + L_5 + L_6 + L_7 + L_8 + L_9, \quad (3\text{-}7)$$

plus the positive coupling terms

$$M_+ = M_{15} + M_{19} + M_{26} + M_{37} + M_{48}, \quad (3\text{-}8)$$

المنارة للاستشارات
www.manaraa.com

minus the negative coupling terms

$$M_{-} = M_{13} + M_{17} + M_{24} + M_{28} + M_{35} + M_{39} + M_{46} + M_{57} + M_{68} + M_{79} + M_{68}\,. \qquad (3\text{-}9)$$

The procedure outlined above is more accurate than the empirical approximations, but it assumes uniform current density in each wire segment. This simplifying assumption does not account for high-frequency current distribution effects, where the current in the conductors travels primarily through the outer skin of the conductor, as shown in Figure 3-4. This phenomenon is known as the skin effect, and the characteristic skin depth can be calculated by

$$\delta_s = \sqrt{\frac{2\rho}{\pi f \mu}}\,, \qquad (3\text{-}10)$$

where ρ is the resistivity of the conductor and f is the frequency. To account for this effect, each of the nine wire segments must be further discretized, as shown in Figure 3-5. Filaments can then replace these wire segments, and the inductance can be calculated as outlined above. An appropriate scaling factor is assigned to each filament to account for the current density in the location of the wire segment. The frequency-dependent scaling factor is found based on the 3D solution to Maxwell's Equations on all of the filaments.

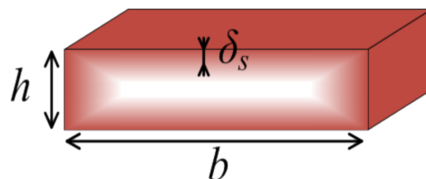

Figure 3-4. Skin depth effect on current density inside a conductor.

Using this technique to account for frequency, the number of filaments in the system and thus the number of elements in the matrix are drastically increased. The total number of filaments, N_{fil} is given by

$$N_{fil} = (4 \cdot N + 1) \cdot N_h \cdot N_b\,, \qquad (3\text{-}11)$$

المنارة للاستشارات
www.manaraa.com

where N is the number of turns, N_h is the discretization of the height and N_b is the discretization of the base. Take for example a basic 5 turn coil with 7 height and 9 base discretizations. This results in a huge 1323 x 1323 matrix with 1,750,329 inductance terms. An ideal technique used in computational electromagnetics for dealing with very large matrices is the method of moments (MoM). FastHenry is part of the Fast Field Solver software package, written at the Massachusetts Institute of Technology, and is a free MoM code for finding the inductances of 3D geometries. It is a text-based code, so a MATLAB code was written to convert the inductor geometry into appropriate input files for use by the FastHenry solver.

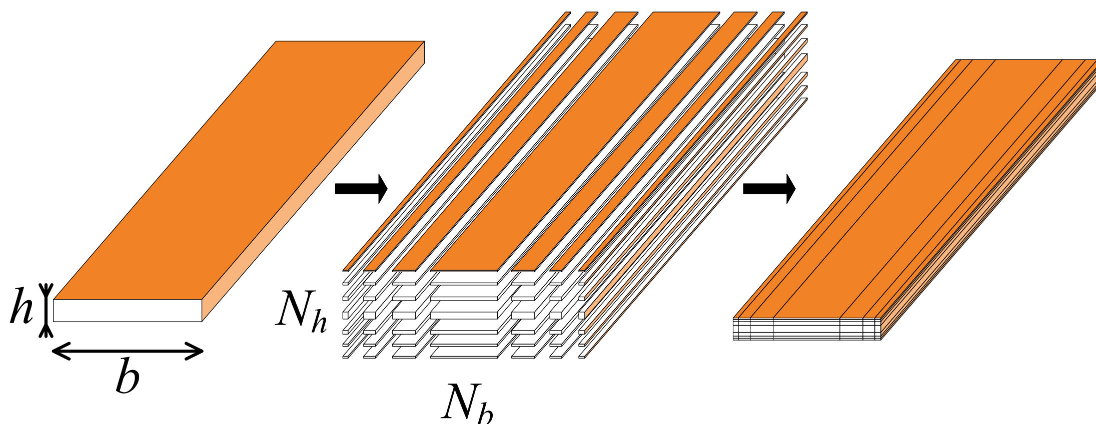

Figure 3-5. Discretization of wire segments for high frequency compensation.

An additional advantage of the FastHenry code is that the wire segments are not limited to the parallel and perpendicular segments shown in Figure 3-3B, so more advanced features like rounded corners can be integrated into the simulation. Rounded corners offer significant advantages in the current distribution of the coil without giving up a significant area that would reduce the total inductance. The current distribution in the lengths of the wires is changed at higher frequencies as described by the skin depth. The current density at the corners, however, is dominated by the geometry. A finite-element simulation (using COMSOL Multiphysics) of four different coil corner geometries is shown in Figure 3-6. The areas of high current density are

المنارة للاستشارات
www.manaraa.com

shown in red, and low current density in blue. Low current density concentrations are desirable to reduce resistive losses. For this reason, the second rounded geometry (Rounded 2) is selected, which actually shows a decrease in the current density around the bend.

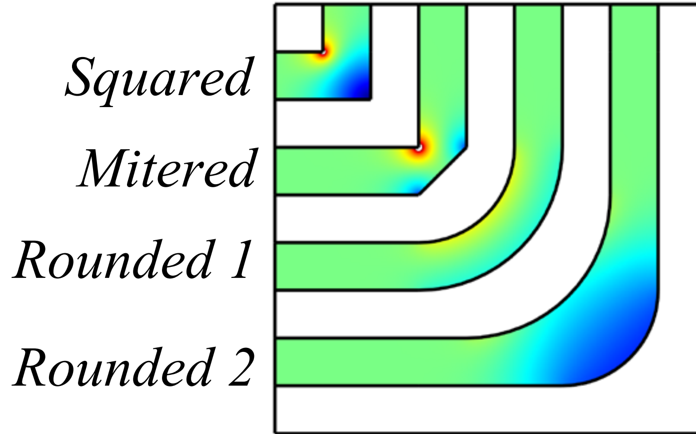

Figure 3-6. Qualitative current-density distributions in various wire bend configurations. Red indicates high current density; blue indicates low current density.

After solving for the inductance of the sensor coil, the antenna inductance is simple. The same model shown in Figure 3-3 can be used by setting the number of turns to one and the pitch to zero. The antenna inductance is solved in the same way using the FastHenry MoM solver. With the self-inductances of both the sensor coil and the antenna, the next step is to determine the mutual coupling between the coil and antenna.

3.1.2 Mutual-Inductance

The sensor coil and loop antenna are placed in close proximity and are treated as mutually coupled coils. The coupling factor

$$k = \frac{M}{\sqrt{L_a L_c}}, \tag{3-12}$$

is a ratio of the mutual-inductance, M to the root product of the self-inductances, L_a and L_c. A transformer is a special case of coupled coils where the windings share nearly all of their flux. A

المنارة للاستشارات
www.manaraa.com

transformer often uses a soft magnetic core to direct the flux and achieve a near perfect coupling $k \approx 1$.

For the wireless sensor, a common core is not possible, so only a fraction of the total flux is shared by the loop antenna and the sensor coil. The mutual inductance M can be determined by simulating both the antenna and the sensor coil in a single FastHenry model. The two coils are identified by separate input ports, Port 1 and Port 2, and the software generates a 2 x 2 matrix specifying the mutual-inductances and the self-inductances,

$$\begin{pmatrix} L_{11} & M_{12} \\ M_{21} & L_{22} \end{pmatrix}. \tag{3-13}$$

The mutual-inductance from the antenna to the coil is equal to the mutual-inductance from the coil to the antenna, that is

$$M = M_{12} = M_{21}. \tag{3-14}$$

The antenna is identified as Port 1 so

$$L_a = L_{11}, \tag{3-15}$$

and the sensor coil is identified as Port 2

$$L_c = L_{22}. \tag{3-16}$$

To represent the non-ideal coupling, two equivalent two-port circuit representations are possible, as shown in Figure 3-7. The first uses an ideal transformer with a turns ratio of

$$a = \frac{L_a}{M}, \tag{3-17}$$

a shunt inductor on the input side, and a series inductor on the sensor side. Alternatively, a T-circuit can be used, as shown in the second circuit. To simplify the circuit analysis, the T-circuit is used for the wireless sensor model.

المنارة للاستشارات
www.manaraa.com

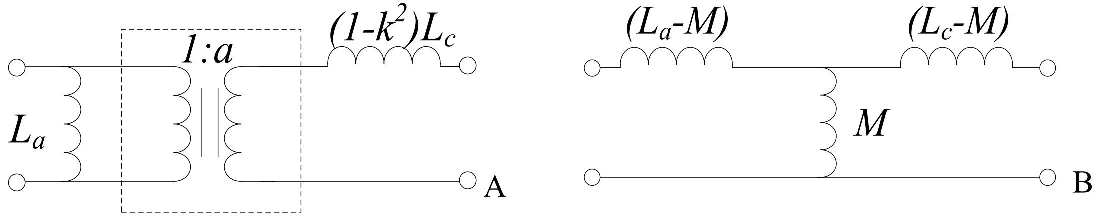

Figure 3-7. Equivalent transformer model circuits for coupled coils. A) Ideal transformer model with shunt and series inductors. B) T-circuit model.

3.1.3 Parasitics

There are both reactive and resistive parasitics that have to be accounted for in the models of both the sensor coil and the antenna. These parasitics are inherent in any real system and can be reduced by careful design, but not eliminated entirely. The equivalent circuits shown in Figure 3-8 and Figure 3-9 include the parasitic components for the inductor coil and loop antenna, respectively.

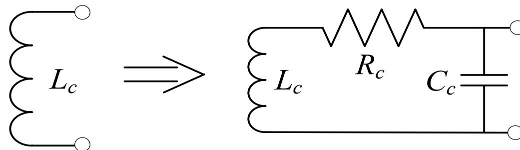

Figure 3-8. Non-ideal circuit model for the sensor coil.

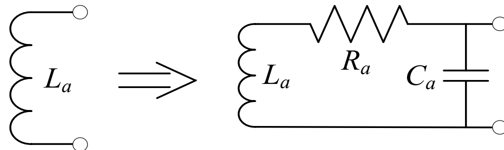

Figure 3-9. Non-ideal circuit model for the antenna.

The resistive components, R_c and R_a respectively, account for the energy loss in the circuits. There are several sources of energy loss, including far field radiation, eddy current generation, conduction in the substrate, and I^2R conductive heating in the winding. Electrically conductive surfaces must be kept at a distance from the wireless link, so that eddy current generation is minimized. The coils are made on FR4 substrates with reasonably low loss tangent, so the conduction losses should not be a major factor. The coil lengths are much less than the

المنارة للاستشارات
www.manaraa.com

wavelengths around 100 MHz, so the radiation losses should also be minimized. This leaves I^2R heating as the dominant resistive parasitic source for both the antenna and inductor coil.

For long, thin conductors, the resistance is given by

$$R = \frac{\rho \cdot l_{tot}}{A}, \tag{3-18}$$

where ρ is the resistivity, l_{tot} is the total length, and A is the cross-sectional area. For a spiral coil, where the length of each turn gets progressively smaller toward the center, the length can be calculated given the number of turns N, the turn to turn pitch p, the base width b, and the inner diameter D_i, by

$$l_{tot} = 4\left[N\left(D_i + b\right) + 2p\sum_{n=1}^{N}\left(n-1\right)\right]. \tag{3-19}$$

The effective area of current flow through the wire is a function of frequency. At dc, current flows through the entire cross section, and given the height h, the area is simply

$$A_{dc} = bh. \tag{3-20}$$

As the frequency increases, however, the skin effect shown in Figure 3-4, restricts the current to the outer shell of the wire. To account for this, the center of the conductor is removed for the ac effective area given by

$$A = A_{dc} - \left(b - 2\delta_s\right)\left(h - 2\delta_s\right). \tag{3-21}$$

The resistance for the sensor coil is found by combining Equations 3-18, 3-19, and 3-21 to get

$$R_c = \frac{2\rho\left[N\left(D_i + b\right) + 2p\sum_{n=1}^{N}\left(n-1\right)\right]}{\delta_s\left(b+h\right) - 2\delta_s^{\,2}}. \tag{3-22}$$

For the single turn loop antenna, $N = 1$, $p = 0$ and the resistance simplifies to

المنارة للاستشارات
www.manaraa.com

$$R_a = \frac{2\rho(D_i + b)}{\delta_s(b+h) - 2\delta_s^2}. \quad (3\text{-}23)$$

The inductors are intended to operate as reactive components, but there are still undesirable reactive parasitics that can limit the performance of the inductor. Any structure or mechanism that stores energy in a magnetic field adds to the inductance of the coil, while any structure or mechanism that stores energy in an electric field acts as a capacitance and degrades the inductance. The parasitic reactance can be modeled as parallel capacitors, C_c and C_a, as shown in Figure 3-8 and Figure 3-9. The parasitic capacitance subtracts from the total reactance of the inductor and sets up a self-resonant situation at a specific frequency where the total reactance is effectively zero. Inductors must be used below their self-resonant frequency, and so the parasitic capacitance parameters are of vital concern.

The primary parasitic capacitance in the coil arises from inter-winding capacitances, as illustrated in Figure 3-10. To calculate the inter-winding capacitance, some approximations must be made. First the coil is unwrapped, and segments 1 through 4 and 5 through 8 from Figure 3-3 are placed in parallel, separated by a gap of $p - b$. A well-known equation for the capacitance of two parallel wires on a substrate [68-70] is

$$C_c = \frac{\pi\varepsilon_o\varepsilon_{PCB}}{l\ln\left(\frac{2p}{b+h} + \sqrt{\frac{2p}{b+h} - 1}\right)}, \quad (3\text{-}24)$$

where $\varepsilon_{PCB} = \varepsilon_{FR4} \approx \varepsilon_{Mask} \approx 3$ and l is the length of the segments. For more than two turns, the same procedure is used with the capacitance of each successive loop being added in series to give

$$C_c = \frac{\pi\varepsilon_o\varepsilon_{PCB}}{\ln\left(\frac{2p}{b+h} + \sqrt{\frac{2p}{b+h} - 1}\right)} \cdot \frac{1}{\left(\sum_{n=1}^{N-1} \frac{1}{4\left[D_i + b + 2p(n-1)\right]}\right)}. \quad (3\text{-}25)$$

المنارة للاستشارات
www.manaraa.com

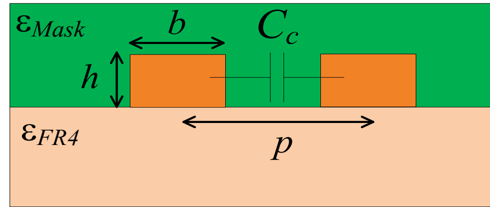

Figure 3-10. Cross section side view showing two wires of the coil.

For the antenna parasitic capacitance, a one-turn coil is undefined according to Equations 3-24 and 3-25. Looking at the geometry, the wire elements are now separated by D_i, which is much larger than p - b. Thus, the resulting capacitance is negligible for a single turn loop antenna. The dominant source of parasitic capacitance for the antenna comes from the RF coaxial adapters that connect the antenna to the external circuitry. The parasitic capacitance of the adapters is the same for all of the tests and is simply measured prior to attaching the antenna.

3.2 Capacitive Shear Stress Sensor

The first step in defining the relationship between the input shear and the resulting capacitance change is to determine the displacement of the sensor resulting from the shear stress input. The displacement is then used with a variable gap capacitive transduction derivation to find the change in capacitance. Sources of parasitics are identified at the end of the sensor capacitance section, since they are inherent to the sensor and affect its sensitivity.

3.2.1 Mechanical Model

Figure 3-11 shows the floating element structure of the sensor. The checkered area in the figure indicates the floating element; this is the primary surface area that the in-plane shearing forces will act on to cause a displacement. The four tethers attached to the sensing area hold the sensing structure suspended and act as restoring springs to return the sensor to its neutral position when the input force is reduced back to zero. The deflection equation for the sensor is vital to the rest of the modeling, because it relates shear input to deflection used in the capacitive transduction equations in Section 3.2.2. For a more detailed treatment of the sensor mechanics,

المنارة للاستشارات
www.manaraa.com

including dynamics and nonlinear deflection, the reader may refer to the previous floating element shear stress sensor literature [21,22,71,72].

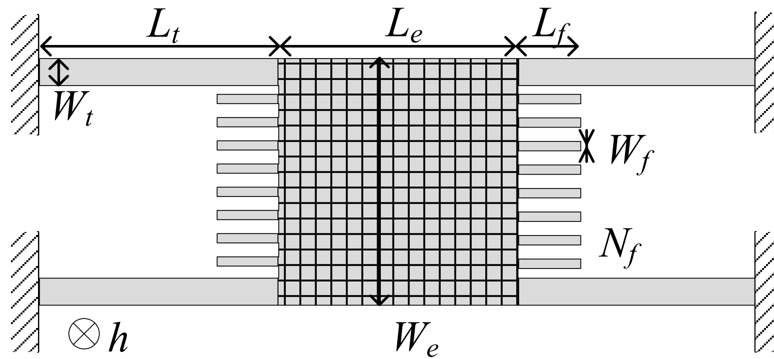

Figure 3-11. Mechanical diagram of the floating element sensor structure.

The deflection of the floating element is obtained by solving the Euler-Bernoulli beam equation on a simplified mechanical model. The floating element is presumed to be perfectly rigid and can be replaced by a point load. The sensor is also assumed to be perfectly symmetric, so each of the two pairs of tethers should support half of the floating element load. This reduces the point load by a factor of two and simplifies the system to a single clamped-clamped beam shown in Figure 3-12. Shear stress will also act on the surfaces of the tethers and is represented by a distributed load across the beam.

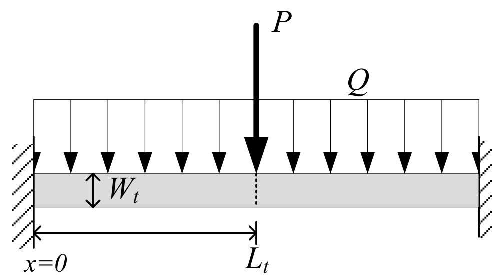

Figure 3-12. Simplified clamped-clamped beam mechanical model of sensor with force vectors.

The deflection at the center of the beam in the simplified model will be the same as the floating element displacement needed for the sensor model. The resulting equation modified from the derivation in [21] is

المنارة للاستشارات
www.manaraa.com

$$w(\tau)=\frac{\tau A_e}{4Eh}\left(\frac{L_t}{W_t}\right)^3\left(1+\frac{2A_t}{A_e}\right), \quad (3\text{-}26)$$

where τ is the input shear stress; E is the Young's modulus; and h, L_t, and W_t are the thickness, length, and width of the tethers. This equation and the nonlinear equation [21] for deflection are given in the discussion of nonlinearity in Appendix A. The area of the tethers A_t is given by

$$A_t = W_t L_t \,. \quad (3\text{-}27)$$

The area of the floating element A_e is given by

$$A_e = W_e L_e + N_f W_f L_f \,, \quad (3\text{-}28)$$

where L_e and W_e are the length and width of the floating element and L_f, W_f, and N_f are the length, width, and number of comb fingers on the floating element. The linear mechanical shear to displacement sensitivity $S_{\tau w}$ in nm/Pa is purely a function of geometry and material properties and can be written as

$$S_{\tau w}=\frac{w}{\tau}=\frac{A_e}{4Eh}\left(\frac{L_t}{W_t}\right)^3\left(1+\frac{2A_t}{A_e}\right). \quad (3\text{-}29)$$

3.2.2 Capacitance Model

A capacitive transduction model is used to find the change in capacitance when the sensor's floating element is displaced by an input shear, as found in Section 3.2.1. This section presents the capacitive structures used to develop the model. Only the variable capacitive structures that contribute to the transduction are considered. All other fixed capacitive structures are addressed in the next section and are considered parasitic.

As shown in Figure 3-13, there are three electrically isolated regions on the sensor, which form two sets of variable capacitors. The capacitive structures were designed in complementary pairs, red-blue and green-blue, for a wired differential readout. For the wireless technique, only a

المنارة للاستشارات
www.manaraa.com

single variable capacitor is needed. In this example, red-blue is chosen and green is left floating. The primary structure is the comb finger C_1 at the edge of the floating element. The sensor also leverages the gaps between the fixed sidewalls and the free end of the floating element C_2 and the moving tethers C_3.

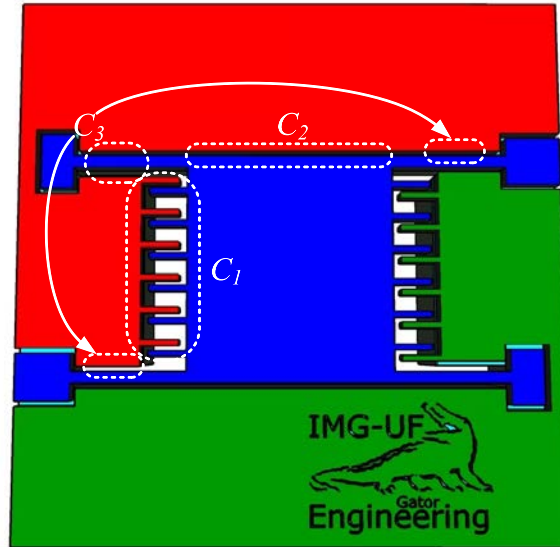

Figure 3-13. A 3D graphic of the sensor with variable capacitive structures indicated (not to scale).

The parallel plate capacitance assumption is used, defining the capacitance as

$$C = \frac{\varepsilon \cdot A}{g}, \tag{3-30}$$

in which, $\varepsilon = \varepsilon_o$ is the permittivity of free space, since the medium in the gaps is air. A is the area of the sidewalls, and g is the gap. The three variable capacitors are in parallel, so their capacitances are simply summed. The total capacitance is then

$$C_s = C_1 + C_2 + C_3. \tag{3-31}$$

Each of the three capacitors can be represented by a nominal capacitance and a change in capacitance and defined by

$$C_i = C_{oi} + \Delta C_i(w). \tag{3-32}$$

المنارة للاستشارات
www.manaraa.com

The nominal capacitance C_{oi} is a constant and is simply given by the parallel plate equation for the respective geometry. The change in capacitance ΔC_i is the amount the sensor capacitance changes and is a function of the displacement of the floating element w given by Equation 3-26.

To simplify the fabrication, an asymmetric comb with primary gap g_{o1} and secondary gap g_{o2} is used, as shown in Figure 3-14. This enables the use of the more sensitive variable gap for sensing without needing to isolate and run overlapping traces to each finger. The number of fingers N_f includes all of the fingers attached to the floating element, so when using only one set of fingers, this value must be halved. The number of fingers that will fit on the floating element is given by

$$N_f = 2\frac{W_e - 2W_t}{2W_f + g_{o1} + g_{o2}}, \tag{3-33}$$

rounded down to the nearest even number. The distance x_o is the nominal overlap of the fingers, and h is the height. The nominal capacitance for this structure is

$$C_{o1} = \frac{\varepsilon_o x_o h}{2}\left(\frac{N_f}{g_{o1}} + \frac{(N_f - 2)}{g_{o2}}\right) \tag{3-34}$$

and the change in capacitance is

$$\Delta C_1(w) = \frac{\varepsilon_o x_o h}{2}\left(\frac{N_f}{g_{o1} - w} + \frac{(N_f - 2)}{g_{o2} + w} - \frac{N_f}{g_{o1}} - \frac{(N_f - 2)}{g_{o2}}\right). \tag{3-35}$$

The next capacitive structure is the sidewall of the floating element, as shown in Figure 3-15. The nominal capacitance for this structure is simply

$$C_{o2} = \frac{\varepsilon_o L_e h}{g_{o1}} \tag{3-36}$$

المنارة للاستشارات
www.manaraa.com

and the change in capacitance is

$$\Delta C_2(w) = \varepsilon_o L_e h\left(\frac{1}{g_{o1} - w} - \frac{1}{g_{o1}}\right). \tag{3-37}$$

The tether shown in Figure 3-16 uses the asymmetric gap as well, but there is a further complication. When the sensor moves, the tethers bend, and the separation is no longer uniform. At the clamped end the deflection is zero, while at the floating element it is *w*. To compensate for this, a piston equivalent area is used. With this approximation, half of the tether is included in the variable capacitance and the other half is left as a fixed capacitance [21]. The fixed capacitance adds to the parasitics of the sensor, but the added sensitivity offsets this negative effect. In addition to the two gaps shown in Figure 3-16, there are two more narrow gaps indicated by the arrows in Figure 3-13. The nominal capacitance for this structure is

$$C_{o3} = \frac{\varepsilon_o L_t h}{2}\left(\frac{3}{g_{o1}} + \frac{1}{g_{o2}}\right), \tag{3-38}$$

and the change in capacitance is

$$\Delta C_3(w) = \frac{\varepsilon_o L_t h}{2}\left(\frac{3}{g_{o1} - w} + \frac{1}{g_{o2} + w} - \frac{3}{g_{o1}} - \frac{1}{g_{o2}}\right). \tag{3-39}$$

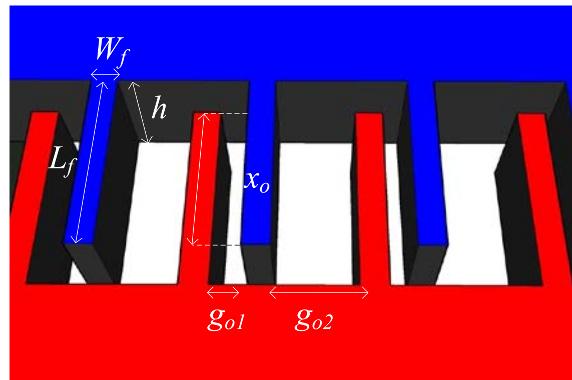

Figure 3-14. Zoomed in 3D graphic showing capacitive comb fingers (not to scale).

www.manaraa.com

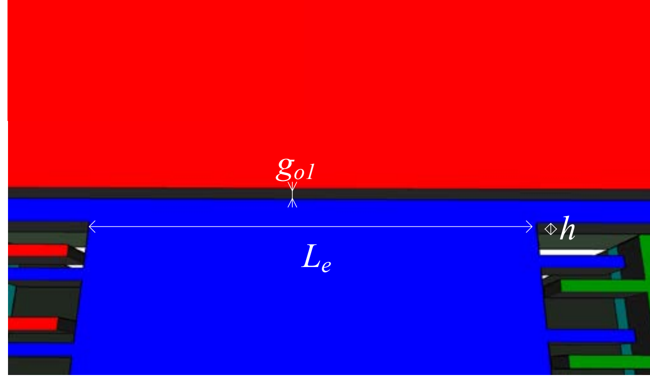

Figure 3-15. Zoomed in 3D graphic showing element end capacitance (not to scale).

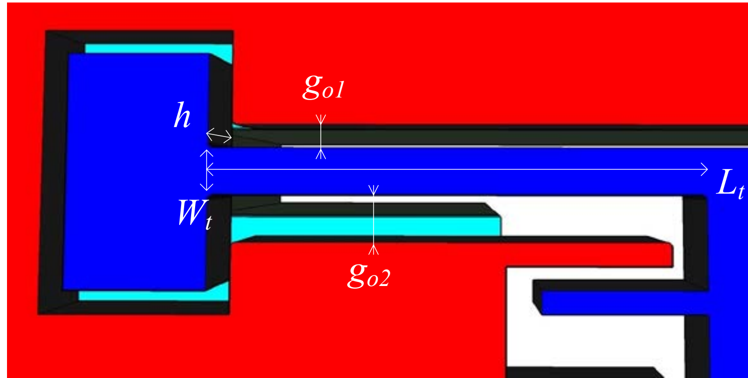

Figure 3-16. Zoomed in 3D graphic showing tether capacitance (not to scale).

Adding Equations 3-34, 3-36, and 3-38, the nominal capacitance, which is only a function of the sensor geometry, is

$$C_{os} = \frac{\varepsilon_o h}{2}\left(\frac{N_f x_o + 2L_e + 3L_t}{g_{o1}} + \frac{(N_f - 2)x_o + L_t}{g_{o2}}\right). \tag{3-40}$$

The total change in capacitance is inherently nonlinear given by

$$\Delta C_s(w) = \frac{\varepsilon_o h}{2}\left(\frac{N_f x_o + 2L_e + 3L_t}{g_{o1} - w} + \frac{(N_f - 2)x_o + L_t}{g_{o2} + w} - \frac{N_f x_o + 2L_e + 3L_t}{g_{o1}} - \frac{(N_f - 2)x_o + L_t}{g_{o2}}\right), \tag{3-41}$$

but using a linear approximation as derived in Appendix A the equation is reduced to

$$\Delta C_s(w) \approx \frac{\varepsilon_o h w}{2}\left(\frac{N_f x_o + 2L_e + 3L_t}{g_{o1}^{\ 2}} - \frac{(N_f - 2)x_o + L_t}{g_{o2}^{\ 2}}\right). \tag{3-42}$$

المنارة للاستشارات
www.manaraa.com

The displacement to change in capacitance sensitivity S_{wc} in fF/nm is purely a function of geometry and can be written as

$$S_{wc} = \frac{\Delta C_s}{w} = \frac{\varepsilon_o h}{2}\left(\frac{N_f x_o + 2L_e + 3L_t}{g_{o1}^{2}} - \frac{\left(N_f - 2\right)x_o + L_t}{g_{o2}^{2}}\right). \tag{3-43}$$

3.2.3 Parasitics

As with the coils, there are both resistive and reactive parasitics on the capacitive shear stress sensor. The three conductive regions on the sensor shown in Figure 3-13 are electrically isolated, so at dc the conduction between them will be zero. However, as the frequency is increased, there will be finite ac losses in the conductive layers of the device. For a capacitor, this can be represented by a conductance term G between the capacitive terminals as shown in Figure 3-17. Also shown is the reactive parasitic component, C_p which represents all of the fixed capacitance. It is considered parasitic, because it adds to the total capacitance without contributing to the change in capacitance. In the next section, this will be shown to effectively decrease the overall sensitivity. First, the major sources of parasitic capacitance will be identified, and then the primary conductance source will be explained.

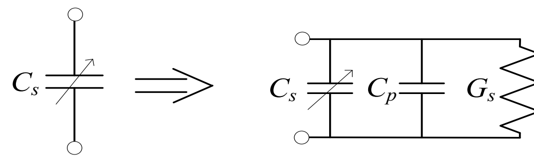

Figure 3-17. Non-ideal circuit model for capacitive shear stress sensor.

There are three sources of fixed or parasitic capacitance in the sensor. The first source, C_{p1} consists of all the gaps in the sensor that must be included in the design for isolation purposes but that do not vary with an input shear. This includes the trenches around the pads that the tethers are anchored to as shown in Figure 3-18. There is two of each type on the die. These trenches are

www.manaraa.com

required to isolate the floating element from the rest of the die to form the three isolated conductors shown in Figure 3-13.

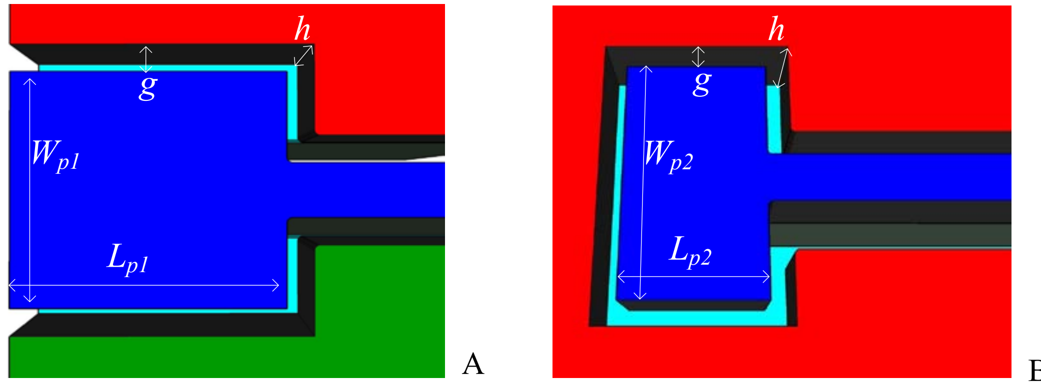

Figure 3-18. Two 3D pad structures showing dimensions for parasitic calculations. A) Type one, large pad used to electrically connect to and anchor the floating element. B) Type two, small pad used to anchor the tether.

The total capacitance of the pads is

$$C_{pads} = \frac{\varepsilon_o h}{g}\left(W_{p1} + 2W_{p2} + 2L_{p1} + 2L_{p2}\right), \tag{3-44}$$

where g is the trench gap, W_{p1} and L_{p1} are the width and length of the first pad, and W_{p2} and L_{p2} are the width and length of the second pad. The gap is maximized in the design to minimize the contribution of this source of fixed capacitance. The pads have differing lengths, so that type one can extend all the way to the edge of the die, isolating the two major regions. In contrast, type two is thin enough to provide a conduction path that connects in parallel the three variable capacitances, described in Section 3.2.2. The equivalent model for the variable tether capacitance in Equations 3-38 and 3-39 includes only half of the tether to account for the difference in displacement along the length of the tether. The other half is effectively unchanging and must be added to this first parasitic capacitance term, such that

$$C_{p1} = C_{pads} + C_{o3}. \tag{3-45}$$

المنارة للاستشارات
www.manaraa.com

The second source C_{p2} of parasitic capacitance comes from the fringing fields of all the gaps in the sensor. A parallel plate assumption was used to derive all of the equations for capacitance thus far. This only accounts for the electric fields directly between the structure sidewalls and also assumes that those fields are all perpendicular to the sidewalls. All capacitors have fringing fields at the edges. The contribution of these fields to the total capacitance are dependent on the relative permittivity of the dielectric in the gap and the ratio of the height to the gap width. In the shear stress sensor, the plates must be free to move, so the dielectric in the gap is simply air, the same as the surrounding medium, making the permittivity ≈ 1 and providing no field guidance in the gap. The sidewall height and gap widths are chosen to maximize sensitivity to shear while minimizing sensitivity to other forces, so there is a limit to this ratio. The analysis and quantification of these fringing fields form a complex problem, so 2D finite element analysis (FEA) simulations using COMSOL Multiphysics is used. All of the different capacitive geometries discussed are analyzed in COMSOL to quantify the contribution to the total capacitance by the fringing fields.

First, the variable gap capacitive structures are simulated. The fingers are shown in Figure 3-19 with both a vertical cross section to show the top and bottom fringe fields and a horizontal cross section to show the fringing fields at the tips of the fingers. To simplify the simulation, a single set of fingers was drawn with periodic boundary conditions to account for the surrounding sets of fingers. Next, the end of the element capacitance is shown in Figure 3-20, which again shows a vertical cross section to illustrate the top and bottom fringes. There will not be any end fringes, as the element gaps end where the tethers begin with no geometry change. There are two types of capacitive configurations for the tethers, as shown in Figure 3-21. The first type has a small gap on both sides and effectively separates the two large conducting surfaces. As such, it

المنارة للاستشارات
www.manaraa.com

consists of three separate conductors with only two being used for the wireless sensor. This simulation is performed by floating the third structure with the source and ground on the other two. The second tether has one large gap and one small gap and is surrounded by a common electrode. For all three of these variable capacitive structures, the fringing field adds an additional 30% of static parasitic capacitance.

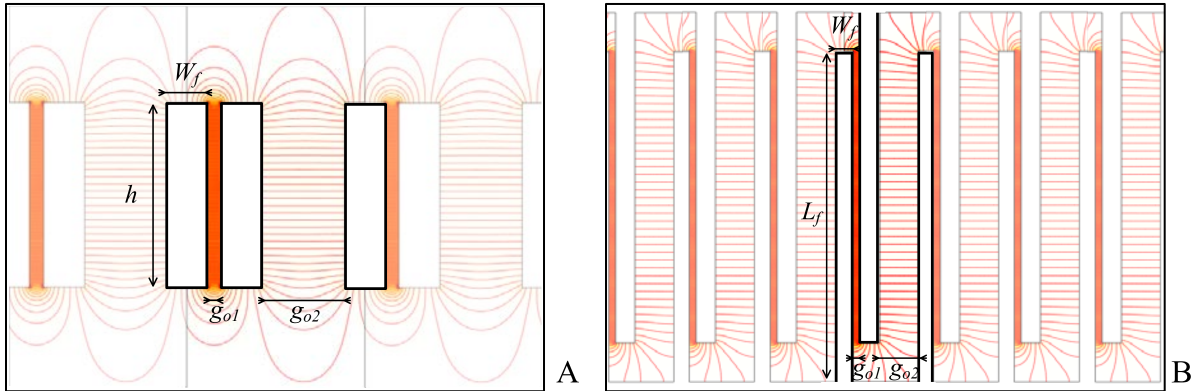

Figure 3-19. Finger fringe simulation results. A) Cross section cutting through fingers to show top and bottom fringe patterns. B) Top view of fingers showing tip fringes.

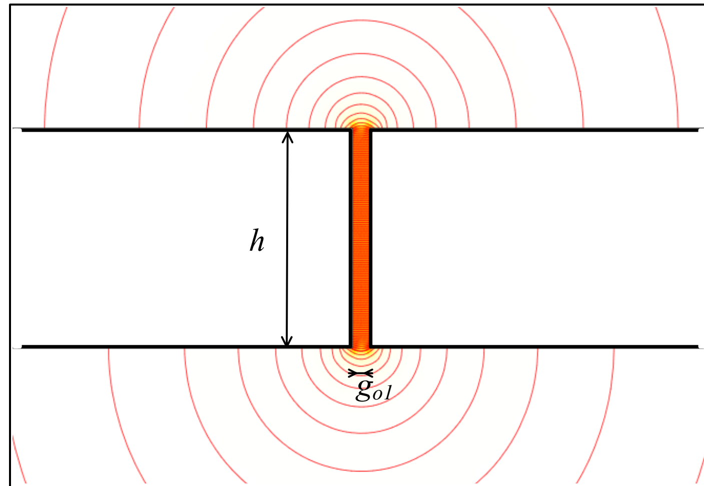

Figure 3-20. Element end fringe field simulation results.

The final gap structure to be analyzed for fringing fields is the gap between the pads described as part of the first source of parasitic capacitance. In this case, there is a change in dielectric permittivity between the gap and the medium occupied by the fringe fields. The gap and the area above the gap is still air, but beneath the pads is an oxide (ε_r = 3.9) layer and the

المنارة للاستشارات
www.manaraa.com

bulk silicon (ε_r = 11.6) layer. As shown in Figure 3-22, this actually has the effect of preferentially pulling the electric field towards this medium, which completely invalidates the parallel plate approximation. The resulting capacitance is an order of magnitude larger than estimated by Equation 3-44.

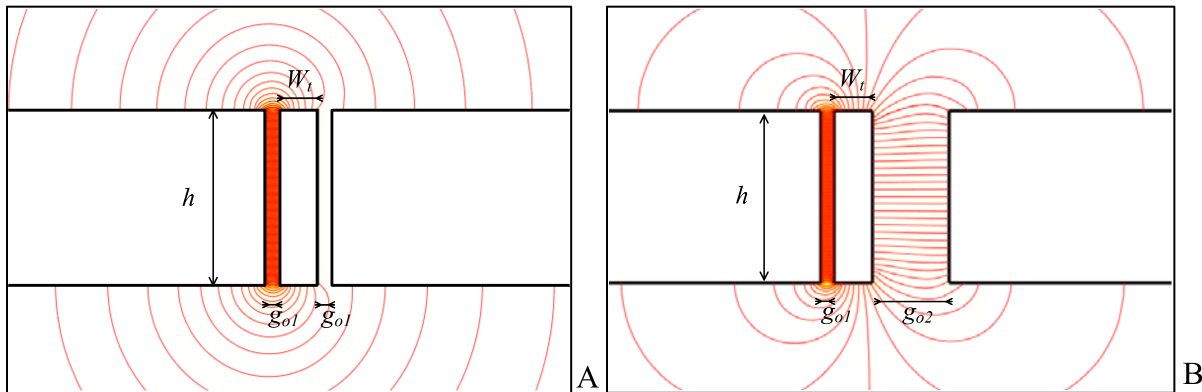

Figure 3-21. Tether cross sections and fringing simulation results. A) Small-small gap tether with one side floating. B) Small-large gap tether with both sides grounded.

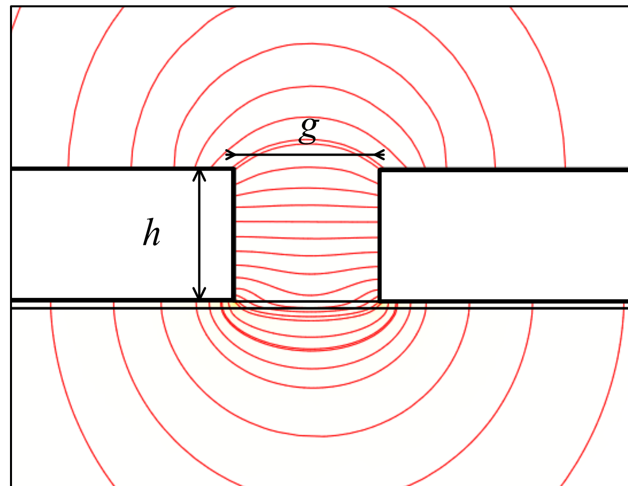

Figure 3-22. Pad gap cross section showing simulated fringing fields and the effect of the substrate beneath the pads.

The third source of parasitic capacitance C_{p3} comes from the electrode-to-bulk capacitance. At dc, this is the largest source of parasitic capacitance, but it has a frequency dependence that minimizes its effect at the RF frequencies of operation for the wireless sensor. The areas that make up the electrodes in this sensor are far larger than most other sensors, as shown in Figure 3-13. This simplified the fabrication, allowing all of the trenches to be etched in one step, forming

المنارة للاستشارات
www.manaraa.com

the sensor structures and the pads at once. This creates a problem, in that the pads are separated from the bulk by a thin oxide layer of thickness t_{ox} with a relative permittivity of 3.9. The large area, small gap, and increased permittivity make for a very large parasitic capacitance. Figure 3-23 shows the electrode pads with a cross section of the sensor to illustrate the circuit connections. The two capacitances C_s each represent the combined trench parasitic and variable sensor capacitance. The center pad to bulk capacitance is

$$C_{b1} = \frac{\varepsilon_{ox} A_{pads}}{t_{ox}}, \tag{3-46}$$

where the area is defined as

$$A_{pads} = 2W_{p1}L_{p1} + 2W_{p2}L_{p2}. \tag{3-47}$$

The larger surrounding pads have a capacitance of

$$C_{b2} = \frac{\varepsilon_{ox} A_{sur}}{t_{ox}}, \tag{3-48}$$

where the area is defined as

$$A_{sur} = \frac{A_{die} - (A_{pads} + A_{element})}{2}. \tag{3-49}$$

The electrical conductivity of the underlying bulk silicon is represented by a conductance G_b and will be determined experimentally in Chapter 5 by fitting measured impedance vs. frequency data using calculated values for C_s, C_{b1} and C_{b2}.

The circuit shown in Figure 3-23 can be simplified at high and low frequencies. At low frequencies (<1 MHz), the high impedances of the capacitors C_{b1} and C_{b2} dominate over the conductance G_b. Replacing the conductances with shorts, the series combination of C_s and C_{b2} is added in parallel with C_{b1}, all of which are combined in series with C_{b2}. Due to the magnitudes of these capacitances, the effective capacitance combination reduces to approximately C_{b1}. As the

المنارة للاستشارات
www.manaraa.com

frequency increases, the impedances of the capacitors are reduced, and at very high frequencies the conductance terms dominate. In this case, all that is left is G_b across the terminals of the sensor capacitance. These results are summed up by the following four equations:

$$C_{p3} \overset{f_{low}}{\approx} C_{b1} \quad , \quad C_{p3} \overset{f_{high}}{\approx} 0 \tag{3-50}$$

and

$$G \overset{f_{low}}{\approx} 0 \quad , \quad G \overset{f_{high}}{\approx} G_b \, . \tag{3-51}$$

The frequency at which this transition occurs is determined experimentally along with the value of G_b. The circuit in Figure 3-23 reduces to one of the two shown in Figure 3-24, depending on the frequency range.

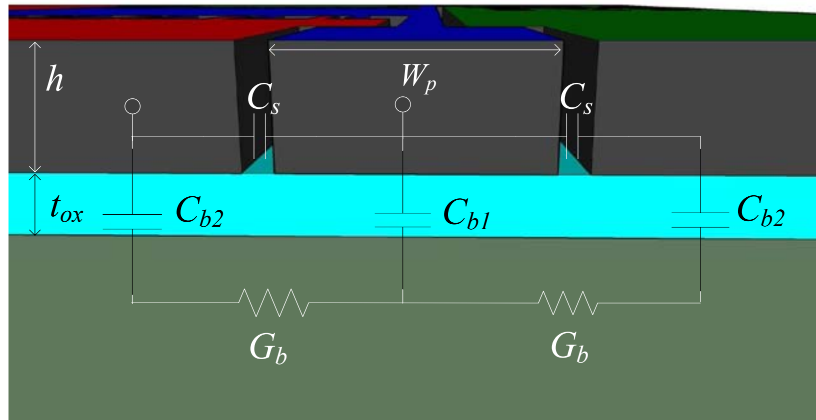

Figure 3-23. A 3D graphic showing the side view of the pads with overlaid circuit model of the bulk parasitic capacitive structures (not to scale).

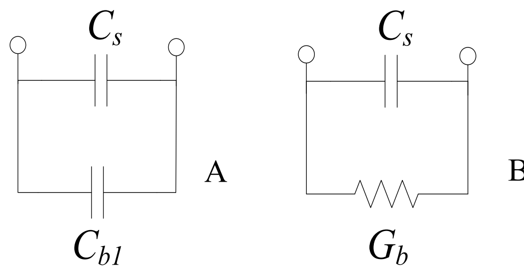

Figure 3-24. Equivalent circuit models for pad-to-bulk parasitics. A) Low frequency equivalent circuit valid when capacitance dominates. B) High frequency equivalent circuit valid when conductance dominates.

The final parasitic values to be used in the final model are the parallel combination of all three parasitic capacitances given by

المنارة للاستشارات
www.manaraa.com

$$C_p = C_{p1} + C_{p2} + C_{p3}. \tag{3-52}$$

The primary source of conduction at high frequency is given by

$$G = G_b. \tag{3-53}$$

Using these parameters along with those from the preceding sections, a full model is described in the next section.

3.3 Full Sensor Model

All of the components discussed thus far are put together in this section to describe the full sensor system. First, the complete electrical equivalent circuit is given. The output resonant frequency of the sensor is determined from this circuit. In operation, the resonance is tracked to determine the input shear stress. This is best illustrated as a waterfall plot in Figure 3-25 where the frequency shift can be seen in time. Next, a general theory of coupled resonators is presented to analyze the effect of coupling on the resonant frequency. The quality factor *Q* will be defined and related to the minimum detectable signal (*MDS*). At the end of the section, assumptions are given to extend this model to an array of sensors.

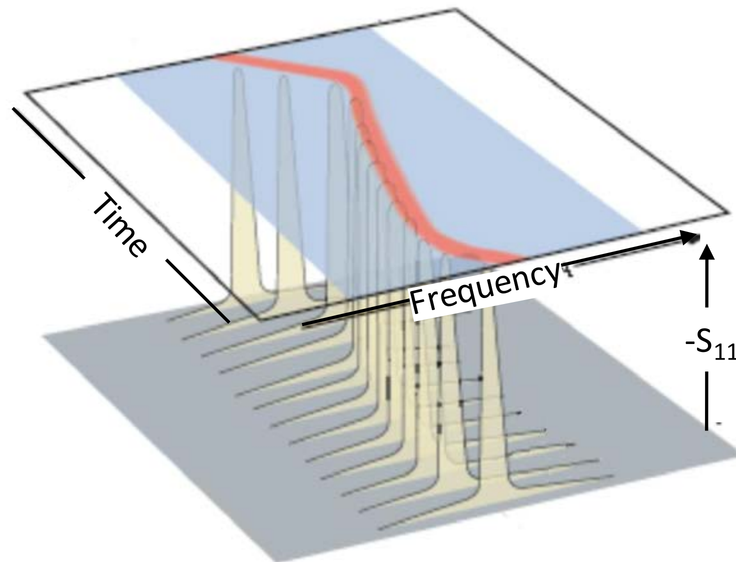

Figure 3-25. A generic waterfall plot showing a resonant frequency shifting in time.

www.manaraa.com

3.3.1 Single Sensor Model

The full circuit model is given in Figure 3-26. This model is made up of quantities determined analytically, numerically, and experimentally. The sensor parasitic conductance, *G,* variable capacitance, C_s and parasitic capacitance, C_p were described in Section 3.2. The self-inductances for the coil, L_c, the antenna, L_a, and the mutual-inductance, *M* from Section 3.1.1 are represented in the T-circuit given in Section 3.1.2. C_c, C_a, R_c and R_a represent the parasitics of the coils given in Section 3.1.1.

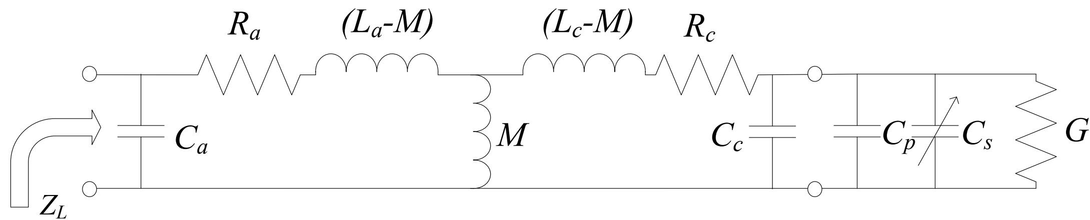

Figure 3-26. Full circuit model for a single wireless shear stress sensor.

To analyze this model and determine the resonant frequency of the sensor, the impedance at the input to the device Z_L is derived by standard circuit analysis (see Appendix B).

$$Z_L = \left(\frac{1}{j\omega C_a}\right) \| \left(R_a + j\omega L_a + \frac{\omega^2 M^2}{R_c + j\omega L_c + \left(j\omega\left(C_c + C_p + C_s\right) + G\right)^{-1}}\right) \tag{3-54}$$

Since a network analyzer is ultimately used to measure the sensor response, this impedance is then transformed into a reflection coefficient

$$|\Gamma| = \left|\frac{Z_L - Z_o}{Z_L + Z_o}\right|, \tag{3-55}$$

using the standard characteristic impedance

$$Z_o = 50\Omega. \tag{3-56}$$

The reflection coefficient, also known as the scattering parameter S_{11}, is the value measured by the network analyzer that will be connected to the output of the antenna. The resonance of the

المنارة للاستشارات
www.manaraa.com

sensor shows up as a dip in the magnitude of the reflection coefficient, as shown in Figure 3-27. The frequency is given by

$$f_o = \frac{1}{2\pi \sqrt{L_c\left(C_s + C_p + C_c\right)}}. \tag{3-57}$$

As the capacitance of the sensor C_s changes with input shear, the resonant dip shifts in frequency.

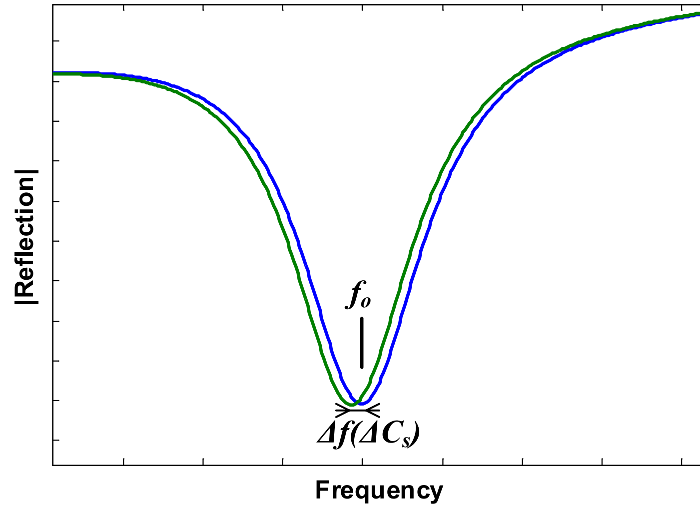

Figure 3-27. Sensor spectrum showing resonant peak and the shift due to a change in capacitance.

The relationship between change in capacitance ΔC_s and change in frequency Δf is inherently nonlinear, but assuming $\Delta C_s \ll \left(C_{os} + C_p + C_c\right)$ the local slope (and hence sensitivity) can be obtained by taking the derivative of Equation 3-57 with respect to C_s. See Appendix A for a detailed derivation. The resulting equation is related to the static resonance and the ratio of the change in capacitance over the total static capacitance,

$$\Delta f(\Delta C_s) \approx -\frac{f_o}{2}\frac{\Delta C_s}{\left(C_{os} + C_p + C_c\right)}. \tag{3-58}$$

The change in capacitance to change in frequency sensitivity in kHz/fF can then be written as

المنارة للاستشارات
www.manaraa.com

$$S_{cf} = \frac{\Delta f}{\Delta C_s} = -\frac{f_o}{2\left(C_{os} + C_p + C_c\right)}, \quad (3\text{-}59)$$

and the total shear stress to change in frequency sensitivity in kHz/Pa can then be written as

$$S_{\tau f} = -\frac{\frac{f_o A_e \varepsilon_o}{16E}\left(\frac{L_t}{W_t}\right)^3\left(1+\frac{2A_t}{A_e}\right)\left(\frac{N_f x_o + 2L_e + 3L_t}{g_{o1}^2} - \frac{\left(N_f - 2\right)x_o + L_t}{g_{o2}^2}\right)}{\frac{\varepsilon_o h}{2}\left(\frac{N_f x_o + 2L_e + 3L_t}{g_{o1}} + \frac{\left(N_f - 2\right)x_o + L_t}{g_{o2}}\right) + C_p + C_c}, \quad (3\text{-}60)$$

where $S_{\tau f} = S_{\tau w} S_{wc} S_{cf}$. A more important metric for wireless sensors, whose static resonances tend to span a wide range of frequencies, is the normalized sensitivity expressed in ppm/Pa as

$$S_n = \frac{S_{\tau f}}{f_o} = -\frac{\frac{A_e \varepsilon_o}{16E}\left(\frac{L_t}{W_t}\right)^3\left(1+\frac{2A_t}{A_e}\right)\left(\frac{N_f x_o + 2L_e + 3L_t}{g_{o1}^2} - \frac{\left(N_f - 2\right)x_o + L_t}{g_{o2}^2}\right)}{\frac{\varepsilon_o h}{2}\left(\frac{N_f x_o + 2L_e + 3L_t}{g_{o1}} + \frac{\left(N_f - 2\right)x_o + L_t}{g_{o2}}\right) + C_p + C_c}. \quad (3\text{-}61)$$

The normalized force sensitivity is given by

$$S_F = \frac{S_n}{A_e} = -\frac{\frac{\varepsilon_o}{16E}\left(\frac{L_t}{W_t}\right)^3\left(1+\frac{2A_t}{A_e}\right)\left(\frac{N_f x_o + 2L_e + 3L_t}{g_{o1}^2} - \frac{\left(N_f - 2\right)x_o + L_t}{g_{o2}^2}\right)}{\frac{\varepsilon_o h}{2}\left(\frac{N_f x_o + 2L_e + 3L_t}{g_{o1}} + \frac{\left(N_f - 2\right)x_o + L_t}{g_{o2}}\right) + C_p + C_c}. \quad (3\text{-}62)$$

The independent geometric variables in this equation are W_e, L_e, W_t, L_t, h, W_f, L_f, g_{o1} and g_{o2}. By changing each variable independently the sensitivity of Equation 3-62 to fabrication uncertainties is shown in Figure 3-28. It is clear that the most important quantities are W_t, L_t, g_{o1} and g_{o2}.

3.3.2 Coupled Resonators

The full model presented is a pair of mutually coupled resonators. Theory for these types of systems is used in electroacoustics [73]. The most relevant aspect for this work is the effect that coupled resonators have on each other's resonant frequencies. This poses a potential

المنارة للاستشارات
www.manaraa.com

problem, since the resonance of the sensor is sensitive to a change in the coupling or the resonance of the antenna. This is interpreted as a change in shear stress, giving a false output. This effect is minimized through careful design of the system.

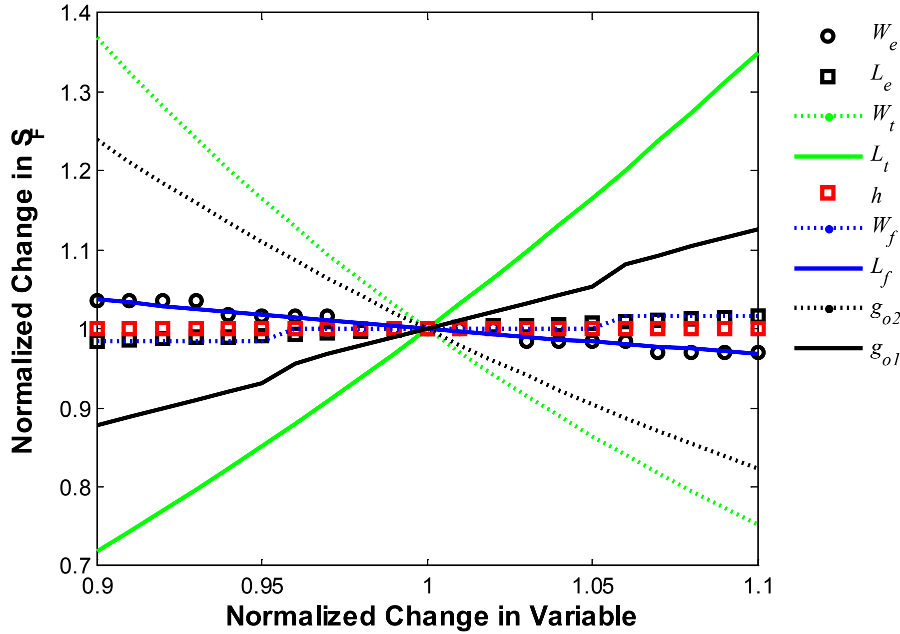

Figure 3-28. Normalized sensitivity of the sensor response to 10 % variations in fabricated geometries.

Two situations are described for a general pair of coupled resonators shown in Figure 3-29. First, the capacitances and inductances are set equal ($L_1 = L_2 = L$ and $C_1 = C_2 = C$) so that both have the same resonant frequency

$$f_{o1,o2} = \frac{f_o}{\sqrt{1 \pm k}}, \tag{3-63}$$

where
$$f_o = \frac{1}{2\pi\sqrt{LC}} \tag{3-64}$$

would be the resonance of both sides in the absence of one another, and

$$k = \frac{M}{\sqrt{L_1 L_2}} \tag{3-65}$$

المنارة للاستشارات
www.manaraa.com

is the coupling coefficient. For zero coupling, both resonators resonate at a frequency described by the standard second order equation and given by Equation 3-64. As soon as they couple, they interact with each other, resulting in a splitting of the resonance as shown in Figure 3-30. Two peaks appear at frequencies defined by Equation 3-63. A sensitivity analysis shown in Figure 3-31A,B is performed at around 100 MHz by varying the five parameters and quantifying the resonance shift that results. These plots show that the resonant frequency is highly sensitive to changes in all capacitive and inductive parameters. It also shows that the variation is highly nonlinear which invalidates the models developed in Section 3.3.1.Another problem is that an antenna is most sensitive to noise from EMI at its self-resonant frequency. This noise affects the sensor output if it is resonating at the same frequency as the antenna.

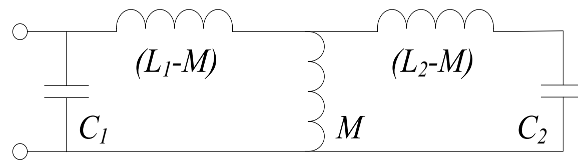

Figure 3-29. Basic T circuit for magnetically coupled resonators.

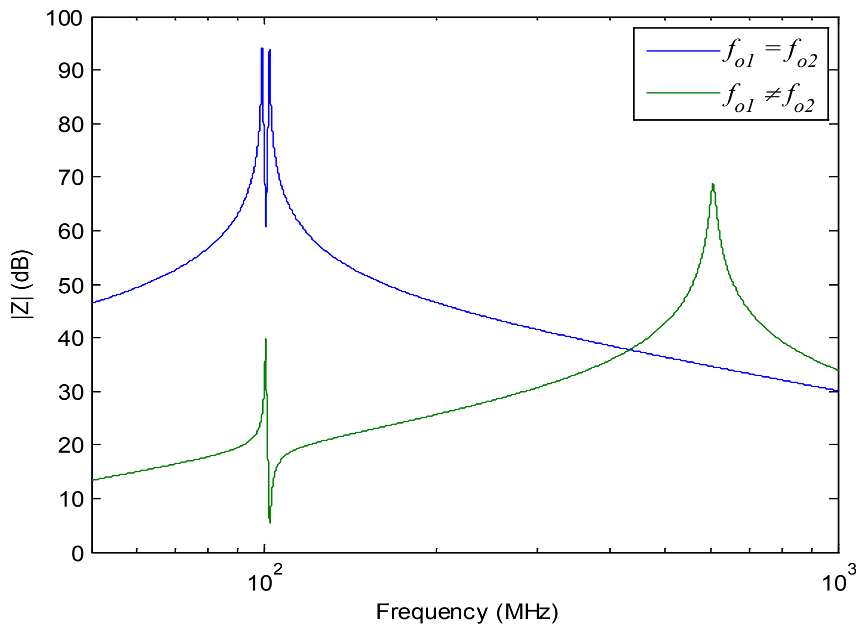

Figure 3-30. Coupled resonator plot showing overlapping and separated resonances.

المنارة للاستشارات
www.manaraa.com

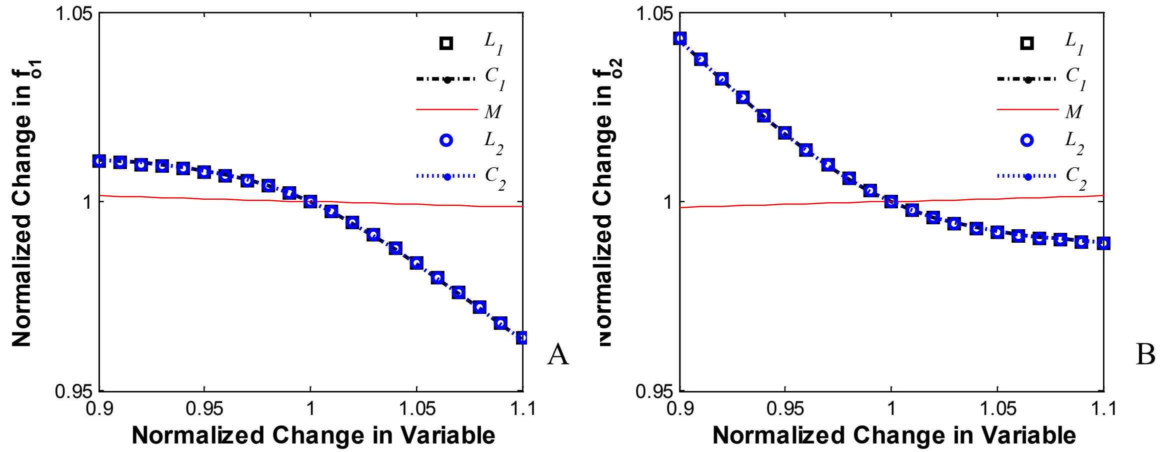

Figure 3-31. Resonant frequency sensitivities to electrical parameters. A) Sensitivity for f_{o1} with $f_{o1} = f_{o2}$. B) Sensitivity for f_{o2} with $f_{o1} = f_{o2}$.

To reduce the sensors sensitivity to the coupling k, antenna parasitics, and EMI, separated resonances are used. When $L_1 \neq L_2$ and $C_1 \neq C_2$,

$$f_{o1,o2} = \frac{1}{2\pi\sqrt{\dfrac{2C_1C_2L_1L_2\left(1-k^2\right)}{C_1L_1 + C_2L_2 \pm \sqrt{C_1^2L_1^2 + C_2^2L_2^2 - C_1C_2L_1L_2\left(2-4k^2\right)}}}} \tag{3-66}$$

gives the two separated resonant frequencies derived in Appendix C. By choosing the first resonance as the sensor resonance, the effect of changes in M is reduced. To confirm this assumption, a sensitivity analysis shown in Figure 3-32A,B is also performed for the two resonances in the hundreds of MHz range and separated by 0 and 500 MHz. The most advantageous resonance for the sensor is the first resonance where changes in M are minimized. Using a fixed inductance L_2 the sensitivity analysis in Figure 3-32A shows the ideal situation with the resonant frequency being sensitive to only changes in the variable capacitive shear stress sensor.

المنارة للاستشارات
www.manaraa.com

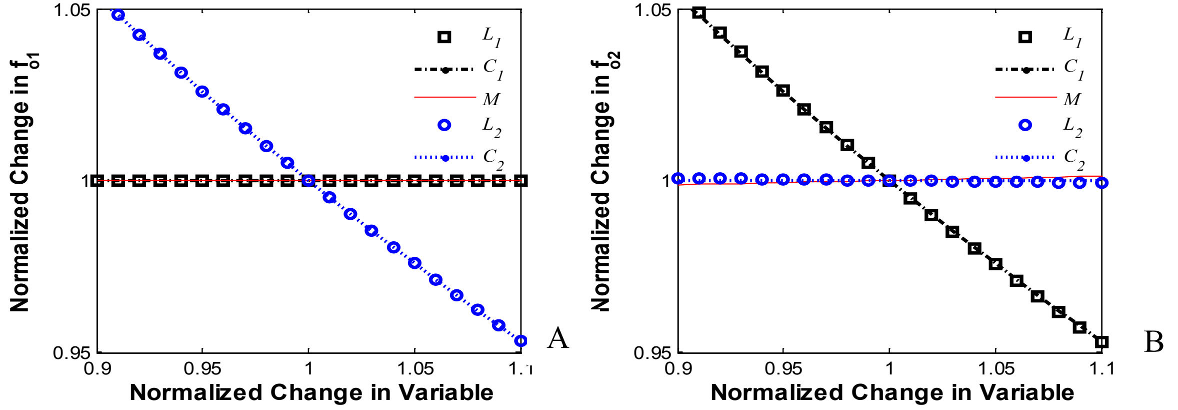

Figure 3-32. Resonant frequency sensitivities to electrical parameters. A) Sensitivity for f_{o1} with $f_{o1} \neq f_{o2}$. B) Sensitivity for f_{o2} with $f_{o1} \neq f_{o2}$.

3.3.3 Quality Factor at Resonance

The quality factor of a resonator is a unitless quantity that relates the maximum energy stored to the total energy lost in one cycle of resonance. The effect of Q on the output of the sensor is shown in Figure 3-33 where the higher the Q, the narrower the resonant dip. The sensor resonance has energy storage elements L_c, C_c, C_p and C_s and energy dissipative terms R_c, and G. As derived in Appendix D, at resonance, the quality factor of the sensor is given by

$$Q = \frac{1}{R_c + \dfrac{G}{G^2 + \left(C_c + C_p + C_s\right)/L_c}} \sqrt{\frac{1}{G^2 + \left(C_c + C_p + C_s\right)/L_c}} . \tag{3-67}$$

It is desirable to maximize the quality factor to achieve the sharpest dip. The sharper the dip, the lower the noise floor and the smaller the *MDS* will be. Additionally for arrays, the sharper the dip, the less bandwidth it will occupy, enabling more sensors to fit in the bandwidth below the antenna resonance. The noise floor of the sensor is given by

$$n_f = \frac{f_o n_a}{2Q} \text{ [74]}, \tag{3-68}$$

المنارة للاستشارات
www.manaraa.com

as shown in Figure 3-33. The *MDS* in Pa is obtained using the standard definition

$$MDS = \frac{n_f}{S_{\tau f}} = \frac{n_a\left[\left(\frac{N_f x_o + 2L_e + 3L_t}{g_{o1}} + \frac{(N_f - 2)x_o + L_t}{g_{o2}}\right) + C_p + C_c\right]}{Q\frac{A_e}{4Eh}\left(\frac{L_t}{W_t}\right)^3\left(1 + \frac{2A_t}{A_e}\right)\left(\frac{N_f x_o + 2L_e + 3L_t}{g_{o1}{}^2} - \frac{(N_f - 2)x_o + L_t}{g_{o2}{}^2}\right)}. \qquad (3\text{-}69)$$

From Equation 3-67, we see that to increase the quality factor and minimize the *MDS*, the parasitics C_c, C_p, R_c, and G must be minimized and the self-inductance L_c must be maximized. There is a trade off in the sensor capacitance between quality factor and sensitivity that will affect the *MDS*. This will be balanced in the final design by maximizing the ratio $\Delta C_s/C_{os}$.

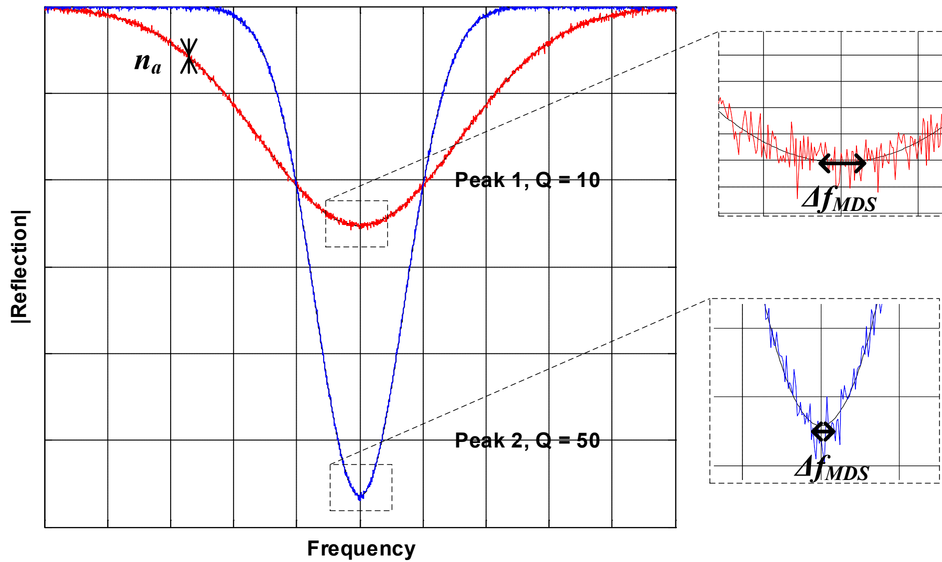

Figure 3-33. Plot showing MDS dependence on Q. For the same amplitude noise in both spectrums, a higher Q results in a smaller MDS.

3.3.4 Multiple Sensor Array Model

To apply the single sensor model to an array of sensors, superposition must be valid. It is desired that the frequency shift of each sensor's resonance be related to an input shear stress on that sensor. For this to be true, the sensors must not have strong coupling between their individual coils. If this is the case then the resonant frequency, quality factor, sensitivity and

المنارة للاستشارات
www.manaraa.com

noise floor will all be given for each of the individual sensors by the equations developed for the single wireless sensors.

The total impedance and reflection spectra will be different and requires more development that is presented in Appendix B for a generic number of sensors in the array. The parasitics are removed from this discussion for simplicity but they can easily be added the same way they were added to the single sensor equations. For the case of four wireless sensors, each with mutual-inductances to each other and to the antenna. If the sensor to sensor coupling is negligible then

$$M_{12} = M_{13} = M_{14} = M_{23} = M_{24} = M_{34} \approx 0 \tag{3-70}$$

The circuit diagram in Figure 3-34 shows the case where only coupling between the sensors and the antennas are present. The full coupling model is also derived in Appendix B. For this circuit the four sensors will be defined by

$$Z_i = R_i + j\left(\omega L_i - \frac{1}{\omega C_i}\right). \tag{3-71}$$

The total input impedance is given by

$$Z_L = R_a + j\omega L_a + \frac{\omega^2 {M_{a1}}^2}{Z_1} + \frac{\omega^2 {M_{a2}}^2}{Z_2} + \frac{\omega^2 {M_{a3}}^2}{Z_3} + \frac{\omega^2 {M_{a4}}^2}{Z_4} \tag{3-72}$$

The spacing between the sensors and their orientation should minimize the inter-sensor coupling enough to satisfy this requirement. The simulated spectrum in Figure 3-35 shows a single peak for each sensor located at

$$f_{oi} = \frac{1}{2\pi\sqrt{L_i C_i}}. \tag{3-73}$$

The bandwidths shown in the figure are limited by the Q of the sensors and given by

www.manaraa.com

$$BW_i = \frac{f_{oi}}{Q_i} \tag{3-74}$$

The spacing between the resonances must satisfy the Rayleigh Criterion in order to be distinguishable as separate peaks. This minimum spacing is given by

$$\Delta f_{\min} = \frac{BW_i}{2} \tag{3-75}$$

Provided the design of the sensors meets these criteria the array can be interrogated with each spatial location in the array corresponding to the frequency shifts in the assigned bandwidth.

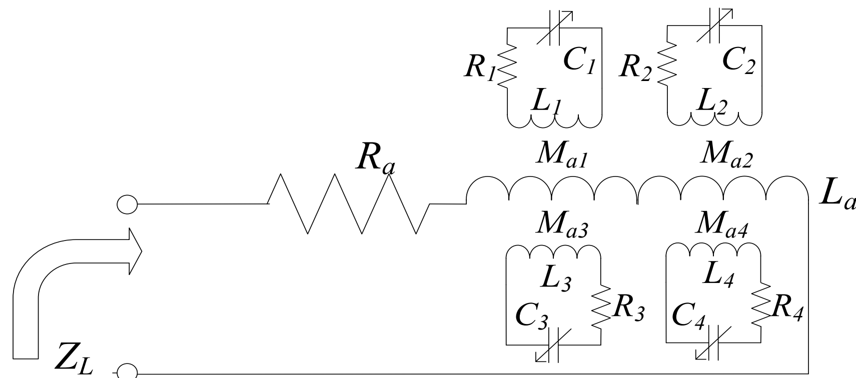

Figure 3-34. Circuit model for a 2 x 2 sensor array.

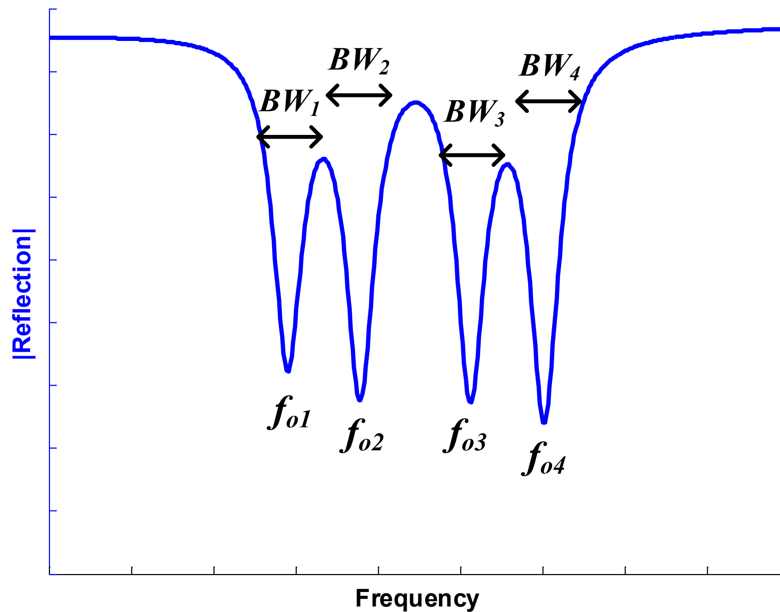

Figure 3-35. Array spectrum sowing individual bandwidths for four sensors.

المنارة للاستشارات
www.manaraa.com

CHAPTER 4
EXPERIMENTAL SETUPS

The experimental setups and methods used to characterize the wireless shear stress sensors are described in this chapter. Before packaging, the individual capacitive shear stress sensors are visually inspected to sort out clearly damaged die. Impedance measurements are then made using die-level electrical probing to extract relevant electrical model parameters. Electrostatic actuation of the comb fingers ensures that there are no mechanical obstructions to the free-floating structures on the sensors. After packaging dies to form the wireless sensor packages, the inherent noise floor and stability are determined with zero input. Humidity testing is also conducted to explore the sensor's sensitivity to humidity. Next, the static (dc) shear stress sensitivity is determined by performing device calibration in a flow cell. The final test setup described in this chapter is a wind tunnel at NASA Langley in Virginia. Subsequent chapters will present the actual data and results from these tests on first-generation and second-generation devices.

4.1 Die Level Testing

Before packaging the capacitive shear stress sensors, die-level characterization is performed to identify the best candidates as well as to extract parameters and confirm model predictions from Section 3.2. The finished wafers are diced into 5 mm x 5 mm die and sorted by sensor design. Visual inspections of each die are performed under an optical microscope (100x - 1000x magnification) to check for defects. Die that pass the visual inspection undergo impedance testing and actuation testing before being packaged and tested wirelessly.

4.1.1 Electrical Impedance Testing

After the die are individually inspected, a full electrical characterization is performed on the good die. The setup for these tests is shown in Figure 4-1. Two impedance analyzers are used to cover the broad frequency range necessary for fully evaluating the model parameters. First, the

المنارة للاستشارات
www.manaraa.com

HP4294A is used to test the devices at low frequencies from 100 Hz to 100 MHz. Next, the E4991A is used to cover the high frequency testing from 1 MHz to 1 GHz. A Cascade M150 measurement platform is used to perform the required die-level tests. The probe tips are observed under a microscope, while the manipulators are used to land them on the contact pads of the sensors. A rising stage and movable chuck are used to maintain probe orientation from test to test.

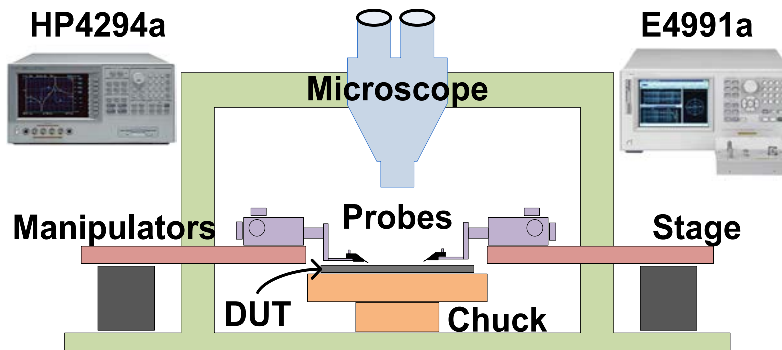

Figure 4-1. Probe station setup for impedance characterizations.

For the HP4294A, a set of Cascade Microtech DCP 150R coaxial shielded probes are used with four 3' SMAA to BNC cables that connect directly to the instrument. First, a four-point probe (4TP 1M) cable phase correction is performed to remove the effect of the cable length on the measurement. Next, a GGB Industries impedance standard substrate (ISS) model 40A-GS-150-C is used to perform open, short, and load compensation tests. All of the testing parameters for the E4991A are given in Table 4-1.

Table 4-1. Agilent E4991A material property analyzer settings.

Parameter	Setting
Number of points	801
Oscillation level	100 mV
Start	1 MHz
Stop	1 GHz
Scale	log
Calibration	Open, Short, Load

المنارة للاستشارات
www.manaraa.com

For the E4991A, a single GGB Industries 40A-GS-150-C RF probe is used, which again is calibrated using the ISS. The RF probe is connected to an Agilent E4991A Opt 010 test box, mounted to a single specialized Cascade Microtech probe manipulator with a short semi-rigid SMA cable. This reduces test variation and improves repeatability. All of the testing parameters for the HP 4294A are given in Table 4-2.

Table 4-2. HP 4294A impedance analyzer settings.

Parameter	Setting
Number of points	801
Oscillation level	500 mV
Bandwidth	5
Start	100 Hz
Stop	100 MHz
Scale	log
Compensation	4TP 1M
Calibration	Open,Short,Load

4.1.2 Electrostatic Actuation Testing

To ensure that the sensors are ready for packaging, an electrostatic test is also performed on each sensor. For a sensor to work properly, it must be free and clear of any materials that could restrict the free motion of the floating-element structures. These obstructions can be difficult to detect visually even with the aid of a high power microscope, and if an obstruction is non-conductive, it may not show up in the electrical impedance tests described in Section 4.1.1. However, an electrostatic force applied to the sensors will result in an observable, predictable, and repeatable displacement if the sensor is fully released and free of obstructions.

The setup used for this test is shown in Figure 4-2. A square wave voltage signal is applied to the sensor die via needle probes. At the same time, a camera mounted to a 500x microscope is

www.manaraa.com

used to collect video of the sensor as it is actuated. Video processing is then used to measure the resulting displacement.

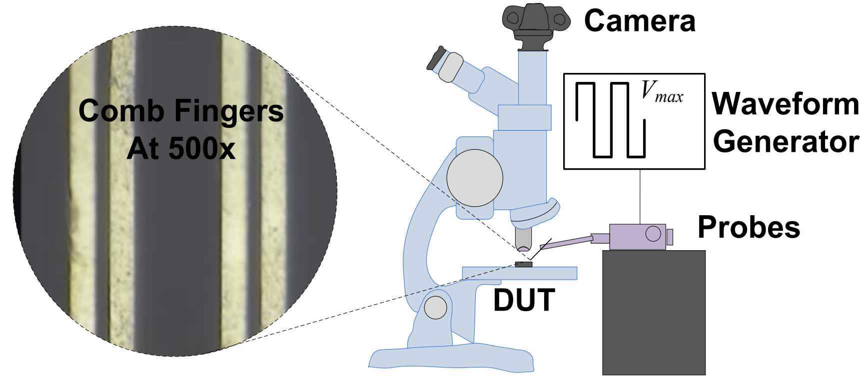

Figure 4-2. Electrostatic actuation test setup.

The voltages used to actuate the sensors must be determined based on the geometry of the comb fingers and tethers. The voltage level used to actuate the comb fingers needs to be large enough so that the displacement is visible under a 500x microscope. However, if the displacement becomes too large, the attractive gap-closing electrostatic force may overcome the restoring spring forces, and the fingers will clamp shut. This phenomenon is referred to as "pull-in" and ultimately results in the destruction of the sensor, because the fingers become welded together from the current spike when the sensor shorts out. To prevent this pull-in, the forcing voltage is limited to 80% of the calculated pull-in voltage. The pull-in voltage is a function of the finger geometry and the spring constant, in this case, the tethers. From previous work on H-Bar structures[21,22,75,76], the spring constant of the tethers is given by

$$k = \frac{4Eh\left(\frac{W_t}{L_t}\right)^3}{\left(1+2\frac{A_t}{A_e}\right)^2}\left(1+4\frac{A_t}{A_e}+\frac{64}{15}\left(\frac{A_t}{A_e}\right)^2\right), \tag{4-1}$$

where the geometric and material properties are defined in Section 3.2.1 and illustrated in Figure 3-11. The pull-in voltage, derived in Appendix E, is given by

المنارة للاستشارات
www.manaraa.com

$$V_{pi} = \sqrt{\frac{k}{\varepsilon_o x_o h\left(\frac{N_f}{\left(g_{o1}-x_{pi}\right)^3} - \frac{N_f - 1}{\left(g_{o2}+x_{pi}\right)^3}\right)}}, \tag{4-2}$$

where the geometric and material properties are defined in Section 3.2.2 and illustrated in Figure 3-14. The pull-in displacement x_{pi} is determined from the nonlinear equation

$$\frac{(g_{o1}-3x_{pi})}{\left(g_{o1}-x_{pi}\right)^3} = \frac{(N-1)}{N}\frac{(g_{o2}-x_{pi})}{\left(g_{o2}+x_{pi}\right)^3}, \tag{4-3}$$

and must be solved numerically (see Appendix E). MATLAB is used to solve for x_{pi} and V_{pi} for each design. This is then used to set $V_{max} = 0.8V_{pi}$ on the waveform generator.

4.2 Wireless Sensor Testing

Once a good capacitive sensor die is identified, it is flush-mounted in a printed circuit board (PCB) and wire-bonded to the on-board coil. On the backside of the PCB, an RF connector is soldered to the loop antenna to complete the wireless shear stress sensors. Next, a set of tests is performed to characterize the wireless devices. For all of the tests described in this section, a LabVIEW control program is used to automate and allow continuous monitoring of the test progress.

4.2.1 Network Analyzer Resonance Tracking

A network analyzer is used to track the resonant frequency of the wireless shear stress sensor in all of the experimental tests. An HP8719D [77] with an operational frequency range from 50 MHz to 13.5 GHz is used. A network analyzer measures the scattering parameters of a DUT (device under test). For a single port device, such as the wireless shear stress sensor, all that is required to electrically characterize the DUT is the scattering parameter S_{11}. This is also

المنارة للاستشارات
www.manaraa.com

referred to as the "reflection coefficient" or Γ. It is a complex non-dimensional parameter relating the reflected to the incident voltage by

$$S_{11} = \frac{A}{R}, \tag{4-4}$$

in which A is the incident voltage and R is the reflected voltage. As shown in Figure 4-3, the source voltage V_{oc} is split, and half is sent to the DUT while the other half is measured at A. The reflected voltage is separated by a directional coupler and measured at R. A single frequency tone is used as the input voltage V_{oc}. To obtain a spectrum, the frequency is swept through a user-defined set of frequencies, and S_{11} is measured at each tone. If the frequency range includes the resonance of the wireless sensor, there will be a dip in the magnitude of the reflection coefficient as shown in Figure 3-27. The resonance shifts of the sensor are determined by tracking this dip.

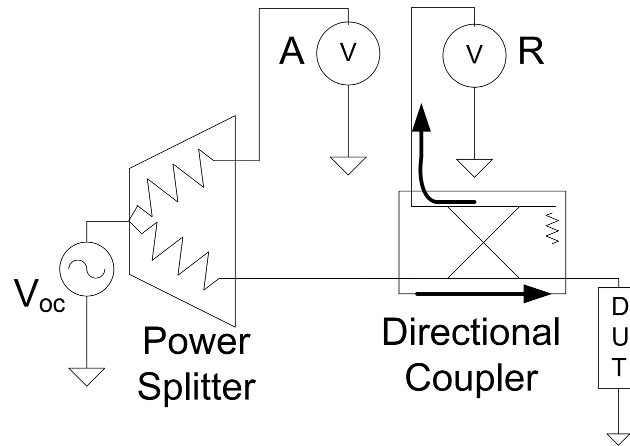

Figure 4-3. Network analyzer operation. The DUT includes the antenna and the wireless sensor.

For all tests, a full one-port calibration is preformed using the Agilent 85050B 7 mm calibration kit. This includes measuring open, short, and 50 Ω load terminations. A 7 mm-SMB adapter is used to connect the antenna to the network analyzer after the calibration is complete. Frequency sweeps consisting of 1601 points are taken with an IF-BW of 300 Hz and a source level of 125 mV. The frequency sweep center and range depend on the sensor being tested. The

www.manaraa.com

center point is always set to the resonant frequency of the sensor, but the span depends on the purpose of the sweep. A wide bandwidth search span of 1 GHz is used to identify the resonant frequency of the sensor. The frequency resolution at 1601 points is inadequate for resonance tracking, so a narrow bandwidth test span from 1.6 to 16 MHz, depending on the Q of the sensor, is used. The setup parameters for the network analyzer are given in Table 4-3.

Table 4-3. Agilent 8719D network analyzer settings.

Parameter	Setting
Number of points	1601
Oscillation level	125 mV
IF-BW	300 Hz
Sweep Time	6 seconds
Center	f_o
Search Span	1 GHz
Test Span	1.6 - 16 MHz
Scale	linear
Compensation	Open, Short, Load

4.2.2 Noise Floor and Frequency Stability Testing

The noise floor of the sensor determines the minimum detectable input shear, which is then used to determine the dynamic range of the sensor. For the wireless sensor, the noise floor is related to the quality factor, Q, the resonant frequency, f_o and the amplitude noise, n_a in the frequency sweep of the network analyzer by Equation 3-68. The Q and the resonant frequency can be determined by taking a wideband sweep to capture the entire resonant dip, and the amplitude noise is determined at the narrow bandwidth that the resonant frequency will be tracked. The inherent noise floor of the device includes only sources within the sensor and measurement system, so to remove outside source like electromagnetic interference (EMI), these tests are performed in a grounded faraday cage (Figure 4-4).

www.manaraa.com

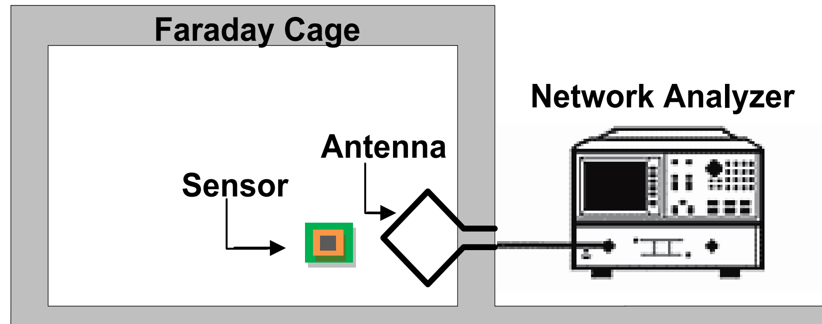

Figure 4-4. Diagram of a single sensor placed in a faraday cage to reduce external noise. This setup will be used to determine the noise floor and stability of the device.

In addition to the noise floor testing, the faraday cage is used for long-term stability tests to measure the drift of the resonant frequency. Frequency drift is a phenomenon that has been shown to affect previous wireless sensors [31,41,58,60,78] and must be explored to eliminate false readings of input shear. The sensor is tested in the faraday cage with zero input shear. Ideally, the resonant frequency should remain constant in time. Frequency sweeps are taken every six seconds with the same settings as the noise floor tests. This process is repeated for three hours to get an estimate of the long-term drift.

4.2.3 Humidity Sensitivity Testing

During the course of this research, while performing static calibrations in the flow cell, a change in sensor sensitivity was observed at the start of the test. If the same test was repeated immediately, this phenomenon disappeared. After a detailed analysis of the problem, humidity was identified as the root cause of the sensitivity variation. The compressed air used to drive the flow in the flow cell was drier than the air in the room due to treatment at the compressor and inline desiccants. Once this phenomenon was identified, it was easily avoided by setting a constant low flow condition until the humidity stabilized, after which the static sensor calibrations were performed to determine the sensitivity to shear stress. This testing procedure did nothing to quantify or improve the root problem though.

المنارة للاستشارات
www.manaraa.com

The sensitivity to humidity is an undesirable effect of the capacitive structures responding to a change in permittivity [79-85] rather than the change in the comb finger gaps due to input shear stress, as described in Section 3.2.2. This happens when water molecules adhere to the sidewalls of the fingers and can be estimated by

$$C_{eff} = \frac{\left(\varepsilon + \Delta\varepsilon_{H_2O}\right)A}{g}. \tag{4-5}$$

To characterize this phenomenon and investigate future improvements to reduce this undesirable sensitivity, a dedicated test setup is required. A simple humidity test chamber is devised wherein the sensor performance is measured with varying relative humidity (zero shear stress). The construction included a sealed chamber with a Lascar USB temp/humidity data logger (EL-USB-2) and a desiccant, as shown in Figure 4-5. The data logger is synchronized with the time stamp of the computer controlling the network analyzer for post-test comparison of the frequency shifts to the humidity changes.

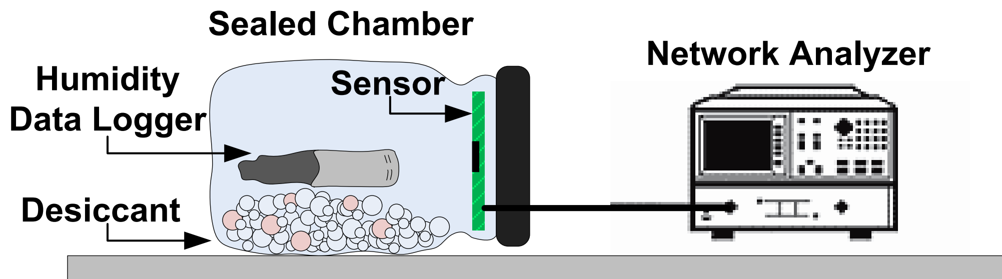

Figure 4-5. Humidity sensitivity test setup.

For testing, the sample rate of the data logger and the sensor are set to 0.1 Hz, which is the highest available rate for the data logger used. At the beginning of the test, the shear stress sensor and humidity sensor are subjected to room humidity (50 %RH). This establishes a stable baseline. Next, both sensors are sealed in the chamber with fresh desiccant causing the humidity to drop from 50% RH to 5 % RH. Once the humidity stabilizes, the chamber is opened and the humidity settles back to room humidity. Variations in humidity are very slow, with time

المنارة للاستشارات
www.manaraa.com

constants on the order of approximately 20 minutes in comparison to electrical and mechanical time constants for this device, which are on the order of milliseconds or less. This experiment enables reasonable characterization of the humidity sensitivity. Improvements to the sensors through hydrophobic treatments are evaluated with this test setup.

4.2.4 Static Calibration Testing

The static (dc) shear stress sensitivity is characterized using a calibration flow cell, as shown in Figure 4-6. The flow cell operates on the assumption of Poiseuille flow between stationary infinite parallel plates. The flow cell duct is 330 mm x 100 mm x 1 mm, so the duct height is two orders of magnitude smaller than the length or width, validating the infinite parallel plate assumption. Two taps measure the pressure drop along the flow direction in the flow cell. The sensor is placed 240 mm from the flow entrance, ensuring that the flow is fully developed by the time it reaches the sensor. A dielectric plug is located in the back plate directly opposite to the sensor that constrains the size of the antenna and coil windings.

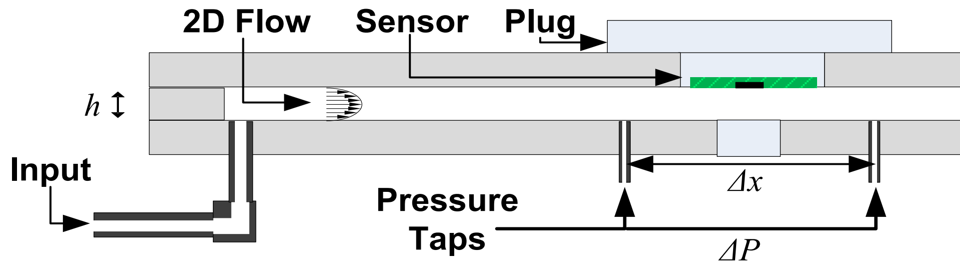

Figure 4-6. Static calibration flow cell.

The 2D fully developed Poiseuille flow [1] is given by

$$u(y) = 2\mu \frac{\Delta P}{\Delta x}\left(hy - y^2\right), \tag{4-6}$$

where h is the height of the chamber, μ is the viscosity of the fluid, ΔP is the differential pressure between the taps, and Δx is the distance between the taps. To find the shear stress at the wall, the velocity gradient at $y = 0$ is determined by

المنارة للاستشارات
www.manaraa.com

$$\left.\frac{du}{dy}\right|_{y=0} = \frac{h}{2\mu}\frac{\Delta P}{\Delta x}. \tag{4-7}$$

Using the relationship between the velocity profile and shear stress at the wall,

$$\tau = \mu \left.\frac{du}{dy}\right|_{y=0}, \tag{4-8}$$

the shear can be calculated, resulting in

$$\tau = \frac{h}{2}\frac{\Delta P}{\Delta x}. \tag{4-9}$$

The pressure difference ΔP is measured across the sensor at two pressure taps, 76.2 mm apart, on the opposite wall of the flow cell. The height of the channel *h* is set by a shim (1 mm for the first-generation or 0.5 mm for the second generation) placed between the top and bottom plates. A smaller channel height results in higher flow rates and higher maximum shear stress levels. A Heise pressure meter with a 50 in H_2O (12.5 kPa) pressure module is used to get the best measurement resolution without over ranging at the maximum flow rate.

For calibration, the flow is stepped from 0 to 2 Pa for the first-generation devices and 0 to 4 Pa (ΔP_{max} = 12.2 kPa) for the second-generation devices. The flow rate is increase in regular intervals, using an AALABORG mass flow controller operated by a Keithley voltage source, until the maximum shear stress is reached. After increasing the flow rate and prior to triggering the sensor measurement, the flow is allowed to stabilize for 60 seconds. This ensures that any transients will have died out and that the flow will be fully developed for the measurement. Twenty pressure measurements are taken with the Heise and averaged to determine the input shear stress given in Equation 4-9. After the 60-second dwell time, the HP 8719D network analyzer is triggered. The resonant frequency is then extracted, and a plot of resonant frequency versus shear stress is generated.

المنارة للاستشارات
www.manaraa.com

Ideally, the plot should show a linear change, where the slope is the sensitivity of the device. This sensitivity $S_{\tau f}$ is divided by the resonant frequency to get a normalized sensitivity S_n, which is a better metric with which to evaluate the sensor. Using this sensitivity and the noise floor found using the test setup in Section 4.2.1, the *MDS* of the sensors can be determined by Equation 3-69. The dynamic range (*DNR*) of the devices is then calculated using this *MDS* as

$$DNR = 20\log\left(\frac{\tau_{Max}}{MDS}\right), \tag{4-10}$$

where τ_{max} is the maximum input shear before the nonlinearity of the sensitivity $S_{\tau f}$ reaches 3%.

4.2.5 Wind Tunnel Testing

In addition to the bench-top testing described above, one of the first-generation wireless sensor designs is tested in "real world" flow conditions in a functional wind tunnel. The sensor was brought to NASA Langley in the summer of 2010 to be tested in the 20" x 28" Shear Flow Control Tunnel. This wind tunnel is a fan-driven open-loop tunnel with a 15-foot-long, 20" x 28" test section. Figure 4-7 shows the tunnel with the intake on the right and the exhaust on the left.

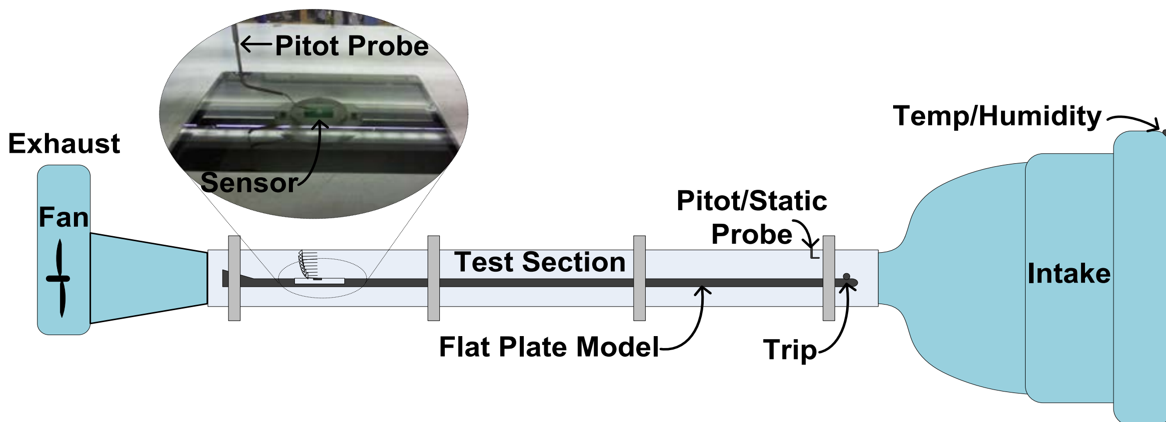

Figure 4-7. NASA 20" x 28" wind tunnel setup showing the location of the sensor in the model.

To simplify the number of variables in the test, a flat plate model with a well-known behavior is used, and the flow conditions are set to achieve a fully developed turbulent boundary layer. The sensor is located in the third chamber of the test section, approximately 10 feet from

المنارة للاستشارات
www.manaraa.com

the leading edge of a flat plate model. The flat plate model extends the entire length of the test section and from wall to wall, as shown in Figure 4-7. A 2D trip wire is located close to the leading edge to initiate mixing and ensure the boundary layer is fully developed by the time it reaches the sensor location. The length scale x of the model is defined as the separation between the trip and the sensor. The ceiling of the test section is made up of adjustable plates and monitored with an array of pressure taps to control the pressure gradient in the stream-wise direction. This is used to set a zero pressure gradient along the model, ensuring that the flow remains attached and predictable all the way to the trailing edge of the model.

Using equations for turbulent flow over a flat plate [86-89], experimental parameters are chosen to closely match calibrations performed in the flow cell. Table 4-4 shows the settings and expected flow conditions for each test. Standard values are chosen for the viscosity, $\mu = 17.98 \times 10^{-6}$ Pa s and density, $\rho = 1.218$ kg/m^3 of air [90]. The sensor is located at $x = 3.47$ m from the trip, which is used as the length scale for the Reynolds number calculation given by

$$Re_x = \frac{U_\infty x \rho}{\mu}, \tag{4-11}$$

in which U_∞ is the freestream velocity. For $5 \cdot 10^5 \leq Re_x \leq 10^7$ the nondimensional friction coefficient [1] is given by

$$C_{f,x} = 0.059\, Re_x^{-\frac{1}{5}}. \tag{4-12}$$

The y locations for the Pitot profiles are predetermined by the total thickness of the boundary layer, such that the range extends into the freestream and has sufficient resolution to capture the important regions. The boundary layer thickness δ is given by [1]

$$\delta = 0.38\, x\, Re_x^{-\frac{1}{5}}. \tag{4-13}$$

المنارة للاستشارات
www.manaraa.com

The shear stress values are determined by

$$\tau_w = \frac{1}{2} C_{f,x} \rho U_\infty^2 . \tag{4-14}$$

Table 4-4. NASA tunnel test configuration settings and conditions

Test	U_∞ [m/s]	ρ [kg/m^3]	μ [Pa s]	Re_x	$C_{f,x}$	δ [mm]	τ_w [Pa]
1	0	1.218	17.98E-6	0	0	0	0
2	5	1.218	17.98E-6	1.19E6	3.59E-3	80	0.06
3	10	1.218	17.98E-6	2.39E6	3.13E-3	70	0.19
4	15	1.218	17.98E-6	3.58E6	2.88E-3	64	0.40
5	20	1.218	17.98E-6	4.77E6	2.72E-3	61	0.67
6	25	1.218	17.98E-6	5.97E6	2.60E-3	58	1.00
7	30	1.218	17.98E-6	7.16E6	2.51E-3	56	1.38
8	35	1.218	17.98E-6	8.35E6	2.44E-3	54	1.83
9	40	1.218	17.98E-6	9.54E6	2.37E-3	53	2.32

A full set of tunnel conditions are collected for all tunnel tests. This includes freestream static pressure P_∞, freestream stagnation pressure P_o, temperature T, relative humidity RH, streamwise tap array pressures $P_{1\text{-}30}$, and the traverse location y. The density ρ and viscosity μ of the air are calculated as functions of $f(P_\infty, T, RH)$, and freestream velocity U_∞ is calculated as a function of $f(P_\infty, P_o, T)$. This data was used to correct for flow variations between tests.

Before testing the wireless shear stress sensor, the boundary layer is fully characterized at each of the test conditions. The first step in characterizing the flow is to confirm the zero pressure gradient assumption. The array of pressure ports $P_{1\text{-}30}$ extending from the leading edge to the trailing edge of the flat plate model are tested at each flow condition. Plotting pressure versus distance from the leading edge, the slope of the curve should be zero in the vicinity of the sensor. This is found to be the case for all test conditions, as shown in Figure 4-8.

المنارة للاستشارات
www.manaraa.com

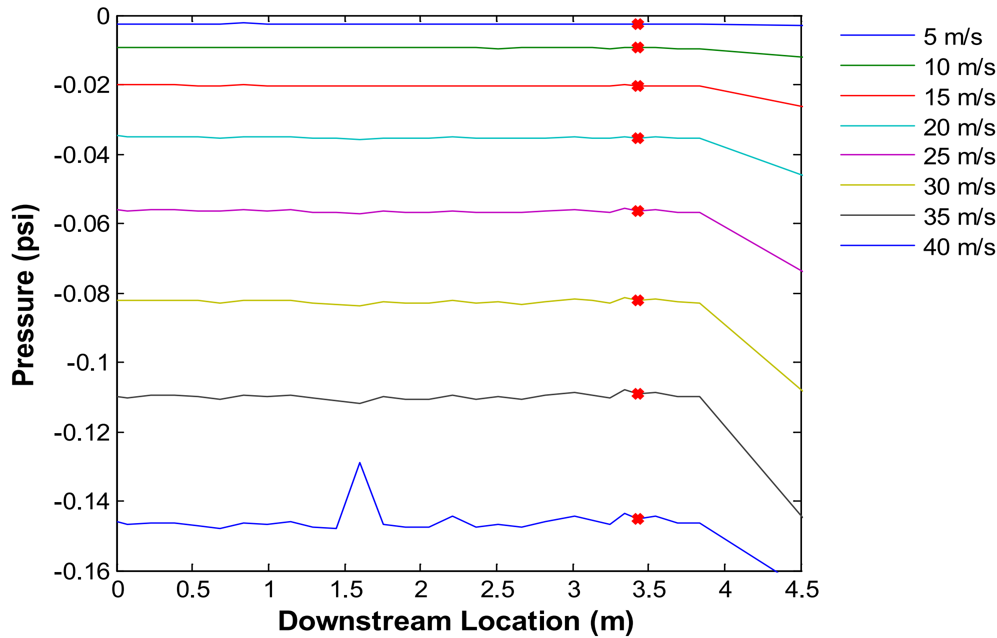

Figure 4-8. Pressure tap readings from the ceiling of the Shear Flow Control Tunnel for all test points. The sensor location is indicated in the plot around 3.5 m.

The next assumption to be confirmed is the establishment of a stable, fully developed turbulent boundary layer. The boundary layer at the sensor location is tested by taking Pitot profiles at each flow condition. The probe tip is raised incrementally from the surface until it reaches the freestream. An example of a typical profile taken at a 15 m/s test condition is shown in Figure 4-9. Converting to wall units and plotting on a log scale gives a better indication of the state of the boundary layer. Wall units are calculated as

$$y+=\frac{u_{*}\rho}{\mu}y, \tag{4-15}$$

where the physical parameters are density, ρ and viscosity, μ of the flow and u_{*} is the friction velocity. The friction velocity is calculated by

$$u_{*}=U_{\infty}\sqrt{\frac{C_f}{2}}, \tag{4-16}$$

المنارة للاستشارات
www.manaraa.com

in which U_∞ is the freestream velocity and C_f is the friction coefficient. The nondimensional velocity defined by

$$u+ = \frac{U}{u_*} \tag{4-17}$$

is plotted versus. $y+$ and shown in Figure 4-10.

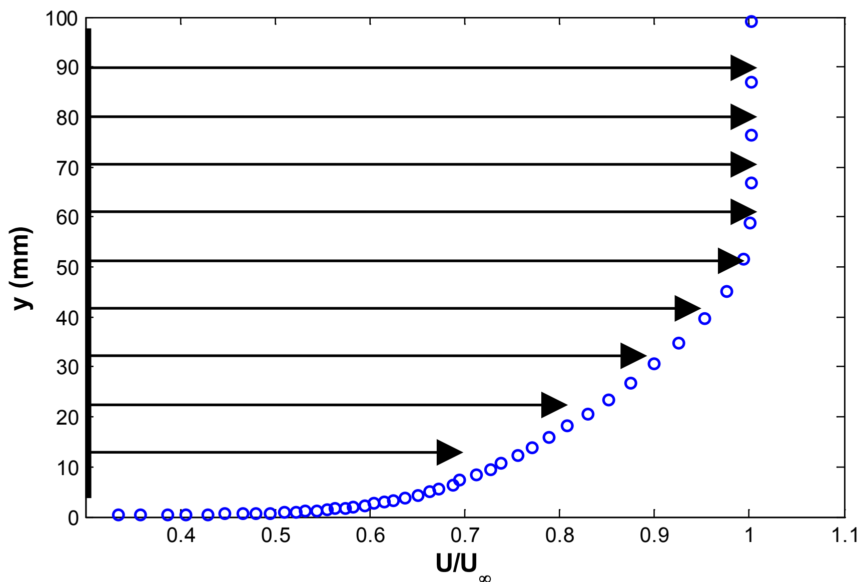

Figure 4-9. Turbulent boundary layer profile for 15 m/s flow over a flat plate.

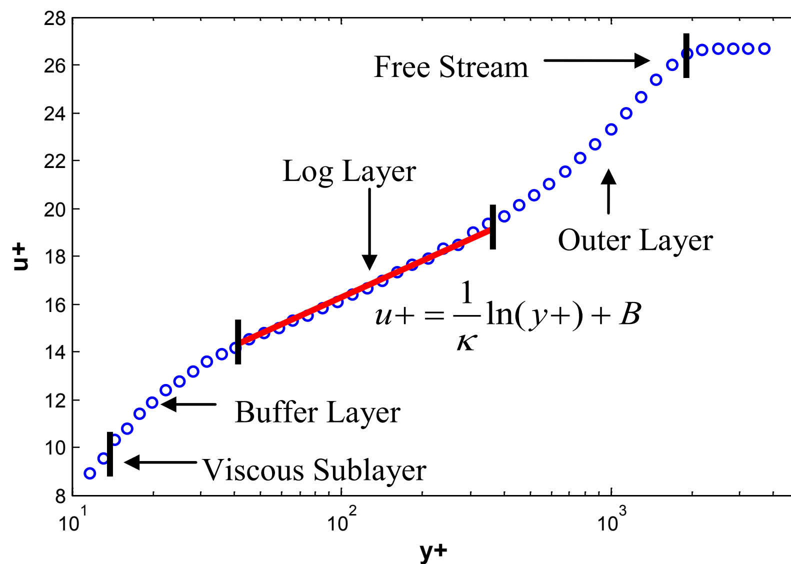

Figure 4-10. Turbulent boundary layer plotted in + units to illustrate the Law of The Wall. The different regions in the boundary layer are identified in this figure.

المنارة للاستشارات
www.manaraa.com

Five distinct regions in the boundary layer are indicated in Figure 4-10. The freestream is where the boundary layer height δ is estimated. The buffer layer and the outer layers are transitional layers and are not scrutinized. The viscous sublayer is very thin, and due to the size of the Pitot probe tip, the number of data points is insufficient to accurately determine the shear stress from the gradient at the wall. Instead the log layer is used by fitting a line to this region defined by

$$u+ = \frac{1}{\kappa}\ln(y+) + B\,, \tag{4-18}$$

where $\kappa = 0.41$ and $B = 5.0$ are constants. A fit is performed using a LabVIEW program from NASA Langley to implement Spalding's Law of the Wall [91]. This program gives the C_f where the Law of the Wall best fits the profiles. The shear stress at the wall for each flow velocity is then calculated using Equation 4-14.

There are many additional tests that could be performed on the sensors. Dynamic shear stress testing, pressure rejection, vibration sensitivity, stress testing and many more boundary layer studies are a few of the possibilities. These test will all require additional resources and time that would be better invested once the technology matures. Additional generations and testing are all left to future work.

المنارة للاستشارات
www.manaraa.com

CHAPTER 5
FIRST-GENERATION DEVICES

This chapter presents design, fabrication, and characterization of two first-generation devices. First, the design and predicted performance is presented, using the modeling techniques presented in Chapter 3. Next, details of the fabrication and packaging are described. Last, using the experimental techniques described in Chapter 4, the performance of each device is fully characterized. The results are then compared against the model predictions.

5.1 Device Overview

The modeling of the wireless shear stress sensor consists of a combination of analytical, numerical, and empirical results. This section presents specific modeling results for two wireless sensor designs, labeled “Design 1” and “Design 2.” First, the coil and antenna results are presented, including their associated parasitics. Next the results for the capacitive shear stress sensor shown in Figure 5-1 are presented, followed by a combination of the results into the final complete wireless sensor performance.

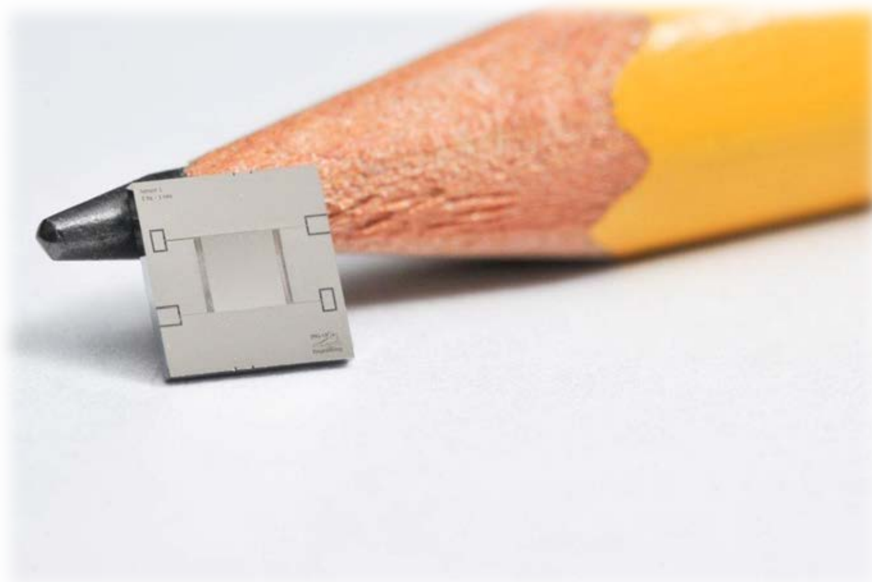

Figure 5-1. Optical image showing the Design 2 capacitive shear stress sensor next to a pencil for scale.

المنارة للاستشارات
www.manaraa.com

5.1.1 Coil and Antenna Modeling Results

The simulated and realized geometries for the coil inductors for both designs are shown in Figure 5-2. The loop antenna design used for both sensors is shown in Figure 5-3. The design parameters corresponding to the variables in Figure 3-3 are given in Table 5-1. The center diameters D_c are constrained by the capacitive shear stress sensor die size, which are different for the two designs. Design 1 uses a 3.5 x 3.5 mm^2 die, while Design 2 uses a 5 x 5 mm^2 die. The pitch *p* and coil widths *b* are constrained by manufacturing limits, and the height is determined by the thickness of the 1 oz copper clad FR4 used to make the coils. The number of turns is maximized within a 10 x 10 mm^2 footprint defined by the dielectric window between the pressure taps, shown in Figure 4-6, in the metal flow cell used to characterize the devices. The antenna diameter D_a is similarly constrained by this window.

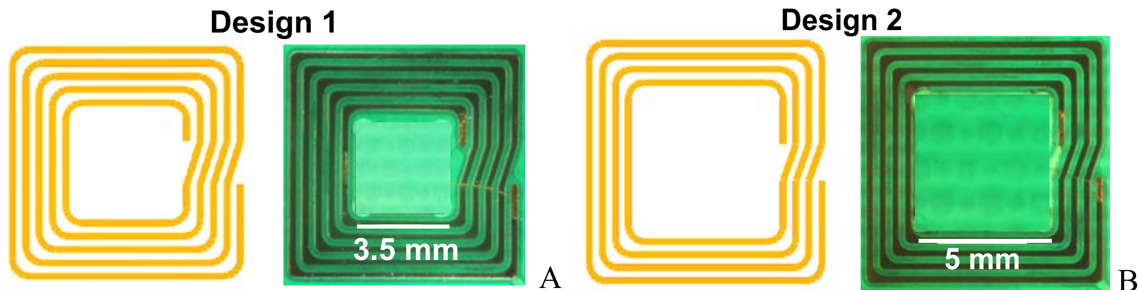

Figure 5-2. Coil designs showing simulated and realized inductors. A) Design 1 is a 5-turn coil with a 3.5 mm inner diameter. B) Design 2 is a 4-turn coil with a 5 mm inner diameter.

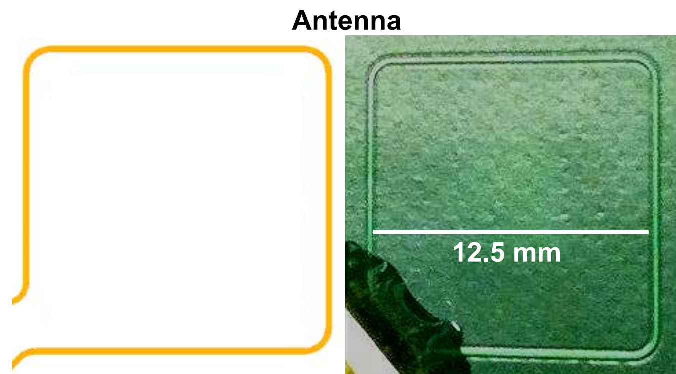

Figure 5-3. Design showing both the simulated and realized loop antenna.

المنارة للاستشارات
www.manaraa.com

Table 5-1. Geometric parameters used for the spiral coil inductors and loop antenna in the first generation wireless design.

Variable	Design 1	Design 2
D_c [mm]	3.5	5
p_c [µm]	500	500
b_c [µm]	250	250
h_c [µm]	35	35
N_c	5	4
D_a [mm]	12.5	12.5
b_a [µm]	250	250
h_a [µm]	35	35

The wireless sensors operate in the hundreds of MHz range. Simulations in the range of 50 MHz to 1 GHz are performed on the coil design to ensure that this full range is covered. As discussed in Section 3.1.1, the current in the coils is constrained to the outer surfaces at high frequencies. This skin depth is an important consideration for the discretization of the wire segments performed by FastHenry prior to simulation. If the filaments of the discretization are larger than this depth, then the simulation results will be inaccurate. A visualization tool is created as part of a MATLAB code written to both generate the geometry input files for FastHenry and analyze the results. The skin depth for copper between 50 MHz and 1 GHz is plotted in Figure 5-4. Considering the skin depth at 1 GHz, this plot shows that the minimum filament must be below 2 µm. Figure 5-5 shows that the discretization input parameters produce an accurate numerical result.

For the first sets of tests, the antenna is located coaxially with the coil on the backside of the board (Figure 5-6) in order to maximize the coupling factor. This means that the separation between the antenna and the coil is defined by the thickness of the FR4, which is 1.5 mm. In later tests, the antenna is moved to a separate board, making the separation gap 3 mm or more. The coupling results for both 1.5 mm and 3 mm is reported for completeness. The FastHenry

المنارة للاستشارات
www.manaraa.com

simulation results as a function of frequency for Design 1 are given in Figure 5-7 and for Design 2 in Figure 5-8. In both of these plots, the inductance drops with frequency, while the resistance rises. This indicates that the lower the operating frequency, the higher the mutual inductance and the lower the resistive losses.

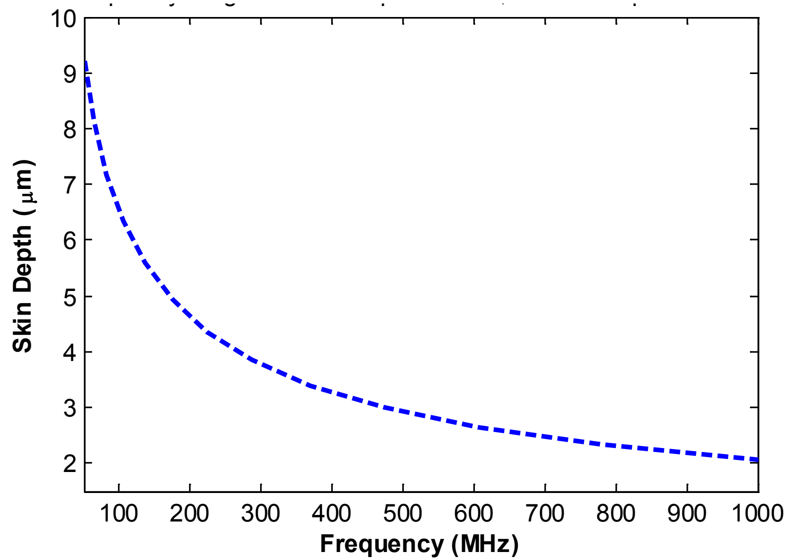

Figure 5-4. Skin depth vs. frequency for copper.

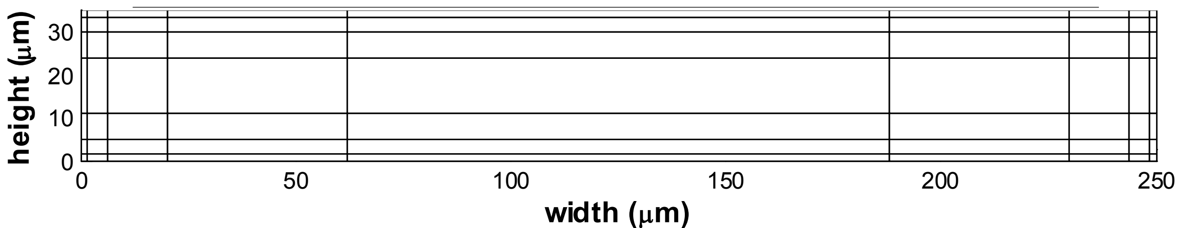

Figure 5-5. Coil discretization plot looking at the cross-sectional area of a wire trace.

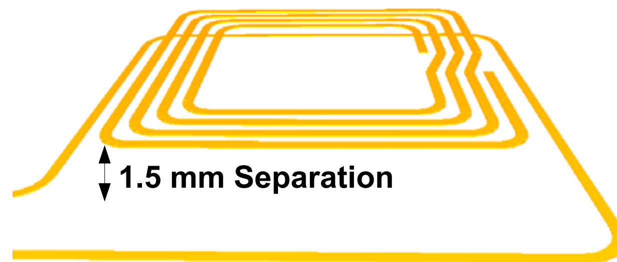

Figure 5-6. Inductive coupling was simulated with the coil and antenna coaxially aligned with a 1.5 mm separation.

المنارة للاستشارات
www.manaraa.com

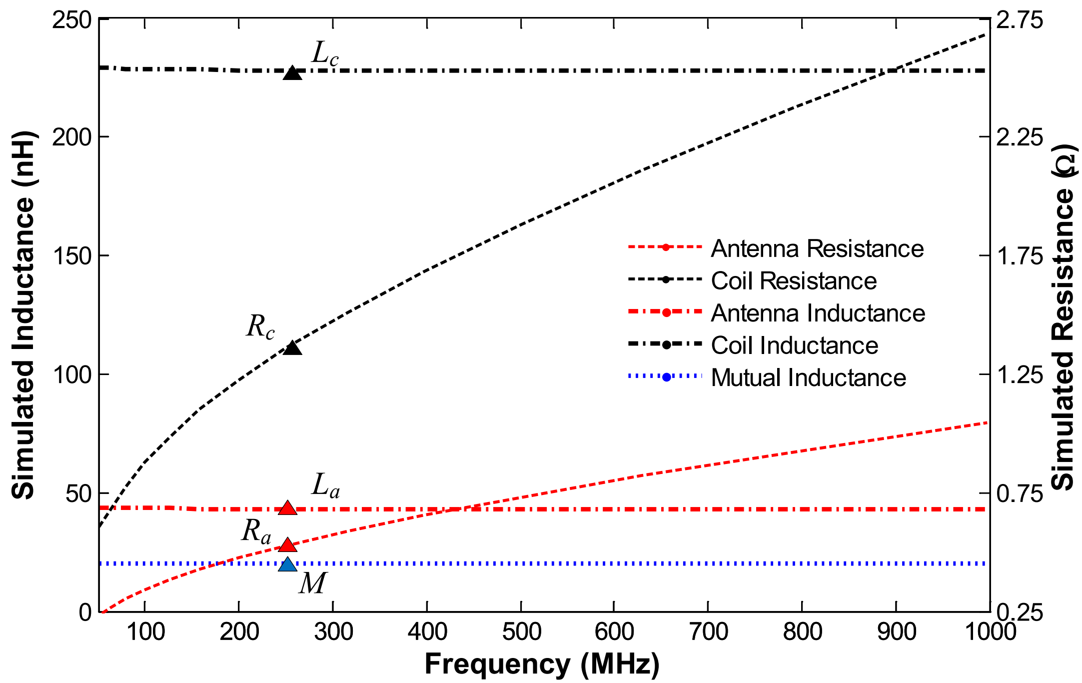

Figure 5-7. FastHenry simulation results for Design 1. The parameters are indicated at the resonant frequency of this device.

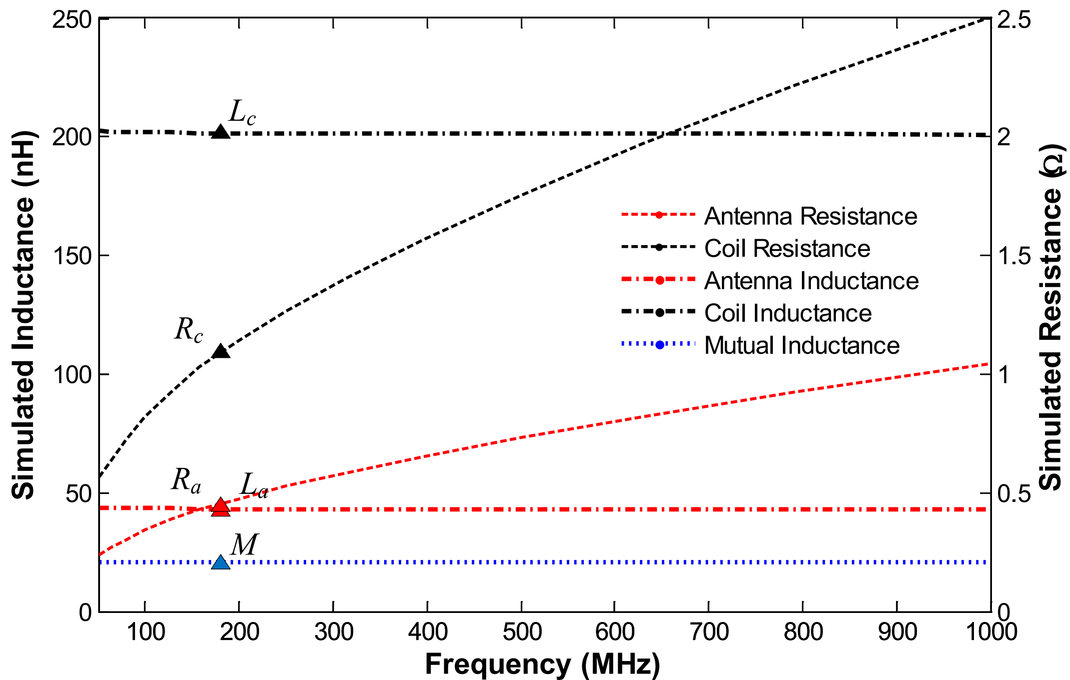

Figure 5-8. FastHenry simulation results for Design 2. The parameters are indicated at the resonant frequency of this device.

المنارة للاستشارات
www.manaraa.com

The inductance values are extracted and used to determine the resonant frequency of both devices. This is then used to determine the appropriate parasitic resistance values to use from the plots. These frequencies and their associated parameter values are indicated in the plots. All of the results from these tests are reported in Table 5-2. The modeling results for the two designs are comparable in inductance, resistance, and coupling. This means that differences in their performance are dominated by the capacitive shear stress sensor performance.

The other two remaining parasitics are the capacitances C_a and C_c. The coil parasitic capacitance C_c is obtained analytically using Equation 3-25 and is also reported in Table 5-2. The RF connectors between the antenna and the network analyzer dominated the antenna parasitic capacitance C_a. The network analyzer has a 7 mm port, so a 7 mm to SMA connector and an SMA to SMB connector are both required to attach to the SMB terminal soldered to the antenna. The capacitances of these connectors and the terminal are measured, and the results are shown in Figure 5-9. The total accumulated capacitance is indicated in the plot and added to the results in Table 5-2.

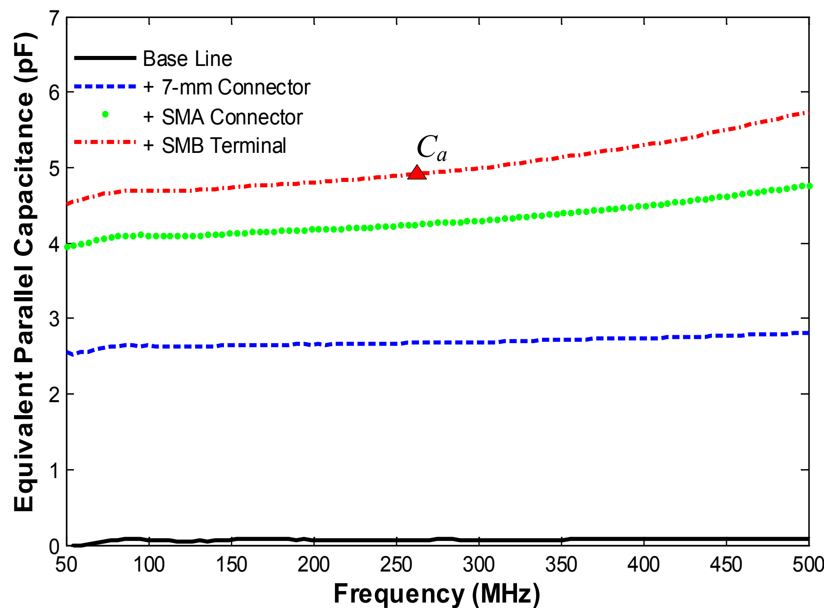

Figure 5-9. Parasitic capacitance due to RF connectors between the network analyzer and the loop antenna.

المنارة للاستشارات
www.manaraa.com

Table 5-2. Parameter values extracted numerically, analytically, and experimentally for the coupled inductor model. Coupling values are given for 1.5 mm (3 mm) separation.

Variable	Design 1	Design 2
L_c [nH]	228*	202*
R_c [Ω]	1.22*	1.14*
L_a [nH]	43.2*	43.2*
R_a [Ω]	0.50*	0.50*
M [nH]	19.8 (14.7)*	21.0 (15.2)*
k	0.20 (0.15)	0.22 (0.16)
C_c [fF]	230	377
C_a [pF]	4.9†	4.9†

† Obtained experimentally. * Obtained though numerical simulations

5.1.2 Capacitive Sensor Modeling Results

Two designs for the MEMS capacitive sensor, shown in Figure 5-1, are described in this section. The analytical models in Section 3.2 are used to predict the static sensor capacitance and part of the parasitic capacitance. The models also predict the total shear to displacement and displacement to change in capacitance sensitivities. Using these sensitivities and the maximum input shear stress, the full-scale displacement and change in capacitance are determined.

The sensors are both shown in magnified optical images in Figure 5-10. The tethered floating element is visible with comb fingers along either side. The capacitive sensor geometries are selected based on an optimization of this structure reported by V. Chandrasekharan [21], who studied a wired version of the shear stress sensor. The optimized 1 mm and 2 mm floating element designs from his work were slightly modified to obtain larger displacements by sacrificing unneeded mechanical bandwidth. The primary purpose of the wireless sensor is to make mean shear measurements, so high bandwidth is not necessary. Both devices have the same tether and finger geometries, except that the 2 mm element can hold more fingers due to the added length. All of the geometric design variables for the sensor, as illustrated in Figure 3-11 and Figure 3-14, are given in Table 5-3.

المنارة للاستشارات
www.manaraa.com

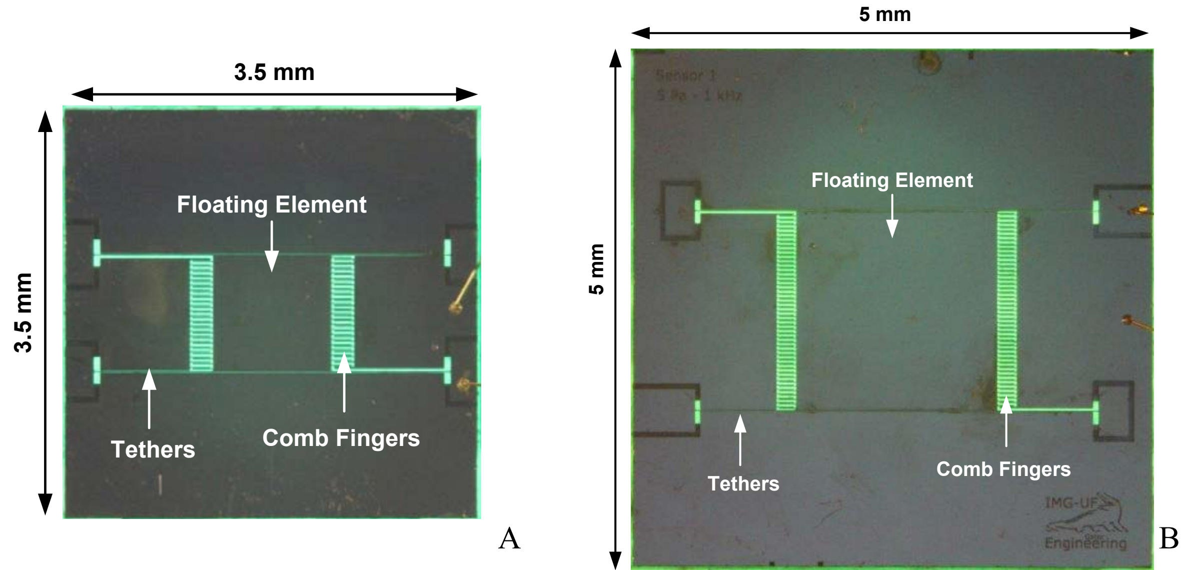

Figure 5-10. Optical images of the MEMS capacitive sensors highlighting the vital components. A) Design 1 is 3.5 x 3.5 mm^2 and has a 1 x 1 mm^2 floating element. B) Design 2 is 5 x 5 mm^2 and has a 2 x 2 mm^2 floating element.

Table 5-3. Geometric parameters from the two capacitive MEMS sensors used for the first generation wireless tests.

Variable	Design 1	Design 2
W_e [μm]	1000	2000
L_e [μm]	1000	2000
W_t [μm]	10	10
L_t [μm]	1000	1000
W_f [μm]	10	10
L_f [μm]	170	170
x_o [μm]	150	150
g_{o1} [μm]	3.5	3.5
g_{o2} [μm]	20	20
h [μm]	45	45
N_f	22	45

The capacitive modeling results are given in Table 5-4. The most important parameters for the complete wireless model are C_{os}, ΔC_s and $S_{\tau c}$. The full-scale values are calculated assuming a maximum shear stress input of 2 Pa. As described in Appendix A, the 3% nonlinearity point defines this limit. Because of the complex chain of events—shear stress creates a displacement,

المنارة للاستشارات
www.manaraa.com

which causes a capacitance change that leads to a resonant frequency shift—various sensitivities are reported. $S_{\tau w}$ is given by Equation 3-29 and relates the floating element displacement to the input shear stress. S_{wc} is given by Equation 3-43 and relates the change in capacitance to the floating element displacement. $S_{\tau c}$ is the product of the first two sensitivities.

Table 5-4. Analytical modeling results for the MEMS capacitive sensors.

Variable	Design 1	Design 2
τ_{max} [Pa]	2	2
$w(\tau_{max})$ [nm]	72.4	276
C_{o1} [fF]	438	900
C_{o2} [fF]	114	228
C_{o3} [fF]	181	181
C_{os} [pF]	0.73	1.31
$\Delta C_1(\tau_{max})$ [fF]	7.71	64.0
$\Delta C_2(\tau_{max})$ [fF]	2.40	19.5
$\Delta C_3(\tau_{max})$ [fF]	3.57	14.5
$\Delta C_s(\tau_{max})$ [fF]	13.7	98.0
$S_{\tau w}$ [nm/Pa]	36.2	138
S_{wc} [fF/nm]	0.19	0.33
$S_{\tau c}$ [fF/Pa]	6.70	45.5

The parasitic structures of the capacitive shear stress sensor are covered in Section 3.2.3. The remaining geometries that are purely parasitic are given in Table 5-5. A summary of the results is tabulated in Table 5-6. The results of the parasitics are derived from three sources. The isolation gaps around the contact pads and the stationary end of the tethers are calculated analytically in Equation 3-45 and reported as C_{p1}. The fringing field capacitances are simulated in a COMSOL finite element model as described in Section 3.2.3 and are represented as C_{p2}. The pad areas coupling with the bulk substrate are separated into C_{b1}, C_{b2} and G_b.

www.manaraa.com

Table 5-5. Geometries of parasitic capacitive structures in the capacitive MEMS sensors.

Variable	Design 1	Design 2
L_{p1} [μm]	250	300
L_{p2} [μm]	250	500
W_{p1} [μm]	430	430
W_{p2} [μm]	500	500
g [μm]	50	50
h_{ox} [μm]	2	2

Table 5-6. Parasitic results for the MEMS sensor derived using analytical, numerical and experimental models.

Variable	Design 1	Design 2
C_{p1} [fF]	200	204
C_{p2} [fF]	451^*	687^*
C_{b1} [pF]	8.03	12.6
C_{b2} [pF]	92.5	174
G_b [mS]	$0.1^\dagger$	$0.1^\dagger$
C_{p3} [fF]	$130^\dagger$	$1000^\dagger$
G [mS]	$0.62^\dagger$	$1.32^\dagger$

† Obtained experimentally. * Obtained though numerical simulations.

The plots in Figure 5-11 show the simulated total shunt capacitance, C_{p3} and conductance, G that result from the circuit combination of C_{b1}, C_{b2} and G_b. The high capacitance seen at low frequency is attributed to the parallel combination of the sensor capacitance C_{os}, the parasitic capacitances, C_{p1} and C_{p2}, and the pad to bulk capacitance, C_{b1}. The low capacitance seen at high frequency is attributed to the parallel combination of the sensor capacitance, C_{os} and the parasitic capacitances, C_{p1} and C_{p2}. The frequency at which the transition occurs is a function of G_b. This frequency is known from experiments and is used to determine G_b. The equivalent C_{p3} and G are determined iteratively to account for slight inconsistencies. The die from the first-generation wafers were originally 5 x 5 mm^2, but the capacitive sensor die for Design 1 was diced down to 3.5 x 3.5 mm^2 to reduce the size of the contact pads. This corresponds to a significant reduction

المنارة للاستشارات
www.manaraa.com

in C_{p3} and G when compared to Design 2. It can be seen that with this reduction, the fringe field parasitic capacitance becomes the dominant source.

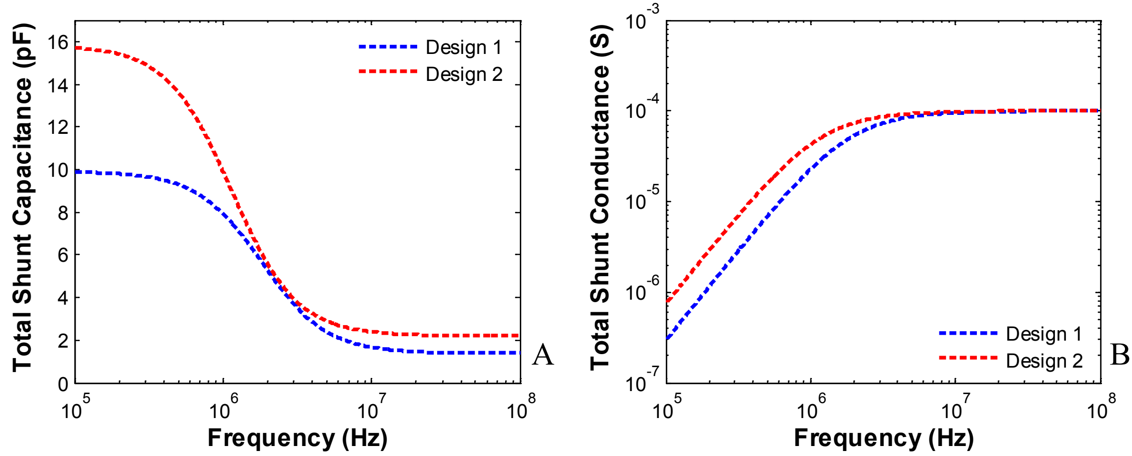

Figure 5-11. Simulated capacitance and conductance factoring in the bulk layer model. A) Shunt capacitance model. B) Shunt conductance model.

5.1.3 Completed Model Results

With all of the parameters from the coils and capacitive sensor defined, the complete device performance can be predicted. The resonant frequency f_o is given by Equation 3-57 and quality factor Q by Equations 3-67. The results for both devices are presented in Table 5-7. The resonant frequency of Design 2 is lower due to the larger floating element size, which has more fingers and thus gives a higher static capacitance. The lowest resonant frequency possible is desirable to reduce coil resistances, but the reduction of the capacitive sensor parasitics achieved in Design 1 had a greater effect on Q. This shows that for the present designs the dominant parasitics are from the capacitive sensor. This is uncommon in LC resonators where the resistive losses of the coil usually dominate.

The final device sensitivity needed to relate a change in the resonant frequency to the input shear stress is determined based on the complete wireless model shown in Figure 3-26. The sensitivities relating displacement to shear and change in capacitance to displacement are reported in the previous section. The final sensitivity S_{cf} relates the resonance shift to a change in

المنارة للاستشارات
www.manaraa.com

capacitance and is given by Equation 3-59. The full device sensitivity $S_{\tau f}$ is the product of S_{tc} from Table 5-4 and S_{cf}. The normalized sensitivity S_n is reported in units of parts per million [ppm]. This normalized sensitivity is useful for comparing wireless devices that operate in different frequency bands. The predicted normalized sensitivities are over two orders of magnitude larger than previously reported wireless sensors [31,42,50,51,53,54,58,60]. This improved sensitivity is necessary for the application of detecting the minute tangential shear forces in subsonic flows.

Table 5-7. Full wireless system resonance and sensitivity results.

Variable	Design 1	Design 2
f_o [MHz]	252	187
Q	4.58	3.59
$\Delta f(\tau_{\max})$ [MHz]	0.95	2.33
S_{cf} [kHz/fF]	70.9	25.9
$S_{\tau f}$ [kHz/Pa]	475	1167
S_n [ppm/Pa]	1885	6241
S_F [1/N]	1885	1560

The reflection coefficient spectrum of the wireless sensors are used to detect and track the wireless resonance as described in Section 4.2.1. At each frequency, the reflection coefficient is given by Equation 3-55. The theoretical spectrums showing the resonant dips for both sensor designs are plotted in Figure 5-12. Design 1 shows a minimum in the reflection coefficient at 252 MHz, and Design 2 shows a minimum in the reflection coefficient at 187 MHz. As expected, the minimums are located at the resonant frequencies of the devices.

5.2 Fabrication and Packaging

The system uses a hybrid packaging approach that combines the silicon capacitive MEMS sensor with an inductive coil fabricated in a PCB substrate. An alternative configuration for the devices would have been to fabricate and integrate the coils on the silicon capacitive sensor dies.

المنارة للاستشارات
www.manaraa.com

Realizing such structures, however, would involve a complicated and expensive fabrication process, so a hybrid packaging approach is selected. The silicon die is flush-mounted in a recess in the PCB to provide a smooth surface for exposure to the flow. In the current design, the MEMS capacitive sensors are connected to the inductor coils via gold wire bonds, but future implementations may use other interconnect technologies, such as through wafer vias to eliminate the wire bonds and ensure a hydraulically smooth surface.

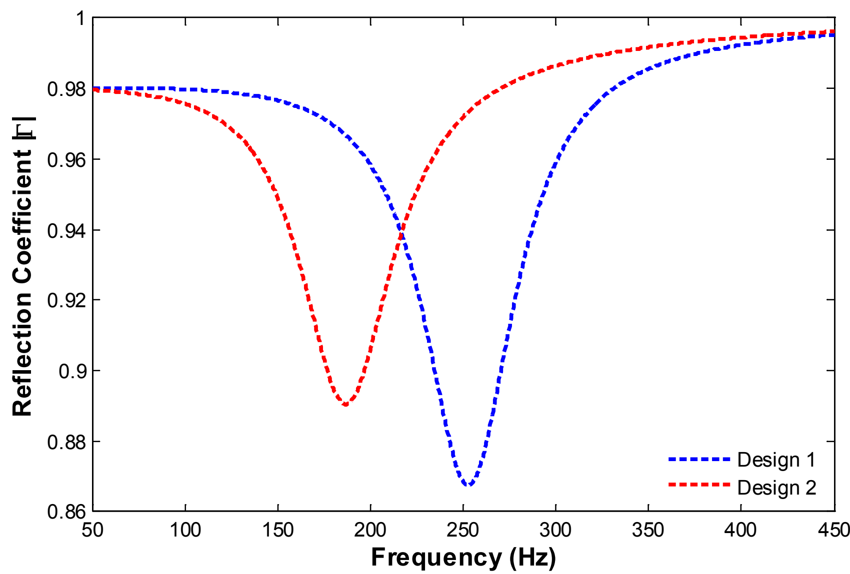

Figure 5-12. Resonant dips in the reflection coefficient predicted by the model for both Design 1 and Design 2.

5.2.1 Process Flow

A simple two-mask fabrication process is used to create the sensor. These sensors were incorporated into the mask files with V. Chandrasekharan's designs [21] and fabricated at the same time using the same process. A more detailed description of the fabrication can be found in his dissertation. An overview of the fabrication process flow is illustrated in Figure 5-13. A silicon on insulator (SOI) wafer with a highly doped device layer is etched via deep reactive ion etching (DRIE) to define the sensor structures using Mask 1 (Figure 5-14A). The highly doped silicon (Si^{++}) is then electroplated with nickel (Ni). The nickel is intended to reduce conductivity

المنارة للاستشارات
www.manaraa.com

and eliminate charge accumulation in the native oxide that naturally grows on the surfaces of the silicon. A front to back alignment is used to pattern a photoresist layer with Mask 2 (Figure 5-14B) to define the backside cavity etch underneath the floating element. To release the mechanical structures, a buffered oxide etch (BOE) is used to remove the underlying oxide.

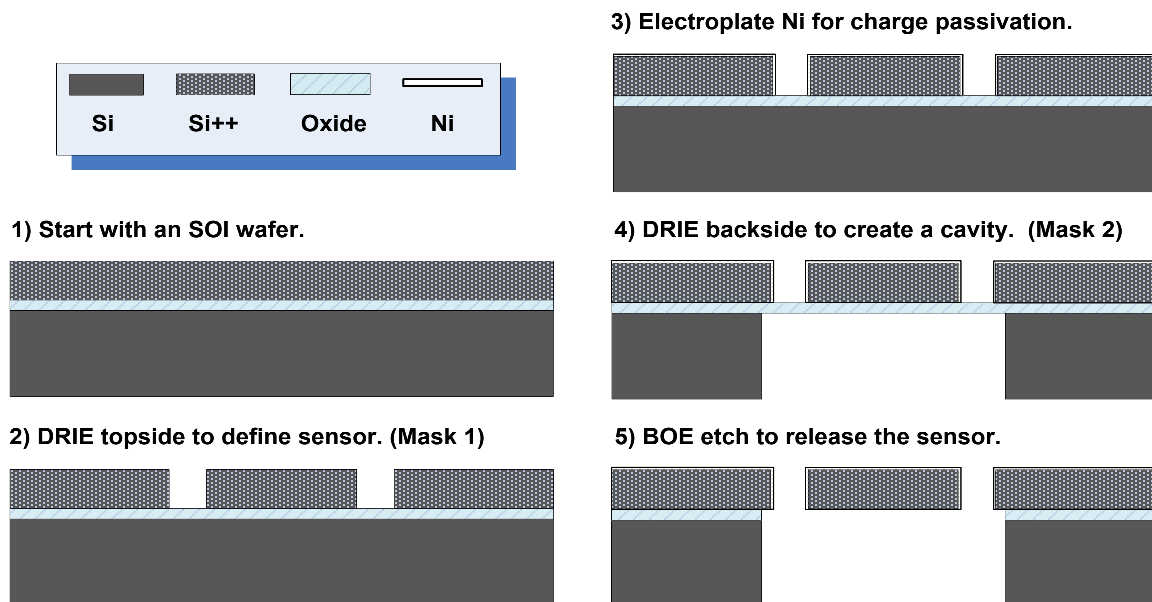

Figure 5-13. Generation 1 MEMS sensor fabrication process flow.

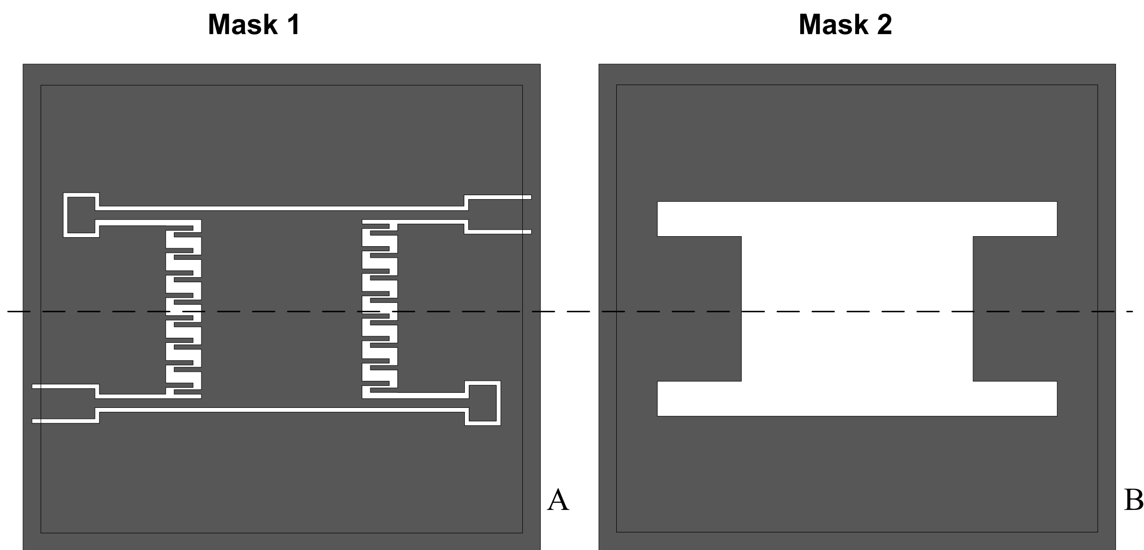

Figure 5-14. Photolithography dark field mask set used to define etches in the process flow. A) Sensor structure etch. B) Back cavity etch.

المنارة للاستشارات
www.manaraa.com

5.2.2 Hybrid Packaging

The hybrid-packaging scheme enables fast turnaround time, increased flexibility, and separates testing of the sensor capacitances and coil inductances. The coils and antennas are fabricated using a PCB milling machine. The sensor die is then mounted into a recess in the PCB and connected via gold wire bonds. A top view of this concept is illustrated in Figure 5-15 for both a single device as well as an array. The dashed lines indicate the antenna, which exists on the backside of the board. More specific details are described in the following paragraphs.

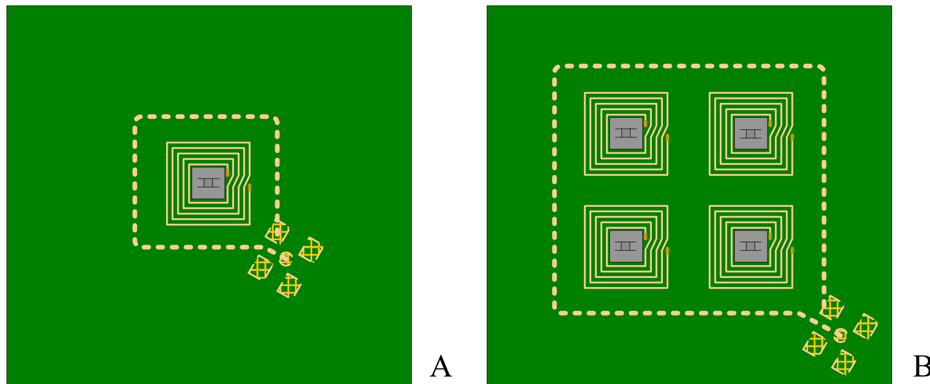

Figure 5-15. Packaging concept for hybrid wireless shear stress sensors. A) Single sensor design. B) A 2 x 2 array design.

The packaging process is shown in Figure 5-16. A copper-clad FR4 board is milled to create the inductor coil and loop antenna. The coil is electroplated with Ni to enable electroless deposition of Au for wire bonding to the sensor die in the final step. A photo-definable solder mask polymer is then applied to reduce the surface roughness due to the Cu traces. Contact window openings are made in the solder mask and Au is plated to facilitate electrical connections to the inductor bond pads. A cavity is milled in the top surface of the board to accommodate the sensor die. DualBond 707 epoxy is applied to only one corner of the die to affix it in the cavity and avoid mechanical stresses on the die as the glue dries. Gold ball-wedge wire bonding is used to connect the sensor to the inductor. The final device footprint for the single-sensor construction is 10 mm x 10 mm in the center of a 30 mm x 30 mm x 1.5 mm board.

المنارة للاستشارات
www.manaraa.com

The board size allows room for up to a four-sensor array. Figure 5-17 shows the die packaged in the PCB with a U.S. penny for perspective.

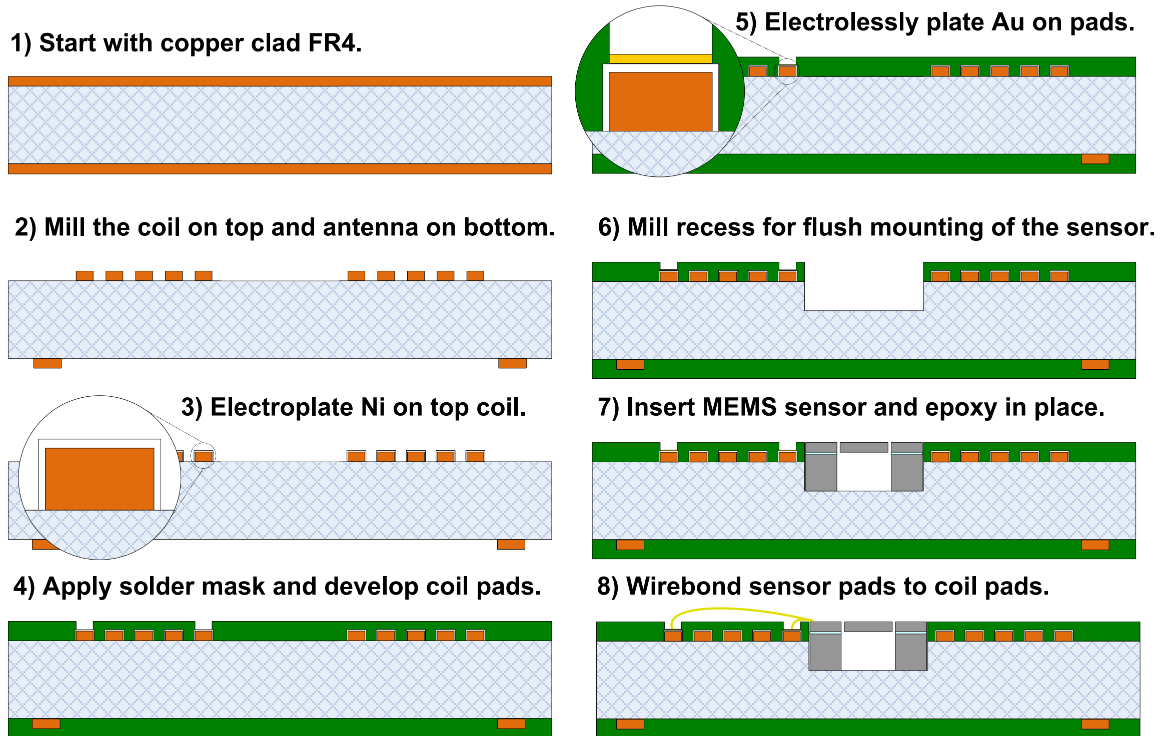

Figure 5-16. Process flow for hybrid wireless packaging.

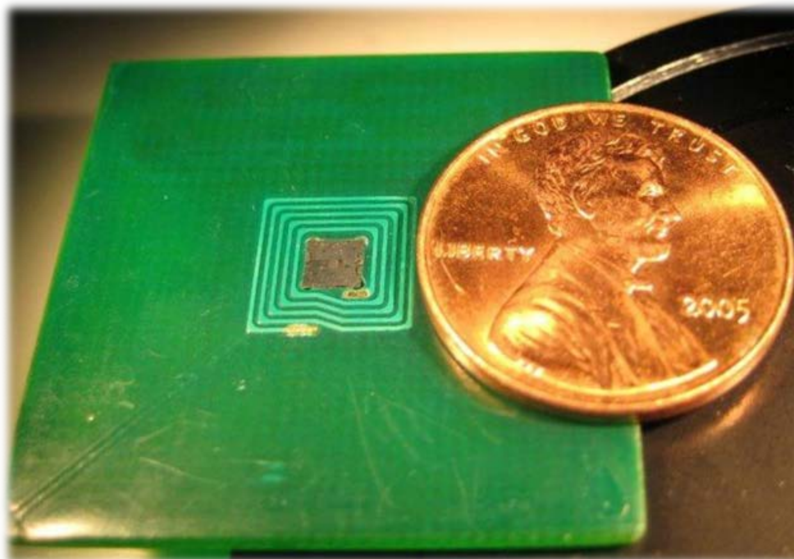
Figure 5-17. Final packaged wireless sensor shown next to a U.S. penny for perspective.

المنارة للاستشارات
www.manaraa.com

The boards are housed in an acrylic plug, which enables mounting to calibration flow cells and installation in wind tunnel models. The topside of the plug is designed with a smooth, flush surface, and the backside has a SMB connector for electrical connection of the loop antenna to an interrogation circuit or network analyzer. An illustration of the front and backside of this plug with the sensor in place is shown in Figure 5-18.

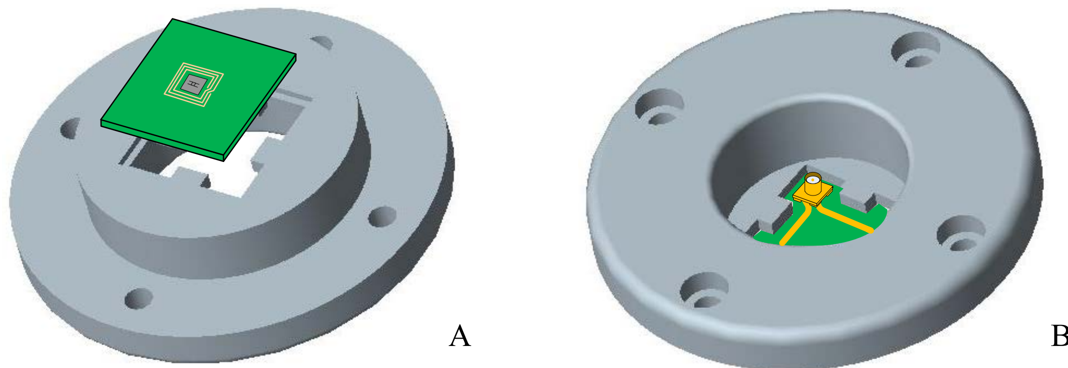

Figure 5-18. Wireless sensor boards flush mounted in test plugs used for the flow cell calibration and wind tunnel tests. A) Frontside showing sensor being fit into the plug. B) Backside view showing antenna and RF connector.

5.3 Experimental Results

The experimental test results for Design 1 and Design 2 are presented in this section using the test setups described in Chapter 4. These tests are performed to fully characterize the performance of the sensors. First, impedance characteristics are obtained on individual sensor die prior to packaging in the wireless boards. Next, the die are evaluated electrostatically to ensure the free-floating structures on the die were free of obstructions. The stability, noise floor, and sensitivity are obtained in a series of tests giving the minimum detectable signals (*MDS*) and dynamic ranges (*DNR*) of the devices. A simple range test is presented to evaluate the coil antenna separation limitations. During testing, an unexpected and undesirable sensitivity to humidity was found, and therefore dedicated humidity tests were also conducted to quantify this

www.manaraa.com

sensitivity. Finally, baseline shear stress measurements from a real world wind tunnel are presented.

5.3.1 Impedance Characterization

Two sets of impedance data are taken for the two capacitive shear stress sensor designs as described in Section 4.1.1. First, a high accuracy low frequency test is performed on an impedance analyzer to compare to the capacitive shear stress sensor model results from Section 5.1.2. The maximum frequency of the impedance analyzer is below the resonant frequencies of the devices, so a high frequency test is conducted. A material property analyzer (RF impedance analyzer) is used to extend the range of these tests and obtain values for the parasitic capacitance and conductance.

5.3.1.1 Impedance analyzer 100 kHz to 100 MHz

Since each sensor design actually includes differential capacitors, both sides of the differential capacitor were measured. The resulting shunt capacitance and shunt conductance for each of the four capacitors are plotted in Figure 5-19. Additionally, the measurement error is also shown; the random error is plotted using a 95% t-distribution, and the bias error is calculated according to the impedance analyzer manual [92]. For the tests, the random error is several orders of magnitude less than the bias error, indicating that the measurements are repeatable from sweep to sweep and will also be repeatable from die to die. The bias error is an inherent limitation of the analyzer and cannot be improved upon, but since it is several orders of magnitude lower than the measured values, it is not a limiting factor in the overall wireless sensor model accuracy.

Comparing the measured data in Figure 5-19 against the theory in Figure 5-11, one major discrepancy is observed. The high frequency response never flattens out; dotted lines in Figure 5-19 show where the data was expected to asymptote. This effect is consistent for both devices and

المنارة للاستشارات
www.manaraa.com

points to some higher order effects that are not captured in the simple model. The impedance data seems to point to an additional leakage path between the terminals of the capacitive sensor. One possibility is dust or debris that has entered the gaps and bridges between the two capacitor structures. Another possibility is a poor quality oxide with pinholes or other defects. Whatever the source, as the conductance climbs the quality factor *Q* drops. This creates a design challenge, since *MDS* is a function of *Q*.

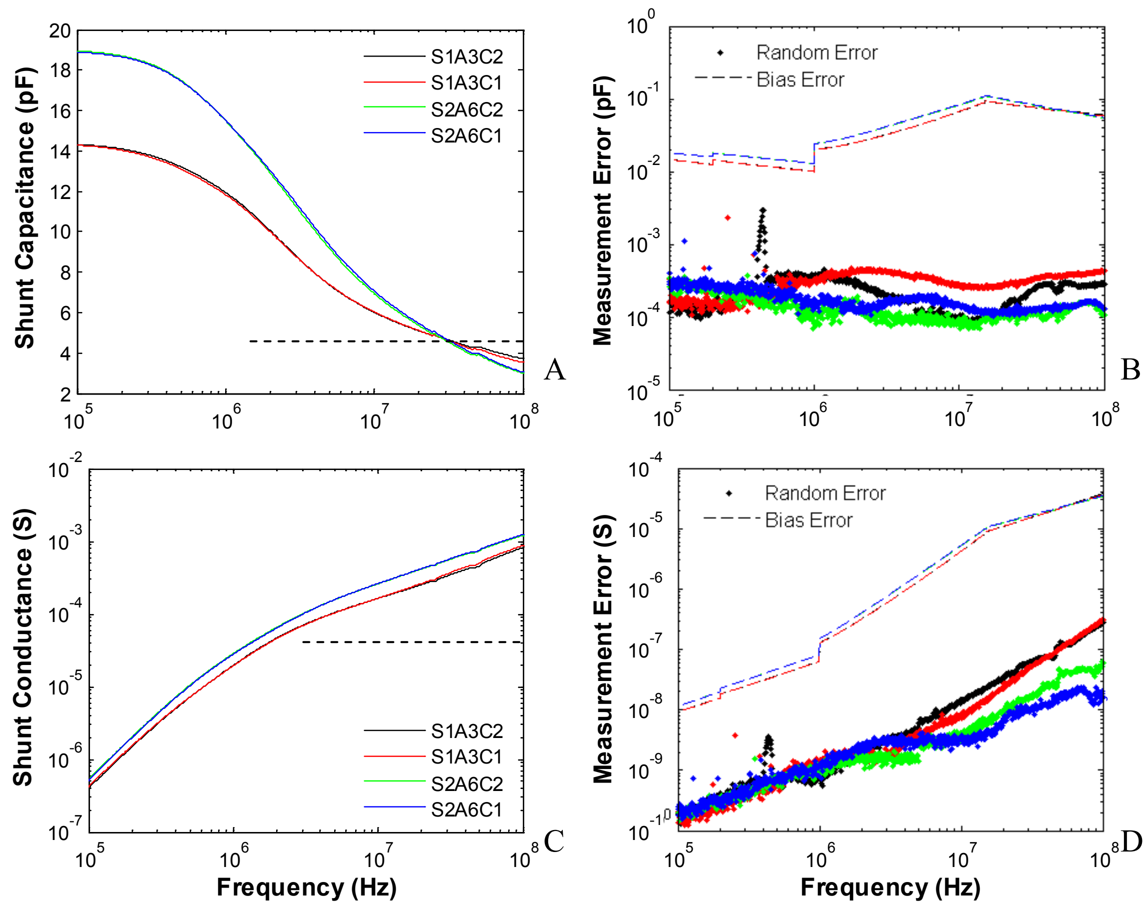

Figure 5-19. Capacitance measurement and error for Design 1 and 2. A) Mean shunt capacitance. B) Measurement errors. C) Mean shunt conductance. D) Measurement errors.

5.3.1.2 Material property analyzer 1 MHz to 1 GHz

The same test was repeated with the Agilent E4991A material property analyzer at a different frequency range. For these tests, the same sensor designs were tested, but more dies were tested to get a better sample population. The results for Design 1 are plotted in Figure 5-20,

www.manaraa.com

and the results for Design 2 are plotted in Figure 5-21. These tests confirm that the shunt conductance continues to rise without leveling off, as was suspected in the first set of impedance tests. These tests provide data in the operation range of the wireless sensor that is used to estimate the shunt conductance, G and capacitance, C_{p3} for the full wireless sensor models. The bias and random errors for these tests are higher due to the reduced accuracy of the material property analyzer with respect to the impedance analyzer. The bias errors are still several orders of magnitude lower than the measured values, so they will not affect the overall accuracy of the wireless model.

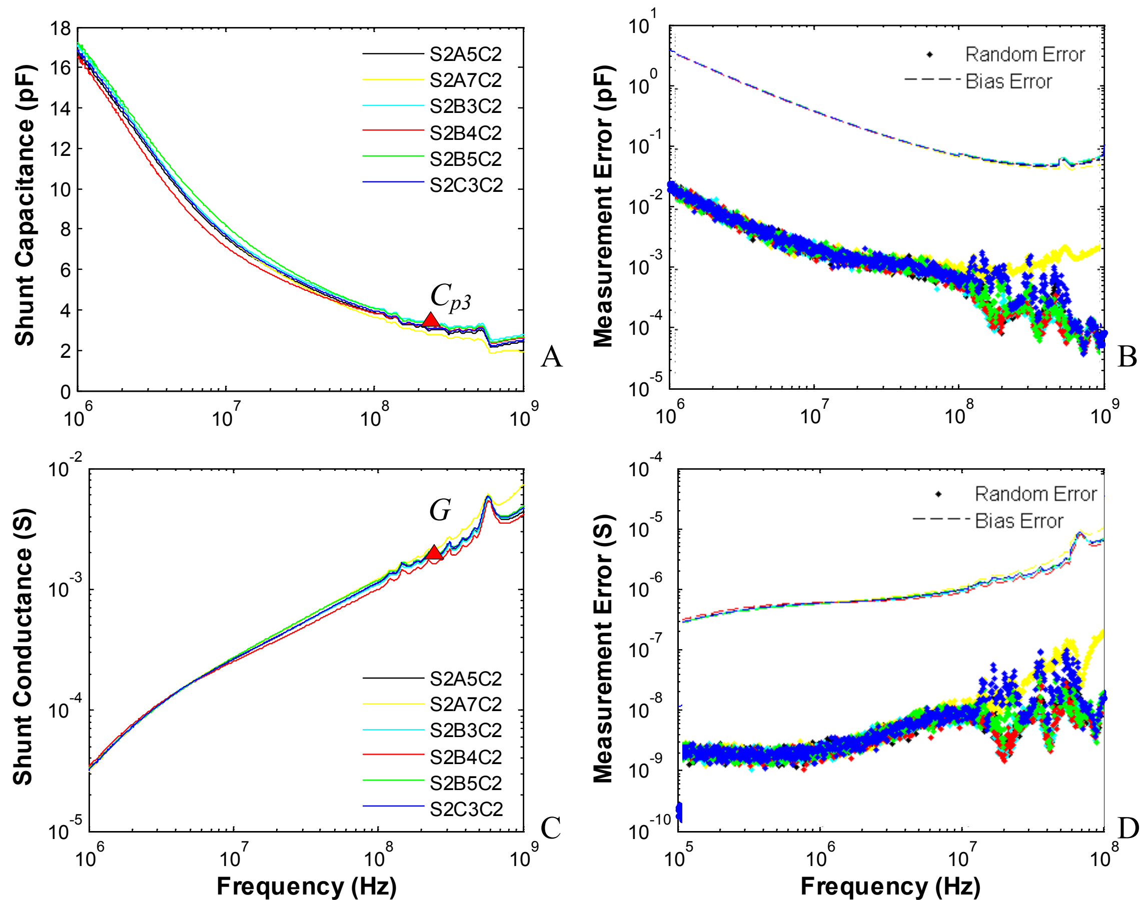

Figure 5-20. Die level high frequency impedance sweeps for six Design 1 sensors. A) Mean shunt capacitance. B) Random and bias error for the capacitance measurements. C) Mean shunt conductance. D) Random and bias error for the conductance measurements.

المنارة للاستشارات
www.manaraa.com

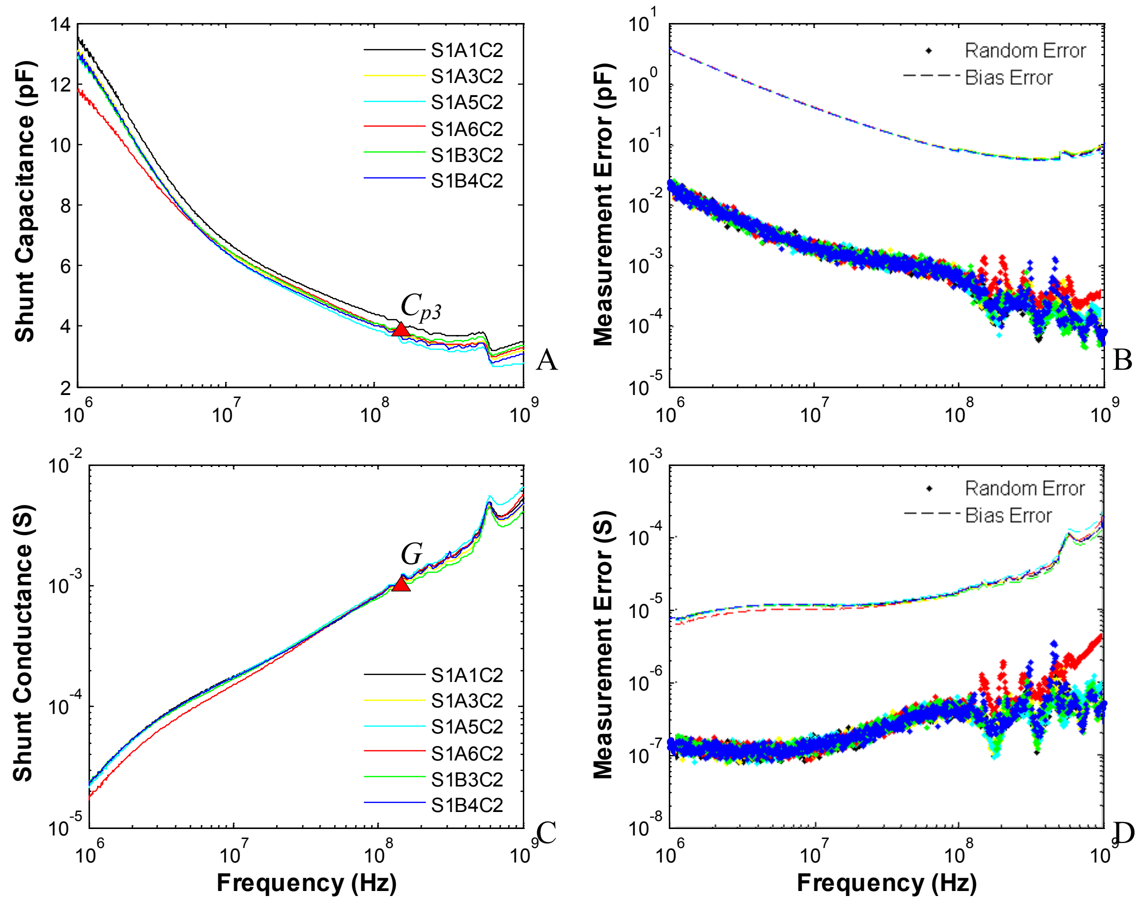

Figure 5-21. Die level high frequency impedance sweeps for six Design 2 sensors. A) Shunt capacitance. B) Random and bias error for the capacitance measurements. C) Shunt conductance. D) Random and bias error for the conductance measurements.

5.3.2 Electrostatic Actuation Test

The primary purpose of this test is to provide a qualitative result to determine the best sensors for testing. Before applying an actuation voltage, the pull-in characteristics have to be determined so that the maximum input voltage does not exceed these limits. The pull-in displacement is given by Equation 4-3, and the pull-in voltage is given by Equation 4-2 in Section 4.1.2. The geometries from Table 5-3 are used, and the results are given in Table 5-8. Forcing voltages of 80% of the pull-in are used to induce a visible displacement.

With the microscope focused on a few sets of fingers, the voltage signal is applied and video is taken of the moving fingers at 25 frames per second. The video file is processed in

www.manaraa.com

MATLAB to identify the fingers, as shown in Figure 5-22, and tracked to find the variations in the gap width. The results of 8 seconds of this test is plotted in Figure 5-23. The displacement is roughly 600 nm from the nominal 3.5 μm gap of the sensor. This result is estimated using a pixel to distance calibration in the code.

Table 5-8. Electrostatic pull-in parameters for the first-generation designs.

Variable	Design 1	Design 2
k [N/m]	30.2	30.2
x_{pi} [μm]	1.16	1.16
V_{pi} [V]	17.2	12.0
V_{max} [V]	14	10

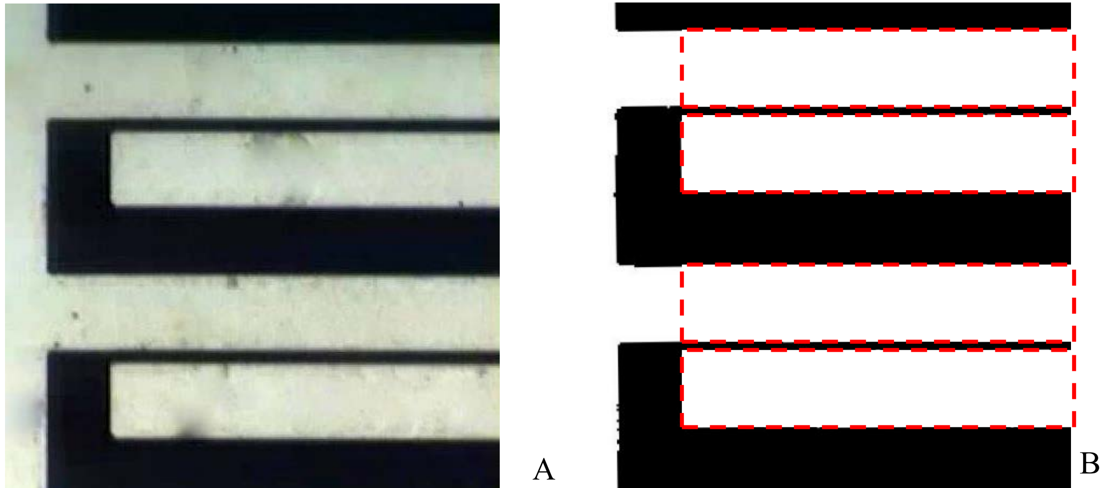

Figure 5-22. Video frame from electrostatic forcing test. A) Raw image showing two sets of fingers. B) Formatted image used to track finger displacements.

5.3.3 Wireless Resonant Frequency, Stability, and Noise Floor

After the capacitive shear stress sensor die has been characterized it is packaged with the coil and antenna to form a wireless shear stress sensor. The first test that is performed on the wireless sensor is to determine the resonant frequencies of the devices. A wideband search sweep is performed with the network analyzer, as described in Section 4.2.1, and the resonant frequency is identified by dips in the reflection coefficient. The results are shown in blue for Design 1 in Figure 5-24A and for Design 2 in Figure 5-24B. The model spectrums from Figure 5-12 are

المنارة للاستشارات
www.manaraa.com

plotted in black. As can be seen in the plots, the model is a very good approximation to the actual device responses.

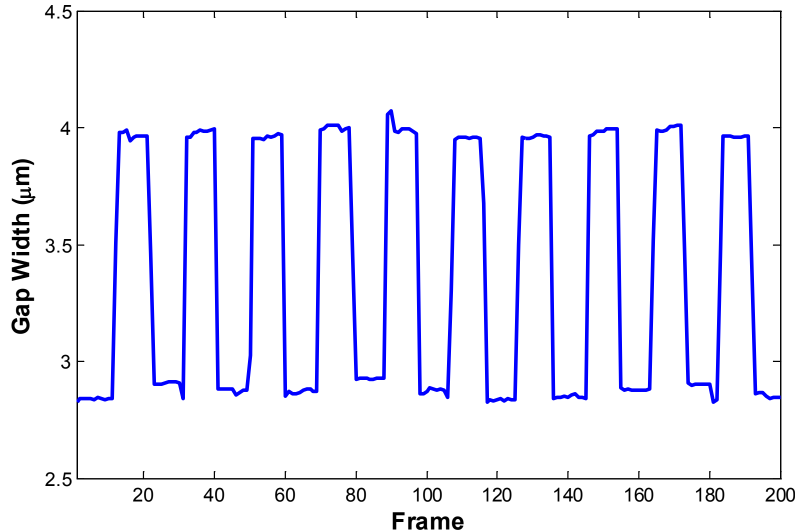

Figure 5-23. Displacement results processed by MATLAB. Plot shows 8 seconds worth of video at 25 frames/s.

A common problem with passive wireless sensors is frequency drift. To quantify this effect, a three-hour drift test is conducted in a Faraday cage to measure the inherent drift of the sensor. The resonant frequency is tracked using a network analyzer as described in Section 4.2.1. The results from these stability tests are plotted in Figure 5-25. The overall drift of the sensors is found to be 0.57 kHz/min for Design 1 and 0.22 kHz/min for Design 2. This corresponds to an equivalent drift in shear stress of 1.2 mPa/min and 0.19 mPa/min, using the sensitivities given in Table 5-7. This means that the drift can rise above the noise floor of the sensors within a matter of minutes. Extended tests will be unreliable unless a new base line frequency is updated periodically, which will add more complexity to the test procedure. A reduction in the frequency drift is one of the goals for future sensor generations.

www.manaraa.com

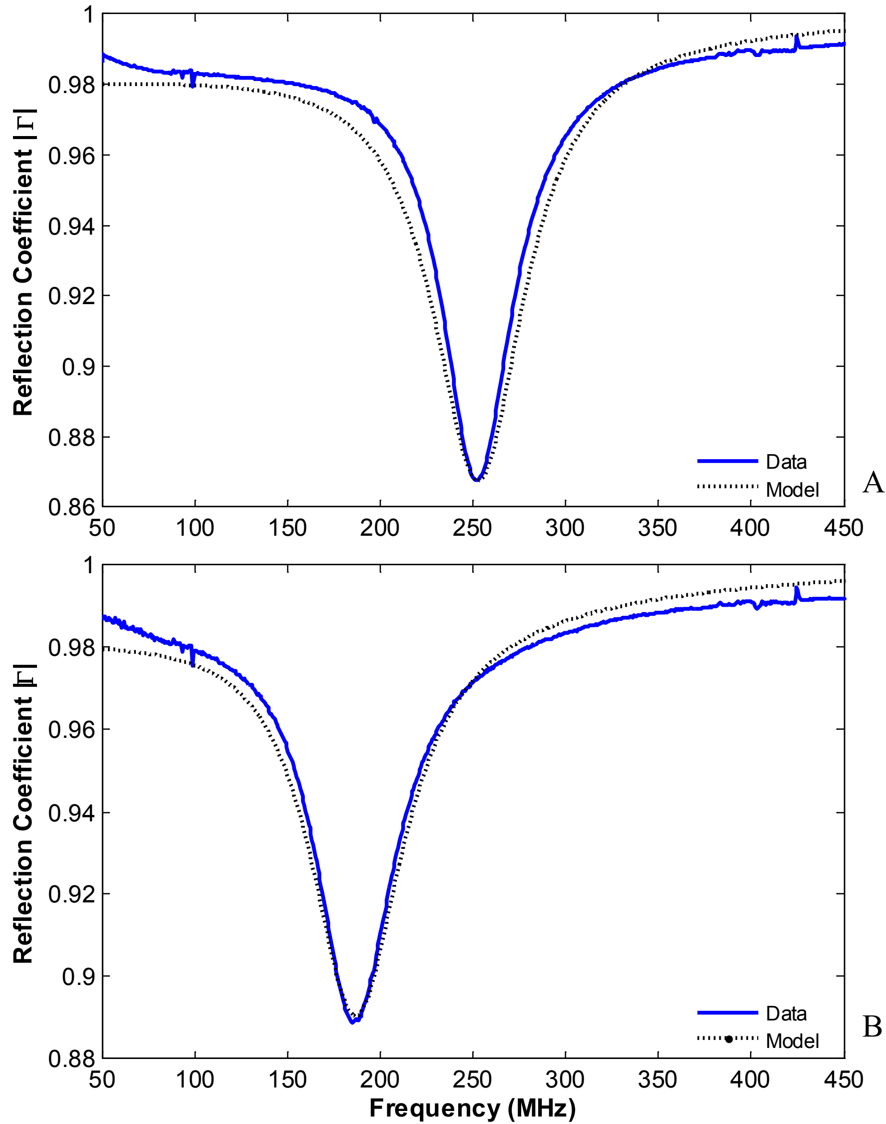

Figure 5-24. Resonant dips showing the accuracy of the model. A) Design 1. B) Design 2.

The noise floor is a vital parameter required to determine the dynamic range of the sensor. The noise floor for the sensor was derived in Section 3.3.3, Equation 3-68. The amplitude noise in the reflection coefficient n_a was extracted from the plot of a resonant dip shown in Figure 5-26. Using this parameter, the resonant frequency, and quality factor of the devices, the "frequency noise level" is around 5 kHz. This value is used to determine the minimum detectable signal given by Equation 3-69 and dynamic range given by Equation 4-10 of the sensors,

المنارة للاستشارات
www.manaraa.com

assuming a maximum input shear τ_{Max} of 2 Pa. The results are given in Table 5-9. These results are based on the predicted sensitivities given in Table 5-7.

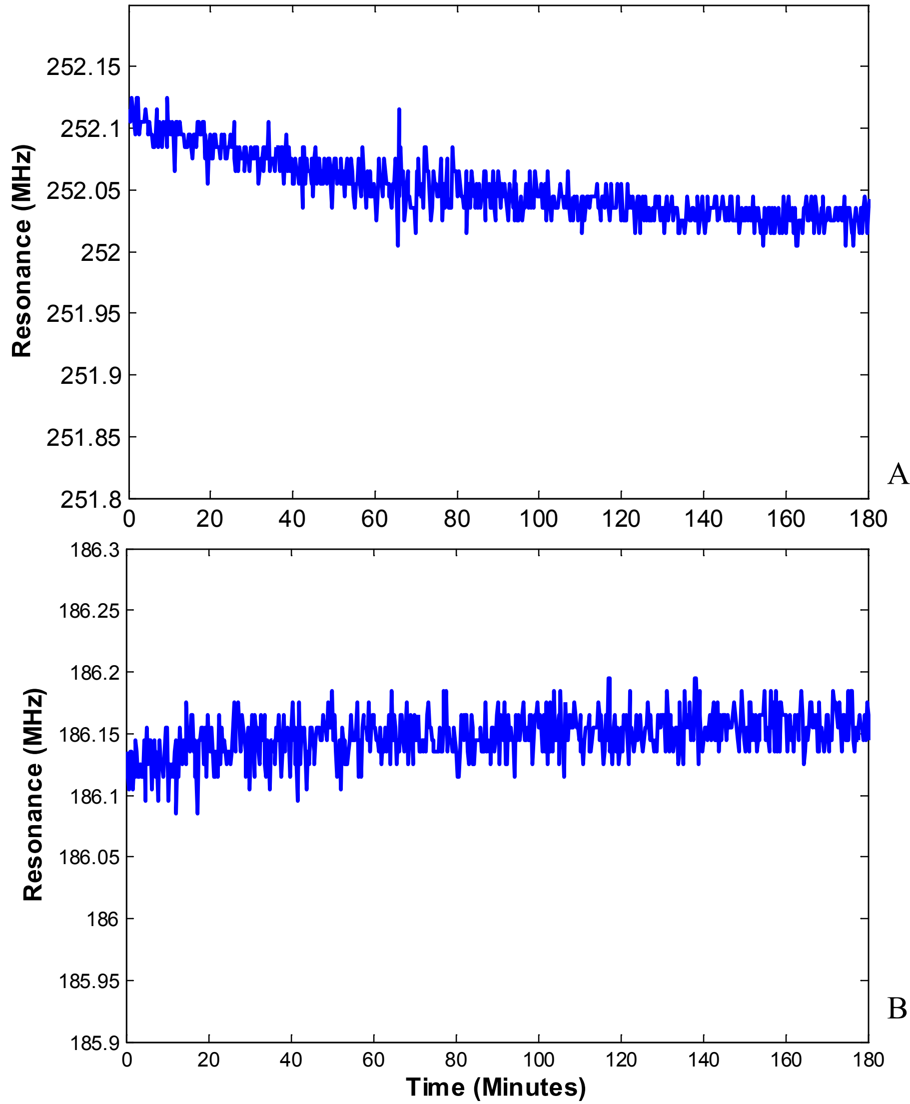

Figure 5-25. Sensor resonance drift. A) Design 1. B) Design 2.

Table 5-9. Results predicted by the model.

Variable	Design 1	Design 2
n_a	0.0002	0.0002
n_f [kHz]	5.97	4.37
MDS [mPa]	12.6	3.74
DNR [dB]	44.0	54.6
Drift [kHz/min]	0.56	0.22

المنارة للاستشارات
www.manaraa.com

5.3.4 Static Shear Flow Calibrations

Using the setup described in Section 4.2.4, a shear stress calibration is performed on Design 1 by monitoring the resonant frequency of the sensors while incrementing the input shear from 0 to 1.6 Pa. The results of this test are shown in Figure 5-27, indicating a linear (R^2 = 0.994) sensitivity of 219 kHz/Pa. This corresponds to a normalized sensitivity of 865 ppm/Pa.

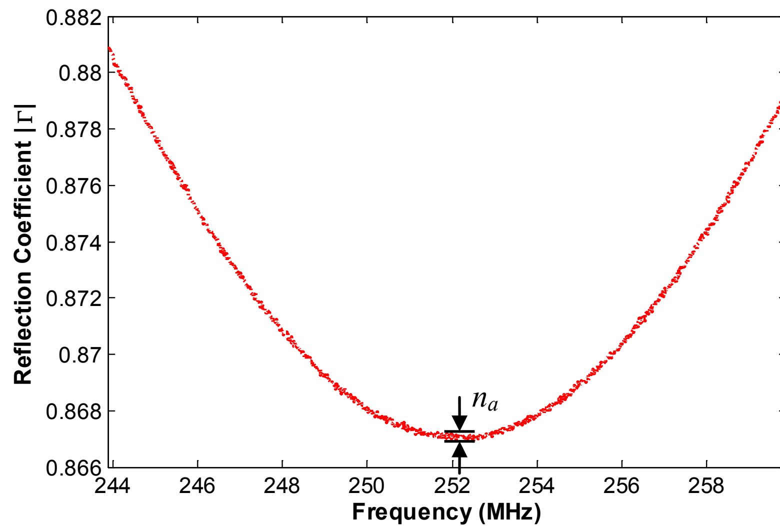

Figure 5-26. Noise plot.

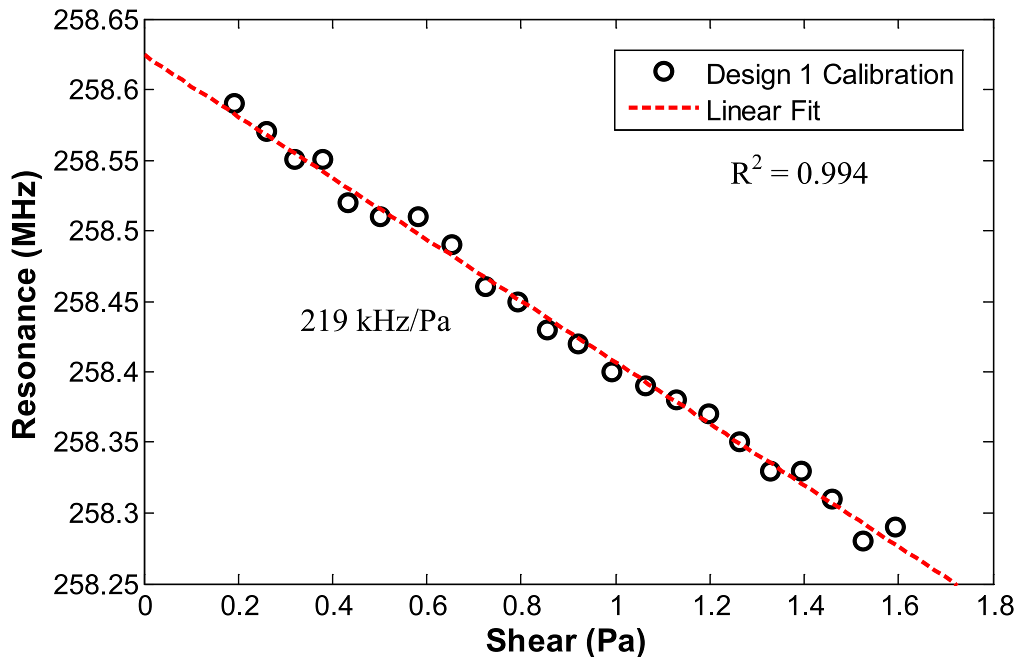

Figure 5-27. Linear static calibration for sensor Design 1.

www.manaraa.com

Design 2 is also tested using the same flow cell. The measurement range is increased slightly for an input shear from 0 to 2.25 Pa. The results of this test are shown in Figure 5-28, indicating a linear (R^2 = 0.996) sensitivity of 894 kHz/Pa. This corresponds to a normalized sensitivity of 4,781 ppm/Pa, which is better than Design 1, as predicted. The trade off is spatial resolution. Design 2 has a 2 x 2 mm^2 floating element, which is four times the area of the 1 x 1 mm^2 floating element on Design 1. A large sensitivity is very important for shear stress measurement in air, where the shear forces are extremely small. To check the repeatability of the measurement, the test is repeated three times. Figure 5-29 shows that the results are repeatable.

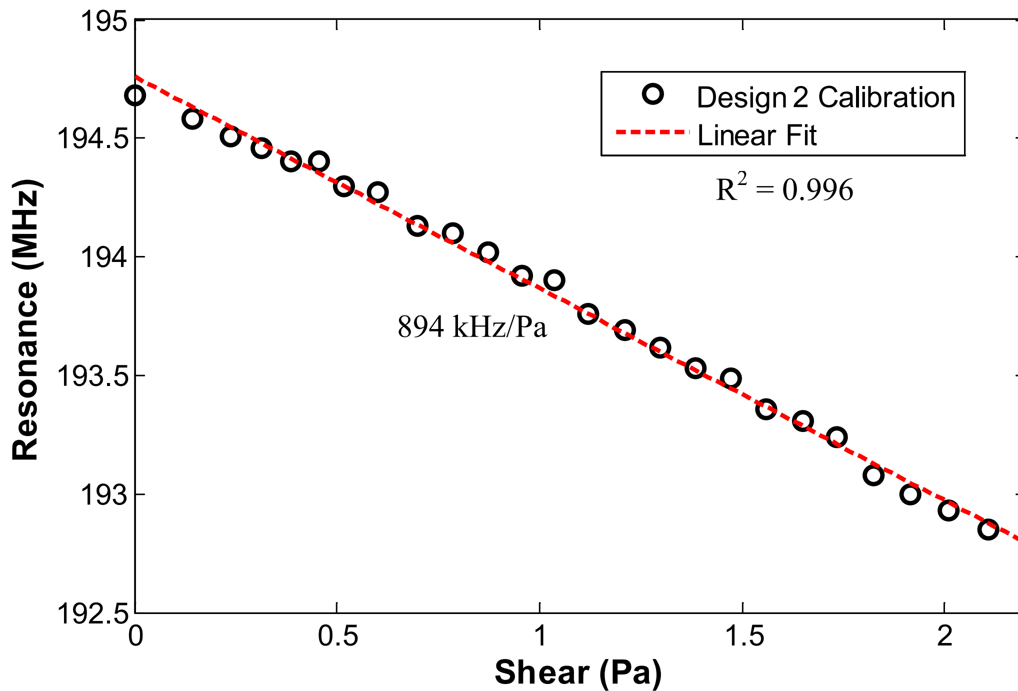

Figure 5-28. Static shear stress calibration for Design 2.

The final experimental results for sensitivity, *MDS*, and *DNR* are reported in Table 5-10. The sensitivity values do not quite match the predicted values. This could be due to a wide array of sources, but the most likely reason is reduced deflections due to higher stiffness than expected or nonlinear Duffing spring deflections. Overall, the devices performed extremely well, given the low quality factors and testing non-idealities.

المنارة للاستشارات
www.manaraa.com

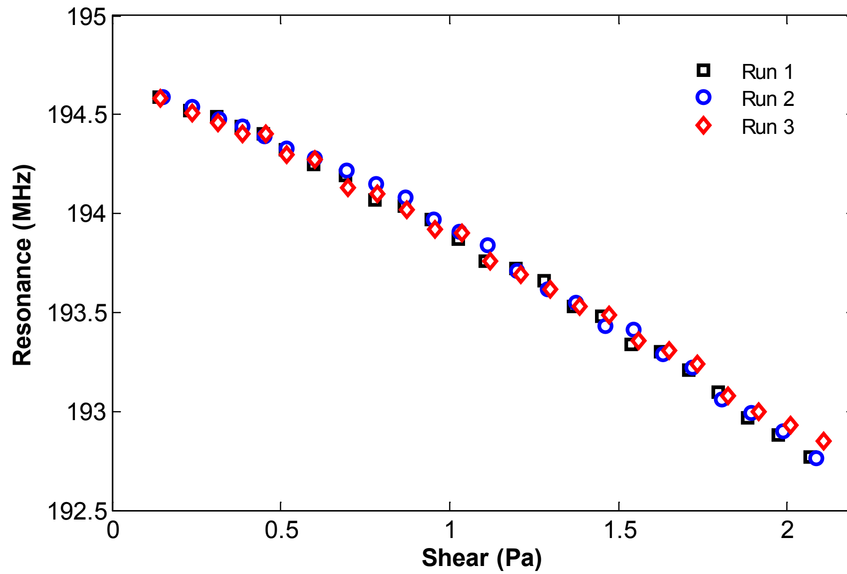

Figure 5-29. Repeatability shear stress calibrations for Design 2.

Table 5-10. Final experimental sensitivity, minimum detectable signal and dynamic range.

Variable	Design 1		Design 2	
	Predicted	Realized	Predicted	Realized
$S_{\tau f}$ [kHz/Pa]	475	218	1167	894
S_n [ppm/Pa]	1885	865	6241	4781
S_F [1/N]	1885	865	1560	1195
MDS [mPa]	12.6	27.4	3.74	4.89
DNR [dB]	44.0	37.3	54.6	52.2

5.3.5 Wireless Range Test for Design 1

Another metric of interest for a wireless sensor is the effective range of the device. The maximum wireless range has serious implications for the successful implementation of the device in any useful application. To test the range of the sensor, the gap between the coil and the antenna for Design 1 is incremented from the minimum of 3 mm (limited by PCB thickness) to 11 mm, where the signal disappears into the noise as seen in Figure 5-30. The maximum power of the 8719D, which is limited to 5 dBm (3.4 mW,125mV), is used for all measurements.

المنارة للاستشارات
www.manaraa.com

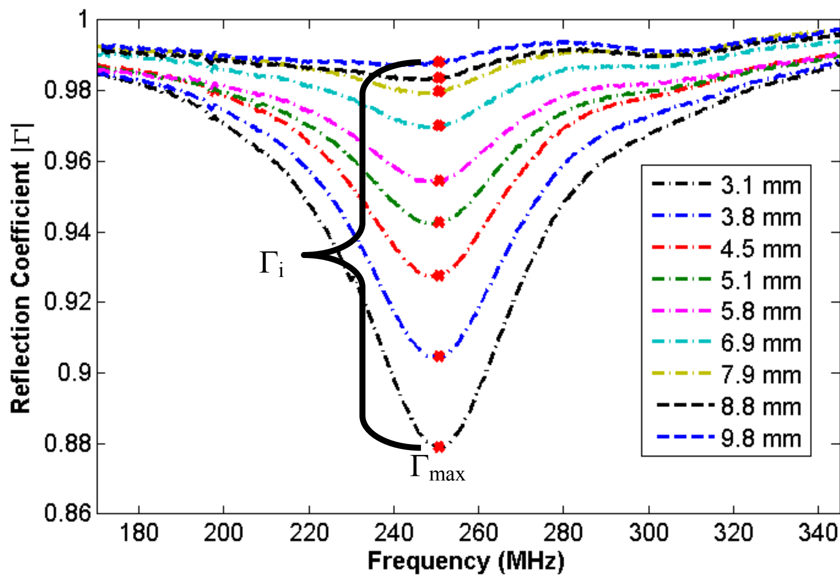

Figure 5-30. Frequency sweeps showing resonant frequency dip height reduction with increasing coil antenna separation.

At each gap, a resonant peak magnitude is measured. The peak height is normalized by the maximum peak height found with the minimum gap of 3 mm. This normalized peak height is plotted versus the gap in Figure 5-31. The signal strength decays exponentially with distance, as expected for electromagnetic coupling of the sensor to the antenna. Even with proper network analyzer correction performed before each measurement, the reflection coefficient spectrum is not perfectly flat when the wireless sensor is absent. The resonant frequency estimation becomes unreliable when the resonant peak is reduced to the same order of magnitude as the amplitude variations at around 9 mm separation. This value is defined as the noise floor for the signal strength in the range test and is indicated by the blue line in Figure 5-31. The effective range for this configuration with this specific network analyzer is around 9 mm, which should be adequate for many test applications if the airfoil skin or pipe wall is the limiting factor for sensor to antenna separation. This range requires that any material separating the antenna from the sensor is of a dielectric nature.

المنارة للاستشارات
www.manaraa.com

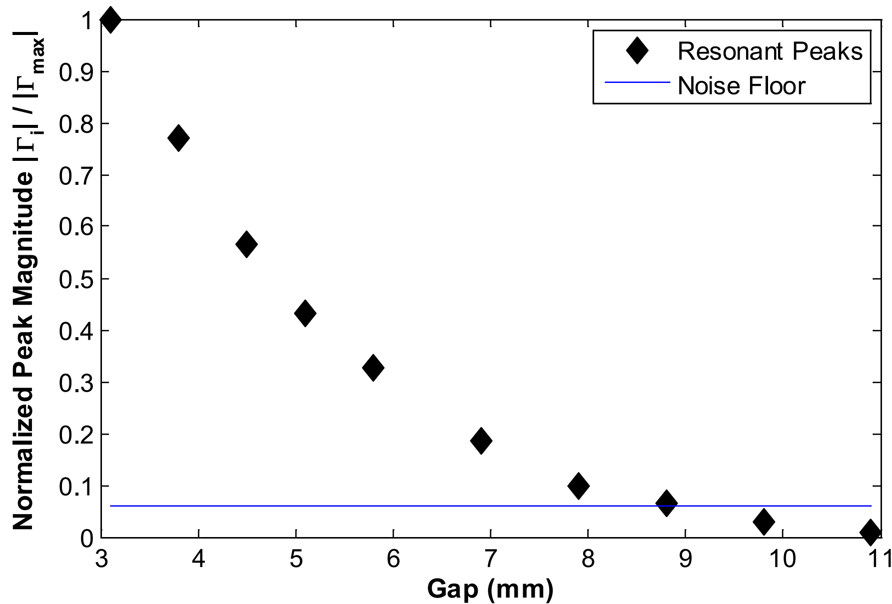

Figure 5-31. Range test results showing the maximum separation within which resonance can be determined.

5.3.6 Wireless Humidity Test for Design 1

During initial tests, a large, unexpected frequency drift was observed during the static shear stress calibrations. The source of this drift was eventually attributed to humidity differences between the ambient air and the compressed dry air being used in the flow cell. The sensors respond to this change in humidity as described in Section 4.2.3 and the change in frequency from the humidity cannot be separated from the change in frequency from the input shear stress. Running a low flow in the flow cell to "dry out" the sensor prior to the shear calibration tests eliminates this effect.

For completeness, the humidity sensitivity is further investigated. A humidity test described in Section 4.2.3 is performed on Design 1. As shown in Figure 5-32, the resonant frequency rise is correlated with the humidity drop measure with a humidity sensor. The response of both signals is exponential, with a time constant of around 20 minutes. The

المنارة للاستشارات
www.manaraa.com

frequency drop is ~20 kHz/% RH, which corresponds to 0.3 fF/% RH. Mitigation of this humidity effect is explored in Chapter 6 with the presentation of a second-generation design.

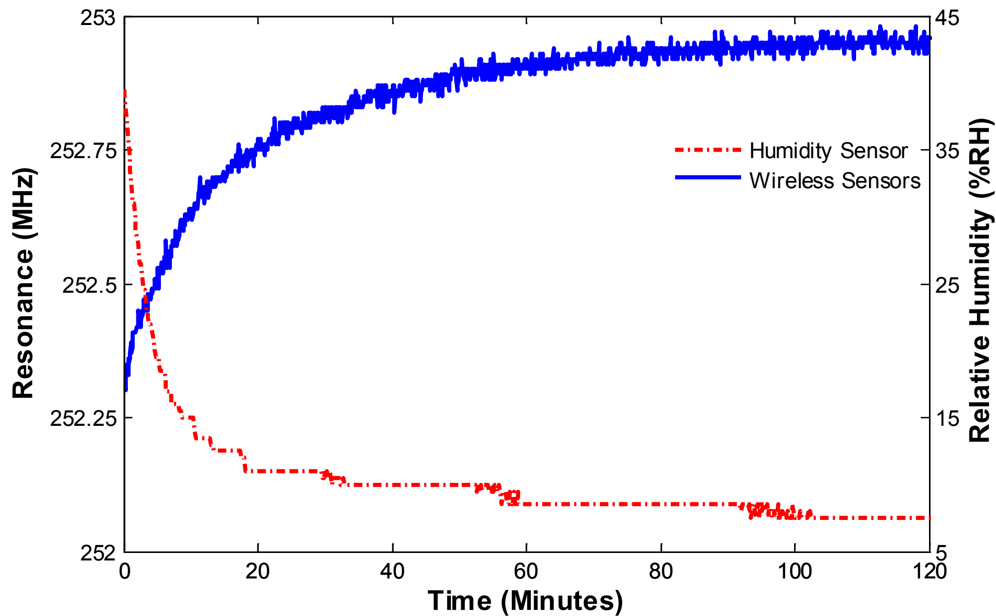

Figure 5-32. Wireless sensor response to humidity.

5.3.7 NASA 20 x 28 Wind Tunnel Test of Design 2

The final sensor characterization for the first-generation sensor involves measurements in a wind tunnel facility. Before the sensor is tested in the wind tunnel, the flow conditions of the tunnel must be well characterized. A flat plate turbulent boundary layer is chosen for the first "real world" test of the wireless sensors. The full test process is described in Section 4.2.5. The tunnel flow velocities are chosen to match the maximum input shear stress of the wireless sensor. The input shear stress at each flow velocity is determined by a boundary layer profile prior to testing the wireless sensor. The profiles for all velocities are given in Figure 5-33. The log regions used to extract the friction coefficient, and thus the shear stress, is highlighted in each of the profiles. All of the parameters from the wind tunnel characterization are presented in Table 5-11. The wireless sensor data is shown in Figure 5-34.

المنارة للاستشارات
www.manaraa.com

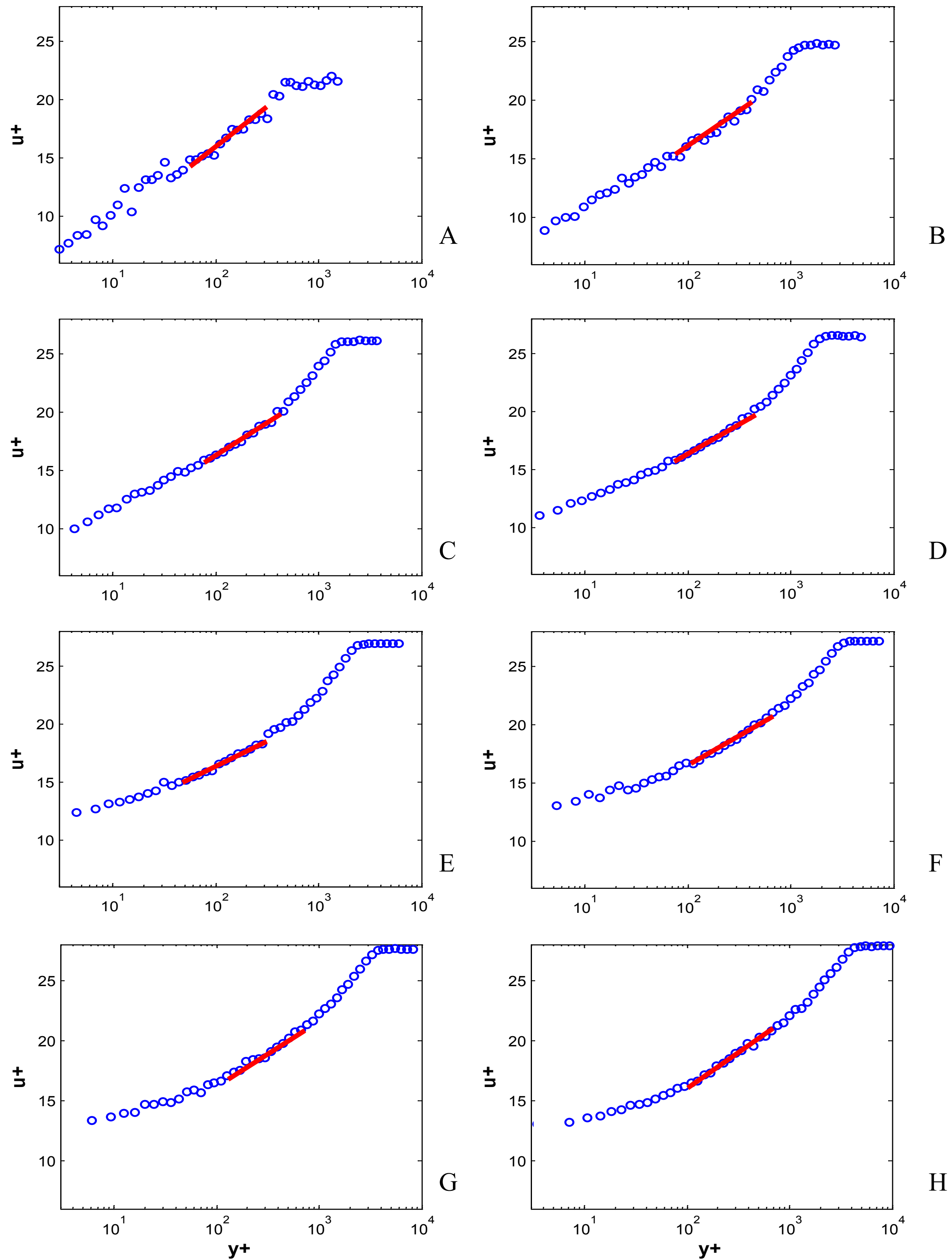

Figure 5-33. Boundary layer profiles for all test cases. A) 5 m/s freestream velocity. B) 10 m/s freestream velocity. C) 15 m/s freestream velocity. D) 20 m/s freestream velocity. E) 25 m/s freestream velocity. F) 30 m/s freestream velocity. G) 35 m/s freestream velocity. H) 40 m/s freestream velocity.

المنارة للاستشارات
www.manaraa.com

Table 5-11. Flat plate turbulent boundary layer test results

Test	U_∞ [m/s]	ρ [kg/m^3]	μ [μPa s]	δ [mm]	u_*[m/s]	C_f	τ_w [Pa]
1	0	-	-	-	-	-	0
2	5.12	1.19	17.97	73.90	0.24	4.30E-3*	0.07
3	10.16	1.19	17.96	58.90	0.41	3.26 E-3*	0.21
4	14.94	1.19	17.98	49.72	0.57	2.93E-3*	0.40
5	19.67	1.19	17.95	47.51	0.74	2.84E-3*	0.68
6	24.88	1.19	17.96	45.03	0.92	2.76E-3*	1.05
7	30.08	1.19	17.96	44.79	1.11	2.71E-3*	1.51
8	34.95	1.17	18.05	44.54	1.27	2.62E-3*	1.97
9	40.54	1.17	18.08	44.31	1.45	2.56E-3*	2.59

* Estimated by the law of the wall

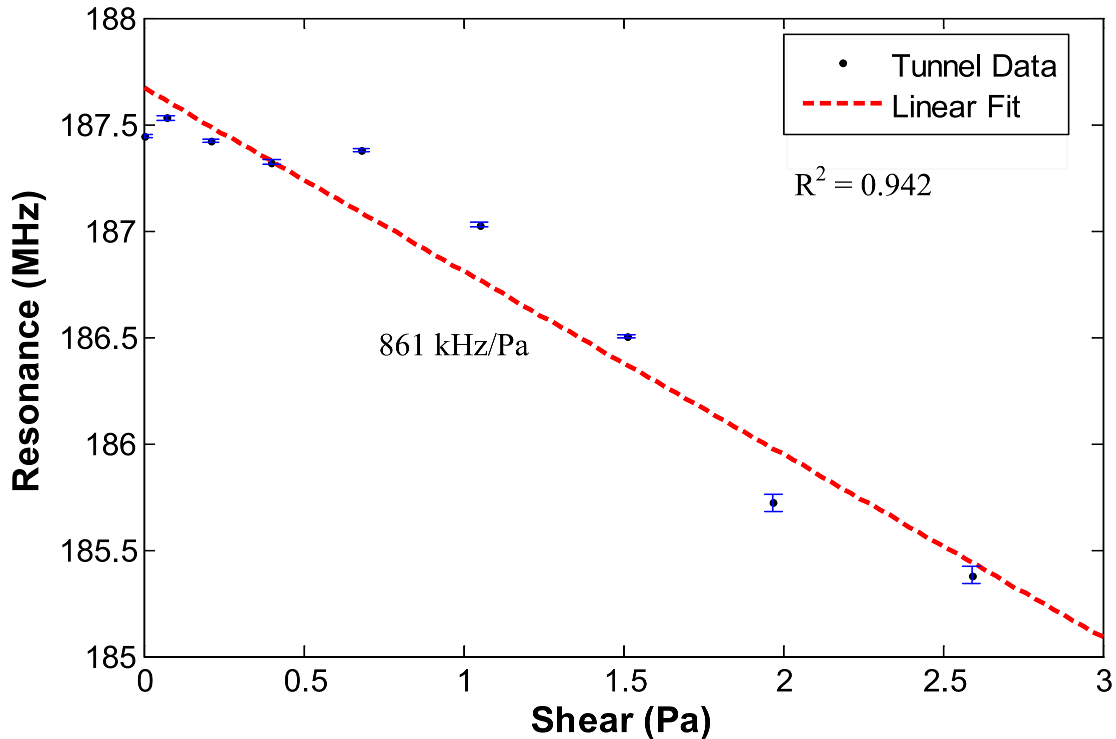

Figure 5-34. Wind tunnel calibration for Design 2.

After the flow is characterized at the preset test conditions, the sensor is inserted into the model for the wireless measurements. To determine the response of the sensor, 20 averages are taken at each test condition. The average resonance frequency of the sensor at each condition is then plotted versus the approximated shear obtained from the flow characterizations in Table 5-

المنارة للاستشارات
www.manaraa.com

11. The results of the test are shown in Figure 5-34, with a maximum shear of 2.5 Pa at 40 m/s. The results show a linear trend (R^2 = 0.942) with a sensitivity of 861 kHz/Pa and a normalized sensitivity of 4,599 ppm/Pa. These results are within 5% of the 894 kHz/Pa and 4,781 ppm/Pa obtained in the flow cell calibrations.

المنارة للاستشارات
www.manaraa.com

CHAPTER 6
SECOND-GENERATION DEVICES

This chapter presents a second-generation capacitive shear stress sensor, shown in Figure 6-1. As described in Chapter 5, some design flaws were identified with the first-generation sensors. With an understanding of the limitations of the first-generation design, a second-generation design was developed. The limitations of the first generation and the proposed design improvements are first discussed. Next, an overview of the complete wireless sensor, incorporating a re-designed capacitive shear stress sensor, is given. This overview repeats the modeling for the new sensor, and provides new performance predictions. The fabrication and packaging is also presented, focusing on the new fabrication techniques used to realize the second-generation capacitive shear stress sensors. Details and results from die-level and device-level characterizations are presented at the end of the chapter.

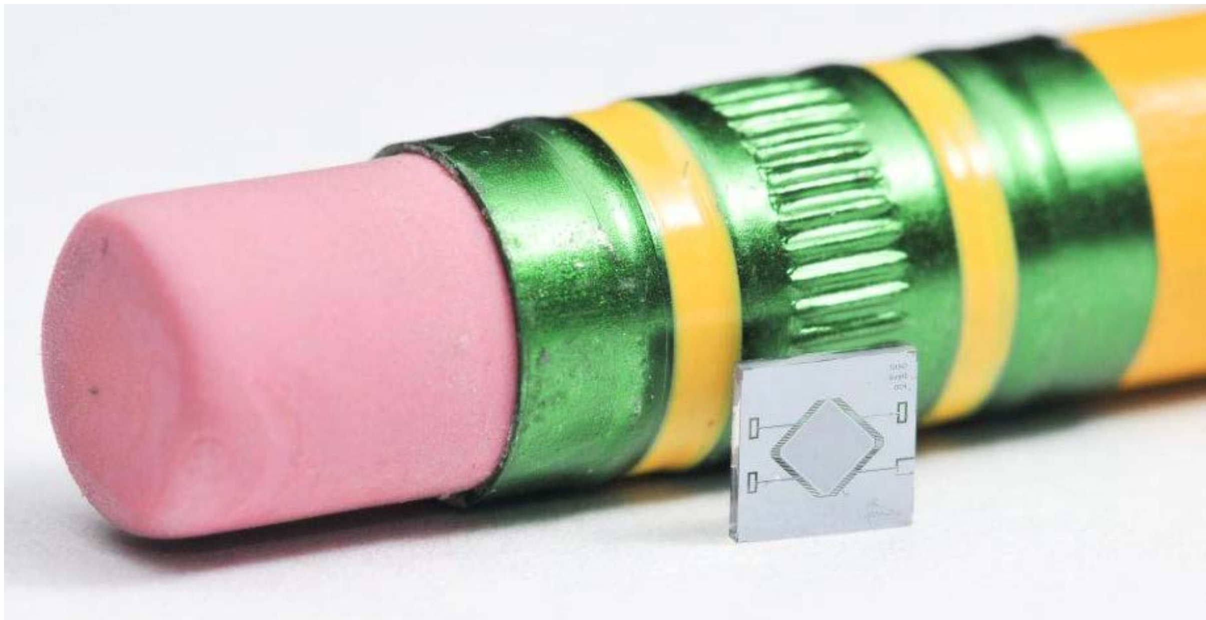

Figure 6-1. Optical image showing the second-generation capacitive shear stress sensor next to a pencil for scale.

المنارة للاستشارات
www.manaraa.com

6.1 Design Improvements

The first-generation capacitive shear stress sensors represent a significant leap forward in passive wireless sensing, but there are several problems and inefficiencies in the design for practical applications. The first-generation sensor has very high parasitic capacitance and conductance, which limits the Q. There is a significant humidity sensitivity that gives false shear stress readings and causes frequency drift. The sensor structure—originally designed as a wired device—is implemented in a differential configuration with two complementary variable capacitors. The passive wireless implementation only uses one side of this pair, so the other side is wasted. To address these limitations, improvements are made in the material selection and sensor geometry. These design changes are implemented into a new fabrication run for realization of second-generation sensors.

6.1.1 Sensor Structure

The physical layout of the floating element, tethers, and comb fingers is an important consideration that affects the performance of the capacitive shear stress sensor. In the first-generation die shown in Figure 6-2A, only one side of the floating element has fingers that are used in transduction (the sections colored red and blue). The other side is used for the differential wired shear stress sensor [21]. The second-generation design, shown in Figure 6-2B, makes use of a diamond-shaped floating element that enables all four sides of the floating element to have comb fingers. A 1.5 x 1.5 mm^2 floating element is rotated 45 degrees, and 1 mm tethers are attached at the mid points, allowing a more compact design. The sensor fits on a 3.5 mm x 3.5 mm die.

Another important geometrical difference is the back cavity of the floating element. In the first-generation sensor, shown in Figure 6-3A, the back cavity depth is the total thickness of the bulk wafer. The bulk silicon is etched from the back side to fully release the floating element.

المنارة للاستشارات
www.manaraa.com

The large cavity (0.5 mm in height) provides very little resistance to pressure-driven flow underneath the floating element. The flow cell test setup described in Section 4.2.4 has a channel height of 0.5 to 1 mm, which is on the order of backside cavity height. In contrast, the second-generation cavity, shown in Figure 6-3B, can be set to a specific depth and thus becomes a design parameter that can be optimized. The cavity height is set to 6 μm in this design and presents a very large resistance compared to any feasible test channel height. This design rejects pressure-driven flow under the element and improves confidence in the calibration procedures and the overall accuracy of the sensor.

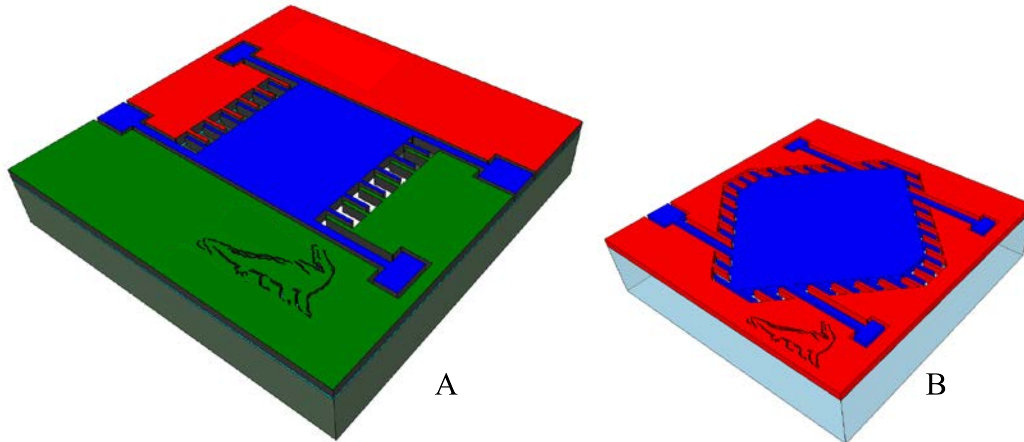

Figure 6-2. Representations of the sensor structures shown out-of-scale. A) First-generation design. B) Second-generation design.

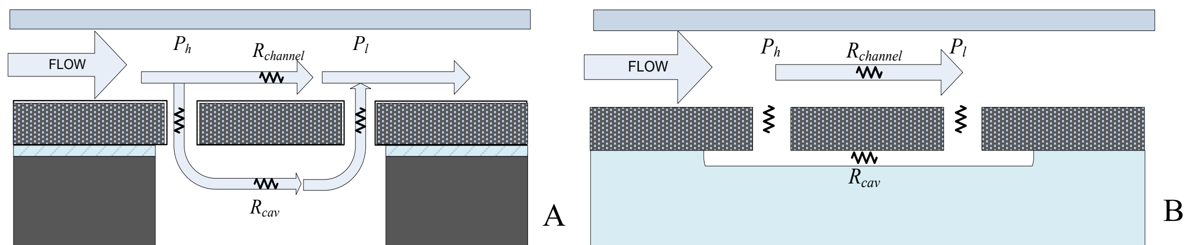

Figure 6-3. Pressure driven flow diagrams. A) First-generation sensor with flow under and over the floating element. B) Second-generation sensor with flow only over the floating element.

المنارة للاستشارات
www.manaraa.com

6.1.2 Parasitics

The materials used for the second-generation sensor are chosen to drastically reduce the parasitics discovered while characterizing the first-generation sensors. The material properties of the bulk silicon in the first generation causes parasitic capacitance orders of magnitude larger that the active variable capacitance. The parasitic conductance from the bulk silicon causes the capacitive sensor to be the *Q*-limiting factor in the resonant circuit. For the second generation, the bulk silicon underneath the floating element is replaced with Pyrex (7740 equivalent). Pyrex is a borosilicate glass that provides excellent dielectric properties in addition to having thermal expansion properties that match Si for fabrication. In using a non-conductive bulk substrate, the floating element layer is the only conductive layer. As shown in Figure 6-4, this eliminates the device-to-bulk parasitic capacitance and conductances. The only remaining parasitics are the capacitances associated with the stationary gaps around the pads (required for electrical isolation) and the fringing fields around the comb fingers.

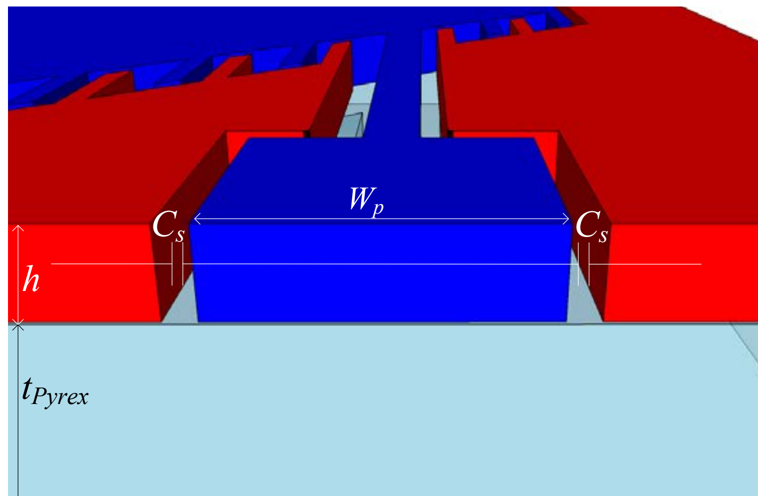

Figure 6-4. Illustration of second-generation sensor bond pad.

6.1.3 Humidity Sensitivity

Another important change in the second-generation design addresses the humidity sensitivity found with the first-generation sensors. In the first-generation process flow, Ni was

المنارة للاستشارات
www.manaraa.com

electroplated onto the comb fingers of the capacitive sensor in an effort to ensure a highly conductive surface and eliminate possible charge accumulation. Tests were completed on the first-generation capacitive sensors with and without the Ni plating, and there was not any noticeable difference in drift. In essence, the Ni did not really seem to have an effect. Rather, the electroplating step added unnecessary complexity to the fabrication process. Moreover, it is believed that the process of applying the Ni coating contributed to the large humidity sensitivity seen in the first-generation sensors.

One of the methods for reducing the humidity sensitivity is the application of a hydrophobic coating to the surfaces of the sensors. The theory is that this coating rejects the condensation of water molecules onto the surfaces of the capacitive plates. Water has a very high dielectric permittivity of around 80, which changes the total effective permittivity in the gap. This causes a shift in resonant frequency without any movement of the fingers. Parylene-C was found to have some humidity sensitivity-reducing effects, but the process was never perfected for the capacitive shear stress sensors. Hydrophobic self-assembled monolayers [93] were also investigated, but the capability to deposit these layers was not easily accessible. Another coating that was researched, but not systematically tested, was the Teflon-like passivation layer used in the BOSCH deep reactive ion etch (DRIE) process for silicon [94,95]. DRIE is already part of the fabrication process, so it is the best candidate with which to start.

In the first-generation process flow, after the DRIE etch and before the Ni plating, the wafers were dipped in a piranha (H_2SO_4:H_2O_2) etch to remove the passivation layer, followed by an HF etch to remove any oxide formed on the surfaces. This process stripped the comb finger sidewalls of the hydrophobic Teflon-like coating and applied a hydrophilic Ni coating to replace

المنارة للاستشارات
www.manaraa.com

it. For the second-generation process flow, the Ni plating step is eliminated, and the DRIE passivation layer is intentionally left on the sidewalls at the end of the process.

6.2 Device Overview

The modeling results of the second-generation wireless sensors are determined using the same procedures as the first-generation in Chapter 5. First, the coil and antenna results are presented, including their associated parasitics. Next, the capacitive sensor results are predicted, followed by the combination of the results into the final complete wireless sensor performance. This section presents all of these results and compares them to the first-generation sensors.

6.2.1 Coil and Antenna Modeling Results

The same coil and antenna designs that were used for the first-generation sensors are used for the second-generation wireless shear stress sensors. This allows for a more accurate comparison of the first- and second-generation capacitive shear stress sensors. Improvements in the overall performance are then directly attributable to improvements in the capacitive sensor. This wireless sensor is referred to as Design 3 in this dissertation. Using FastHenry for electromagnetic simulation, the resulting parameters are given in Table 6-1. A backlit picture of the wireless sensor with the second-generation die is shown in Figure 6-5.

Table 6-1. Parameter values extracted numerically, analytically, and experimentally for the coupled inductor model.

Variable	Design 3
L_c [nH]	335.7[*]
R_c [Ω]	1.77[*]
L_a [nH]	43.2[*]
R_a [Ω]	0.50[*]
M [nH]	28.3[*]
k	0.23
C_c [fF]	198
C_a [pF]	4.9[†]

[†] Obtained experimentally. [*] Obtained though numerical simulations.

المنارة للاستشارات
www.manaraa.com

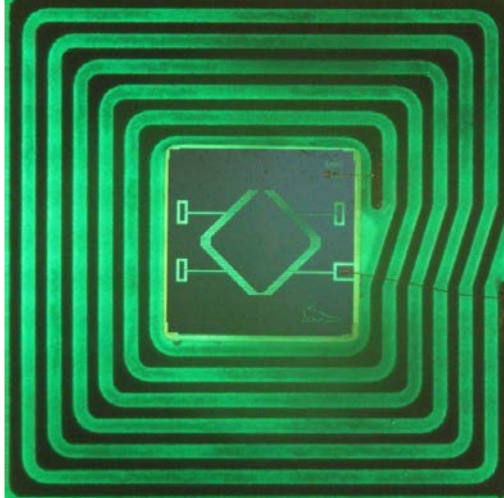

Figure 6-5. Backlit photograph of the second-generation wireless sensor showing a 6-turn coil with a 3.5 mm inner diameter and diamond-design capacitive sensor.

6.2.2 Capacitive Sensor Modeling Results

The capacitive modeling for the second-generation sensor is similar to the modeling for the first-generation sensors. The sensor geometry is shown in an SEM in Figure 6-6. The sensor still consists of a floating element area, tethers, and comb fingers. The tethers and the floating element function and are analyzed in the same way as the first-generation. The fingers still have the same gap widths and overlapping areas. There are, however, a few key design changes for the model. Mechanically, the tethers are made thicker to make the sensor more robust, improve yield, and push the maximum shear stress up to 5 Pa. Electrostatically, the number of fingers changed by a factor of four. The only equations that have to be modified are Equations 3-38 and 3-39, which become

$$C_{o3} = 2\varepsilon_o L_t h\left(\frac{1}{g_{o1}} + \frac{1}{g_{o2}}\right) \tag{6-1}$$

and

$$\Delta C_3(w) = 2\varepsilon_o L_t h\left(\frac{1}{g_{o1} - w} + \frac{1}{g_{o2} + w} - \frac{1}{g_{o1}} - \frac{1}{g_{o2}}\right). \tag{6-2}$$

These equations are different because of the single-sided capacitor configuration, and $C_2 = 0$ since there is no floating element end in the diamond design.

المنارة للاستشارات
www.manaraa.com

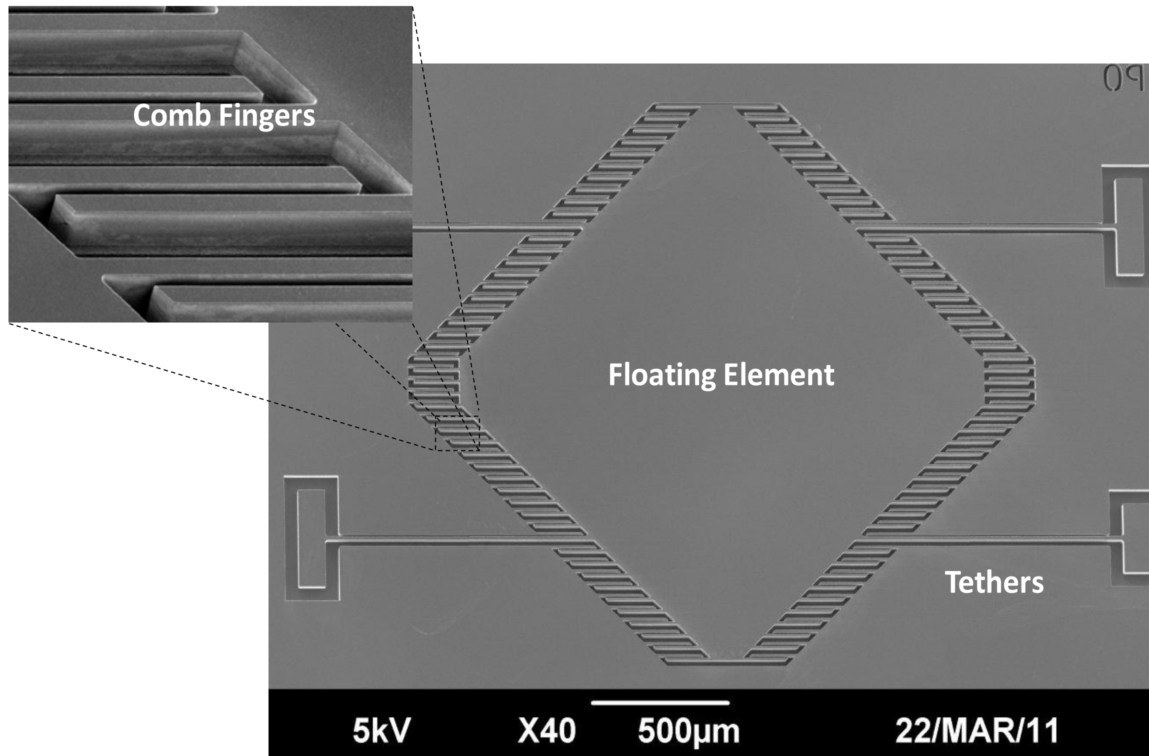

Figure 6-6. SEM image of the second-generation sensor die highlighting the vital components.

Using the geometric parameters given in Table 6-2 and the modeling methods described in Chapter 3 with the modifications mentioned, the predicted results are given in Table 6-3. The second-generation sensor has a 1.5 x 1.5 mm^2 floating element, which is in between the two first-generation floating element areas. A direct comparison of the results without considering the floating element areas does not provide a fair assessment. Instead, a correction factor is applied to each comparison using a ratio of the floating element areas. The static capacitance for the second-generation Design 3 is 180% higher than the first-generation Design 1 and 26% higher than the first-generation Design 2. Normalizing for these areal differences, the full-scale capacitance change ratio for Design 3 is 109% higher than Design 1 and 16% higher than Design 2.

The parasitics of the second-generation device are expected to be greatly reduced. In addition to the elimination of the Si bulk substrate, the pads are smaller. The Design 3 geometry

المنارة للاستشارات
www.manaraa.com

for the pads is given in Table 6-4, and the resulting parasitics are given in Table 6-5. The parasitic capacitance is reduced by an order of magnitude for the low-frequency case and by half for the high-frequency case.

Table 6-2. Geometric parameters for the second-generation capacitive sensor.

Variable	Design 3
W_e [µm]	1500
L_e [µm]	1500
W_t [µm]	15
L_t [µm]	1000
W_f [µm]	10
L_f [µm]	170
x_o [µm]	150
g_{o1} [µm]	3.5
g_{o2} [µm]	20
h [µm]	45
N_f	90

Table 6-3. Analytical modeling results for the second-generation capacitive sensor.

Variable	Design 3
τ_{max} [Pa]	5
$w(\tau_{max})$ [nm]	119
C_{o1} [fF]	1800
C_{o2} [fF]	268
C_{os} [pF]	2.07
$\Delta C_1(\tau_{max})$ [fF]	56
$\Delta C_2(\tau_{max})$ [fF]	8.3
$\Delta C_s(\tau_{max})$ [fF]	64.3
$S_{\tau w}$ [nm/Pa]	25.3
S_{wc} [fF/nm]	0.49
$S_{\tau c}$ [fF/Pa]	12.4

The parasitic conductance of the second-generation Design 3 was expected to be negligible, but experimentally it was found to still have a quantifiable degradation to the sensor's quality factor. Possible sources of this conductance are leakage paths through debris left during

www.manaraa.com

the dicing process or links of conductive sodium from the bonding step. Later experiments show that the parasitic conductance dropped to half the value of Design 1 and 21% of the value of Design 2.

Table 6-4. Geometries of parasitic capacitive structures in the second-generation capacitive sensors.

Variable	Design 3
L_{p1} [μm]	250
L_{p2} [μm]	100
W_{p1} [μm]	150
W_{p2} [μm]	350
g [μm]	50

Table 6-5. Parasitic results for the second-generation capacitive sensor derived using numerical and experimental models.

Variable	Design 3
C_{p1} [fF]	285
C_{p2} [fF]	525*
G [mS]	0.28†

† Obtained experimentally. * Obtained though numerical simulations.

6.2.3 Completed Model Results

With all of the parameters from the coils and capacitive sensor defined, the complete device performance can be predicted. The resonant frequency and quality factor for the second-generation sensor is presented along with the full-scale frequency shift and sensitivities in Table 6-6. Compared to the first-generation design, the higher sensor capacitance results in a lower resonant frequency. The comparison of the predicted and tested frequency response curves are shown in Figure 6-7. The frequency responses of Design 1 and 2 from the first-generation sensors are plotted on the same axes for comparison.

A comparison of the modeling results shows an overall improvement in the wireless sensor performance. First, the Q is doubled to 8.6 by the reduction in conductance. This results in a

المنارة للاستشارات
www.manaraa.com

larger resonant dip, as shown in Figure 6-7. Again, the ratio of the sensors' floating element areas are used as a factor to compare the three designs. The total normalized sensitivity dropped for this generation as a result of the decision to use thicker (15 μm instead of 10 μm), less compliant tethers. The effective compliance, given by Equation 4-1 for the second-generation tethers is 102 which is 3.3 x higher than 30.2 N/m for the first-generation. However, the overall dynamic range is predicted to increase due to the increase in maximum shear and the decrease in minimum detectable shear from the improvement in Q.

Table 6-6. Full wireless system resonance and sensitivity results for the second-generation wireless sensor.

Variable	Design 3
f_o [MHz]	168
Q	8.6
$\Delta f(\tau_{max})$ [MHz]	1.56
S_{cf} [kHz/fF]	25.1
$S_{\tau f}$ [kHz/Pa]	311
S_n [ppm/Pa]	2004
S_F [1/N]	890

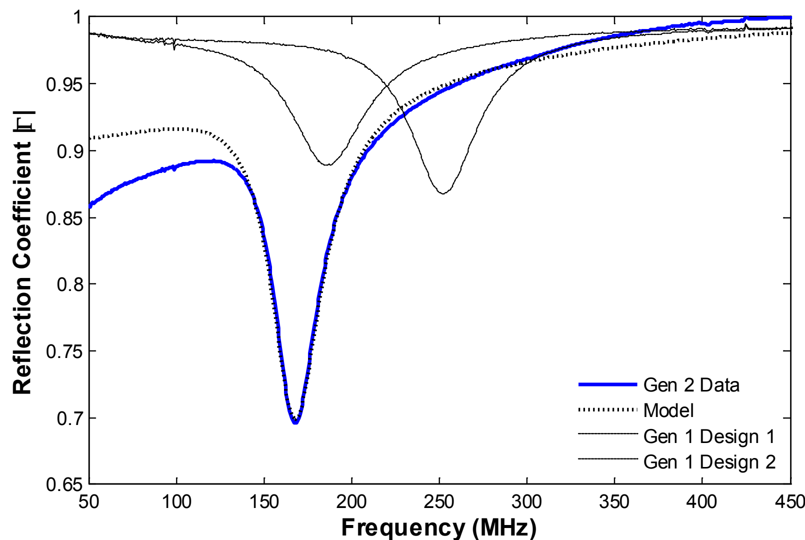

Figure 6-7. Second-generation frequency response showing the accuracy of the model and a comparison to the first generation.

المنارة للاستشارات
www.manaraa.com

6.3 Fabrication And Packaging

The second-generation sensor uses a simple two-mask fabrication process as well. The replacement of the Si bulk layer with Pyrex requires a completely new fabrication process. The process employs anodic wafer bonding to realize a silicon floating-element structure on a thick Pyrex structure for mechanical support.

The fabrication process is illustrated in Figure 6-8. It starts with a 100 mm diameter, double-side-polished Corning 7740 Pyrex wafer. This specific Pyrex is chosen to match the thermal expansion coefficient of Si. This reduces (ideally eliminates) thermal stresses that could destroy the bond during thermal cycles. Another important consideration required for anodic bonding of glass to Si is the sodium content of the glass. Pyrex has a 4% sodium content, which is sufficient for a successful bond. The next four steps create a cavity in the glass while leaving the bonding areas planar and clean. A Cr hard mask, defined using Mask 1 from Figure 6-9A, is used to protect the Pyrex surface during the cavity etch with HF. Without the hard mask, the HF would rapidly etch between the photoresist and the Pyrex, resulting in undercuts that extend for hundreds of microns. The Cr layer acts as an adhesion promoter between the photoresist and the glass surface, limiting the undercut. Undercut on the order of the depth of the cavity still occurs due to the isotropic nature of the HF etchant.

The next steps are for anodic bonding of the Pyrex wafer and a separate SOI wafer. After the photoresist and Cr are removed from the wafer, both the Pyrex wafer and an SOI wafer are cleaned in a 3:1 H_2SO_4:H_2O_2 “piranha etch,” which removes any particulates that could interfere with the bond. This etch also hydrates the surfaces by growing a thin oxide on the Si, which is another important property for the formation of a good bond. The wafers are then aligned and bonded with the device layer of the SOI facing the Pyrex. An EVG 501 Anodic bonder is used with the following process parameters: temperature = 400 ^{o}C, force = 200 N, and voltage = 1 kV.

المنارة للاستشارات
www.manaraa.com

The bond is performed in a nitrogen environment at ~ 0.5 atm. The peak current for the bond is limited to 50 mA.

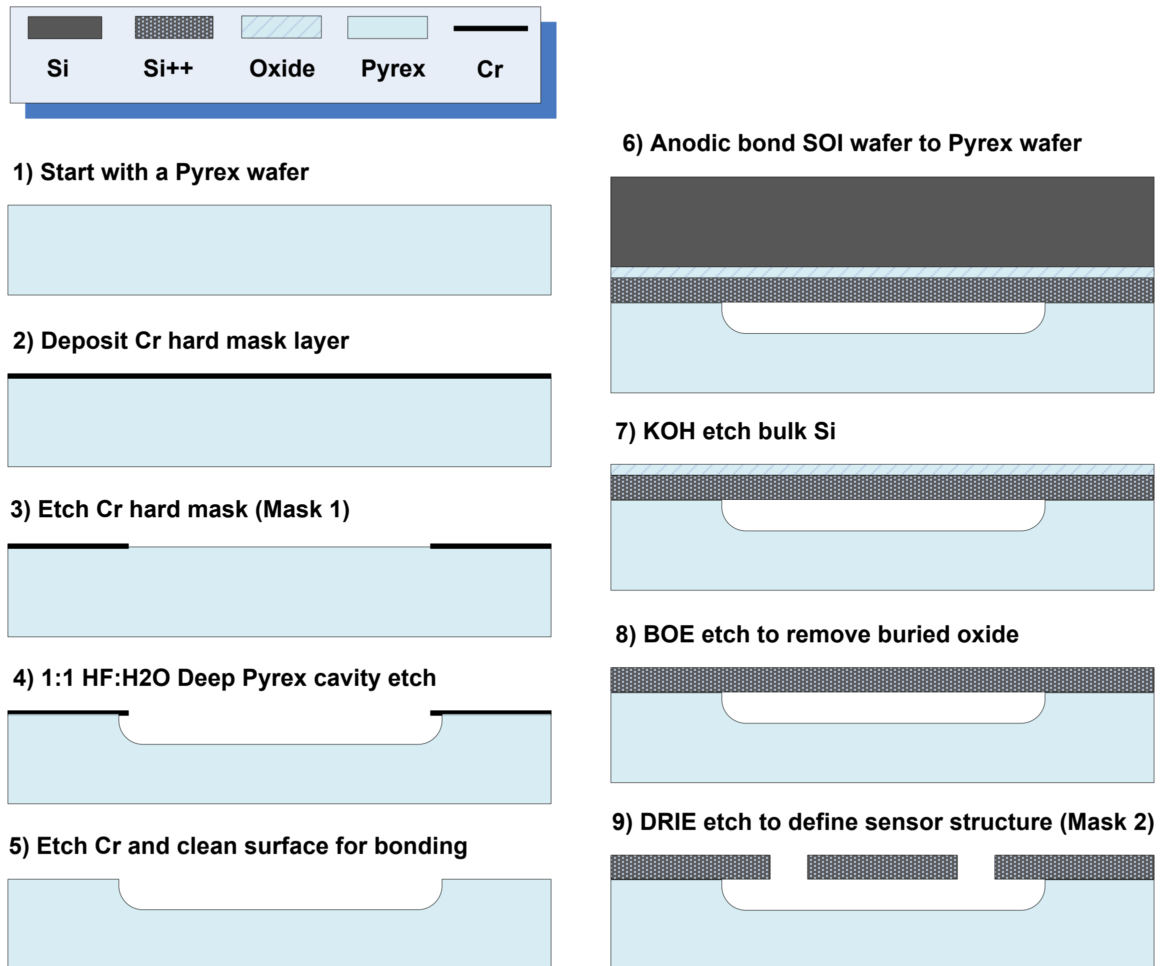

Figure 6-8. Fabrication process flow for second-generation device.

After bonding, the majority of the SOI wafer is removed by KOH etching, leaving just the thin device layer. First, a thin wax is applied to the edge of the wafer stack to protect the device layer from being etched away from the outside in. Then, the wafer stack is inserted into a 20% KOH bath heated to 80°C for 8 hours to etch the bulk Si layer. After the silicon is removed, a buffered oxide etch (BOE) is performed to remove the buried oxide, leaving only the device layer suspended across the Pyrex cavities.

المنارة للاستشارات
www.manaraa.com

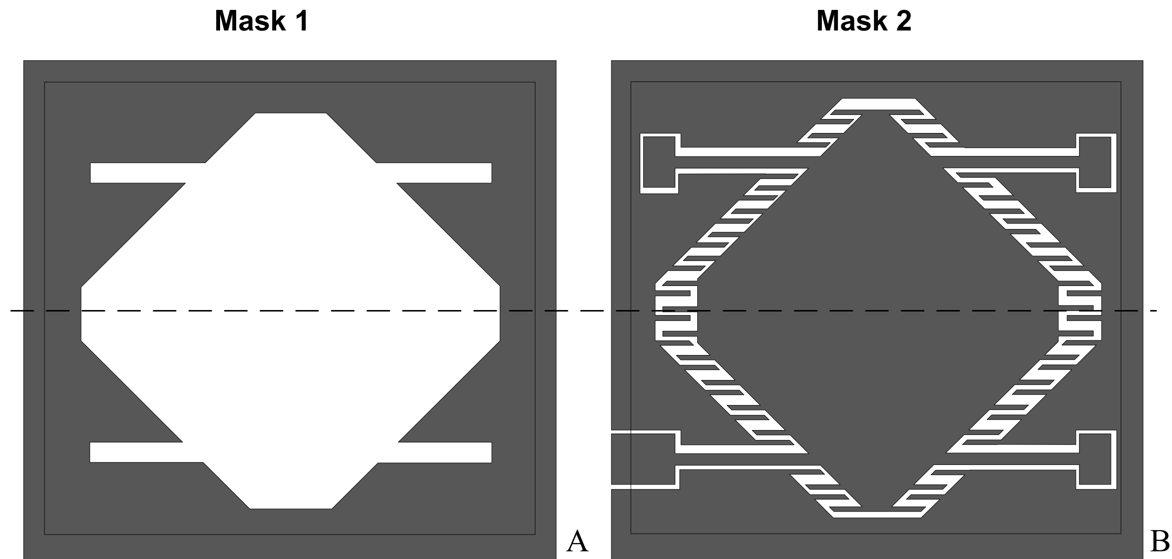

Figure 6-9. Mask set used for photolithography in steps 3 and 9. A) Cavity defining mask. B) Sensor structure mask.

The final step in the process uses Mask 2 from Figure 6-9B to define the sensor structures. Photoresist is first patterned, and DRIE is used to etch the silicon, defining the floating element, comb fingers, and bond pads. An O_2 clean is performed in the DRIE chamber to remove the photoresist, and a clean finished wafer is removed from the machine ready to be diced.

The wafers are diced by first applying a thermal release tape (Nitto Denko Revalpha No.3195M) to cover and protect the sensitive mechanical structures during the dicing procedure. Pyrex has an increased hardness and a reduced thermal conductivity in comparison to Si. As a result, thicker resin-bonded blades have to be used instead of the standard Ni-bonded blades, and much slower cutting speeds are required to prevent the thermal tape from being released. After dicing and sorting, electrical testing is performed and then the hybrid packaging, described in Figure 5-16, is used to complete the second-generation wireless sensor.

6.4 Experimental Results

The experimental test results for the second-generation wireless sensor are presented in this section using the test setups described in Chapter 4. First, impedance characteristics are obtained

المنارة للاستشارات
www.manaraa.com

on the capacitive sensor die prior to packaging. After packaging, the stability, noise floor, and sensitivity are obtained in a series of tests giving the minimum detectable signal (*MDS*) and dynamic range (*DNR*) of the new sensor. In addition to the standard flow calibration tests, two new tests are added. A hysteresis test and a rotation test both provide further confidence in the sensor's operation. Because of time and resource limitations, no wind tunnel tests are performed with the second-generation device. The results for the second-generation Design 3 are compared with Design 1 and Design 2 from the first generation.

6.4.1 Impedance Characterization

Impedance measurements on the second-generation die confirm the elimination of the bulk substrate capacitance. Results of the tests are presented in Figure 6-10. The measurements show that the capacitance is steady and flat at around 2.25 pF, near the theoretically predicted value. This measurement includes the parasitics from the pads and the fringing fields. The shift from large capacitance values at low frequency (due to the bulk capacitance) to low capacitance values at high frequency (due to the sensor's capacitance) is clearly absent. This confirms that the Si bulk layer was the source of this phenomenon in the first-generation devices. The plot shows a stable sensor capacitance with very little parasitics. The bias error for the capacitance shows that the measurement is not useful below 1 kHz, even though the random error is several orders of magnitude lower than the measured values. The conductance still increases with frequency, which in turn reduces the *Q* factor of the wireless sensor. The exact cause for this conductance rise was not explored in detail. Moreover, the error for the conductance measurements is practically the same as the measured values, which hampers any quantitative analysis.

المنارة للاستشارات
www.manaraa.com

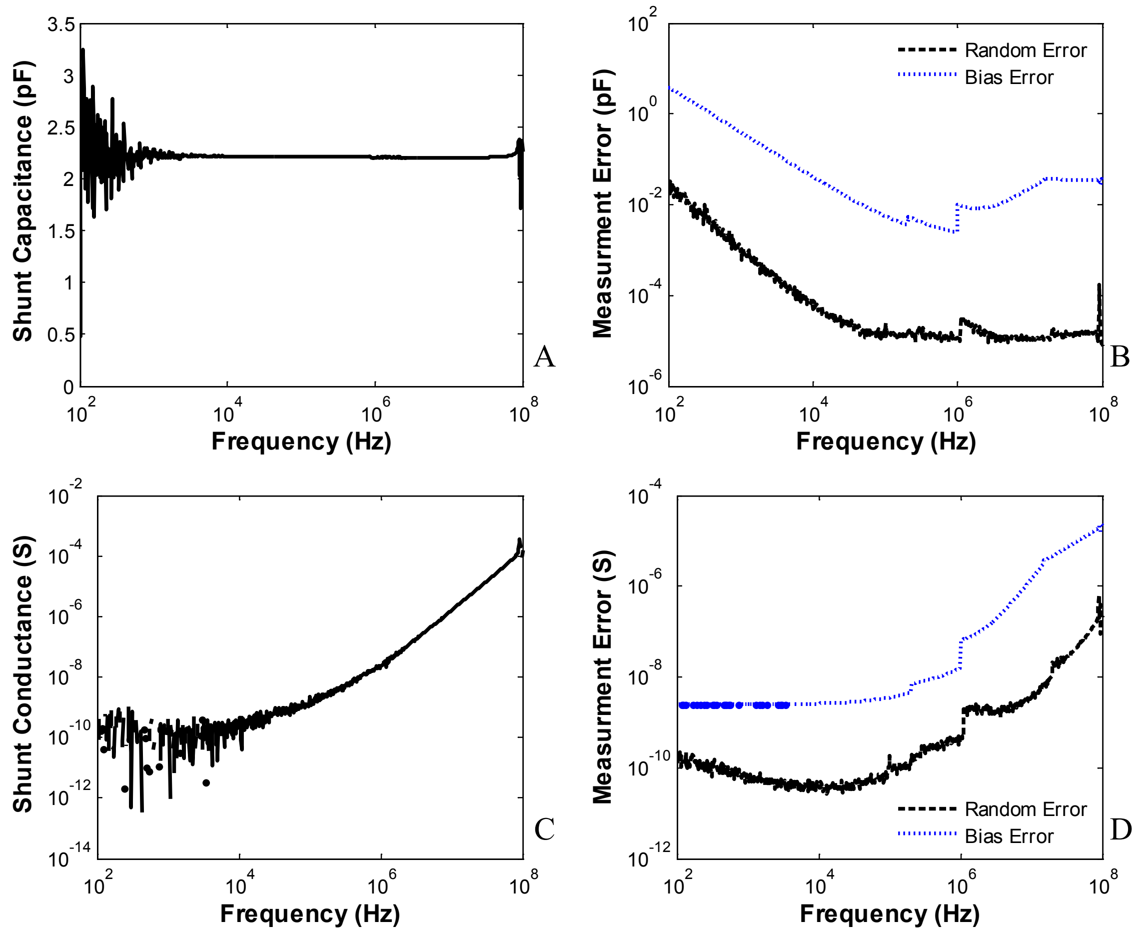

Figure 6-10. Capacitance and conductance impedance sweeps for second-generation sensor. A) Mean shunt capacitance. B) Measurement errors for capacitance. C) Mean shunt conductance. D) Measurement errors for conductance.

6.4.2 Wireless Resonance Stability

After packaging the second-generation capacitive sensor with the coil and antenna, a stability test is performed. Figure 6-11 shows a stable response with resonance around 168 MHz for the entire three-hour-long test. The measured drift for this test is around 60 Hz/min, which corresponds to a 9x improvement over the first-generation Design 1 and a 4x improvement over Design 2. Using the predicted sensitivity, this corresponds to a drift of 190 μPa/min. The amplitude noise is dominated by the network analyzer and remains the same for the second-generation sensor. Using the theoretical values from Table 6-6, the noise floor is

المنارة للاستشارات
www.manaraa.com

calculated to be 1.95 kHz, resulting in an *MDS* of 6.3 mPa. This gives a theoretical dynamic range of 58 dB. These results are tabulated in Table 6-7.

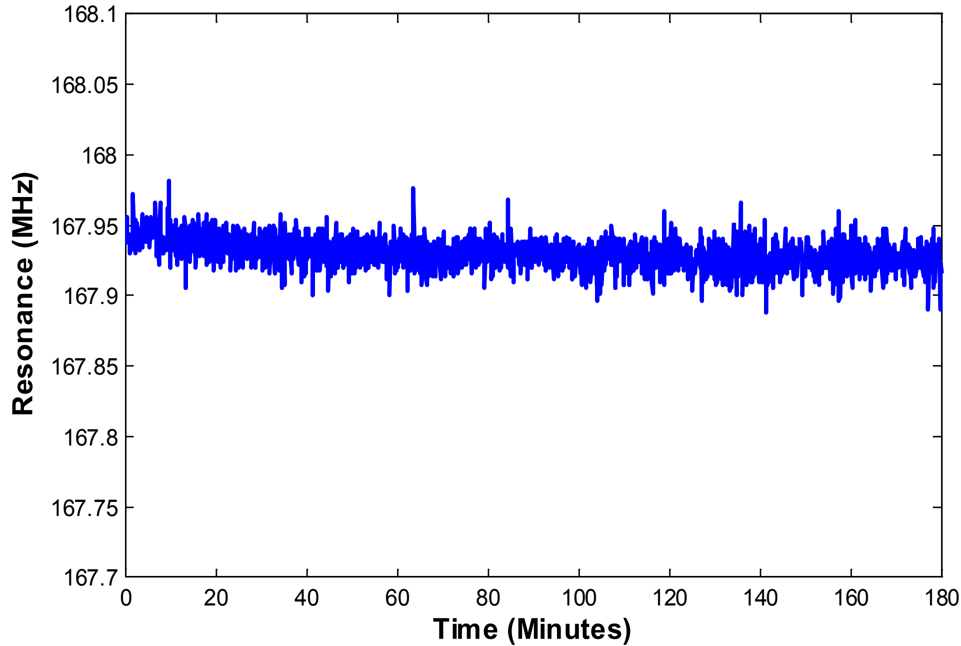

Figure 6-11. Measured second-generation device drift.

Table 6-7. Results predicted by the model for the second-generation device.

Variable	Design 3
n_a	0.0002
n_f [kHz]	1.95
MDS [mPa]	6.3
DNR [dB]	58
Drift [kHz/min]	0.06

6.4.3 Wireless Humidity Tests

A humidity test is also conducted on the second-generation sensors. A surprising result of the new fabrication process is a dramatically reduced humidity sensitivity, as seen in Figure 6-12. From this test, the humidity sensitivity is less than 1 kHz/%RH, which corresponds to 40 aF/% RH (essentially negligible). This test was repeated to confirm the results. Additionally, it was noted that during the flow cell calibrations, there was no long-term transient (dry-out time), as observed in the first-generation sensor calibrations.

المنارة للاستشارات
www.manaraa.com

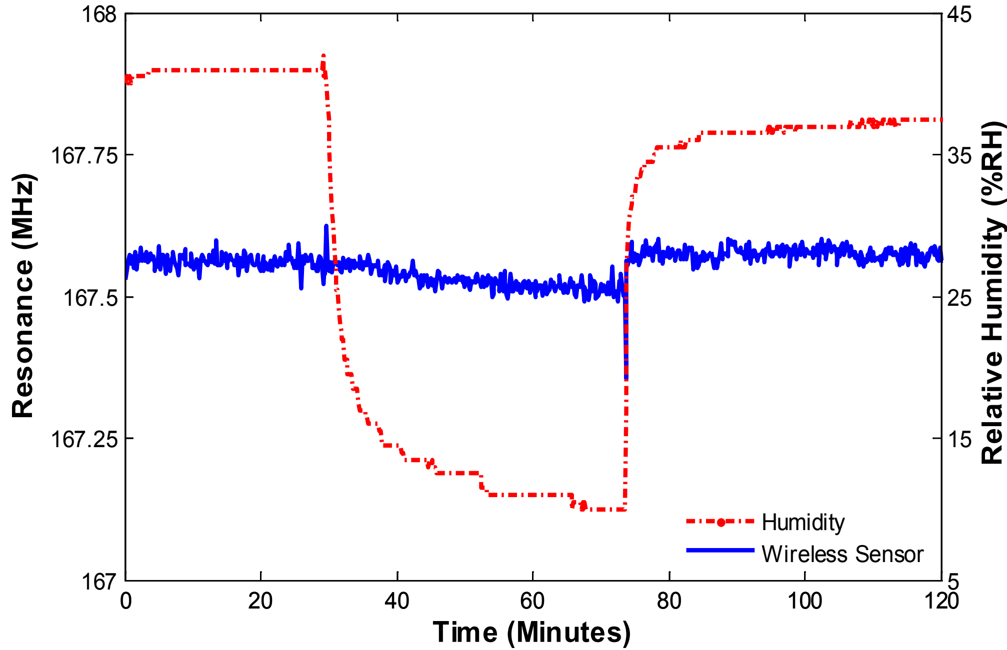

Figure 6-12. Second-generation sensor response to humidity.

A convenient result of the second-generation process flow is that the DRIE is the last step before dicing. This means that the sidewalls of the sensors are left with a Teflon-like polymer passivation layer [95]. This layer has good hydrophobic properties, and from the results of the humidity test, this appears to help mitigate the humidity sensitivity which is now below the noise floor of the wireless sensor.

6.4.4 Static Shear Flow Calibrations

A static shear stress calibration is performed in the flow cell, as described in Section 4.2.4. The maximum shear stress that the second-generation sensor is designed for is 5 Pa. The results of the calibration test are shown in Figure 6-13. Ten sweeps were taken at each flow condition and 20 shear averages were taken for each sweep. The 95% confidence error bars are shown for both the resonance and the shear. The shear stress sensitivity is around 474 kHz/Pa, determined by a linear fit (R^2 = 0.997) to the date shown in red. This is even higher than the predicted 311 kHz/Pa. The normalized sensitivity is 2729 ppm/Pa. Using the experimental sensitivity, the *MDS* and *DNR* are 4.1 mPa and 61.7 dB, respectively. Compared to the larger first-generation Design

المنارة للاستشارات
www.manaraa.com

2 sensor, this second-generation Design 3 sensor achieved a higher dynamic range by 9.5 dB, while increasing the spatial resolution by 43 %. The second-generation Design 3 sensor also beat the smaller first-generation Design 1 sensor by 24.4 dB in dynamic range, but with a decrease in spatial resolution by 44%. A summary of the device performance is given in Table 6-8.

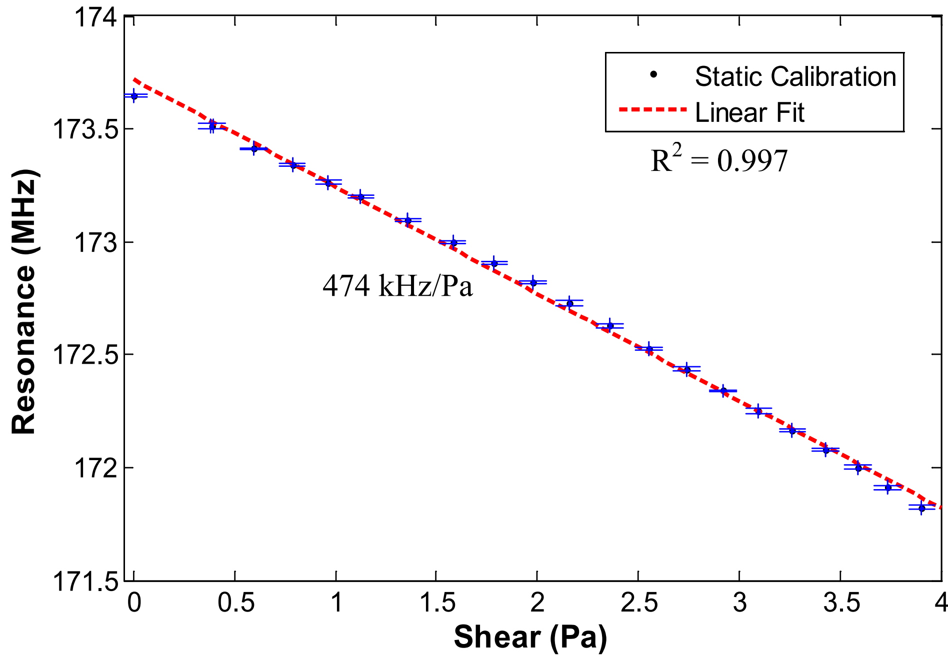

Figure 6-13. Linear static calibration for the second-generation sensor.

Table 6-8. Final experimental sensitivity, minimum detectable signal, and dynamic range for the second-generation sensor.

Variable	Design 3	
	Predicted	Realized
$S_{\tau f}$ [kHz/Pa]	311	474
S_n [ppm/Pa]	2004	2729
S_F [1/N]	890	1213
MDS [mPa]	6.3	4.1
DNR[dB]	58	61.7

Another set of tests are conducted to add to the confidence in the sensors performance and to explore repeatability and hysteresis effects. Using the flow cell, the shear stress (flow) is ramped up and then backed down, and this is repeated a second time. If there are any delays,

المنارة للاستشارات
www.manaraa.com

drift, or other hysteretic phenomenon in the sensor response, they would show up in this test. The test results are shown in Figure 6-14. With the exception of one anomaly in the second flow increase, the sensor shows no hysteresis, and the resonance tracks the shear stress repeatedly.

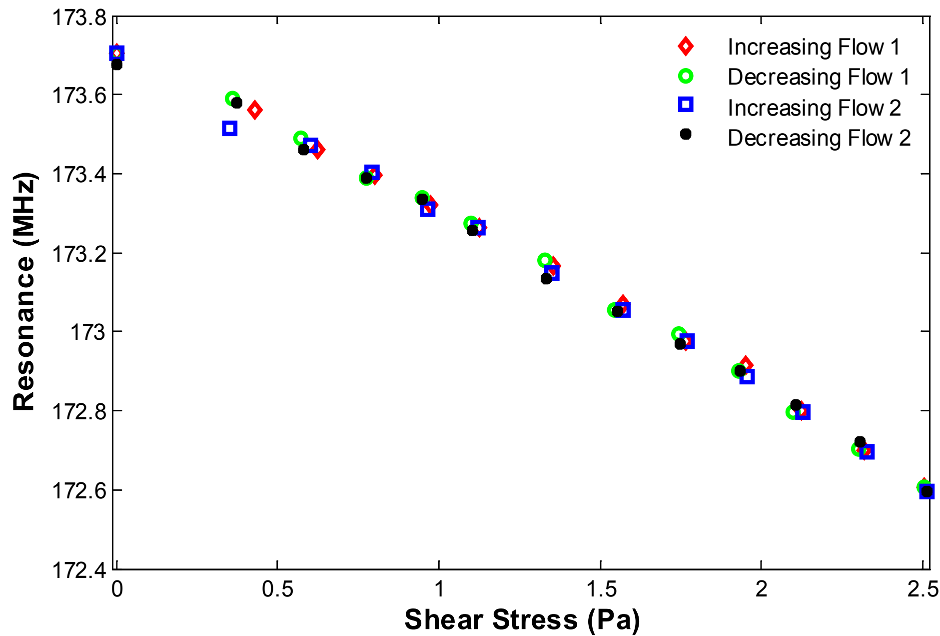

Figure 6-14. Second-generation hysteresis test results showing two full cycles.

The final set of flow tests demonstrates the flow directionality sensitivity of the sensor. Ideally, the sensor should only be sensitive to shear when a component of shear is perpendicular to the tethers. As illustrated in Figure 6-15, at 0° flow causes an increase in the sensor capacitance, which results in a decrease in the resonant frequency. At 90° flow causes no change in the sensor capacitance, which results in no change in the resonant frequency. At 180° flow causes a decrease in the sensor capacitance, which results in an increase in the resonant frequency. To confirm this behavior, the sensor plug in the flow cell was rotated in three positions—0°, 90°, and 180°—to test these cases. The result of the test is plotted in Figure 6-16, which shows good agreement with the predicted response.

www.manaraa.com

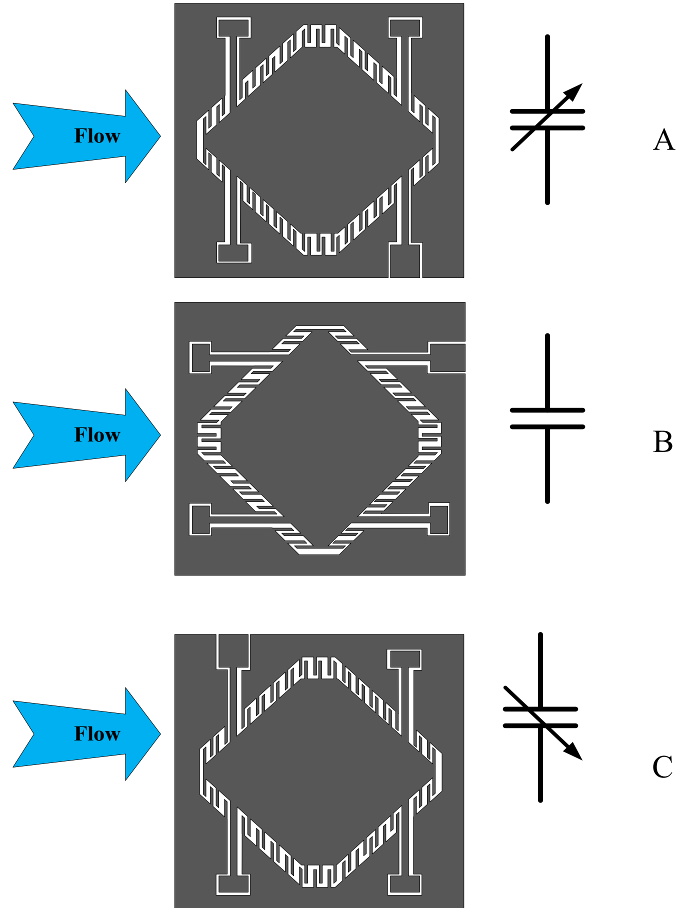

Figure 6-15. Rotation test illustration. A) Sensor at 0° rotation. B) Sensor at 90° rotation. C) Sensor at 180° rotation.

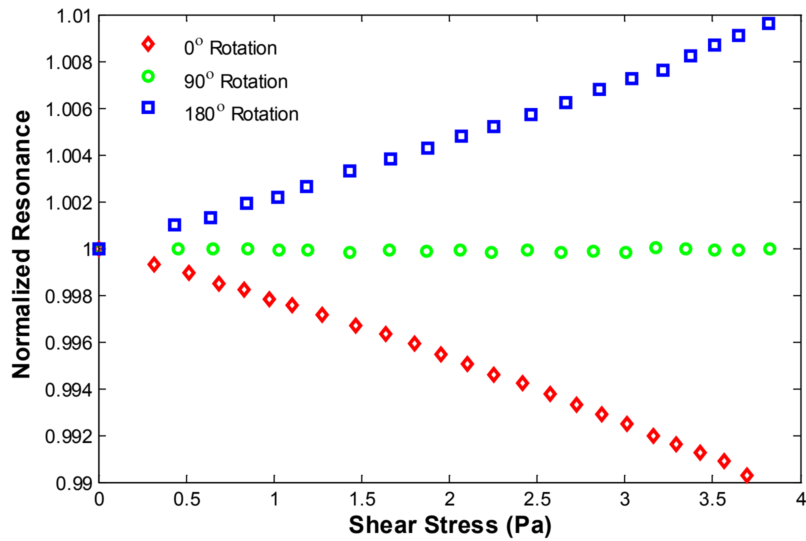

Figure 6-16. Rotation test results showing directional response of the sensor.

www.manaraa.com

CHAPTER 7
CONCLUSIONS AND FUTURE WORK

The final chapter in this dissertation provides a summary of the work and key conclusions. The fundamental research contributions are then listed. The dissertation concludes by describing opportunities for future work.

7.1 Summary

This dissertation presented the first passive wireless shear stress sensor ever developed. The passive wireless interrogation strategy was adapted from work dating back to the 1960s. These earlier sensors were primarily developed to detect static pressures for medical purposes where the normal forces are very large. In contrast, shear stress sensors must be capable of detecting minute *tangential* forces that are orders of magnitude smaller than pressure force. To achieve this level of detection, the sensor requires a much larger sensitivity. Normalized sensitivities of 0.1 to 20 ppm/Pa were demonstrated in the previous works. The normalized sensitivities for the shear stress sensors presented in this dissertation were much greater, between 865 to 4781 ppm/Pa.

A detailed model was presented for the passive wireless sensor. This model included analytical calculations for the floating element mechanics and electrical capacitive transduction of the shear stress sensor. Numerical methods were used to predict the inductances and fringing field parasitic capacitances. The rest of the conductive losses were determined experimentally and can be used as empirical "correction factors" for future designs. A linear sensor response was predicted using these models, and this linear behavior was confirmed in later testing.

Two generations of the sensor were designed, fabricated, packaged, and tested. A hybrid package was used for both generations in which the inductive coil and antenna were milled in a printed circuit board (PCB), and the capacitive shear stress sensor was added to complete the

المنارة للاستشارات
www.manaraa.com

devices. The first-generation sensor used a modified version of a previously developed *wired* shear stress sensor [21]. For the second-generation devices, a completely new fabrication process was developed to improve upon the first-generation designs, with the goal of reducing unwanted parasitic effects and sensitivity to humidity.

Both generations were subjected to a series of tests at both the die level and as finished wireless sensors. Two first-generation designs, with different floating element sizes, and one second-generation design were characterized. The small floating element (Design 1), high spatial resolution, first-generation sensor showed a *MDS* of 27.4 mPa, a dynamic range of 37.3 dB and a maximum coupling distance of 9 mm. The large floating element (Design 2), low spatial resolution, first-generation sensor had a much better *MDS* of 4.89 mPa, a dynamic range of 52.2 dB, and was successfully tested in a flat plate turbulent boundary layer at NASA Langley.

The second-generation sensor had an improved *MDS* of 4.1 mPa, while the maximum input shear stress increased from 2 Pa to 5 Pa and the spatial resolution improved compared to Design 2 of the first-generation sensor. The resulting dynamic range was 61.7 dB. This second-generation sensor is able to test the equivalent of a turbulent flat plate boundary layer with speeds from 1 m/s to 60 m/s, which corresponds to a range from 2 mph to over 130 mph. The second-generation sensor was also shown to have a directional response, enabling a vector flow measurement (direction and magnitude) to be determined with two perpendicular sensors positioned next to each other. Furthermore, in the second generation, the parasitics were dramatically decreased by over an order of magnitude and the humidity sensitivity was reduced to below the noise floor. These improvements make the sensor viable for realistic test environments. All of the performance parameters for the three sensors tested are summarized in Table 7-1, along with two of the best-performing passive wireless *pressure* sensors from the

المنارة للاستشارات
www.manaraa.com

literature for comparison. The normalized force sensitivity defined as the normalized sensitivity divided by the active area in [1\N] shows a three order of magnitude increase over previous work.

Table 7-1. Performance summary and comparison with previous work from the literature.

	Shear Stress Range [Pa]	Dynamic Range [dB]	Normalized Sensitivity [ppm/Pa]	Force Sensitivity [1/N]
First-Generation Design 1	0.013 – 1.60	37.3	865	865.0
First-Generation Design 2	0.004 – 2.25	52.2	4781	1195
Second-Generation Design 3	0.004 – 3.90	61.7	2729	1213
Collins [31]	67.0 – 13,000*	45.7	6.25	0.079
Fonseca et al. [58]	3,800 – 400,000*	40	0.043	0.091
Chen et al. [60]	333 –13,300*	32	1.20	1.085

* Equivalent force in pressure

7.2 Research Contributions

- Developed and demonstrated the first passive wireless shear stress sensor capable of measurement without direct electrical wire connections.
- Developed and validated comprehensive electromagnetic models for passive wireless sensing, which can be extended to other passive wireless sensor systems.
- Demonstrated silicon-on-pyrex microfabrication process that can be adapted to enable other high-performance silicon-MEMS-based passive wireless transducers.
- Identified and reduced parasitic capacitance and humidity sensitivity, which can be extended to other wired or wireless MEMS capacitive sensors.

7.3 Future Work

Suggested future work proposed for the sensor system focuses on two key enhancements. The first is to design and develop a new fabrication process where the inductor coil is monolithically integrated on the MEMS sensor die. The second is development of RF electronics to dynamically track the sensor resonant frequency. The new circuitry will enable the sensor to

المنارة للاستشارات
www.manaraa.com

detect the dynamic variations in shear stress to fully characterize a turbulent boundary layer. Potential designs for the future generation can be optimized using the models developed in this dissertation for the mechanics, electrostatics, and magnetic coupling. The RF electronics design can also be incorporated into the optimization.

7.3.1 Future Generations

The next generation for the sensor is planned with integration of the coil into a single chip device as the primary goal. An optimization routine can be used to decide on the geometry, and the previous fabrication work can be integrated into the process flow. Pyrex wafers with through glass vias (TGVs) may be used to enable the coil to be placed on the backside of the sensors, as shown in Figure 7-1. The TGVs enable connection of the coil to the capacitive sensor structure on the topside. The sensor die can still be 3.5 mm x 3.5 mm and have a spiral inductor electroplated on the backside. The integrated coil diameter would be smaller than the hybrid coils by a factor of approximately three, but the number of turns would be increased by a factor of approximately three. The inductance is proportional to D, but it is also proportional to N^2 so the integrated inductor can actually achieve a greater inductance L than the hybrid designs in the first two generations. Adding a second layer to the coil would bring the connection point back to the perimeter of the die and would double the number of turns. A novel fabrication process to create the second layer is presented in [96].

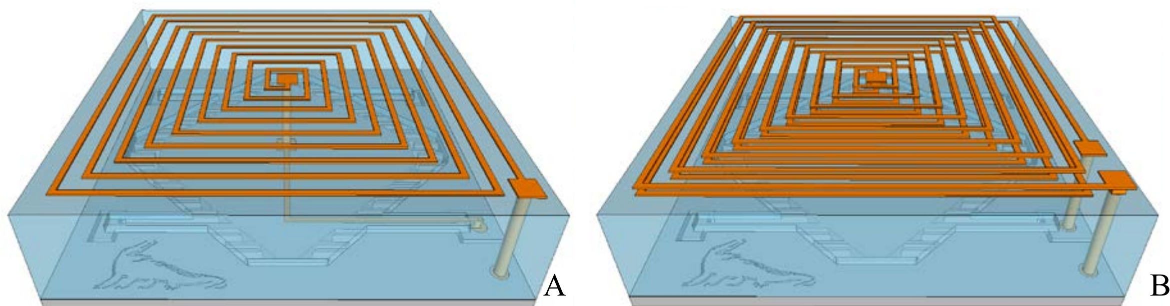

Figure 7-1. Back side of the third generation concept sensors. A) Single layer coil. B) Dual layer coil.

www.manaraa.com

The fabrication of this sensor can follow the same process flow developed for the second-generation sensor with the addition of a few steps. At the beginning of the process, coils and vias can be first created in the Pyrex wafer. At the end of the process, copper plugs can be deposited to connect the device layer to the vias. The fabrication steps in between have all been proven with the successful creation of the second-generation sensor. The additional steps needed have also been developed separately. Through Pyrex, vias have been drilled using picosecond laser ablation, and the 500 μm-deep vias have been cut down to 50 μm in diameter. The results for a 200 μm via are shown in the SEMs in Figure 7-2A. This can then be filled by copper electroplating to connect the topside capacitive structures to the backside coils. These coils have also been developed by electroplating copper in photoresist molds. A copper seed layer is sputtered onto the surface of the Pyrex, and photolithography is used to define the coil geometry. After plating, the photoresist and seed layer are removed, and a coil, shown in Figure 7-2B, is left behind to complete the integrated wireless shear stress sensors.

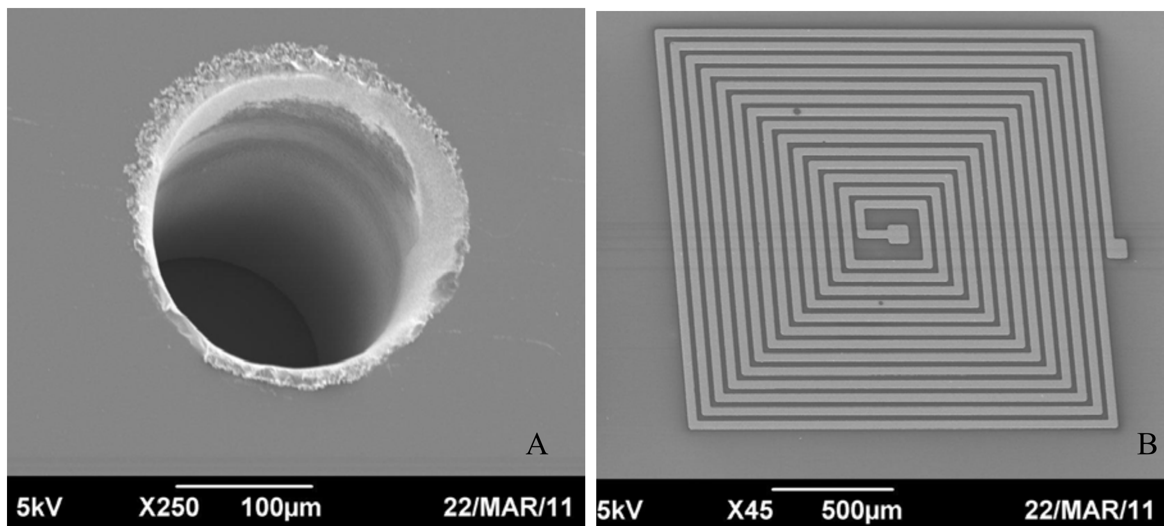

Figure 7-2. Fabrication technologies required to realize third-generation integrated wireless shear stress sensors. A) Laser drilled Pyrex through holes. B) Electroplated planar copper coils.

المنارة للاستشارات
www.manaraa.com

Once fabricated, this design will require virtually no packaging to test the sensors. A mounting strategy, similar to the one used before, can be used in which the chips are mounted in a recess on a PCB that has the interrogating antenna patterned on the opposite side. This board will then be compression fit into the Lucite plug used for experimental tests. With no metal traces or wire bonds protruding into the flow, the packaged sensors should be hydraulically smooth. The devices can be mounted in single and array formats and tested in the same way as the previous sensors. The sensor array layout can be designed into the mask, depending on the application. Cutting the standard wafer layout into blocks of devices would produce an array on a single large die, as illustrated in Figure 7-3. The chip itself would be the package and needing only to be mounted on a supporting structure in proximity to the antenna. This would also enable micron level position accuracy of the sensors in the array. Circular packages are more common than squares in testing environments and could be realized by using the laser, used for the vias to cut out the array.

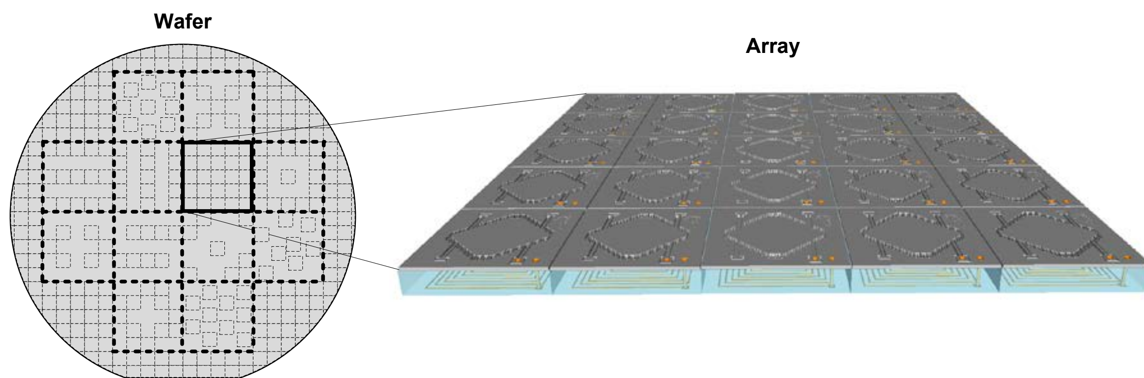

Figure 7-3. Wireless arrays realized by dicing devices in blocks.

7.3.2 Additional Testing

The wireless sensors presented were used to detect static shifts in shear stress. The frequency sweep time of the network analyzer limited the frequency response to less than 1 Hz.

المنارة للاستشارات
www.manaraa.com

The sensors themselves have a bandwidth of several kHz, set by the mass spring damper resonance of the mechanics. To achieve dynamic sensing, a new electronics system is needed.

There are many possible RF circuit topologies that can be used to convert the frequency shift of the sensor into an electronic signal [97-102]. One of the best candidates is shown in Figure 7-4. This circuit works by placing the antenna into the feedback loop of an oscillator. When the antenna is placed in proximity to the sensor, the resonance of the sensor will affect the frequency characteristics of the feedback, and the oscillator frequency will shift with changes in shear stress. The output is a frequency-modulated signal, in which the shear stress input on the sensor modulates the carrier frequency of the oscillator. An FM demodulator can then be used to convert this signal to baseband, and the voltage on the output can be read by a data acquisition card.

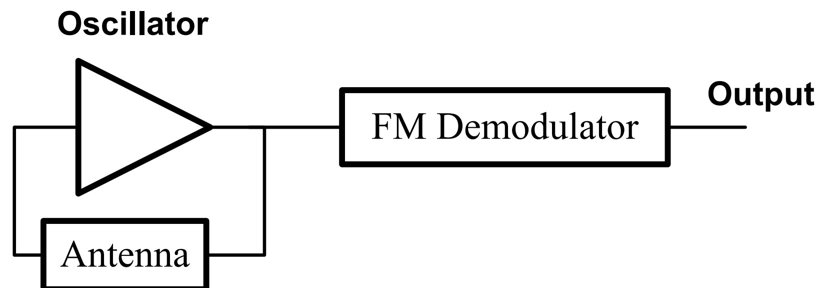

Figure 7-4. Basic concept for RF circuitry that would enable dynamic shear stress testing.

With appropriate RF electronics, dynamic characterization would be possible. For dynamic calibration, the setup and theory are much more complex than the static flow cell calibration. As shown in Figure 7-5, a speaker creates acoustic waves that propagate down a square duct. These waves are terminated at the end with an anechoic wedge to reduce reflections and prevent standing waves from forming. The compression waves set up oscillating pressure gradients that form a Stokes boundary layer along the walls. The one-dimensional solution for Stokes layer excitation in a square duct [103] is

المنارة للاستشارات
www.manaraa.com

$$\tau(t) = P' \sqrt{\frac{\nu\omega}{c^2}} e^{j\left(\omega t - \frac{\pi}{2}\right)} \tanh\left(\frac{h}{2}\sqrt{\frac{j\omega}{\nu}}\right). \quad (7\text{-}1)$$

P' is the magnitude of the acoustic excitation from the speaker and is measured by the reference microphone. The constants are the acoustic excitation frequency ω, the kinematic viscosity of air ν, the speed of sound in air c, and the height of the chamber h. The dynamic sensitivity is found by varying the amplitude of the excitation while keeping the frequency constant. This ramps up the input shear stress in a similar manner to the flow cell experiment. The response of the sensor is measured at each amplitude and plotted versus the input shear stress. Like the mean measurement, this should be a linear relationship, the slope of which is the sensitivity.

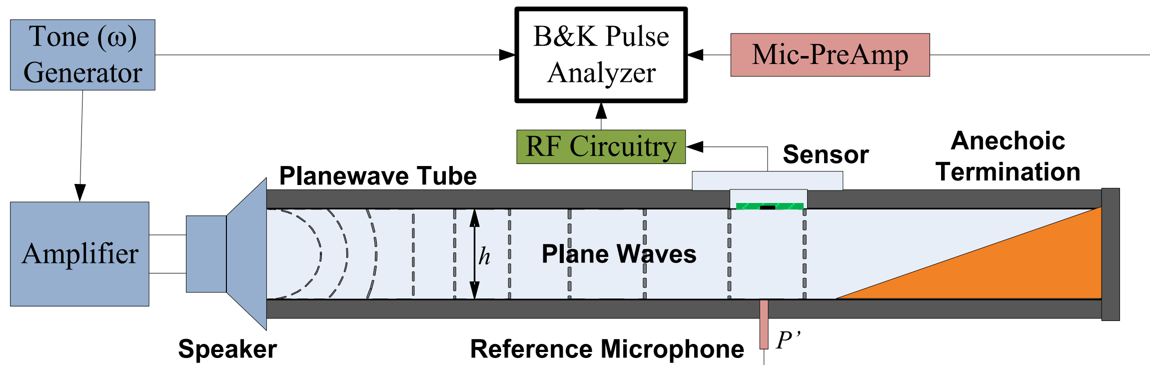

Figure 7-5. Diagram of the plane wave tube used for dynamic shear stress characterization.

7.3.3 System Optimization

Using the full model developed and confirmed in this dissertation, it will now be possible to employ formal design optimization techniques to realize the best possible performance. The material properties are assumed constant while the geometries are left as variables. The mechanical and capacitive structures can be included in the optimization as well as the coils and RF electronics. The minimum detectable signal should be chosen for the objective function used in the optimization loop. To achieve the best *MDS* (Equation 3-69), the *Q* of the system and

www.manaraa.com

sensitivity must be maximized while limited to size and fabrication constraints. A basic flow for the optimization program should look like Figure 7-6.

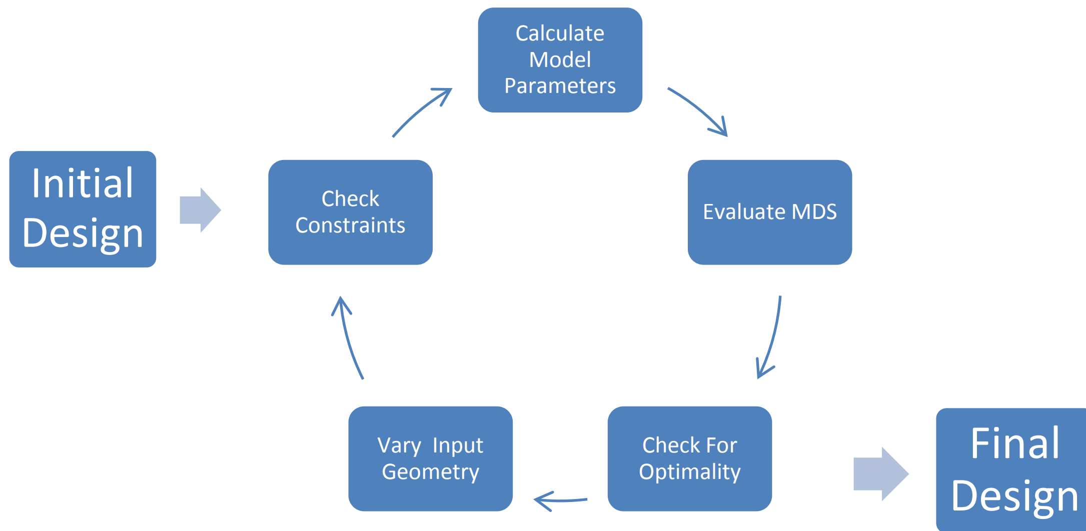

Figure 7-6. General system optimization loop.

These optimized designs can be integrated into all future generations of the sensor. In the future if this device is commercialized there will be a need to vary the specifications based on customer applications. The work presented in this dissertation will make that process possible.

المنارة للاستشارات
www.manaraa.com

APPENDIX A
LINEARITY DERIVATIONS

The sensitivity equations given in the modeling Chapter 3 are all small perturbation linear approximations. The maximum input shear stress is determined by the point at which these linearization's deviate from the true sensitivity by 3%. There are three sensitivities defined as S_{tw} for the mechanical deflection, S_{wc} for the capacitive transduction and S_{cf} for the resonant frequency shifts. These sensitivities are cascaded to find the total input shear stress to resonant frequency shift. The 3% nonlinearity point is defined for the total sensitivity. The linear and nonlinear sensitivities are derived in this appendix and compared using a generic geometry from the second generation sensors with a maximum input shear stress of 5 Pa.

A.1 Mechanical Nonlinearity

The linear and nonlinear beam equations for the sensor structure are given in V. Chandrasekharan's dissertation [21]. The linear equation is

$$w(\tau) = \frac{\tau A_e}{4Eh}\left(\frac{L_t}{W_t}\right)^3\left(1+\frac{2A_t}{A_e}\right), \qquad \text{(A-1)}$$

and is used in the sensitivity derivation in Chapter 3.

The nonlinear "Duffing Spring" equation adds an axial force F_a to the analysis[21]. The displacement w is

$$w = \frac{P}{2F_a}\left[-\left(\frac{\left(\cosh(\lambda L_t)-1\right)}{\lambda \sinh(\lambda L_t)}\left(1+\frac{2QL_t}{P}-\cosh(\lambda L_t)\right)\right)-\frac{\sinh(\lambda L_t)}{\lambda}+\frac{Q}{P}L_t^2+L_t\right] \qquad \text{(A-2)}$$

The axial force is given by

$$F_a = \frac{Eh}{2}\frac{W_t}{L_t}\int_0^{L_t}\left(\frac{\partial w}{\partial x}\right)^2 dx\,. \qquad \text{(A-3)}$$

www.manaraa.com

where $$\frac{\partial w}{\partial x}=\frac{P}{2F_a}\left[\left(\frac{\sinh(\lambda x)}{\sinh(\lambda L_t)}\left(1+\frac{2QL_t}{P}-\cosh(\lambda L_t)\right)\right)+\cosh(\lambda x)-\frac{2Qx}{P}-1\right]. \quad \text{(A-4)}$$

The input shear is incorporated into P an Q by

$$P=\tau A_e \quad \text{(A-5)}$$

and $$Q=\tau W_t. \quad \text{(A-6)}$$

The Eigen function λ is given by

$$\lambda=\sqrt{\frac{12F_a}{EhW_t^3}}. \quad \text{(A-7)}$$

This shows that the displacement w is a function of the force F_a and the force F_a is a function the displacement w. This loop means that it cannot be solved for analytically, instead the displacement is determined by an iterative approach. A guess of the axial force is used to solve for the displacement. This displacement is then used to find the force and the loop continues until the axial force derived changes by less than 10^{-8} from iteration to iteration.

The mechanical nonlinearity solution is plotted in Figure A-1. By comparing with the linear plot given by Equation A-1 the 3% nonlinearity point can be determined. This would be the maximum input shear stress for the sensor based purely on mechanical deflection. There are two more stages to get the output frequency change used for the sensor so they must be analyzed and cascaded to determine the final 3% point. The maximum input shear stress shown is less than the 5 Pa that it was designed for. This will be explained at the end of this appendix.

A.2 Capacitive Nonlinearity

The next stage in the sensitivity derivation that has to be linearized is the deflection to change in capacitance. The capacitance at any given deflection w is by

www.manaraa.com

$$C_s = \frac{\varepsilon_o h}{2}\left(\frac{N_f x_o + 2L_e + 3L_t}{g_{o1} - w} + \frac{(N_f - 2)x_o + L_t}{g_{o2} + w}\right). \tag{A-8}$$

This equation is nonlinear with respect to *w* but a linear approximation can be made by finding the slope given by

$$\frac{dC_s}{dw} = \frac{\varepsilon_o h}{2}\left(\frac{N_f x_o + 2L_e + 3L_t}{(-g_{o1} + w)^2} - \frac{(N_f - 2)x_o + L_t}{(g_{o2} + w)^2}\right). \tag{A-9}$$

At zero shear there will be no deflection so at the origin $w = 0$ and

$$\Delta C_s(w) \approx \frac{\varepsilon_o h w}{2}\left(\frac{N_f x_o + 2L_e + 3L_t}{g_{o1}^{\ 2}} - \frac{(N_f - 2)x_o + L_t}{g_{o2}^{\ 2}}\right). \tag{A-10}$$

Both the linear and nonlinear equations are plotted in Figure A-2. For small deflections the linear approximation holds to within 3%. This gives the range of displacements for the full scale input shear stress.

A.3 Resonant Nonlinearity

The same linearization technique is used for the change in the resonant frequency which is the final output of the sensor. The resonant frequency is given by

$$f = \frac{1}{2\pi\sqrt{L_c\left(C_s + C_p + C_c\right)}}. \tag{A-11}$$

The sensor has a static capacitance at zero shear of C_{os} and the slope is found at this point by

$$\left.\frac{df}{dC_s}\right|_{C_s = C_{os}} = \frac{1}{4\pi\left(C_{os} + C_p + C_c\right)\sqrt{L_c\left(C_{os} + C_p + C_c\right)}}. \tag{A-12}$$

The linear change in frequency is given by

$$\Delta f \approx -\frac{f_o}{2}\frac{\Delta C_s}{\left(C_{os} + C_p + C_c\right)} \tag{A-13}$$

المنارة للاستشارات
www.manaraa.com

where $$f_o = \frac{1}{2\pi\sqrt{L_c\left(C_{os} + C_p + C_c\right)}}. \quad \text{(A-14)}$$

Both the linear and nonlinear equations are plotted in Figure A-3. For small changes in capacitance the linear approximation holds to within 3%. This gives the range of capacitance change for the full scale input shear stress.

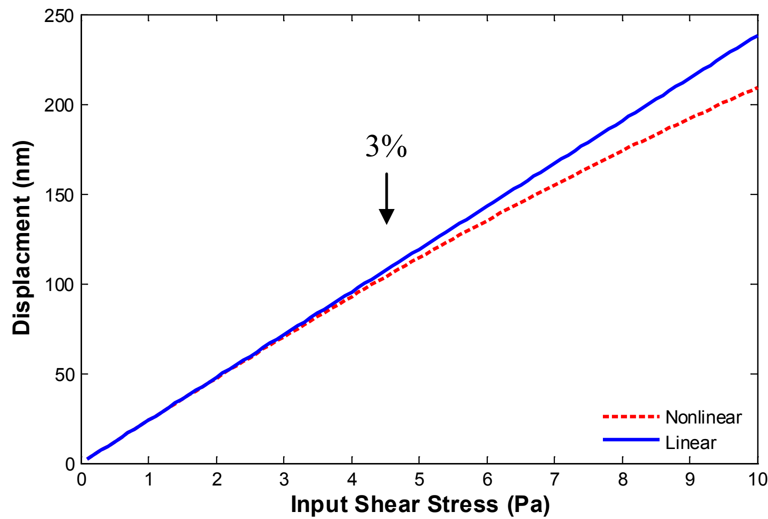

Figure A-1. Capacitive shear stress sensor mechanical nonlinearity plot.

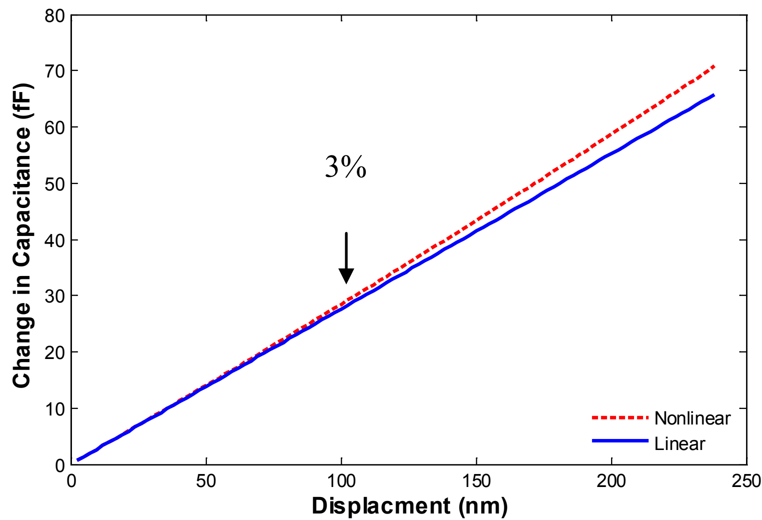

Figure A-2. Capacitive shear stress sensor capacitive nonlinearity plot.

المنارة للاستشارات
www.manaraa.com

A.4 Cascaded Results

The maximum input shear stress for the wireless shear stress sensor is found by cascading all three of these sensitivities together. The product of the linear approximations and the total nonlinear results are plotted in Figure A-4. This shows that the maximum input shear stress for the total wireless case (~5 Pa for this example) is actually higher than just the capacitive shear stress sensor (~4 Pa for this example). This is because the linear approximations of stage 1 and 3 over predict while stage 2 under predicts. This balances out and extends the total range.

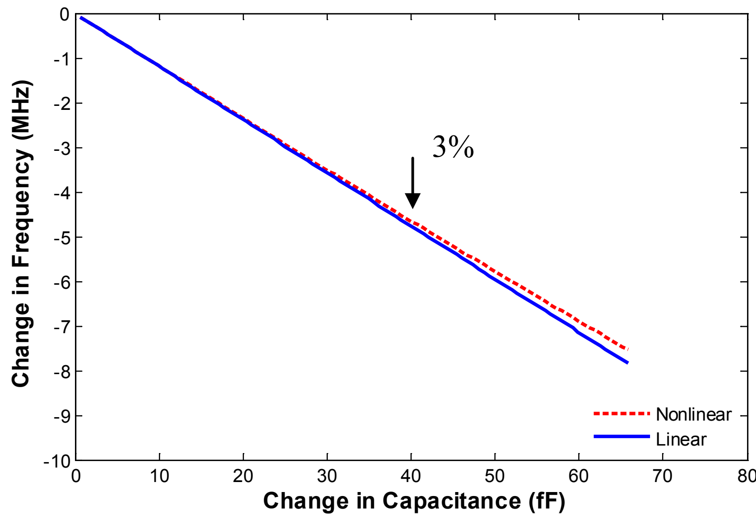

Figure A-3. Capacitive shear stress sensor resonant nonlinearity plot.

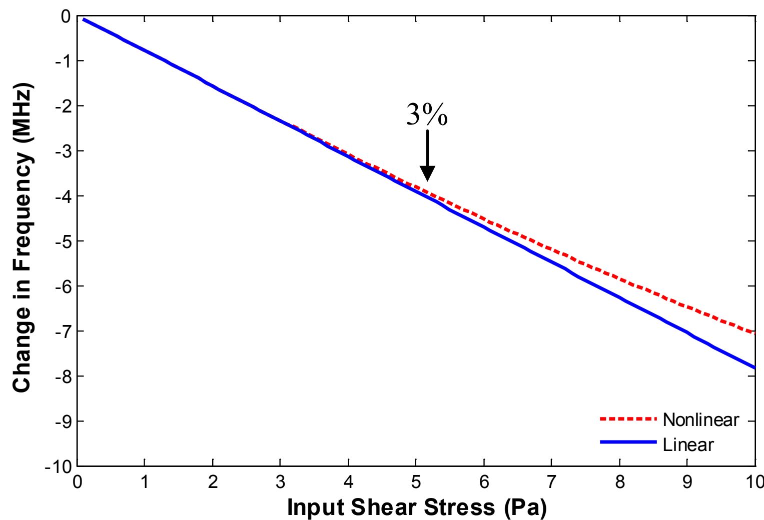

Figure A-4. Capacitive shear stress sensor cascaded nonlinearity plot.

المنارة للاستشارات
www.manaraa.com

APPENDIX B
IMPEDANCE DERIVATIONS

The derivations for the full impedance models from Section 3.3 are presented. First the single senor equation is developed base on the T-model for the coupled coils and including all of the parasitic values. The simplified array model is presented for an arbitrary number of wireless sensors. This model assumes zero inter-sensor coupling and only resistive parasitics. Based on this analysis a complete model is derived for the array that considers all coupling terms and parasitics.

B.1 Single Sensor

The single sensor model presented in Chapter 3 is shown in Figure B-1. The derivation of the input impedance Z_L is done in sections starting from the right. The impedance of all of the capacitance terms in parallel with the conductance G is given by

$$Z_1 = \left(G + j\omega\left(C_c + C_p + C_s\right)\right)^{-1}. \tag{B-1}$$

This is combined in series with the inductance and resistance such that

$$Z_2 = R_c + j\omega L_c + \left(G + j\omega\left(C_c + C_p + C_s\right)\right)^{-1} - j\omega M\ . \tag{B-2}$$

The parallel connection of the mutual coupling term gives

$$Z_3 = \frac{\left(R_c + j\omega L_c + \left(G + j\omega\left(C_c + C_p + C_s\right)\right)^{-1} - j\omega M\right) j\omega M}{R_c + j\omega L_c + \left(G + j\omega\left(C_c + C_p + C_s\right)\right)^{-1} - \cancel{j\omega M} + \cancel{j\omega M}}. \tag{B-3}$$

Adding the antenna terms in series simplifies the expression to

$$Z_4 = R_a + j\omega L_a - \cancel{j\omega M} + \frac{\left(\cancel{R_c + j\omega L_c + \left(G + j\omega\left(C_c + C_p + C_s\right)\right)^{-1}} - j\omega M\right) j\omega M}{R_c + j\omega L_c + \left(G + j\omega\left(C_c + C_p + C_s\right)\right)^{-1}} \tag{B-4}$$

المنارة للاستشارات
www.manaraa.com

The parasitic antenna capacitance is left with a simplified parallel notation to give the final solution

$$Z_L = \left(\frac{1}{j\omega C_a}\right) || \left(R_a + j\omega L_a + \frac{\omega^2 M^2}{R_c + j\omega L_c + \left(G + j\omega\left(C_c + C_p + C_s\right)\right)^{-1}}\right). \tag{B-5}$$

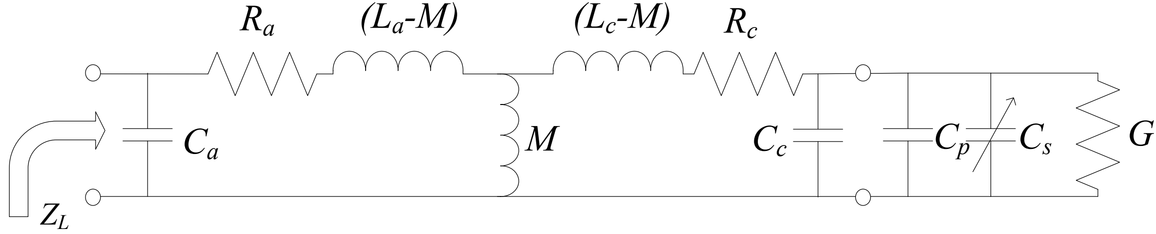

Figure B-1. Full single wireless sensor model for impedance derivations.

B.2 Array of Sensors With No Inter-Sensor Coupling

For the array derivations it is assumed that the coupling between the wireless sensors is zero. In this case the impedance can be derived using the results found for the single sensor. The circuit model for this case is shown in Figure B-2. The impedance for each of the sensors is given by the generic equation

$$Z_i = R_i + j\left(\omega L_i - \frac{1}{\omega C_i}\right), \tag{B-6}$$

where i is the index of the sensor in the array. The sensor parasitic capacitance and conductances have been lumped into R_i and C_i for this derivation. The capacitive term is given by

$$C_i = \frac{G_i^2 + \omega^2\left(C_{ci} + C_{pi} + C_{si}\right)^2}{\omega^2\left(C_{ci} + C_{pi} + C_{si}\right)} \tag{B-7}$$

The resistive term is given by

$$R_i = R_{ci} + \frac{G_i}{G_i^2 + \omega^2\left(C_{ci} + C_{pi} + C_{si}\right)^2} \tag{B-8}$$

For an array of N_s sensors the impedance is given by

المنارة للاستشارات
www.manaraa.com

$$Z_L = \left(R_a + j\omega L_a + \sum_{i=1}^{N_s} \frac{\omega^2 M_{ai}{}^2}{Z_i} \right). \quad \text{(B-9)}$$

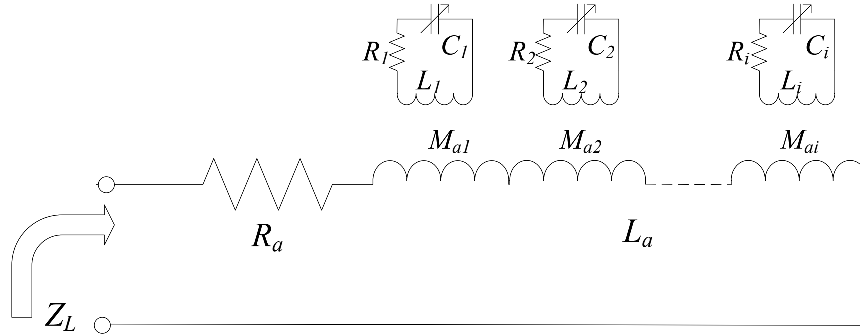

Figure B-2. Wireless sensor array model for impedance derivations with no inter-sensor coupling.

B.3 Array of Sensor With Inter-Sensor Coupling

In reality there will be some finite coupling between the sensors. All of these coupling terms are given by the FastHenry simulations in Chapter 3 and so a model was developed to use these values for a complete model that considers all parasitics and coupling terms. The circuit in Figure B-3 shows the added coupling terms. For this solution an N_s by N_s matrix inversion must be calculated

$$B = \begin{pmatrix} j\omega L_a & j\omega M_{a1} & j\omega M_{a2} & \cdots & j\omega M_{ai} \\ j\omega M_{1a} & R_1 + j\left(\omega L_1 - \frac{1}{\omega C_1}\right) & j\omega M_{12} & \cdots & j\omega M_{1i} \\ j\omega M_{2a} & j\omega M_{21} & R_2 + j\left(\omega L_2 - \frac{1}{\omega C_2}\right) & \cdots & j\omega M_{2i} \\ \vdots & \vdots & \vdots & \ddots & \vdots \\ j\omega M_{ia} & j\omega M_{i1} & j\omega M_{i2} & \cdots & R_i + j\left(\omega L_i - \frac{1}{\omega C_i}\right) \end{pmatrix}^{-1}, \quad \text{(B-10)}$$

where B is an arbitrary matrix designator. Again R and C contain both the capacitive and conductive parasitics given by Equations B-7 and B-8.This matrix gives the admittance for all of

المنارة للاستشارات
www.manaraa.com

the terminals involved in the inductive coupling on the diagonal axis. It is based on the current and voltage matrices from an arbitrary number of ports as shown in Figure B-4

$$\begin{pmatrix} I_1 \\ I_2 \\ I_3 \\ I_4 \\ \vdots \\ I_i \end{pmatrix} = B \begin{pmatrix} V_1 \\ V_2 \\ V_3 \\ V_4 \\ \vdots \\ V_i \end{pmatrix}. \tag{B-11}$$

The impedance at the input to the antenna is simply given by the inverse of the first component of B which gives

$$Z_L = R_a + \frac{1}{B_{11}}. \tag{B-12}$$

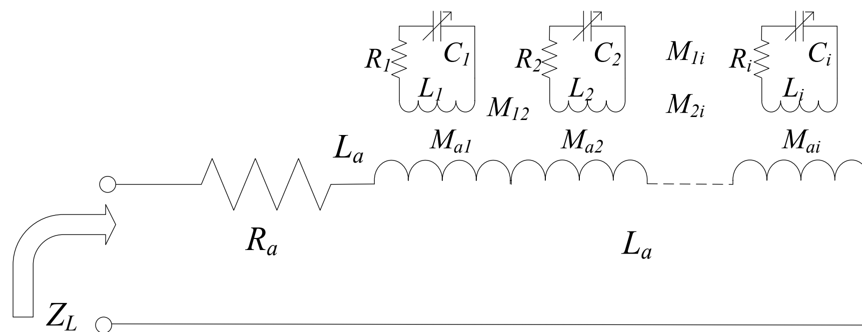

Figure B-3. Wireless sensor array for impedance derivations with full coupling model.

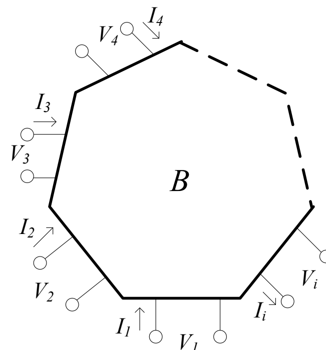

Figure B-4. Multiport impedance model.

www.manaraa.com

APPENDIX C
COUPLED RESONATOR FREQUENCY DEPENDANCE

The resonant frequencies of ideal coupled resonators is analyzed in Section 3.3.2 to show the effect they have on each other's resonant frequencies. This appendix gives the derivations of Equations 3-63 and 3-66. First the case of two resonators with the same components and thus the same resonant frequency is derived. Next resonators with different resonant frequencies are presented. Simple Laplace filter analysis is used to derive the resonant frequencies in these two cases.

C.1 Same Resonant Frequencies

The resonant frequencies will be determined by the denominator of the characteristic equation for the circuit shown in Figure C-1. The characteristic equation is

$$Z=\left[\left(\left[\left(s(L-M)+\frac{1}{sC}\right)^{-1}+(sM)^{-1}\right]^{-1}+s(L-M)\right)^{-1}+\left(\frac{1}{sC}\right)^{-1}\right]^{-1}. \tag{C-1}$$

Simplifying from the inside out gives

$$Z=\left[\left(\left[\frac{sC}{s^2(LC-MC)+1}+(sM)^{-1}\right]^{-1}+s(L-M)\right)^{-1}+\left(\frac{1}{sC}\right)^{-1}\right]^{-1}, \tag{C-2}$$

$$Z=\left[\left(\left[\frac{s^2LC+1}{s^3\left(LMC-M^2C\right)+sM}\right]^{-1}+s(L-M)\right)^{-1}+\left(\frac{1}{sC}\right)^{-1}\right]^{-1}, \tag{C-3}$$

$$Z=\left[\left(\frac{s^3\left(LMC-M^2C\right)+sM}{s^2LC+1}+s(L-M)\right)^{-1}+\left(\frac{1}{sC}\right)^{-1}\right]^{-1}, \tag{C-4}$$

$$Z=\left[\left(\frac{s^3\left(L^2C-M^2C\right)+sL}{s^2LC+1}\right)^{-1}+\left(\frac{1}{sC}\right)^{-1}\right]^{-1}, \tag{C-5}$$

المنارة للاستشارات
www.manaraa.com

$$Z = \left[\frac{s^2 LC + 1}{s^3 \left(L^2 C - M^2 C \right) + sL} + sC \right]^{-1}, \tag{C-6}$$

$$Z = \left[\frac{s^4 \left(L^2 C^2 - M^2 C^2 \right) + s^2 2LC + 1}{s^3 \left(L^2 C - M^2 C \right) + sL} \right]^{-1}, \tag{C-7}$$

$$Z = \frac{s^3 \left(L^2 C - M^2 C \right) + sL}{s^4 \left(L^2 C^2 - M^2 C^2 \right) + s^2 2LC + 1}. \tag{C-8}$$

Using the definition for the coupling factor

$$k = \sqrt{\frac{M^2}{LL}} = \frac{M}{L}, \tag{C-9}$$

gives

$$Z = \frac{s^3 CL^2 \left(1 - k^2 \right) + sL}{s^4 C^2 L^2 \left(1 - k^2 \right) + s^2 2LC + 1}. \tag{C-10}$$

Converting this to the standard format gives

$$Z = \frac{s^3 \frac{1}{C} + s \frac{1}{C^2 L \left(1 - k^2 \right)}}{s^4 + s^2 \frac{2}{CL \left(1 - k^2 \right)} + \frac{1}{C^2 L^2 \left(1 - k^2 \right)}}. \tag{C-11}$$

Factoring the denominator gives

$$Z = \frac{s^3 \frac{1}{C} + s \frac{1}{C^2 L \left(1 - k^2 \right)}}{\left(s^2 + \frac{1}{\left(1 - k \right) LC} \right) \left(s^2 + \frac{1}{\left(1 + k \right) LC} \right)}, \tag{C-12}$$

which gives two resonant frequencies

$$f_{o1} = \frac{1}{2\pi \sqrt{LC \left(1 - k \right)}} \tag{C-13}$$

and

$$f_{o2} = \frac{1}{2\pi \sqrt{LC \left(1 + k \right)}}. \tag{C-14}$$

المنارة للاستشارات
www.manaraa.com

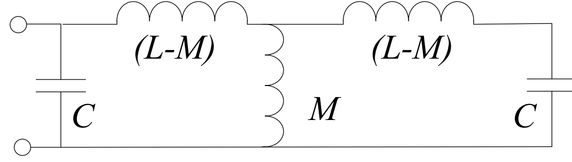

Figure C-1. Simple coupled resonator circuit.

C.2 Different Resonant Frequencies

The resonant frequencies will be determined by the denominator of the characteristic equation for the circuit shown in Figure C-2. Following the same procedure as the simple case. The characteristic equation is

$$Z=\left[\left(\left[\left(s\left(L_2-M\right)+\frac{1}{sC_2}\right)^{-1}+\left(sM\right)^{-1}\right]^{-1}+s\left(L_1-M\right)\right)^{-1}+\left(\frac{1}{sC_1}\right)^{-1}\right]^{-1}. \tag{C-15}$$

Simplifying from the inside out gives

$$Z=\left[\left(\left[\frac{sC_2}{s^2\left(L_2C_2-MC_2\right)+1}+\left(sM\right)^{-1}\right]^{-1}+s\left(L_1-M\right)\right)^{-1}+\left(\frac{1}{sC_1}\right)^{-1}\right]^{-1}, \tag{C-16}$$

$$Z=\left[\left(\left[\frac{s^2L_2C_2+1}{s^3\left(L_2MC_2-M^2C_2\right)+sM}\right]^{-1}+s\left(L_1-M\right)\right)^{-1}+\left(\frac{1}{sC_1}\right)^{-1}\right]^{-1}, \tag{C-17}$$

$$Z=\left[\left(\frac{s^3\left(L_2MC_2-M^2C_2\right)+sM}{s^2L_2C_2+1}+s\left(L_1-M\right)\right)^{-1}+\left(\frac{1}{sC_1}\right)^{-1}\right]^{-1}, \tag{C-18}$$

$$Z=\left[\left(\frac{s^3\left(L_1L_2C_2-M^2C_2\right)+sL_1}{s^2L_2C_2+1}\right)^{-1}+\left(\frac{1}{sC_1}\right)^{-1}\right]^{-1}, \tag{C-19}$$

$$Z=\left[\frac{s^2L_2C_2+1}{s^3\left(L_1L_2C_2-M^2C_2\right)+sL_1}+sC_1\right]^{-1}, \tag{C-20}$$

$$Z=\left[\frac{s^4\left(L_1L_2C_1C_2-M^2C_1C_2\right)+s^2\left(L_1C_1+L_2C_2\right)+1}{s^3\left(L_1L_2C_2-M^2C_2\right)+sL_1}\right]^{-1}, \tag{C-21}$$

المنارة للاستشارات
www.manaraa.com

$$Z = \frac{s^3\left(L_1L_2C_2 - M^2C_2\right) + sL_1}{s^4\left(L_1L_2C_1C_2 - M^2C_1C_2\right) + s^2\left(L_1C_1 + L_2C_2\right) + 1}. \tag{C-22}$$

Using the definition for the coupling factor

$$k = \sqrt{\frac{M^2}{L_1L_2}}, \tag{C-23}$$

gives

$$Z = \frac{s^3L_1L_2C_2\left(1-k^2\right) + sL_1}{s^4L_1L_2C_1C_2\left(1-k^2\right) + s^2\left(L_1C_1 + L_2C_2\right) + 1}. \tag{C-24}$$

Converting this to the standard format gives

$$Z = \frac{s^3\frac{1}{C_1} + s\frac{1}{L_2C_1C_2\left(1-k^2\right)}}{s^4 + s^2\frac{\left(L_1C_1 + L_2C_2\right)}{L_1L_2C_1C_2\left(1-k^2\right)} + \frac{1}{L_1L_2C_1C_2\left(1-k^2\right)}}. \tag{C-25}$$

Factoring the denominator gives

$$Z = \frac{s^3\frac{1}{C_1} + s\frac{1}{L_2C_1C_2\left(1-k^2\right)}}{\left(s^2 + \omega_{o1}{}^2\right)\left(s^2 + \omega_{o2}{}^2\right)}, \tag{C-26}$$

where

$$\omega_{o1}{}^2 = \frac{L_1C_1 + L_2C_2 + \sqrt{L_1{}^2C_1{}^2 + L_2{}^2C_2{}^2 - L_1L_2C_1C_2\left(2-4k^2\right)}}{2L_1L_2C_1C_2\left(1-k^2\right)} \tag{C-27}$$

and

$$\omega_{o2}{}^2 = \frac{L_1C_1 + L_2C_2 - \sqrt{L_1{}^2C_1{}^2 + L_2{}^2C_2{}^2 - L_1L_2C_1C_2\left(2-4k^2\right)}}{2L_1L_2C_1C_2\left(1-k^2\right)}. \tag{C-28}$$

This gives two resonant frequencies

$$f_{o1} = \frac{\omega_{o1}}{2\pi} = \frac{1}{2\pi\sqrt{\frac{2L_1L_2C_1C_2\left(1-k^2\right)}{L_1C_1 + L_2C_2 + \sqrt{L_1{}^2C_1{}^2 + L_2{}^2C_2{}^2 - L_1L_2C_1C_2\left(2-4k^2\right)}}}} \tag{C-29}$$

المنارة للاستشارات
www.manaraa.com

and $$f_{o2} = \frac{\omega_{o2}}{2\pi} = \frac{1}{2\pi\sqrt{\dfrac{2L_1L_2C_1C_2\left(1-k^2\right)}{L_1C_1 + L_2C_2 - \sqrt{L_1^2C_1^2 + L_2^2C_2^2 - L_1L_2C_1C_2\left(2-4k^2\right)}}}}. \quad \text{(C-30)}$$

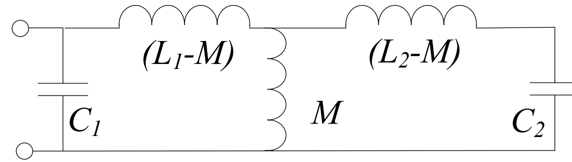

Figure C-2. Coupled resonator circuit.

المنارة للاستشارات
www.manaraa.com

APPENDIX D
QUALITY FACTOR DERIVATIONS

The quality factor Q for the wireless shear stress sensor is given in Section 3.3. The definition and derivations of Q are presented in this appendix. First the quality factor is defined in general using simple *RL* and *GC* circuits. Next the quality factor at resonance is defined and derived for simple *RLC* and *GLC* circuits. This work all leads to the eventual derivation of the quality factor for the sensor.

D.1 Inductors and Capacitors

The quality factor, Q is defined as the peak energy stored in a circuit divided by the energy dissipated in one cycle. This is commonly expressed in terms of radians as

$$Q = \frac{2\pi W_{peak}}{W_{dissipated}}, \tag{D-1}$$

The quality factor will be derived from energy equations for two circuit examples shown in Figure D-1.

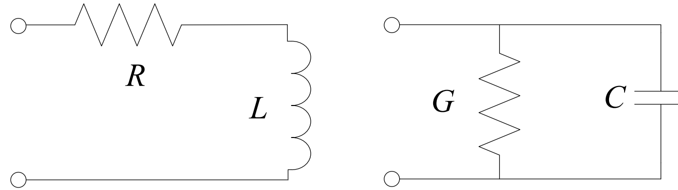

Figure D-1. Simple *RL* and *GC* circuits.

First the quality factor for the *RL* circuit is derived. The energy stored in an inductor is

$$W_{peak} = \frac{1}{2} L I_{peak}{}^{2}. \tag{D-2}$$

The energy lost in one period T in a resistor is

$$W_{dissipated} = P_{dissipated} T, \tag{D-3}$$

where

$$P_{dissipated} = I_{rms}{}^{2} R. \tag{D-4}$$

For a sine wave the rms current is related to the peak current by

www.manaraa.com

$$I_{rms} = \frac{I_{peak}}{\sqrt{2}}. \tag{D-5}$$

Combining Equations D-2 through D-5 into the definition of Q gives

$$Q = 2\pi \frac{\frac{1}{2} L I_{peak}^{2}}{\left(\frac{I_{peak}}{\sqrt{2}}\right)^{2} RT}. \tag{D-6}$$

Replacing the period by a radian frequency

$$\omega = \frac{2\pi}{T}, \tag{D-7}$$

the quality factor simplifies down to

$$Q = \frac{\omega L}{R}. \tag{D-8}$$

For the GC circuit the same procedure is followed with

$$W_{peak} = \frac{1}{2} C V_{peak}^{2}, \tag{D-9}$$

$$P_{dissipated} = V_{rms}^{2} G, \tag{D-10}$$

and

$$V_{rms} = \frac{V_{peak}}{\sqrt{2}}. \tag{D-11}$$

Combining these equations gives

$$Q = 2\pi \frac{\frac{1}{2} C V_{peak}^{2}}{\left(\frac{V_{peak}}{\sqrt{2}}\right)^{2} GT}. \tag{D-12}$$

Once again replacing the period and simplifying gives

$$Q = \frac{\omega C}{G}. \tag{D-13}$$

المنارة للاستشارات
www.manaraa.com

Both of the equations are a function of frequency. The quality factor for all real inductors and capacitors is either defined as the max value or the value at the frequency of interest.

D.2 Simple RLC Resonant Circuits

For resonant circuits the same definition of quality factor applies. There are two simple resonator circuits that will be discussed. The *RLC* and *GLC* resonant circuits are shown in Figure D-2. Since the energy in a resonant circuit alternates back and forth between a current through the inductor and a voltage on the capacitance the peak energy can be defined by either component. Using the inductor for the *RLC* circuit and the capacitor for the *GLC* circuit the quality factors are given by Equations D-8 and D-13 respectively.

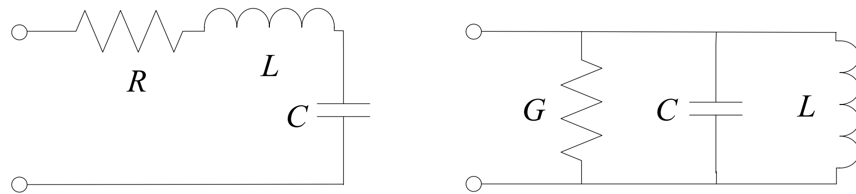

Figure D-2. Simple *RLC* and *GLC* resonant circuits.

For a resonant circuit it is common to define a quality factor at resonance. The resonant frequency in radians for both of these equations is given by

$$\omega_n = \frac{1}{\sqrt{LC}}. \tag{D-14}$$

The quality factor at resonance for the *RLC* circuit is given by

$$Q_n = \frac{\omega_n L}{R} = \frac{1}{R}\sqrt{\frac{L}{C}}, \tag{D-15}$$

and for the *GLC* circuit by

$$Q_n = \frac{\omega_n C}{G} = \frac{1}{G}\sqrt{\frac{C}{L}}. \tag{D-16}$$

المنارة للاستشارات
www.manaraa.com

D.3 Wireless Shear Stress Sensor Quality Factor

The circuit model for the wireless shear stress sensor, including all of its parasitics is shown in Figure D-3. The value of the quality factor at resonance is needed for the model in Chapter 3. The circuit is analyzed as an *RLC* circuit where the stored energy is calculated on the inductor L_c and R and C are functions of the rest of the parameters shown in the figure.

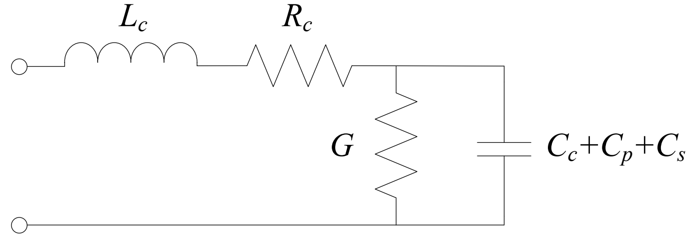

Figure D-3. Wireless shear stress sensor circuit including parasitics.

For this analysis the resistive term is given by the transformation

$$R = R_c + \frac{G}{G^2 + \omega^2 \left(C_c + C_p + C_s\right)^2}. \tag{D-17}$$

The capacitive term is given by the transformation

$$C = \frac{G^2 + \omega^2 \left(C_c + C_p + C_s\right)^2}{\omega^2 \left(C_c + C_p + C_s\right)^2}. \tag{D-18}$$

The inductive term is

$$L = L_c \tag{D-19}$$

These transformations result in the *RLC* circuit shown in Figure D-2 and using Equation D-15 gives

$$Q_n = \frac{1}{R_c + \frac{G}{G^2 + {\omega_n}^2 \left(C_c + C_p + C_s\right)^2}} \sqrt{\frac{L_c}{\frac{G^2 + {\omega_n}^2 \left(C_c + C_p + C_s\right)^2}{{\omega_n}^2 \left(C_c + C_p + C_s\right)^2}}}. \tag{D-20}$$

The resonant frequency for this circuit is

المنارة للاستشارات
www.manaraa.com

$$\omega_n = \frac{1}{\sqrt{L_c\left(C_c + C_p + C_s\right)}}. \tag{D-21}$$

Simplifying Equation D-20 gives

$$Q_n = \frac{1}{R_c + \dfrac{G}{G^2 + \left(C_c + C_p + C_s\right)/L_c}} \sqrt{\frac{1}{G^2 + \left(C_c + C_p + C_s\right)/L_c}}. \tag{D-22}$$

المنارة للاستشارات

www.manaraa.com

APPENDIX E
COMB FINGER ELECTROSTATIC PULL-IN DERIVATIONS

The electrostatic force equations used to derive the pull-in voltage for Section 4.1.2. are derived in this appendix. The derivation is based on the simple pull-in equations for a pair of parallel plates with one plate fixed and the other plate connected to a spring. A voltage is applied to the plates that causes an electrostatic attraction of the two plates. In equilibrium this force is balanced by the force of the spring in the opposite direction. When the voltage is raised to a certain point this equilibrium condition breaks down and the plates will collapse together or "pull-in". First the simple case is derived and then the changes are introduced to apply this analysis to the comb fingers of the capacitive shear stress sensors.

E.1 Parallel Plates

The derivation starts with a pair of parallel plates as illustrated in Figure E-1. A force balance is used to find the limit to the equilibrium condition. The upward mechanical spring force is given by the simple equation

$$F_m = kx \,, \tag{E-1}$$

where k is the spring constant and x is the displacement of the plate from the rest position g_o. The electrostatic force is derived from a differential change in the electrostatic potential energy in the gap with a change in x by

$$F_e = \frac{\partial W_{pe}}{\partial x} \tag{E-2}$$

The potential energy for a capacitor is

$$W_{pe} = \frac{1}{2} C V^2 \,, \tag{E-3}$$

where

$$C = \frac{\varepsilon A}{g_o - x} \tag{E-4}$$

www.manaraa.com

is the capacitance between parallel plates. The area of the plates is A and ε is the permittivity of free space. Combining Equation E-2 through E-4 and taking the derivative gives

$$F_e = \frac{\varepsilon A V^2}{2\left(g_o - x\right)^2}. \tag{E-5}$$

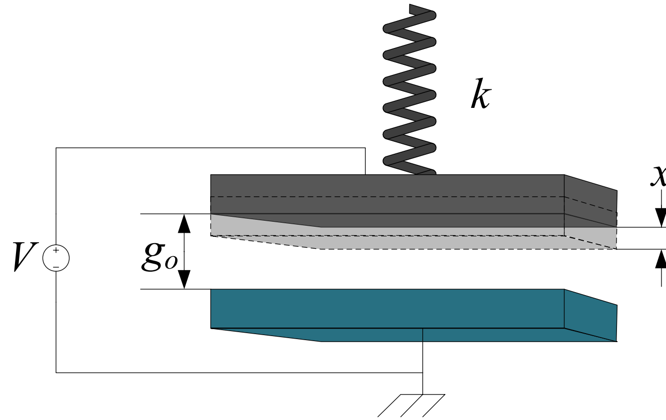

Figure E-1. Basic parallel plate diagram for electrostatic pull-in derivation.

The pull-in voltage is to found by setting the total force on the movable plate to zero where

$$F_{net} = kx - \frac{\varepsilon A V^2}{2\left(g_o - x\right)^2} = 0. \tag{E-6}$$

This gives the voltage on the plates in terms of the geometry

$$V = \sqrt{\frac{2k\left(x^2 g_o - x^3\right)^2}{\varepsilon A}} \tag{E-7}$$

The pull-in voltage V_{pi} is given by Equation E-7 when $x = x_{pi}$ the pull-in displacement. The displacement where the equilibrium condition breaks down is determined by the point where the slope of the net force becomes zero

$$\frac{dF_{net}}{dx} = k - \frac{\varepsilon A V^2}{\left(g_o - x\right)^3} = 0. \tag{E-8}$$

Solving Equation E-8 for k and substituting into E-6 gives

المنارة للاستشارات
www.manaraa.com

$$\frac{x\varepsilon AV^2}{(g_o - x)^3} = \frac{\varepsilon AV^2}{2(g_o - x)^2}, \tag{E-9}$$

and the pull-in displacement is

$$x_{pi} = \frac{g_o}{3} \tag{E-10}$$

Substituting this result into Equation E-7 gives the final result for the pull-in voltage for a pair of parallel plates.

$$V_{pi} = \sqrt{\frac{8}{27}\frac{kg_o^{\ 3}}{\varepsilon A}} \tag{E-11}$$

E.2 Comb Fingers

The pull-in voltage for the capacitive shear stress sensor follows the same steps as outlined in the previous section. The difference in the geometry is shown in Figure E-2. In addition to the downward electrostatic force there is also an upward electrostatic force due to an adjacent finger. The two electrostatic forces are never equal because there are different gap widths in the design of the sensor. The force balance and equilibrium condition therefore become

$$F_{net} = kx - \frac{N\varepsilon AV^2}{2(g_{o1} - x)^2} + \frac{(N-1)\varepsilon AV^2}{2(g_{o2} + x)^2} = 0 \tag{E-12}$$

and

$$\frac{dF_{net}}{dx} = k - \frac{N\varepsilon AV^2}{(g_{o1} - x)^3} + \frac{(N-1)\varepsilon AV^2}{(g_{o2} + x)^3} = 0. \tag{E-13}$$

The spring constant is determined by the tethers attached to the floating element of the sensor. The gaps are given by g_{o1} and g_{o2} and the total number of fingers on the floating element is given by N. Solving Equation E-12 for V gives

www.manaraa.com

$$V = \sqrt{\frac{k}{\varepsilon A\left(\frac{N_f}{\left(g_{o1}-x\right)^3}-\frac{N_f-1}{\left(g_{o2}+x\right)^3}\right)}}. \tag{E-14}$$

Solving Equation E-13 for k and substituting into Equation E-12 gives

$$\frac{(g_{o1}-3x_{pi})}{\left(g_{o1}-x_{pi}\right)^3} = \frac{\left(N-1\right)}{N}\frac{(g_{o2}-x_{pi})}{\left(g_{o2}+x_{pi}\right)^3}. \tag{E-15}$$

This is a nonlinear equation for x_{pi} and must be solved numerically. Once x_{pi} is found it can be inserted in Equation E-14 to find the pull-in voltage

$$V_{pi} = \sqrt{\frac{k}{\varepsilon A\left(\frac{N_f}{\left(g_{o1}-x_{pi}\right)^3}-\frac{N_f-1}{\left(g_{o2}+x_{pi}\right)^3}\right)}}. \tag{E-16}$$

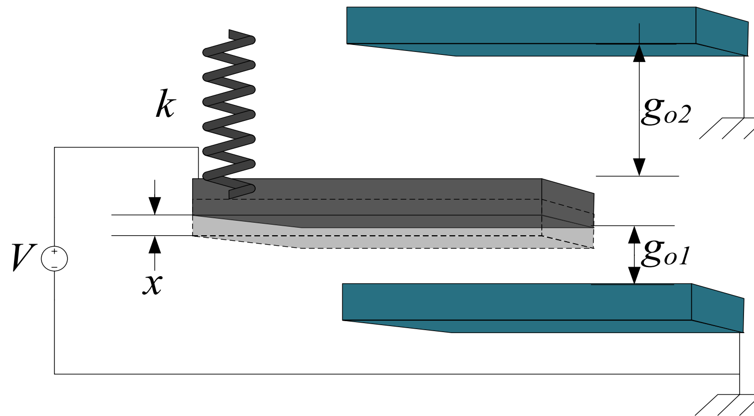

Figure E-2. Comb finger diagram for electrostatic pull-in derivation.

المنارة للاستشارات
www.manaraa.com

LIST OF REFERENCES

[1] Y.A. Çengel and J.M. Cimbala, *Fluid Mechanics: Fundamentals and Applications*, Boston: McGraw-Hill Higher Education, 2010.

[2] S. Anders, W.L. Sellers, and A. Washburn, "Active flow control activities at NASA Langley," *AIAA Flow Control Conference*, Portland, OR: 2004, pp. 1-21.

[3] N.J.W. Brockie and C.J. Baker, "The aerodynamic drag of high speed trains," *Journal of Wind Engineering and Industrial Aerodynamics*, vol. 34, 1990, pp. 273-290.

[4] K. Fujii, "Progress and future prospects of CFD in aerospace—Wind tunnel and beyond," *Progress in Aerospace Sciences*, vol. 41, Aug. 2005, pp. 455-470.

[5] J. Naughton and M. Sheplak, "Modern developments in shear-stress measurement," *Progress in Aerospace Sciences*, vol. 38, Oct. 2002, pp. 515-570.

[6] M. Sheplak, L. Cattafesta, T. Nishida, and C. McGinley, "MEMS shear stress sensors: promise and progress," *AIAA Aerodynamic Measurement Technology and Ground Testing Conference*, 2004, pp. 1-13.

[7] A. Etebari, "Recent innovations in wall shear stress sensor technologies," *Recent Patents on Mechanical Engineering*, vol. 1, Jan. 2008, pp. 22-28.

[8] V. Chandrasekharan, J. Sells, J. Meloy, D.P. Arnold, and M. Sheplak, "A metal-on-silicon differential capacitive shear stress sensor," *Solid-State Sensors, Actuators, and Microsystems*, Denver, CO: 2009, pp. 1537-1540.

[9] T. Chen, D. Mills, V. Chandrasekharan, H. Zmuda, and M. Sheplak, "Optical miniaturization of a MEMS-based floating element shear stress sensor with moiré amplification," *AIAA Aerospace Sciences Meeting*, 2010, pp. 1-13.

[10] A. Padmanabhan, H. Goldberg, K.D. Breuer, and M. a Schmidt, "A wafer-bonded floating-element shear stress microsensor with optical position sensing by photodiodes," *Journal of Microelectromechanical Systems*, vol. 5, 1996, pp. 307-315.

[11] T. Ioppolo, U.K. Ayaz, and M.V. Ötügen, "A micro-optical wall shear stress sensor concept based on whispering gallery mode resonators," *AIAA Aerospace Sciences Meeting*, 2008, pp. 8-11.

[12] Y. Li, T. Nishida, D.P. Arnold, and M. Sheplak, "Microfabrication of a wall shear stress sensor using side-implanted piezoresistive tethers," *Proceedings of SPIE*, 2007, pp. 1-11.

[13] K.-Y. Ng, J. Shajii, and M. a Schmidt, "A liquid shear-stress sensor fabricated using wafer bonding technology," *Solid-State Sensors and Actuators*, 1991, pp. 931-934.

المنارة للاستشارات
www.manaraa.com

[14] M. Schmidt, R. Howe, S. Senturia, and J. Haritonidis, "Design and calibration of a microfabricated floating-element shear-stress sensor," *IEEE Transactions on Electron Devices*, vol. 35, 2002, pp. 750-757.

[15] J. Zhe, V. Modi, and K.R. Farmer, "A microfabricated wall shear-stress sensor with capacitative sensing," *Journal of Microelectromechanical Systems*, vol. 14, Feb. 2005, pp. 167-175.

[16] T. Pan, D. Hyman, M. Mehregany, E. Reshotko, S. Garverick, and C. Western, "Microfabricated shear stress sensors , part 1 : design and fabrication shear stress and its measurement," *AIAA Journal*, vol. 37, 1999, pp. 66-72.

[17] L. Baxter, *Capacitive Sensors Design and Applications*, New York: IEEE Press, 1997.

[18] M. Gad-el-Hak, "Flow control: The future," *Journal of Aircraft*, vol. 38, May. 2001, pp. 402-418.

[19] M.R. Alam, W. Liu, and G. Haller, "Closed-loop separation control: An analytic approach," *Physics of Fluids*, vol. 18, 2006, pp. 1-13.

[20] J.K. Jeyapalan, "Future outlook for pipeline materials, methods, and maintenance," *Pipelines*, 2003, pp. 104-106.

[21] V. Chandrasekharan, "A Microscale Differential Capacitive Direct Wall Shear Stress Sensor," Ph.D. Dissertation: University of Florida, Gainesville, 2009.

[22] Y. Li, "Side-implanted piezoresistive shear stress sensor for turbulent Boundary layer measurement," Ph.D. Dissertation: University of Florida, Gainesville, 2008.

[23] R.S. Mackay and B. Jacobson, "Endoradiosonde," *Nature*, 1957, pp. 1239-1240.

[24] J.T. Farrar, V.K. Zworykin, and J. Baum, "Pressure-sensitive telemetering capsule for study of gastrointestinal motility," *Science*, vol. 126, 1957, pp. 975-975.

[25] H. Sprung and M. Ardenne, "Über Versuche mit einem verschluckbaren Intestinalsender," *Naturwissenschaften*, 1958, pp. 154-159.

[26] F. Heppner, G. Lanner, and H. Rodler, "Telemetry of intracranial pressure," *Acta Neurochirurgica*, vol. 33, Mar. 1976, pp. 37-43.

[27] H. Dill, "Designing inductors for thin-film applications," *Electron. Design*, vol. 12, 1964, pp. 52-59.

[28] A. Kuck, F.M. Liebman, and L. Kussick, "A miniature transmitter for telemetering muscle potentials," *IEEE Transactions on Biomedical Engineering*, vol. 10, Jul. 1963, pp. 117-119.

المنارة للاستشارات

www.manaraa.com

[29] R.S. Mackay, “Radio telemetering from within the body,” *Science*, vol. 134, 1961, pp. 1196-1202.

[30] A.M. Connell and E.N. Rowlands, “Wireless telemetering from the digestive tract,” *Gut*, vol. 1, Sep. 1960, pp. 266-272.

[31] C.C. Collins, “Miniature passive pressure transensor for implanting in the eye.,” *IEEE Transactions on Biomedical Engineering*, vol. 14, Apr. 1967, pp. 74-83.

[32] S. Chatzandroulis and D. Tsoukalns, “Capacitance to frequency converter suitable for sensor applications using telemetry,” *International Conference on Electronics, Circuits and Systems*, 2001, pp. 1791-1794.

[33] A.D. DeHennis and K.D. Wise, “A wireless microsystem for the remote sensing of pressure, temperature, and relative humidity,” *Journal of Microelectromechanical Systems*, vol. 14, Feb. 2005, pp. 12-22.

[34] Q. Huang and M. Oberle, “A 0.5-mW passive telemetry IC for biomedical applications,” *IEEE Journal of Solid-State Circuits*, vol. 33, Jul. 1998, pp. 937-946.

[35] T. Aubert, O. Elmazria, and M.B. Assouar, “Wireless and batteryless surface acoustic wave sensors for high temperature environments,” *International Conference on Electronic Measurement & Instruments*, Aug. 2009, pp. 890-898.

[36] A. Saitoh and T. Nomura, “Wireless sensor system using surface acoustic wave devices,” *ICCAS-SICE, 2009*, IEEE, 2009, pp. 2359-2363.

[37] Y.-S. Huang, Y.-Y. Chen, and T.-T. Wu, “A passive wireless hydrogen surface acoustic wave sensor based on Pt-coated ZnO nanorods.,” *Nanotechnology*, vol. 21, Mar. 2010, pp. 1-6.

[38] M. Zourob, K.G. Ong, K. Zeng, F. Mouffouk, and C.A. Grimes, “A wireless magnetoelastic biosensor for the direct detection of organophosphorus pesticides.,” *The Analyst*, vol. 132, Apr. 2007, pp. 338-43.

[39] M.K. Jain and C.A. Grimes, “A wireless magnetoelastic micro-sensor array for simultaneous measurement of temperature and pressure,” *IEEE Transactions on Magnetics*, vol. 37, Jul. 2001, pp. 2022-2024.

[40] K.G. Ong, K. Zeng, X. Yang, K. Shankar, C. Ruan, and C. a Grimes, “Quantification of multiple bioagents with wireless, remote-query magnetoelastic microsensors,” *IEEE Sensors Journal*, vol. 6, Jun. 2006, pp. 514-523.

[41] T. Harpster, B. Stark, and K. Najafi, “A passive wireless integrated humidity sensor,” *Sensors and Actuators A: Physical*, vol. 95, Jan. 2002, pp. 100-107.

المنارة للاستشارات
www.manaraa.com

[42] K. Ong, C.A. Grimes, C.L. Robbins, and R.S. Singh, "Design and application of a wireless, passive, resonant-circuit environmental monitoring sensor," *Sensors and Actuators A: Physical*, vol. 93, Aug. 2001, pp. 33-43.

[43] J. Garcia-Canton, A. Merlos, and A. Baldi, "High-quality factor electrolyte insulator silicon capacitor for wireless chemical sensing," *IEEE Electron Device Letters*, vol. 28, Jan. 2007, pp. 27-29.

[44] M. Lei, A. Baldi, E. Nuxoll, R.A. Siegel, and B. Ziaie, "A hydrogel-based implantable micromachined transponder for wireless glucose measurement," *Diabetes Technology & Therapeutics*, vol. 8, 2006, pp. 112-122.

[45] K.G. Ong, J. Wang, R.S. Singh, L.G. Bachas, and C. a Grimes, "Monitoring of bacteria growth using a wireless, remote query resonant-circuit sensor: application to environmental sensing.," *Biosensors & bioelectronics*, vol. 16, Jun. 2001, pp. 305-312.

[46] K.G. Ong, K. Zeng, and C.A. Grimes, "A wireless, passive carbon nanotube-based gas sensor," *IEEE Sensors Journal*, vol. 2, Apr. 2002, pp. 82-88.

[47] D.G. Hill and K.L. Allen, "Improved instrument for the measurement of c.s.f. pressures by passive telemetry," *Medical & Biological Engineering & Computing*, vol. 15, Nov. 1977, pp. 666-672.

[48] R.L. Cooper, D.G. Beale, and I.J. Constable, "Passive radiotelemetry of intraocular pressure in vivo: calibration and validation of continual scleral guard-ring applanation transensors in the dog and rabbit.," *Investigative ophthalmology & visual science*, vol. 18, Sep. 1979, pp. 930-938.

[49] L. Rosengren, Y. Backlund, T. Sjostrom, B. Hok, and B. Svedbergh, "A system for wireless intra-ocular pressure measurements using a silicon micromachined sensor," *Journal of Micromechanics and Microengineering*, vol. 2, 1992, pp. 202-204.

[50] L. Rosengren, P. Rangsten, Y. Blacklund, B. Hök, B. Svedbergh, and G. Selén, "A system for passive implantable pressure sensors," *Sensors and Actuators A: Physical*, vol. 43, May. 1994, pp. 55-58.

[51] E.C. Park, J.B. Yoon, and E. Yoon, "Hermetically sealed inductor-capacitor (LC) resonator for remote pressure monitoring," *Japanese Journal of Applied Physics*, vol. 37, 1998, pp. 7124-7128.

[52] K.G. Ong and C.A. Grimes, "A resonant printed-circuit sensor for remote query monitoring of environmental parameters," *Smart Materials and Structures*, vol. 9, 2000, pp. 421-428.

[53] O. Akar, T. Akin, and K. Najafi, "A wireless batch sealed absolute capacitive pressure sensor," *Sensors and Actuators A: Physical*, vol. 95, Dec. 2001, pp. 29-38.

المنارة للاستشارات
www.manaraa.com

[54] A. Baldi, W. Choi, and B. Ziaie, "A self-resonant frequency-modulated micromachined passive pressure transensor," *IEEE Sensors Journal*, vol. 3, Dec. 2003, pp. 728-733.

[55] J.M. English and M.G. Allen, "Wireless micromachined ceramic pressure sensors," *IEEE International Conference on Micro Electro Mechanical Systems*, Ieee, 1999, pp. 511-516.

[56] J.M. English, "Wireless micromachined ceramic pressure sensors for high temperature environments," Ph.D. Dissertation: Georgia Institute of Technology, Atlanta, 2000.

[57] M.A. Fonseca, J.M. English, M. von Arx, and M.G. Allen, "Wireless micromachined ceramic pressure sensor for high-temperature applications," *Journal of Microelectromechanical Systems*, vol. 11, Aug. 2002, pp. 337-343.

[58] M.A. Fonseca, M.G. Allen, J. Kroh, and J. White, "Flexible wireless passive pressure sensors for biomedical applications," *Solid-State Sensors, Actuators and Microsystems*, Hilton Head, SC: 2006, pp. 37-42.

[59] M.G. Allen, "Micromachined endovascularly-implantable wireless aneurysm pressure sensors: from concept to clinic," *Solid-State Sensors, Actuators and Microsystems*, 2005, pp. 275-278.

[60] P.-J. Chen, S. Saati, R. Varma, M.S. Humayun, and Y.-C. Tai, "Wireless intraocular pressure sensing using microfabricated minimally invasive flexible-coiled LC sensor implant," *Journal of Microelectromechanical Systems*, vol. 19, Aug. 2010, pp. 721-734.

[61] P.-J. Chen, D.C. Rodger, S. Saati, M.S. Humayun, and T. Yu-Chong, "Microfabricated implantable parylene-based wireless passive intraocular pressure sensors," *Journal of Microelectromechanical Systems*, vol. 17, Dec. 2008, pp. 1342-1351.

[62] J.E. Acuna, J.L. Rodriguez, and F. Obelleiro, "Modeling double-side printed meander-line inductors on printed circuit boards," *International Journal of RF and Microwave Computer-Aided Engineering*, vol. 13, Mar. 2003, pp. 105-112.

[63] H. Bryan, "Printed inductors and capacitors," *Tele-Tech & Electronic Industries*, vol. 14, 1955, pp. 68-124.

[64] F.W. Grover, "Tables for the calculation of the mutual inductance of any two coaxial single-layer coils," *Proceedings of the Institute of Radio Engineers*, vol. 21, 1933, pp. 1039-1049.

[65] F.E. Terman, *Radio Engineers' Handbook*, McGraw-Hill New York, 1943.

[66] H.A. Wheeler, "Simple inductance formulas for radio coils," *Proceedings of the Institute of Radio Engineers*, vol. 16, 1928, pp. 1398-1400.

[67] H. Greenhouse, "Design of planar rectangular microelectronic inductors," *IEEE Transactions on Parts, Hybrids, and Packaging*, vol. 10, Jun. 1974, pp. 101-109.

المنارة للاستشارات

www.manaraa.com

[68] H. Green, "A simplified derivation of the capacitance of a two-wire transmission line," *IEEE Transactions on Microwave Theory and Techniques*, vol. 47, 1999, pp. 365-366.

[69] C. Neagu, H. Jansen, a Smith, J. Gardeniers, and M. Elwenspoek, "Characterization of a planar microcoil for implantable microsystems," *Sensors and Actuators A: Physical*, vol. 62, Jul. 1997, pp. 599-611.

[70] G. Grandi, M.K. Kazimierczuk, a Massarini, and U. Reggiani, "Stray capacitances of single-layer solenoid air-core inductors," *IEEE Transactions on Industry Applications*, vol. 35, 1999, pp. 1162-1168.

[71] S. Horowitz, T.-an Chen, V. Chandrasekaran, K. Tedjojuwono, L. Cattafesta, T. Nishida, and M. Sheplak, "A wafer-bonded, floating element shear-stress sensor using a geometric moire optical transduction technique," *Proc. Hilton Head Islands*, 2004, pp. 1-6.

[72] S. Horowitz, T. Chen, V. Chandrasekaran, K. Tedjojuwono, T. Nishida, L. Cattafesta, and M. Sheplak, "A micromachined geometric moire interferometric floating-element shear stress sensor," *AIAA Aerospace Sciences Meeting*, Reno, NV: 2004, pp. 1-10.

[73] F.A. Fischer, *Fundamentals of Electroacoustics*, Interscience Publishers, 1955.

[74] J. Weber, W. Albers, J. Tuppurainen, M. Link, R. Gabl, W. Wersing, and M. Schreiter, "Shear mode FBARs as highly sensitive liquid biosensors," *Sensors and Actuators A: Physical*, vol. 128, Mar. 2006, pp. 84-88.

[75] V. Chandrasekharan, J. Sells, D.P. Arnold, and M. Sheplak, "Characterization of a MEMS-based floating element shear stress sensor," *AIAA Aerospace Sciences Meeting*, Orlando, FL: 2009, pp. 1-11.

[76] Y. Li, V. Chandrasekharan, B. Bertolucci, T. Nishida, L. Cattafesta, and M. Sheplak, "A MEMS shear stress sensor for turbulence measurements," *AIAA Aerospace Sciences Meeting*, 2008, pp. 1-11.

[77] Agilent Technologies, *User's Guide: HP 8719D*, 1999.

[78] Y. Wang, Y. Jia, Q. Chen, and Y. Wang, "A passive wireless temperature sensor for harsh environment applications," *Sensors*, vol. 8, Dec. 2008, pp. 7982-7995.

[79] O. Larsson, X. Wang, M. Berggren, and X. Crispin, "Proton motion in a polyelectrolyte: A probe for wireless humidity sensors," *Sensors and Actuators B: Chemical*, vol. 143, Jan. 2010, pp. 482-486.

[80] Z. Chen and C. Lu, "Humidity sensors: A review of materials and mechanisms," *Sensor Letters*, vol. 3, 2005, pp. 274-295.

[81] B. Tao, J. Zhang, F. Miao, H. Li, L. Wan, and Y. Wang, "Capacitive humidity sensors based on Ni/SiNWs nanocomposites," *Sensors and Actuators B: Chemical*, vol. 136, 2009, pp. 144-150.

المنارة للاستشارات
www.manaraa.com

[82] J. Das, S.M. Hossain, S. Chakraborty, and H. Saha, "Role of parasitics in humidity sensing by porous silicon," *Sensors and Actuators A: Physical*, vol. 94, Oct. 2001, pp. 44-52.

[83] F. Miao, B. Tao, L. Sun, T. Liu, J. You, L. Wang, and P.K. Chu, "Capacitive humidity sensing behavior of ordered Ni/Si microchannel plate nanocomposites," *Sensors and Actuators A: Physical*, 2010, pp. 1-29.

[84] H. Li, J. Zhang, B.R. Tao, L.J. Wan, and W.L. Gong, "Investigation of capacitive humidity sensing behavior of silicon nanowires," *Physica E: Low-dimensional Systems and Nanostructures*, vol. 41, 2009, pp. 600-604.

[85] G.D. Francia, A. Castaldo, E. Massera, and I. Nasti, L, "A very sensitive porous silicon based humidity sensor," *Sensors and Actuators B: Chemical*, vol. 111, 2005, pp. 135-139.

[86] D.B. De Graaff and J.K. Eaton, "Reynolds-number scaling of the flat-plate turbulent boundary layer," *Journal of Fluid Mechanics*, vol. 422, Nov. 2000, pp. 319-346.

[87] E.-S. Zanoun, F. Durst, and H. Nagib, "Evaluating the law of the wall in two-dimensional fully developed turbulent channel flows," *Physics of Fluids*, vol. 15, 2003, pp. 3079-3089.

[88] K. Winter, "An outline of the techniques available for the measurement of skin friction in turbulent boundary layers," *Progress in aerospace sciences*, vol. 18, 1979, pp. 1-57.

[89] W.K. George and L. Castillo, "Zero-pressure-gradient turbulent boundary layer," *Applied Mechanics Reviews*, vol. 50, 1997, pp. 689-729.

[90] R.E. Bolz and G.L. Tune, *CRC Handbook of Tables for Applied Engineering Science*, CRC Press, 1973.

[91] K.H. Ng and D.B. Spalding, "Turbulence model for boundary layers near walls," *Physics of Fluids*, vol. 15, 1972, pp. 20-30.

[92] Agilent Technologies, *Agilent 4294A Precision Impedance Analyzer Operation Manual*, 2003.

[93] A. Ulman, "Formation and structure of self-assembled monolayers," *Chemical Reviews*, vol. 96, 1996, pp. 1533-1554.

[94] M. Wasilik and A. Pisano, "Low frequency process for silicon on insulator deep reactive ion etching," *Proc. SPIE*, 2001, pp. 1-11.

[95] J. Wei, T.C. Duc, and P.M. Sarro, "Study on 2-level DRIE for 3D MEMS structures," *stw.nl*, pp. 494-497.

المنارة للاستشارات

www.manaraa.com

[96] C.D. Meyer, S.S. Bedair, B.C. Morgan, and D.P. Arnold, "Micromachined thick-film copper power inductors and transformers for integrated power converters," *Solid-State Sensors, Actuators and Microsystems*, Hilton Head Island, SC: 2010, pp. 455-458.

[97] J. Coosemans, "A readout circuit for an intra-ocular pressure sensor," *Sensors and Actuators A: Physical*, vol. 110, Feb. 2004, pp. 432-438.

[98] H.S. Kim, S. Sivaramakrishnan, A.S. Sezen, and R. Rajamani, "A novel real-time capacitance estimation methodology for battery-less wireless sensor systems," *IEEE Sensors Journal*, vol. 10, Oct. 2010, pp. 1647-1657.

[99] R. Nopper, R. Niekrawietz, L. Reindl, and A.A. Model, "Wireless readout of passive LC sensors," *IEEE Transactions on Instrumentation and Measurement*, vol. 59, 2010, pp. 2450-2457.

[100] M. Nowak, E. Colinet, N. Delorme, F. Conseil, and G. Jacquemod, "A wireless sensing platform for battery-free sensors," *2008 IEEE International Symposium on Circuits and Systems*, May. 2008, pp. 2122-2125.

[101] B. Peterson, A. Olson, and T. Kaiser, "A wireless sensor interrogator design for passive resonant frequency sensors using frequency modulation spectroscopy," *IEEE Sensors Journal*, 2010, pp. 1-8.

[102] S.F. Pichorim and P.J. Abatti, "A novel method to read remotely resonant passive sensors in biotelemetric systems," *IEEE Sensors Journal*, vol. 8, Jan. 2008, pp. 3-8.

[103] V. Chandrasekaran, A. Cain, T. Nishida, L. Cattafesta, and M. Sheplak, "Dynamic calibration technique for thermal shear-stress sensors," *Experiments in Fluids*, vol. 38, Jul. 2005, pp. 56-65.

المنارة للاستشارات

www.manaraa.com

BIOGRAPHICAL SKETCH

Jeremy Sells was born in Key West, Florida, and raised on the island of St. John in the US Virgin Islands. He returned to the mainland to finish high school in New Hampshire and went on to receive his B.S. degree in electrical engineering from the University of Maine at Orono in 2005. His interests in sensors and RF devices brought him to the University of Florida, where he joined the Interdisciplinary Microsystems Group working on capacitive shear stress sensors and wireless sensor array integration. He received his M.S. degree in 2009 and is currently working toward a Ph.D. degree in electrical engineering. He is also a NASA fellow and research assistant at the University of Florida.

المنارة للاستشارات
www.manaraa.com